Distribution Agreement

In presenting this thesis or dissertation as a partial fulfillment of the requirements for an advanced degree from Emory University, I hereby grant to Emory University and its agents the non-exclusive license to archive, make accessible, and display my thesis or dissertation in whole or in part in all forms of media, now or hereafter known, including display on the world wide web. I understand that I may select some access restrictions as part of the online submission of this thesis or dissertation. I retain all ownership rights to the copyright of the thesis or dissertation. I also retain the right to use in future works (such as articles or books) all or part of this thesis or dissertation.

Signature:

_____ _____

Tao Jin Date

Mechanism of Molecular Triplet Excited State Generation in Quantum Dot-Molecule Complex

By

Tao Jin

Doctor of Philosophy

Chemistry

_____

Dr. Tianquan Lian

Advisor

_____

Dr. Brian Dyer

Committee Member

_____

Dr. Francesco Evangelista

Committee Member

Accepted:

_____

Kimberly Jacob Arriola, Ph.D., MPH.

Dean of the James T. Laney School of Graduate Studies

_____

Date

Mechanism of Molecular Triplet Excited State Generation in Quantum Dot-Molecule Complex

By

Tao Jin

B.S., University of Science and Technology of China, P.R. China, 2016

Advisor: Tianquan Lian, Ph.D.

An abstract of

A dissertation submitted to the Faculty of the

James T. Laney School of Graduate Studies of Emory University

in partial fulfillment of the requirements for the degree of

Doctor of Philosophy

in Chemistry

2022

Abstract

Mechanism of Molecular Triplet Excited State Generation in Quantum Dot-Molecule Complex

By Tao Jin

Efficient generation of molecular triplet excited states has been extensively studied as it is a critical step in systems of photon-upconversion, photodynamic therapy and photocatalysis. Recently, quantum dot (QD) has been developed to sensitize or enhance molecular triplet excited state generation (TESG) because of its unique properties compared to traditional molecular sensitizers. Despite the emerging progress achieved in QD sensitized/assisted TESG, thorough understanding of the TESG mechanism in QD-molecule complexes have not been accomplished. In this dissertation, we investigate the TESG mechanism in QD-molecule complexes with transient absorption spectroscopy (TA) and time-resolved photoluminescence (TRPL).

First, we tested whether QD sensitized triplet energy transfer (TET) is mediated by charge transfer virtual state by studying the shell-thickness dependent TET coupling strength in CdSe/CdS core/shell QD attached with 9-anthracene carboxylic acid (ACA). The measured TET coupling strength decreases exponentially with CdS shell thickness, and the exponential decay factor β is smaller than the sum of βs for electron transfer and hole transfer from QD. We propose that core/shell QD sensitized TET is mediated by both higher-energy virtual exciton states in CdSe/CdS QD and the charge transfer virtual state.

Second, we studied the correlation between QD bright/dark states and QD sensitized TET with CdSe/CdS core/shell QD-oligothiophene as a model system. We tuned the equilibrium between QD bright and dark states by varying temperature, and TET dynamics were measured with TA. We demonstrated the significant contribution of both bright and dark states to TET, which was attributed to the components with triplet-state-like spin characters in bright/dark state wavefunctions.

Furthermore, we examined the TET from trap states in CdSe QDs to adsorbed ACA with TA and TRPL and showed that both band edge and trap excitons can be transferred from QDs to generate ACA triplet excited states. The rate of TET decreases with decreasing trap exciton energies and is much slower than the TET rate from band edge excitons.

Finally, we demonstrated the TESG in CdSe QD-modified boron dipyrromethene (BODIPY) with charge separated intermediate state under excitation of either QD or BODIPY, and this TESG pathway kinetically competes the direct TET pathway.

Mechanism of Molecular Triplet Excited State Generation in Quantum Dot-Molecule Complex

By

Tao Jin

B.S., University of Science and Technology of China, P.R. China, 2016

Advisor: Tianquan Lian, Ph.D.

A dissertation submitted to the Faculty of the

James T. Laney School of Graduate Studies of Emory University

in partial fulfillment of the requirements for the degree of

Doctor of Philosophy

in Chemistry

2022

ACKNOWLEDGEMENT

First of all, I would like to express my most sincere gratitude to Dr. Tianquan Lian, for his guidance, support and patience throughout my graduate study. His professional training in project proposal, experiment design, data interpretation and analysis and article writing has equipped me to become a qualified scientist. His expertise in physical chemistry and critical thinking have inspired me to pursue comprehensive understanding of the field of my projects. The discussions with him have always been helpful for me to overcome obstacles and advance my projects. He has also been providing me with valuable advice in scientific career development. The experience with Dr. Lian in my graduate study would be an unforgettable and invaluable part for my whole career. I also would like to extend my deepest gratitude to my committee members, Dr. Brian Dyer and Dr. Francesco Evangelista, for their insightful feedbacks on my research progress.

I am also grateful to Dr. Zihao Xu for his helpful training on management of the laboratory setups, practical suggestions on my research and persistent support in my daily life. Many thanks to my previous and current labmates, Dr. Wenxing Yang, Dr. Aimin Ge, Dr. Laura Kiefer, Dr. Chaoyu Li, Dr. Qiuyang Li, Dr. Jia Song, Dr. Qiongyi Shang, Dr. Yawei Liu, Dr. Dhritiman Bhattacharyya, Qiliang Liu, Sara Gebre, Jinhui Meng, Fengyi Zhao, Sheng He, Sa Suo, Paul Jin, Isaac Tangen and Zhicheng Yang for their kind support both inside and outside labs. I have been enjoying your company during the past six years. I would also appreciate my collaborators, Dr. Eilaf Egap, Dr. Alexey Kaledin, Dr. Ming Lee Tang, Dr. Yifan Zhu and Tingting Huang for their help in providing molecular and nanocrystal samples and calculation support for my projects.

Finally, I would like to express my deep love to my family, my father, my mother and my sister for their firm and selfless support. Their unconditional encouragement always motivates me to charge forward in my entire life.

Table of Contents

List of Figures

List of Tables

rate constant k_{2f}. b_u is the percentage of different configurations of BODIPY binding to QD surface. k_{3u} stands for the rate constant of electron transfer from BODIPY to QD after generation of ^{1}BODIPY*. k_{4u} is the rate constant of intrinsic decay of ^{1}BODIPY* to form ground state. k_{5u} and k_{6u} are the rate constants of charge recombination of CS state to form ground state and ^{3}BODIPY*, respectively. p is the percentage of QD with one or more BODIPY attached..... 206

Chapter 1. Introduction

1.1 Molecular triplet excited state sensitized by quantum dot through triplet energy transfer

1.1.1 Quantum dot sensitized triplet energy transfer in triplet-triplet annihilation based upconversion

Molecular triplet excited states have found promising applications in photon-upconversion, photocatalysis and photodynamic therapy.[1-6] Access of triplet excited states of the photosensitizers with light excitation can initiate photocatalytic organic synthesis reactions and can generate highly reactive singlet oxygen ($^1O_2$) through energy transfer for photodynamic therapy.[4, 6] Another intriguing application of triplet excited states is photon-upconversion based on triplet-triplet annihilation (TTA), which has been applied in solar cells and photocatalysis to overcome the Shockley-Queisser limit by converting photons below the semiconductor bandgap energies into higher-energy photons.[7-10] TTA based upconversion is also appealing in bioimaging application due to its ability to convert near-infrared (NIR) photons with long penetration length in tissues into visible photons.[11] As shown in Figure 1.1a, a conventional TTA scheme involves multiple steps including photo-excitation of the molecular sensitizer, intersystem crossing (ISC) to generate the sensitizer triplet excited states, triplet energy transfer (TET) from the sensitizer to the annihilator, TTA of two annihilators to form one annihilator at singlet excited state and finally the emission of fluorescence from the singlet excited state.[1] The most developed photosensitizer for TTA based upconversion so far is the heavy-metal organic complexes owing to their long-lived triplet states at room temperature.[1, 10, 12-13] One key disadvantage of these photosensitizers is the large energy loss during the ISC, which is detrimental to achieve large anti-stoke shift (ΔE_{UC}) in the

upconversion system.[13-15] In order to overcome this disadvantage, recent research has turned to develop alternative molecular sensitizers including molecules exhibiting thermally activated delayed fluorescence and direct S_0-to-T_1 absorbing osmium complexes.[15] Although inspiring progress has been achieved, these sensitizers still require complicated molecular design and synthesis procedures to acquire desired photophysical properties for the TTA systems.

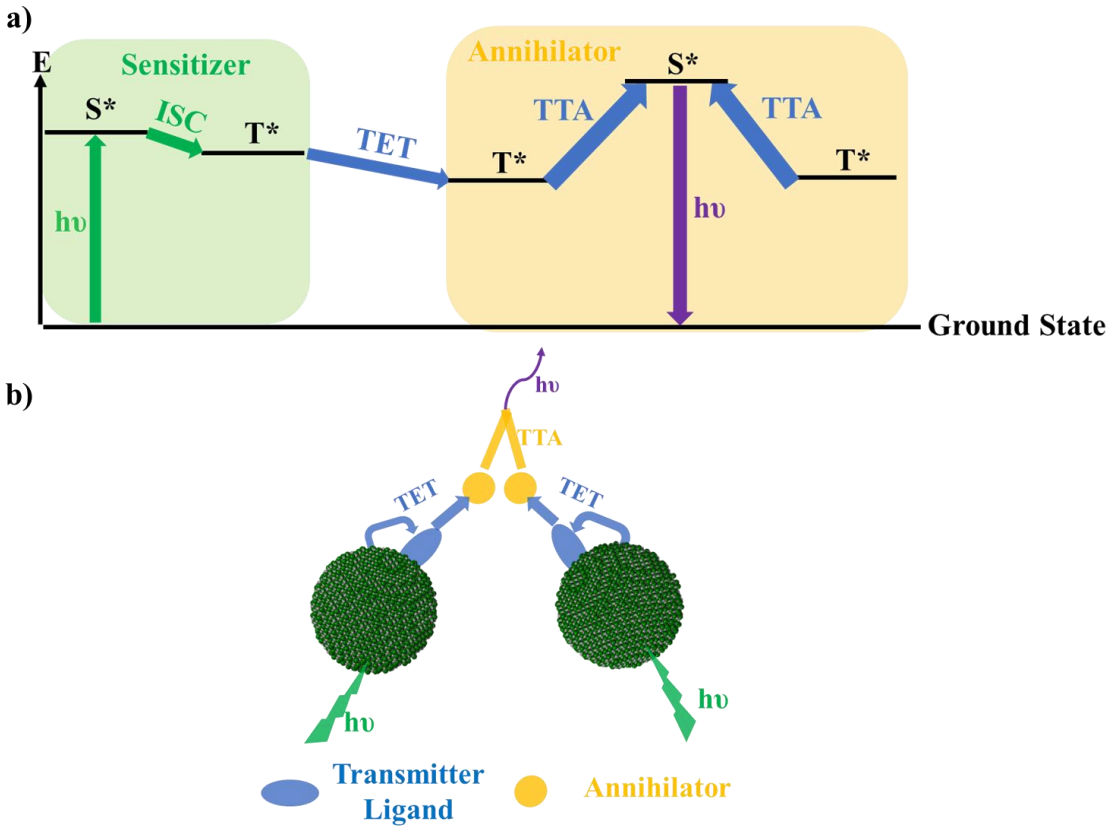

Figure 1.1: a). Energy level diagram and key processes in molecule-based TTA upconversion systems involving ISC of the sensitizer to its triplet excited state (T*), TET from sensitizer to annihilator and TTA of two annihilator triplets. b). Scheme of TTA upconversion with QD as sensitizers.

One effective approach to avoid energy loss in ISC and to achieve relatively simple material

design and synthesis for the sensitizer is to apply quantum dot (QD) as the sensitizer, as shown in Figure 1.1b.[15-16] Because of the strong spin-orbit coupling and electron-hole exchange interaction in QDs, the singlet and triplet characters are mixed in the exciton states (bright and dark excitons), and the energy difference between bright and dark excitons is typically 1-100 meV so that energy loss in ISC is circumvented in QD based TTA systems.[17-19] Photophysical properties of QDs including conduction/valance band edge positions and exciton binding energies can be readily tuned by the size and surface ligand of QD through well-established and feasible synthesis procedures.[19-20] In addition, QDs possess other advantages including broad absorption spectral range and large extinction coefficient compared to molecular sensitizers.[21-22] Inspired by these unique properties of QDs, TTA systems with QDs as photosensitizers have received intense research interest in recent years.[16] Early research by Tang and Bardeen's group demonstrated the TTA based upconversion with PbSe QD as sensitizer and rubrene as annihilator, which could achieve ΔE_{UC} = 0.67 eV with upconversion efficiency Φ_{UC} = 0.01% (with maximum Φ_{UC} of 100%) under 800 nm excitation.[23] The low Φ_{UC} was attributed to inefficient TET from PbSe QD to free rubrene through the tunneling barrier of the long alkyl chain ligand on QD.[23] Aiming to improve the Φ_{UC}, Tang's group attached transmitter ligand 4-(tetracene-5-yl) benzoic acid onto PbSe and PbS QD surface.[24] With triplet excited state energy of the transmitter ligand in between exciton energy of QD and triplet excited state energy of the annihilator, excitons in QD would undergo TET to populate triplet states of the transmitter ligand, followed by TET from the transmitter ligand to the annihilator, as demonstrated in Figure 1.1b.[24] The introduction of the transmitter ligand enhanced Φ_{UC} from 0.021% to 1.7% for PbS QDs.[24] Similar enhancement effect was observed in TTA systems with PbSe QDs and CdSe QDs as sensitizers.[23-24] Based on this TTA scheme, various strategies have been developed to enhance the Φ_{UC}, including but not limited to sub-monolayer

shell growth on QD to passivate trap states, introduction of midgap state or electron/hole level by cation adsorption or doping, shortening of the alkyl chain ligand on QD and quality improvement of QD by synthesis.[25-32] The improved Φ_{UC} reaches 11.8% and 24% for PbS QD and CdSe QD system, respectively.[30, 32] By careful choice and engineering of the transmitter ligand and the annihilator, photons with energy low as or below silicon bandgap (1.12 eV) was successfully upconverted to visible light photons for PbS QD TTA systems.[33-34] Research efforts have also demonstrated the utilization of other QDs including cesium lead halide perovskite QD, $CuInS_2$ QD, Si nanocrystals and InP QD for upconversion of visible or NIR light with efficiency around 10%, as shown in Figure 1.2.[35-40] In addition, the QD sensitized TTA was extended to solid-state architecture by Bulović, Bawendi and Baldo's groups in films of PbS QDs and dibenzotetraphenyl periflanthene-doped rubrene with ΔE_{UC} around 0.49 eV and Φ_{UC} lower than 1% at half sun excitation intensity, and the Φ_{UC} can be further improved to 7% with improved device structure.[31, 41] All the research progress has shown the promising prospect of TTA upconversion based on triplet excited state generation from QD.

In order to improve the overall performance of the QD based TTA upconversion system, one has to consider one key step in the scheme: TET from QDs to the transmitter or to the emitter. Evaluation of the overall performance of TTA systems usually involves two parameters, one of which is threshold excitation intensity I_{th} defined as:

$$I_{th} = (\alpha \Phi_{TET} 8\pi D_T a_0)^{-1} (\tau_T)^{-2} \qquad \text{Eq. 1.1}$$

where α is the absorption coefficient at the excitation wavelength, Φ_{TET} in QD based system is the efficiency of TET from QD (to the transmitter) to the annihilator, D_T is the diffusion constant of triplet state annihilator, a_0 is the annihilation distance between triplet state annihilator, and τ_T is the lifetime of the annihilator triplet excited state.[42] The other parameter is the upconversion efficiency

Φ_{UC}, which can be expressed as:

$$\Phi_{UC} = f\Phi_{ISC}\Phi_{TET}\Phi_{TTA}\Phi_{FL} \qquad \text{Eq. 1.2}$$

where Φ_{ISC}, Φ_{TET}, Φ_{TTA} and Φ_{FL} in QD based TTA systems are the efficiencies of QD ISC (equals 1), TET from QD (to the transmitter) to the annihilator, TTA of annihilators and annihilator fluorescence, respectively, and *f* is the spin statistical factor representing probability of obtaining singlet excited state after TTA of two annihilators.[43] As shown in Eq. 1.1 and Eq. 1.2, improving efficiency of QD sensitized TET is an effective approach to decrease I_{th} and increase Φ_{UC}. Further improvement of QD sensitized TET efficiency requires comprehensive understanding of its mechanism, which involves scientific questions including whether QD sensitized TET follows theoretical models of TET in molecular donor-acceptor complexes and how complexity of band structures and surfaces of QDs would affect TET mechanism and pathways.

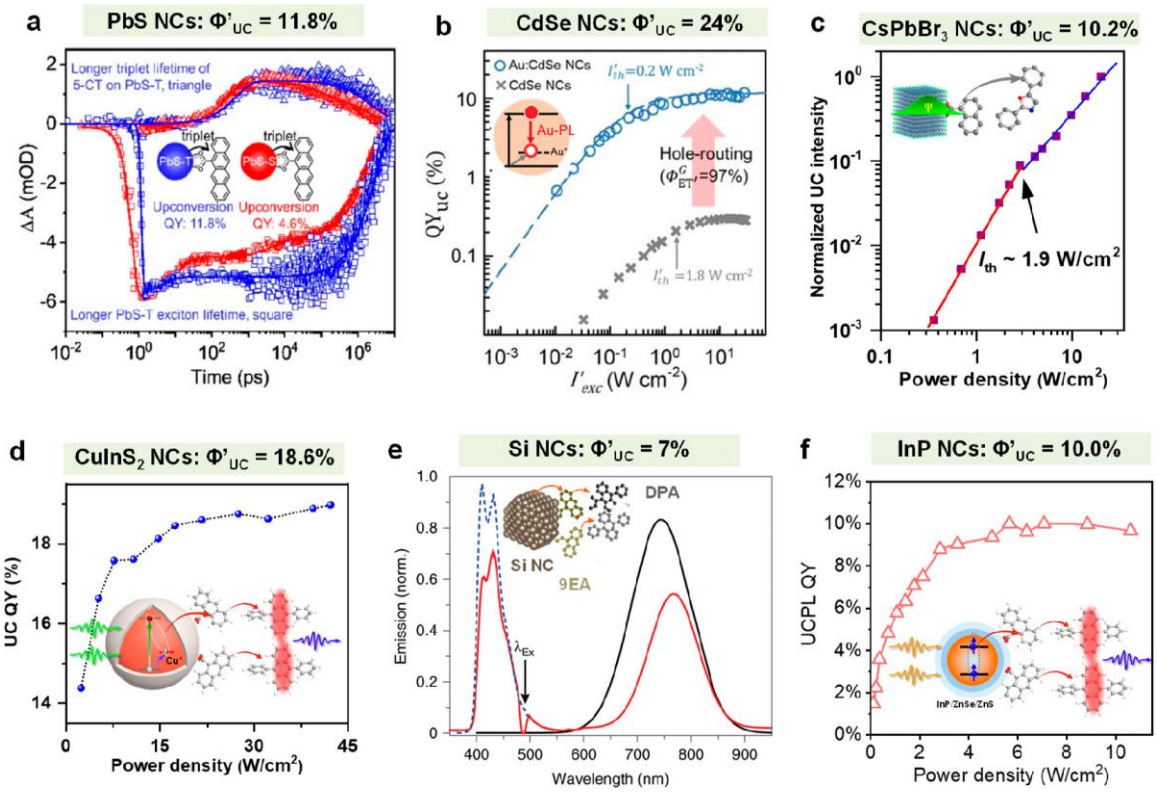

Figure 1.2: QD based TTA upconversion systems with high upconversion efficiency. a). PbS QD

sensitized TTA with Φ_{UC} of 11.8%. Adapted with permission from *J. Am. Chem. Soc.* **2019**, 141, 9769-9772. Copyright American Chemical Society 2019. b). Au doped CdSe QD sensitized TTA with Φ_{UC} of 24%. Adapted with permission from *Adv. Mater.* **2020**, 32, 2002953. Copyright John Wiley & Sons 2020. c). $CsPbBr_3$ QD sensitized TTA with Φ_{UC} of 10.2%. Adapted with permission from *J. Phys. Chem. Lett.* **2019**, 10, 5036-5040. Copyright American Chemical Society 2019. d). $CuInS_2$/ZnS QD sensitized TTA with Φ_{UC} of 18.6%. Adapted with permission from *J. Am. Chem. Soc.* **2019**, 141, 13033-13037. Copyright American Chemical Society 2019. e). Si QD sensitized TTA with Φ_{UC} of 10.0%. Adapted from *Nat. Chem.* **2020**, 12, 137-144. Copyright Springer Nature 2020. f). InP/ZnSe/ZnS QD sensitized TTA with Φ_{UC} of 10.0%. Adapted with permission from *J. Am. Chem. Soc.* **2020**, 142, 19825-19829. Copyright American Chemical Society 2020. This figure is adapted with permission from *ACS Energy Lett.* **2021**, 6, 9, 3151-3166. Copyright American Chemical Society 2021.

1.1.2 Theoretical model for triplet energy transfer

Mechanism of TET was examined originally by Dexter.[44] In the Dexter's model, TET rate follows the Fermi Golden rule:

$$k_{TET} = \frac{2\pi}{\hbar}|V|^2 FCWD \qquad \text{Eq. 1.3}$$

where *V* is the TET coupling strength, and FCWD is the Frank-Condon overlap weighted density of states.[44] It was assumed that *V* for TET is the two-electron exchange integral expressed as:

$$|V|^2 = |Z|^2 \propto \left| \int \varphi_a'^{*}(r_1)\varphi_b'(r_1)\frac{1}{r_{12}}\varphi_a^*(r_2)\,\varphi_b(r_2) \right|_{IF}^2 \qquad \text{Eq. 1.4}$$

where φ_i' and φ_i are the electronic wavefunctions of the excited state and ground state, respectively, and i = a or b represents the donor and the acceptor, respectively. Eq. 1.4 is in the form of electronic wavefunction overlap and decays exponentially with distance:

$$|V|^2 \propto e^{-\beta_{TET} * r} \qquad \text{Eq. 1.5}$$

In Eq. 1.5, β_{TET} is the exponential decay factor, and r is the distance between donor and acceptor.[44] Harcourt et al. later included the ionic configuration terms (charge transfer virtual state) $|a^+b^->$ and $|a^-b^+>$ into initial and final wavefunctions for coupling strength of TET between chemically bond donor and acceptor (as shown in Figure 1.3a) and yielded the coupling strength to be:

$$V \approx \frac{T_{ET}T_{HT}}{A_{ET}} + \frac{T_{HT}T_{ET}}{A_{HT}} - Z \qquad \text{Eq. 1.6}$$

where Z is the two-electron exchange term in Dexter's theory, T_{ET} and T_{HT} are the one-electron matrix elements of virtual electron and hole transfer, respectively, and A_{ET} and A_{HT} are the energy differences between the local donor excited state ($|a^*b>$) and electron/hole transfer virtual states ($|a^+b^->$ and $|a^-b^+>$).[45] Calculations with local molecular orbitals by Scholes et al. showed that the first two terms (through-configuration terms) in Eq. 1.6 dominate over the two-electron exchange term.[46] The result is consistent with the Closs model that TET can be considered as simultaneous electron and hole transfer, as shown in Figure 1.3b.[47-48] Accordingly, exponential decay factor for TET is the sum of those for electron and hole transfer:

$$\beta_{TET} = \beta_{ET} + \beta_{HT} \qquad \text{Eq. 1.7}$$

More recently, Skourtis et al. concluded that contribution of virtual bridge exciton states with electron and hole both on bridge unit to TET coupling strength would be significant for case of long bridge length and lower tunneling energy gap in donor-bridge-acceptor complex, as shown in Figure 1.3c, and β_{TET} in this scheme would deviate from that in TET mediated by charge transfer virtual state.[49-50] It should be noted that the bridge exciton states in the model are not populated during TET and should be differentiated from proposed TET mechanisms of other research in certain systems that TET can switch from tunneling to multistep hopping in donor-

bridge-acceptor systems with real bridge exciton state intermediates when the bridge length is long enough.[51-52]

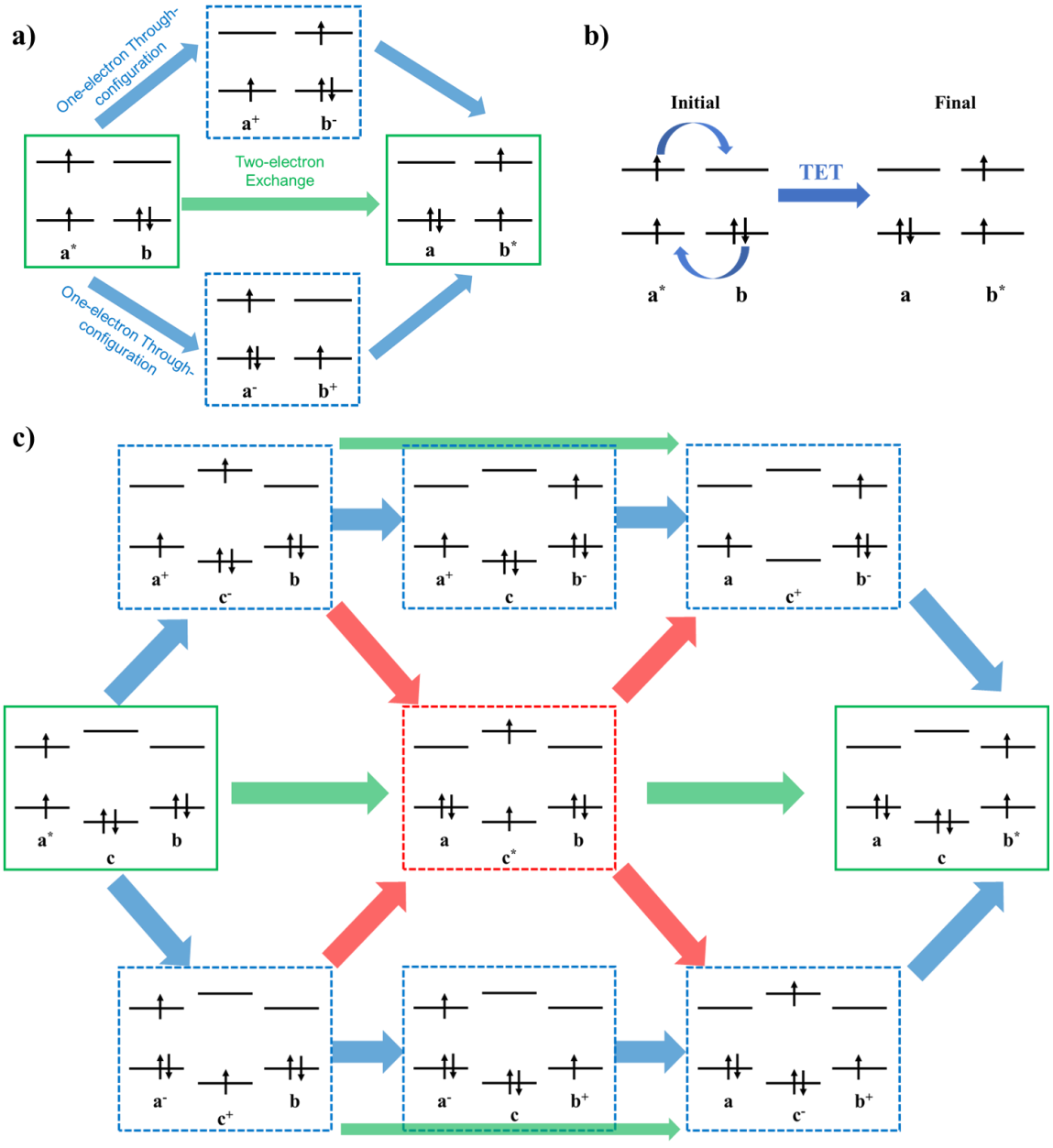

Figure 1.3: TET mechanisms and pathways. a). TET pathways in donor (a)-acceptor (b) systems consisting of direct Dexter exchange mechanism with two-electron exchange integral as coupling strength term (green arrows) and pathways mediated by charge transfer virtual states (dashed blue boxes) with one-electron integral terms as coupling strength (blue arrows). The green boxes denote

local excited states of donor and acceptor. b). With contribution of TET mediated by charge transfer virtual state to TET coupling strength greater than that of exchange integral, TET can be considered as simultaneous electron and hole transfer from the donor to the acceptor. c). Potential TET pathways in donor (a)-bridge (c)-acceptor (b) systems. Green boxes denote local excited states of donor and acceptor, dashed blue boxes represent charge transfer virtual states, and dashed red box represents the virtual bridge exciton state. Green arrows are the two-particle interactions, blue arrows are the one-particle interactions with charge transfer virtual states, and red arrows are the one-particle interactions with virtual bridge exciton state.

FCWD in Eq. 1.3 can be written as the spectral overlap between the donor and the acceptor:

$$FCWD = \int f_a(E)F_b(E)dE \qquad \text{Eq. 1.8}$$

where f_a (E) and F_b (E) are the normalized donor T_1-S_0 emission spectrum and acceptor S_0-T_1 absorption bands.[44, 53-55] Because of the spin forbidden nature of the S_0-T_1 transition, it is hard to evaluate FCWD of TET with Eq. 1.8. Alternatively, within harmonic oscillator approximation, FCWD can be expressed as:

$$FCWD = \frac{1}{(4\pi\lambda_{ab}k_BT)^{1/2}}\sum_{n=0}^{\infty}\sum_{m=0}^{\infty} e^{-s_a}e^{-s_b}\left(\frac{{s_a}^n}{n!}\right)\left(\frac{{s_b}^m}{m!}\right)\exp\left(-\frac{(\Delta G+\lambda_{ab}+n\hbar\omega_a+m\hbar\omega_b)^2}{4\lambda_{ab}k_BT}\right) \qquad \text{Eq. 1.9}$$

in which s_a and s_b are the electron-vibration coupling constants for the donor and the acceptor, $\hbar\omega_a$ and $\hbar\omega_b$ are the spacing of vibrational energy levels for the donor and the acceptor, ΔG is the free energy change for TET and λ_{ab} is the total reorganization energy of the donor and acceptor.[56-59] The parameters in Eq. 1.9 can be obtained from fitting of the phosphorescence spectra of the donor and the acceptor.[60] Within the classical treatment of low-frequency mode, FCWD for TET can be simplified as the formula in Marcus theory:[61]

$$FCWD = \frac{1}{(4\pi\lambda_{ab}k_BT)^{1/2}}\exp\left(-\frac{(\Delta G+\lambda_{ab})^2}{4\lambda_{ab}k_BT}\right) \qquad \text{Eq. 1.10}$$

1.1.3 Mechanism studies of quantum dot sensitized triplet energy transfer

Because TET from quantum dot to the transmitter ligand or to the annihilator is one key step to determine the overall upconversion efficiency in QD sensitized TTA systems, mechanism studies of QD sensitized TET have been conducted since the discovery of QD sensitized TTA.[16, 62] The prerequisite of studying TET mechanism is to determine the TET rate. QD sensitized TET rate k_{TET} can be calculated from the TET efficiency Φ_{TET} as:

$$\Phi_{TET} = \sum_i \frac{a_i k_{TET}}{k_{TET} + k_{QD,i}} \qquad \text{Eq. 1.11}$$

where $k_{QD,i}$ and a_i are the rate constant and amplitude of the *i*th component of the intrinsic decay of QD without attached TET acceptor measured from time-resolved photoluminescence (TRPL) or transient absorption spectroscopy (TA).[52] A more direct approach to obtain TET rate is to measure the decay kinetics of QD excitons with presence of TET acceptor and the growth kinetics of the acceptor triplet excited states with TRPL and TA.[63-65] Direct TET from QD to the acceptor without intermediates can be confirmed by faster QD exciton decay with the acceptor compared to QD without acceptor in TRPL/TA and the simultaneous growth of the acceptor triplet states along with the QD exciton decay in TA, as shown in Figure 1.4a-b.[65] TET rate can be calculated as:

$$k_{TET} = \frac{1}{<\tau_{QD-acceptor}>} - \frac{1}{<\tau_{QD}>} \qquad \text{Eq. 1.12}$$

In the equation, $<\tau_{QD-acceptor}>$ and $<\tau_{QD}>$ are the average weighted lifetimes of QD exciton decay with and without acceptor, respectively, calculated from multiexponential or stretch exponential fitting of the QD exciton decay in TRPL/TA.[64, 66] When the TET acceptor is attached to QD, TET rate is related to the average number of adsorbed acceptors per QD, and it is of interest

to determine TET rate from QD to one attached acceptor (intrinsic TET rate) denoted as $k_{i\,TET}$. The number of adsorbed acceptors on each QD (n) follows Poisson distribution:

$$P(m,n) = \frac{m^n e^{-m}}{n!} \qquad \text{Eq. 1.13}$$

where m is the average number of adsorbed acceptors per QD.[65, 67] Within this model, $k_{i\,TET}$ can be calculated from kinetics of QD exciton decay and acceptor triplet growth as:

$$[A]_T^*(t) = [QD]^*(0) \sum_n P(m,n) \sum_j a_j n k_{i\,TET} \left(1 - \frac{e^{-\left(k_{QD,j} + n k_{i\,TET}\right)t}}{k_{QD,j} + n k_{i\,TET}}\right) \qquad \text{Eq. 1.14}$$

$$[QD]^*(t) = [QD]^*(0)\left(e^{m\left[e^{-k_{i\,TET}} - 1\right]}\right) \sum_j a_j e^{-k_{QD,j}} \qquad \text{Eq. 1.15}$$

where $[A]_T^*(t)$ and $[QD]^*(t)$ are the acceptor triplet states and QD exciton population at time *t* in QD-acceptor complex, respectively, $k_{QD,j}$ and a_j are the rate constant and amplitude of the *j*th component of the intrinsic decay of QD without attached TET acceptor.[65]

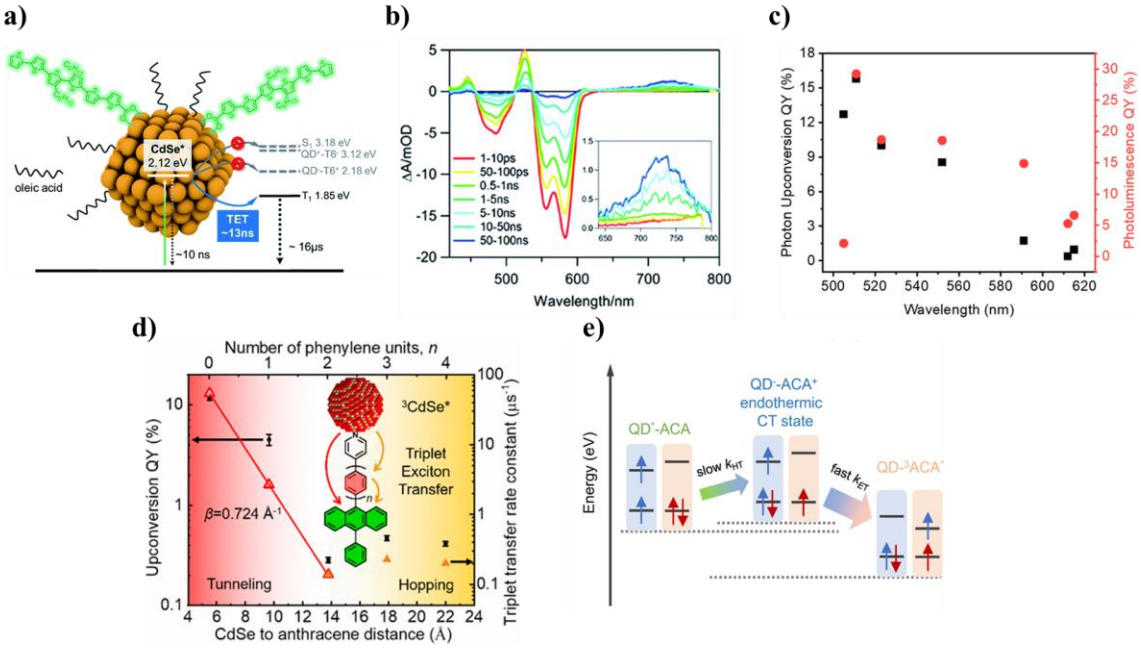

Figure 1.4: Mechanism studies of QD sensitized TET. a). Scheme of direct TET from CdSe QD to attached functionalized oligothiophene (T6). The energy alignment indicates that direct TET from QD to T6 is the only energetically allowed process. b). TA spectra of CdSe QD-T6 complex

after excitation of QD at 520 nm. Simultaneous decay of QD exciton bleach at 580 nm and growth of T6 triplet state absorption at 720 nm suggests direct TET process. a) and b) adapted with permission from *Chem. Sci.* **2019**, 10, 6120-6124. Copyright Royal Society of Chemistry 2019. c). Photominescence quantum yield (red circles) and photon upconversion quantum yield (black squares) as function of $1S_h$-$1S_e$ absorption peak position of CdSe QD in CdSe QD-ACA-diphenyl anthracene (DPA) TTA upconversion system. Adapted with permission from *J. Chem. Phys.* **2020**, 153, 114702. Copyright AIP Publishing 2020. d). Upconversion quantum yield and TET rate constant as function of phenylene bridge length in CdSe QD-anthracene with phenylene bridge-DPA TTA system. Adapted with permission from *J. Am. Chem. Soc.* **2020**, 142, 41, 17581-17588. Copyright American Chemical Society 2020. e). Scheme of endothermic charge transfer mediated TET in CdSe/ZnS core/shell QD-ACA complex. Adapted with permission from *Nat. Commun.* **2021**, 12, 1532. Copyright Springer Nature 2021.

In order to unravel the mechanism of QD sensitized TET, researchers have been focusing on testing whether Eq. 1.3-Eq. 1.10, which describe TET mechanism in molecular donor-acceptor systems, can be applied to QD sensitized TET.[62] The driving force for TET can be tuned by QD size.[68] It has been demonstrated that rate of QD sensitized TET and accordingly the upconversion efficiency increase with decreasing QD size (increasing driving force) in PbS (Se)-rubrene and CdSe-ACA systems, as shown in Figure 1.4c.[68-70] The results may suggest that QD sensitized TET lies in the Marcus normal region described by Eq. 1.10, although it was not demonstrated whether TET rate exactly follows Eq. 1.9 or Eq. 1.10. Another study of PbS QD attached with TIPS-tetracene carboxylic acid by Rao's group shows that while TET from the attached ligand to QD follows Marcus-Hush theory, the reverse process, which is TET from QD to the tetracene ligand,

does not show dependence on QD size and may be rationalized by indirect TET mediated by intermediates.[71] When QD exciton energy is close to energy of acceptor triplets, reverse TET from acceptor back to QD after the initial TET from QD will be manifested and can result in thermally activated delayed fluorescence of QD.[72-74] It should be noted that change of QD size in these systems not only change the driving force for TET but also will alter the coupling strength for TET, which complicates the rigorous examination of Eq. 1.9 or Eq. 1.10 in QD sensitized TET.[75]

Research has also been devoted to studying the factors for changing coupling strength of QD sensitized TET and how these factors will affect the TET rate.[62] It has been demonstrated that the coupling strength and TET rate can be tuned by the length of tunneling barrier between QD and acceptor, which can be changed by inorganic shell thickness, acceptor bridge units and the QD native ligand length.[25, 31, 52, 76-77] In these studies, TET rate generally decreases exponentially with shell thickness, acceptor bridge length and QD native ligand length (shown in Figure 1.4d), which is consistent with model for coupling strength of direct TET in molecule systems described by Eq. 1.4-Eq. 1.6. The studies have also shown that these parameters will bring about additional effects to change the TET mechanism. Growth of sub-monolayer shell may passivate surface trap states and suppress detrimental side pathways, which enhances the TET efficiency.[25, 78] Increase of acceptor bridge units will switch TET from tunneling to hopping from QD to acceptor and result in weak dependence of TET rate on bridge length when bridge unit number reaches 4-5.[52] Decrease of QD native ligand alters TET coupling strength by varying dielectric constant of the medium and leads to deviation of native ligand length dependence of TET rate from Eq. 1.5 at short ligand length.[31] Other studies show that TET coupling strength can also be tuned by QD size and acceptor binding geometry.[79-80]

Despite the promising research progress for studying coupling strength for QD sensitized

TET, the rigorous model for describing the coupling strength has not been fully established. It is unclear whether one-electron integrals representing TET mediated by charge transfer virtual states are the dominating terms in TET coupling strength of QD sensitized TET, and whether QD sensitized TET can be considered as simultaneous electron and hole transfer from QD. There has been only one study on testing this hypothesis by comparing the attenuation of TET rate as function of shell thickness to that of electron and hole surface wavefunction densities as function of shell thickness in CdSe/ZnS core/shell QD-ACA complex.[81] The result shows that exponential decay factor for TET β_{TET} is consistent with that for hole transfer β_{HT} instead of the sum of β for electron and hole transfer, as expressed in Eq. 1.7. The authors proposed the endothermic hole-transfer-mediated TET, in which charge-transfer state is populated transiently by hole transfer from QD to ACA before formation of ACA triplet excited state, to rationalize the results (as shown in Figure 1.4e). However, it is not clear whether such model can be generally applied to other systems. In the work presented in Chapter 3, we studied the coupling strength of TET from CdSe/CdS core/shell QD to ACA by varying shell thickness to test the hypothesis whether QD sensitized TET can be considered as simultaneous electron and hole transfer. The result reveals the shallower dependence of TET coupling strength on shell thickness than those of electron and hole transfer on shell thickness, which cannot be explained by either charge transfer virtual state mediated TET or endothermic charge transfer mediated TET. Instead, TET mediated by virtual exciton states with energy higher than that of $1S_h$-$1S_e$ exciton was proposed to account for the result.

1.2 Quantum dot exciton properties and quantum dot sensitized triplet energy transfer

Besides examining whether TET mechanism in molecular donor-acceptor systems is applicable to QD sensitized TET, one should note the unique QD exciton properties compared to

molecular sensitizers when studying the mechanism of QD sensitized TET. These exciton properties could bring about different TET mechanisms in QD-acceptor systems. This section briefly overviews the two aspects of QD exciton properties: exciton fine structures and trap states, as an introduction to the research work in Chapter 4 and Chapter 5 of this dissertation. The overview would mainly focus on CdSe QD, which is the QD applied for triplet excited state generation in this dissertation.

1.2.1 Exciton fine structures of quantum dot

The QD exciton fine structure generally refers to the modification of the originally degenerate exciton levels by other effects that can cause energy splitting.[17, 82] The wavefunctions of the originally degenerate exciton levels are usually constructed by the product of the electron and hole wavefunctions involved in the exciton transition.[17] These electron/hole wavefunctions can be well described with the multiband effective mass approximation.[83] More specifically, Luttinger & Kohn model has been applied to calculate the electron/hole wavefunctions near the edge of the conduction/valence bands, which are of more interest to researchers.[84] The model considers the coupling between conduction and valence bands by adding contributions of remote bands to electron/hole effective mass and including the Kane matrix element, which reflects the strength of band coupling, into Hamiltonian for electron/hole wavefunctions.[83] For wide bandgap QDs including CdSe QD and $CsPbBr_3$ QD, contribution of the conduction band to the valence band hole wavefunctions is neglected.[83] The basis functions for the Hamiltonian are the Bloch functions of the conduction and valence band u_{J,J_z} characterized by Bloch function angular momentum of electron/hole and the angular momentum projection (J and J_z) because of strong spin-orbit coupling in those QDs.[83] For CdSe QD, the Bloch functions for valence band edge holes u_{J_z} (J = 3/2) are:[17]

$$u_{3/2} = \frac{1}{\sqrt{2}}(X + iY)|\uparrow>, \quad u_{-3/2} = \frac{i}{\sqrt{2}}(X - iY)|\downarrow>$$
$$u_{1/2} = \frac{i}{\sqrt{6}}[(X + iY)|\downarrow> -2Z|\uparrow>], \; u_{-1/2} = \frac{1}{\sqrt{6}}[(X - iY)|\uparrow> +2Z|\downarrow>] \qquad \text{Eq. 1.16}$$

The calculated electron/hole wavefunctions are characterized by the total angular momentum $j = J + L$, where L is the envelope angular momentum, as well as the projection j and denoted as nQ_j, in which Q is the notation of smallest L in the wavefunctions.[83] For CdSe QD, the calculated electron wavefunctions for the lowest $1S_{3/2h}$-$1S_e$ exciton are:

$$\varphi_{\uparrow(\downarrow),e}(\boldsymbol{r}) = \xi_e(\boldsymbol{r})|S> |\uparrow(\downarrow)> \qquad \text{Eq. 1.17}$$

where $\xi_e(\boldsymbol{r})$ is the envelope function of the electron, $|S> |\uparrow(\downarrow)>$ is the Bloch function of the conduction band including the spin wavefunction. The calculated fourfold hole wavefunctions for $1S_{3/2h}$-$1S_e$ exciton characterized by total angular momentum projection M (±3/2 and ±1/2) are:

$$\varphi_M(\boldsymbol{r}) = 2\sum_{l=0,2} R_l(\boldsymbol{r})(-1)^{M-3/2}\sum_{m+\mu=M} C(l,m,M,\mu)Y_{l,m}u_\mu \qquad \text{Eq. 1.18}$$

where $R_l(\boldsymbol{r})$ is the radial function; *C (l, m, M, μ)* is the Wigner 3j symbol factor and $Y_{l,m}$ are spherical harmonic functions.[17] The eight-fold degenerate $1S_{3/2h}$-$1S_e$ exciton wavefunctions are product of electron/hole wavefunctions:

$$\Psi(\boldsymbol{r_e}, \boldsymbol{r_h}) = \varphi_{\uparrow(\downarrow)}(\boldsymbol{r_e})\varphi_M(\boldsymbol{r_h}) \qquad \text{Eq. 1.19}$$

Several factors can split the generate exciton levels. In CdSe QD, nanocrystal asymmetry (lattice asymmetry and the crystal shape asymmetry) and the electron-hole exchange interaction (short-range and long-range) have been included in calculation of exciton fine structure.[17, 85-86] In perovskite $CsPbBr_3$ QD, additional Rashba effect due to inversion-symmetry breaking has been taken into account.[82, 87] For CdSe QD, the corresponding Hamiltonian for $1S_{3/2h}$-$1S_e$ exciton was constructed as:[17]

	$\uparrow,3/2$	$\uparrow,1/2$	$\uparrow,-1/2$	$\uparrow,-3/2$	$\downarrow,3/2$	$\downarrow,1/2$	$\downarrow,-1/2$	$\downarrow,-3/2$
$\uparrow,3/2$	$\frac{-3\eta}{2}-\frac{\Delta}{2}$	0	0	0	0	0	0	0
$\uparrow,1/2$	0	$\frac{-\eta}{2}+\frac{\Delta}{2}$	0	0	$-i\sqrt{3}\eta$	0	0	0
$\uparrow,-1/2$	0	0	$\frac{\eta}{2}+\frac{\Delta}{2}$	0	0	$-i2\eta$	0	0
$\uparrow,-3/2$	0	0	0	$\frac{3\eta}{2}-\frac{\Delta}{2}$	0	0	$-i\sqrt{3}\eta$	0
$\downarrow,3/2$	0	$i\sqrt{3}\eta$	0	0	$\frac{3\eta}{2}-\frac{\Delta}{2}$	0	0	0
$\downarrow,1/2$	0	0	$i2\eta$	0	0	$\frac{\eta}{2}+\frac{\Delta}{2}$	0	0
$\downarrow,-1/2$	0	0	0	$i\sqrt{3}\eta$	0	0	$\frac{-\eta}{2}+\frac{\Delta}{2}$	0
$\downarrow,-3/2$	0	0	0	0	0	0	0	$\frac{-3\eta}{2}-\frac{\Delta}{2}$

Eq. 1.20 (adapted with permission from *Annual Review of Materials Science* **2000**, 30 (1), 475-521, Copyright Annual Reviews 2000)

The Hamiltonian splits the exciton levels into 5 sublevels characterized by total exciton angular momentum projection *F*, and the wavefunctions are:

$$\Psi_{-2}(\boldsymbol{r_e},\boldsymbol{r_h}) = \Psi_{\downarrow,-\frac{3}{2}}(\boldsymbol{r_e},\boldsymbol{r_h}) \qquad \text{Eq. 1.21a}$$

$$\Psi_{2}(\boldsymbol{r_e},\boldsymbol{r_h}) = \Psi_{\uparrow,\frac{3}{2}}(\boldsymbol{r_e},\boldsymbol{r_h}) \qquad \text{Eq. 1.21b}$$

$$\Psi_{1}^{U,L}(\boldsymbol{r_e},\boldsymbol{r_h}) = \mp iC^{+}\Psi_{\uparrow,\frac{1}{2}}(\boldsymbol{r_e},\boldsymbol{r_h}) + C^{-}\Psi_{\downarrow,\frac{3}{2}}(\boldsymbol{r_e},\boldsymbol{r_h}) \qquad \text{Eq. 1.21c}$$

$$\Psi_{-1}^{U,L}(\boldsymbol{r_e},\boldsymbol{r_h}) = \mp iC^{-}\Psi_{\uparrow,-\frac{3}{2}}(\boldsymbol{r_e},\boldsymbol{r_h}) + C^{+}\Psi_{\downarrow,-\frac{1}{2}}(\boldsymbol{r_e},\boldsymbol{r_h}) \qquad \text{Eq. 1.21d}$$

$$\Psi_{0}^{U,L}(\boldsymbol{r_e},\boldsymbol{r_h}) = \mp\frac{1}{\sqrt{2}}i\Psi_{\uparrow,-\frac{1}{2}}(\boldsymbol{r_e},\boldsymbol{r_h}) + \frac{1}{\sqrt{2}}\Psi_{\downarrow,\frac{1}{2}}(\boldsymbol{r_e},\boldsymbol{r_h}) \qquad \text{Eq. 1.21e}$$

where:

$$C^{\pm} = \sqrt{\frac{\sqrt{f^2+d}\pm f}{2\sqrt{f^2+d}}} \qquad \text{Eq. 1.21f}$$

$$f = (-2\eta+\Delta)/2 \qquad \text{Eq. 1.21g}$$

$$d = 3\eta^2 \qquad \text{Eq. 1.21h}$$

$$\eta = \left(\frac{a_{ex}}{a}\right)^3 \hbar\omega_{ST}\chi(\beta) \qquad \text{Eq. 1.21i}$$

Δ is the energy splitting from asymmetry of QD shape and lattice; $\hbar\omega_{ST}$ is the energy splitting of exciton states from electron-hole exchange interaction; a_{ex} is the bulk exciton Bohr radius; a is

the size of the QD; $\chi(\beta)$ is the dimensionless function in terms of electron/hole radial wavefunctions.[17] From the calculation of oscillator strength of these exciton sublevels, ±2 and 0^L have zero oscillator strength and thus are called dark states, while the other three sublevels ($\pm1^L$, $\pm1^U$ and 0^U) have relatively large oscillator strength and thus are called bright states.[17] In ensemble of CdSe QD with spherical shape in average, the energy alignment of the sublevels is shown in Figure 1.5a. Generally, dark states are lower in energy (several to tens of meVs) than bright states in CdSe QD.[17] The calculation result is consistent with the experimental result of PL Stokes shift with resonance excitation and long PL decay time at helium temperatures.[85, 88] Later research on temperature dependent exciton PL decay on CdSe QDs demonstrated the thermal equilibrium between bright and dark states, which can be tuned by varying temperature.[89] Similar calculation can be conducted to other QDs to reveal the exciton fine structure levels, and dark states lie below bright states in energy for most QDs studied.[90-91] However, special calculation result was obtained for $CsPbBr_3$ perovskite QD with bright states lying below dark states due to shift of exciton energy from Rashba effect (shown in Figure 1.5b).[82] For small-size perovskite QD, it was demonstrated experimentally and theoretically that dark states would still be lower in energy than bright states due to stronger electron-hole exchange interaction.[87, 92-94]

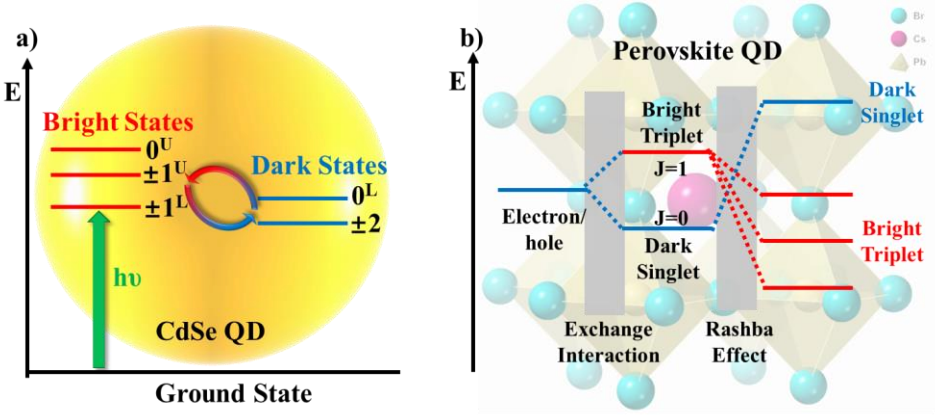

Figure 1.5: Exciton fine structures of CdSe QD (left) and $CsPbBr_3$ perovskite QD (right).

As suggested in QD exciton fine structures, spin of the exciton is not a good quantum number, and instead exciton states possess mixtures of singlet and triplet spin characters in wavefunctions.[17] Because the original TET mechanism is based on molecular donor where spin of the electron pair is good quantum number, whether TET mechanism or scheme varies for QD sensitized TET compared to molecule systems resulting from QD exciton fine structures will be one key question for QD sensitized TET mechanism research. So far it is unclear and has not been examined in experiment how QD exciton fine structures would affect TET process. In Chapter 4, we tuned the thermal equilibrium between bright and dark states in CdSe QD by changing temperature and monitored the QD sensitized TET dynamics. We concluded that both bright and dark states can undergo TET to form molecular triplet excited states due to the spin triplet characters in bright/dark state wavefunctions.

1.2.2 Triplet energy transfer from trap states of quantum dot

Another significant property of QD is the trap states. Trap state usually stems from the surface defects or dangling bond introduced in QD synthesis or post-synthesis treatment.[95-97] For certain QD including $CuInS_2$ QD, trap state is from the intrinsic electron/hole accepting levels of the materials.[98] Trap states can introduce significant change to QD photophysical properties. Because these states can accept electron/hole from band-edge excitons, they could lead to non-unity photoluminescence quantum yield in QD and also non-single-exponential TRPL or TA decay kinetics.[89, 99] In QDs including CdSe QD, CdS QD and InP QD, recombination of band-edge electron with hole in trap states results in trap state emission with lower energy and larger width than band-edge exciton emission, which has been attributed to broad distribution of trap states energies or strong electron-phonon coupling of trap state transition.[100-103] Trap states could also bring about complicated temperature-dependent PL kinetics, which has been rationalized by broad

distribution of trap state energy and trapping process described by Marcus electron transfer theory.[104-105] In addition, as the energy level that electron/hole resides is changed after trapping process, charge transfer dynamics from QDs can also be more complicated due to potential charge transfer from trap states.[106-108] Finally, trap states can be eliminated by inorganic shell growth on QDs and post-synthesis surface treatment, after which near-unity PL quantum yield and single-exponential PL decay can be achieved.[99, 109-110]

As trap states in QD can dramatically alter the QD photophysical properties, these states cannot be neglected in mechanism studies of QD sensitized TET. Unfortunately, how trap states would reshape the TET dynamics is still under debate and poorly understood. Some studies on TET sensitized by CdSe, CdS or PbS QDs have shown the enhanced TET or TTA efficiency with trap state passivation by inorganic shell passivation,[23, 26-27, 111] while other studies have revealed the trap states or surface states as intermediate for PbS, amine capped CdSe and $CuInS_2$ QD sensitized TET.[38, 112-113] The difficulty in studying role of trap states in TET mainly lies in the ambiguous trap state energetics and lack of clear spectroscopic signatures of these states. Herein in Chapter 5, we studied the role of trap states in TET from phosphonic acid capped CdSe QDs to attached ACA acceptor with TA and TRPL. The result shows the trap state mediated TET with slower rate but larger contribution to overall TET process compared to TET from band-edge excitons, and the TET rate from trap states decreases with decreasing trap state energy.

1.3 Molecular triplet excited state generation in quantum dot-molecule complex through charge transfer intermediate

Although molecular triplet excited state can be generated through TET from QD in QD-molecule complexes, an alternative scheme of research interest for harvesting triplet states in these

hybrid structures is through charge transfer intermediate. This scheme has been extensively studied in molecular systems with two moieties linked covalently.[114-119] Typical photophysical processes involved in the scheme include photo-excitation of one moiety in the complex to generate local singlet excited state (^{1}A*-B), electron transfer to the other moiety to form singlet charge separated intermediate state ($^1(A^{+\cdot}\text{-}B^{-\cdot})$) and charge recombination to form the triplet excited state on the excited moiety (^{3}A*-B).[114]

Two mechanisms have been proposed for the charge recombination to form triplet states. The first mechanism, radical pair intersystem crossing (RP-ISC), involves inter-conversion between singlet charge separated state (spin correlated radical pair) and spin correlated triplet radical pair (in between $^1(A^{+\cdot}\text{-}B^{-\cdot})$ and $^3(A^{+\cdot}\text{-}B^{-\cdot})$). The mechanism requires the spin-spin exchange interaction 2J in the radical pair to be comparable to the electron-nuclear hyperfine coupling so that singlet and triplet radical pair can be well mixed.[114] Charge recombination of the triplet radical pair leads to formation of the local triplet excited state. RP-ISC can be well distinguished in time-resolved electron paramagnetic resonance spectroscopy (TREPR) by the polarization pattern of the EPR transitions.[115, 120] Another distinct feature of RP-ISC is the magnetic field effect (MFE) of the triplet yield.[115] With stronger magnetic field, triplet radical pair undergoes Zeeman splitting into T_{+1}, T_0 and T_{-1} sublevels, and either T_{+1} or T_{-1} sublevel would be resonant with the singlet radical pair level S at certain magnetic field depending on the sign of 2J, which leads to the local maximum in the triplet yield as function of magnetic field (as shown in Figure 1.6a).[115] Further increase of magnetic field results in splitting of T_{+1} or T_{-1} away from S and thus decrease of triplet yield. In the other mechanism, spin-orbit charge transfer intersystem crossing (SOCT-ISC), triplet excited states can be generated through direct charge recombination of singlet charge transfer state, and the change in spin of the electron is accompanied by a large change in the molecular orbital angular

momentum.[121-123] As a result, triplet yield in SOCT-ISC is usually maximized when the two moieties are perpendicular to each other in geometry (as shown in Figure 1.6b).[122-123] Another feature of SOCT-ISC is the stronger dependence of triplet yield on solvent polarity compared to RP-ISC, considering that the interconversion of singlet and radical pair in RP-ISC is independent of solvent polarity.[121, 123]

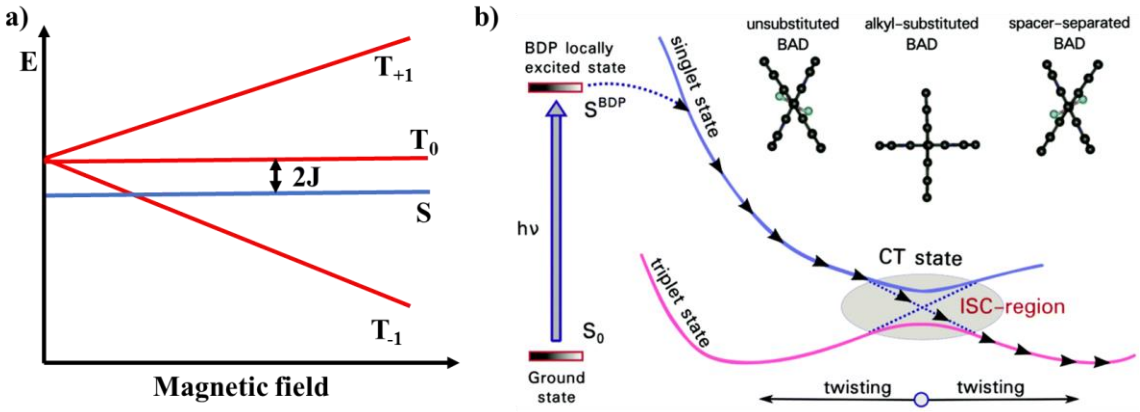

Figure 1.6: a). Energy levels of correlated singlet and triplet radical pair as function of magnetic field. b). Schematic mechanism of SOCT-ISC in a BODIPY (BDP)-anthracene dyads (BADs). Adapted with permission from *Phys. Chem. Chem. Phys.* **2018**, 20, 8016-8031. Copyright Royal Society of Chemistry 2018.

Inspired by the extensive research in triplet formation through charge recombination, researchers have recently demonstrated that similar scheme can be applied in QD-molecule complex to generate molecular triplet states.[124-129] Early research on CdS QD attached with thiol-modified bis(diarylamino)4,4'-biphenyl (TPD) showed that after excitation of TPD, charge transfer to CdS QD generates spin-correlated radical pair, which can form TPD triplet excited states (^{3}TPD*) through charge recombination.[124] Analysis of EPR spectrum of the complex yielded that RP-ISC is the dominating mechanism for charge recombination to form ^{3}TPD*, and the contribution of SOCT-ISC mechanism is relatively small.[124] More recently, sequential charge

transfer to generate molecular triplet excited states has been discovered in QD-molecule complexes.[129] If the initial charge transfer is energetically allowed, and the energy of charge transfer state is higher than molecular triplet excited states, then it is possible that excitation of QD can result in electron/hole transfer to the acceptor, and the following hole/electron transfer from the QD can generate the acceptor triplet states.[125-126] Such scheme has been proposed in PbS QD-pentacene derivatives, $CsPbBr_3$ QD-tetracene, $CsPbBr_3$ QD-Rhodamine B and CdS QD-alizarin complexes.[125-128] However, triplet excited state generation through charge transfer intermediate is still limited to few cases in QD-molecule complex. It is still ambiguous what the actual requirement of the system is for efficient triplet generation through this pathway and how this pathway would compete with other pathways for triplet generation including direct TET without intermediate. Herein, we demonstrated the triplet excited state generation of a modified boron dipyrromethene (BODIPY) in CdSe QD-BODIPY complex after excitation of BODIPY through charge transfer intermediate consisting of electron in QD conduction band and an oxidized BODIPY radical cation in Chapter 6. In Chapter 7, we showed that BODIPY triplet excited states can be generated in CdSe QD-BODIPY after excitation of QD with the same charge transfer intermediate as when BODIPY is excited, and BODIPY triplet generation pathways through this intermediate outcompete the direct TET from QD to BODIPY.

1.5 Reference

1. Singh-Rachford, T. N.; Castellano, F. N., Photon upconversion based on sensitized triplet–triplet annihilation. *Coord. Chem. Rev.* **2010,** *254* (21-22), 2560-2573.
2. Zhao, J.; Ji, S.; Guo, H., Triplet–triplet annihilation based upconversion: from triplet sensitizers and triplet acceptors to upconversion quantum yields. *RSC Advances* **2011,** *1* (6), 937.
3. Yanai, N.; Kimizuka, N., Stimuli-Responsive Molecular Photon Upconversion. *Angewandte Chemie International Edition* **2020,** *59* (26), 10252-10264.
4. Jarvi, Mark T.; Patterson, Michael S.; Wilson, Brian C., Insights into Photodynamic Therapy

Dosimetry: Simultaneous Singlet Oxygen Luminescence and Photosensitizer Photobleaching Measurements. *Biophysical Journal* **2012,** *102* (3), 661-671.
5. Welin, E. R.; Le, C.; Arias-Rotondo, D. M.; McCusker, J. K.; MacMillan, D. W. C., Photosensitized, energy transfer-mediated organometallic catalysis through electronically excited nickel(II). *Science* **2017,** *355* (6323), 380.
6. Strieth-Kalthoff, F.; James, M. J.; Teders, M.; Pitzer, L.; Glorius, F., Energy transfer catalysis mediated by visible light: principles, applications, directions. *Chem. Soc. Rev.* **2018,** *47* (19), 7190-7202.
7. Bharmoria, P.; Bildirir, H.; Moth-Poulsen, K., Triplet–triplet annihilation based near infrared to visible molecular photon upconversion. *Chemical Society Reviews* **2020,** *49* (18), 6529-6554.
8. Nattestad, A.; Cheng, Y. Y.; MacQueen, R. W.; Schulze, T. F.; Thompson, F. W.; Mozer, A. J.; Fückel, B.; Khoury, T.; Crossley, M. J.; Lips, K.; Wallace, G. G.; Schmidt, T. W., Dye-Sensitized Solar Cell with Integrated Triplet–Triplet Annihilation Upconversion System. *The Journal of Physical Chemistry Letters* **2013,** *4* (12), 2073-2078.
9. Lin, Y. L.; Koch, M.; Brigeman, A. N.; Freeman, D. M. E.; Zhao, L.; Bronstein, H.; Giebink, N. C.; Scholes, G. D.; Rand, B. P., Enhanced sub-bandgap efficiency of a solid-state organic intermediate band solar cell using triplet–triplet annihilation. *Energy & Environmental Science* **2017,** *10* (6), 1465-1475.
10. Gray, V.; Dzebo, D.; Abrahamsson, M.; Albinsson, B.; Moth-Poulsen, K., Triplet–triplet annihilation photon-upconversion: towards solar energy applications. *Physical Chemistry Chemical Physics* **2014,** *16* (22), 10345-10352.
11. Wohnhaas, C.; Mailänder, V.; Dröge, M.; Filatov, M. A.; Busko, D.; Avlasevich, Y.; Baluschev, S.; Miteva, T.; Landfester, K.; Turshatov, A., Triplet–Triplet Annihilation Upconversion Based Nanocapsules for Bioimaging Under Excitation by Red and Deep-Red Light. *Macromolecular Bioscience* **2013,** *13* (10), 1422-1430.
12. Nishimura, N.; Gray, V.; Allardice, J. R.; Zhang, Z.; Pershin, A.; Beljonne, D.; Rao, A., Photon Upconversion from Near-Infrared to Blue Light with TIPS-Anthracene as an Efficient Triplet–Triplet Annihilator. *ACS Materials Letters* **2019,** *1* (6), 660-664.
13. Fan, C.; Wei, L.; Niu, T.; Rao, M.; Cheng, G.; Chruma, J. J.; Wu, W.; Yang, C., Efficient Triplet-Triplet Annihilation Upconversion with an Anti-Stokes Shift of 1.08 eV Achieved by Chemically Tuning Sensitizers. *J Am Chem Soc* **2019,** *141* (38), 15070-15077.
14. Nastasi, F.; Puntoriero, F.; Campagna, S.; Diring, S.; Ziessel, R., Photoinduced intercomponent processes in multichromophoric species made of Pt(II)-terpyridine-acetylide and dipyrromethene-BF2 subunits. *Phys. Chem. Chem. Phys.* **2008,** *10* (27), 3982-6.
15. Yanai, N.; Kimizuka, N., New Triplet Sensitization Routes for Photon Upconversion: Thermally Activated Delayed Fluorescence Molecules, Inorganic Nanocrystals, and Singlet-to-Triplet Absorption. *Acc. Chem. Res.* **2017,** *50* (10), 2487-2495.
16. Han, Y.; He, S.; Wu, K., Molecular Triplet Sensitization and Photon Upconversion Using Colloidal Semiconductor Nanocrystals. *ACS Energy Letters* **2021,** *6* (9), 3151-3166.
17. Efros, A. L.; Rosen, M.; Kuno, M.; Nirmal, M.; Norris, D. J.; Bawendi, M., Band-edge exciton in quantum dots of semiconductors with a degenerate valence band: Dark and bright exciton states. *Phys. Rev. B* **1996,** *54* (7), 4843-4856.
18. and, A. L. E.; Rosen, M., The Electronic Structure of Semiconductor Nanocrystals. *Annual Review of Materials Science* **2000,** *30* (1), 475-521.
19. Scholes, G. D.; Rumbles, G., Excitons in nanoscale systems. *Nat. Mater.* **2006,** *5* (9), 683-96.
20. Zhu, H. M.; Lian, T. Q., Wavefunction engineering in quantum confined semiconductor

nanoheterostructures for efficient charge separation and solar energy conversion. *Energy & Environmental Science* **2012,** *5* (11), 9406-9418.
21. Yu, W. W.; Qu, L. H.; Guo, W. Z.; Peng, X. G., Experimental determination of the extinction coefficient of CdTe, CdSe, and CdS nanocrystals. *Chem. Mater.* **2003,** *15* (14), 2854-2860.
22. Cademartiri, L.; Montanari, E.; Calestani, G.; Migliori, A.; Guagliardi, A.; Ozin, G. A., Size-Dependent Extinction Coefficients of PbS Quantum Dots. *J. Am. Chem. Soc.* **2006,** *128* (31), 10337-10346.
23. Huang, Z.; Li, X.; Mahboub, M.; Hanson, K. M.; Nichols, V. M.; Le, H.; Tang, M. L.; Bardeen, C. J., Hybrid Molecule–Nanocrystal Photon Upconversion Across the Visible and Near-Infrared. *Nano Letters* **2015,** *15* (8), 5552-5557.
24. Huang, Z.; Simpson, D. E.; Mahboub, M.; Li, X.; Tang, M. L., Ligand enhanced upconversion of near-infrared photons with nanocrystal light absorbers. *Chem Sci* **2016,** *7* (7), 4101-4104.
25. Mahboub, M.; Huang, Z.; Tang, M. L., Efficient Infrared-to-Visible Upconversion with Subsolar Irradiance. *Nano Lett.* **2016,** *16* (11), 7169-7175.
26. Gray, V.; Xia, P.; Huang, Z.; Moses, E.; Fast, A.; Fishman, D. A.; Vullev, V. I.; Abrahamsson, M.; Moth-Poulsen, K.; Lee Tang, M., CdS/ZnS core-shell nanocrystal photosensitizers for visible to UV upconversion. *Chem. Sci.* **2017,** *8* (8), 5488-5496.
27. Huang, Z. Y.; Xia, P.; Megerdich, N.; Fishman, D. A.; Vullev, V. I.; Tang, M. L., ZnS Shells Enhance Triplet Energy Transfer from CdSe Nanocrystals for Photon Upconversion. *ACS Photonics* **2018,** *5* (8), 3089-3096.
28. Okumura, K.; Mase, K.; Yanai, N.; Kimizuka, N., Employing Core-Shell Quantum Dots as Triplet Sensitizers for Photon Upconversion. *Chem. Eur. J.* **2016,** *22* (23), 7721-6.
29. Mahboub, M.; Xia, P.; Van Baren, J.; Li, X.; Lui, C. H.; Tang, M. L., Midgap States in PbS Quantum Dots Induced by Cd and Zn Enhance Photon Upconversion. *ACS Energy Lett.* **2018,** *3* (4), 767-772.
30. Ronchi, A.; Capitani, C.; Pinchetti, V.; Gariano, G.; Zaffalon, M. L.; Meinardi, F.; Brovelli, S.; Monguzzi, A., High Photon Upconversion Efficiency with Hybrid Triplet Sensitizers by Ultrafast Hole-Routing in Electronic-Doped Nanocrystals. *Advanced Materials* **2020,** *32* (37), 2002953.
31. Nienhaus, L.; Wu, M.; Geva, N.; Shepherd, J. J.; Wilson, M. W. B.; Bulovic, V.; Van Voorhis, T.; Baldo, M. A.; Bawendi, M. G., Speed Limit for Triplet-Exciton Transfer in Solid-State PbS Nanocrystal-Sensitized Photon Upconversion. *ACS Nano* **2017,** *11* (8), 7848-7857.
32. Huang, Z.; Xu, Z.; Mahboub, M.; Liang, Z.; Jaimes, P.; Xia, P.; Graham, K. R.; Tang, M. L.; Lian, T., Enhanced Near-Infrared-to-Visible Upconversion by Synthetic Control of PbS Nanocrystal Triplet Photosensitizers. *J. Am. Chem. Soc.* **2019,** *141* (25), 9769-9772.
33. Nishimura, N.; Allardice, J. R.; Xiao, J.; Gu, Q.; Gray, V.; Rao, A., Photon upconversion utilizing energy beyond the band gap of crystalline silicon with a hybrid TES-ADT/PbS quantum dots system. *Chem. Sci.* **2019,** *10* (18), 4750-4760.
34. Gholizadeh, E. M.; Prasad, S. K. K.; Teh, Z. L.; Ishwara, T.; Norman, S.; Petty, A. J.; Cole, J. H.; Cheong, S.; Tilley, R. D.; Anthony, J. E.; Huang, S.; Schmidt, T. W., Photochemical upconversion of near-infrared light from below the silicon bandgap. *Nature Photonics* **2020,** *14* (9), 585-590.
35. Mase, K.; Okumura, K.; Yanai, N.; Kimizuka, N., Triplet sensitization by perovskite nanocrystals for photon upconversion. *Chem. Commun.* **2017,** *53* (59), 8261-8264.
36. Okumura, K.; Yanai, N.; Kimizuka, N., Visible-to-UV Photon Upconversion Sensitized by Lead Halide Perovskite Nanocrystals. *Chemistry Letters* **2019,** *48* (11), 1347-1350.

37. He, S.; Luo, X.; Liu, X.; Li, Y.; Wu, K., Visible-to-Ultraviolet Upconversion Efficiency above 10% Sensitized by Quantum-Confined Perovskite Nanocrystals. *J Phys Chem Lett* **2019,** *10* (17), 5036-5040.
38. Han, Y.; He, S.; Luo, X.; Li, Y.; Chen, Z.; Kang, W.; Wang, X.; Wu, K., Triplet Sensitization by "Self-Trapped" Excitons of Nontoxic CuInS2 Nanocrystals for Efficient Photon Upconversion. *J. Am. Chem. Soc.* **2019,** *141* (33), 13033-13037.
39. Lai, R.; Sang, Y.; Zhao, Y.; Wu, K., Triplet Sensitization and Photon Upconversion Using InP-Based Quantum Dots. *J. Am. Chem. Soc.* **2020,** *142* (47), 19825-19829.
40. Xia, P.; Raulerson, E. K.; Coleman, D.; Gerke, C. S.; Mangolini, L.; Tang, M. L.; Roberts, S. T., Achieving spin-triplet exciton transfer between silicon and molecular acceptors for photon upconversion. *Nat. Chem.* **2020,** *12* (2), 137-144.
41. Wu, M.; Congreve, D. N.; Wilson, M. W. B.; Jean, J.; Geva, N.; Welborn, M.; Van Voorhis, T.; Bulović, V.; Bawendi, M. G.; Baldo, M. A., Solid-state infrared-to-visible upconversion sensitized by colloidal nanocrystals. *Nat. Photon.* **2015,** *10*, 31-34.
42. Monguzzi, A.; Mezyk, J.; Scotognella, F.; Tubino, R.; Meinardi, F., Upconversion-induced fluorescence in multicomponent systems: Steady-state excitation power threshold. *Physical Review B* **2008,** *78* (19), 195112.
43. Zhou, Y.; Castellano, F. N.; Schmidt, T. W.; Hanson, K., On the Quantum Yield of Photon Upconversion via Triplet–Triplet Annihilation. *ACS Energy Letters* **2020,** *5* (7), 2322-2326.
44. L. J. Dexter, D., A Theory of Sensitized Luminescence in Solid. *J. Chem. Phys.* **1953,** *21*, 836-850.
45. Harcourt, R. D.; Scholes, G. D.; Ghiggino, K. P., Rate expressions for excitation transfer. II. Electronic considerations of direct and through–configuration exciton resonance interactions. *J. Chem. Phys.* **1994,** *101* (12), 10521-10525.
46. Scholes, G. D.; Harcourt, R. D.; Ghiggino, K. P., Rate expressions for excitation transfer. III. An ab initio study of electronic factors in excitation transfer and exciton resonance interactions. *J. Chem. Phys.* **1995,** *102* (24), 9574-9581.
47. Closs, G. L.; Piotrowiak, P.; MacInnis, J. M.; Fleming, G. R., Determination of long-distance intramolecular triplet energy-transfer rates. Quantitative comparison with electron transfer. *Journal of the American Chemical Society* **1988,** *110* (8), 2652-2653.
48. Closs, G. L.; Johnson, M. D.; Miller, J. R.; Piotrowiak, P., A Connection between Intramolecular Long-Range Electron, Hole, and Triplet Energy Transfers. *J. Am. Chem. Soc.* **1989,** *111* (10), 3751-3753.
49. Skourtis, S. S.; Liu, C.; Antoniou, P.; Virshup, A. M.; Beratan, D. N., Dexter energy transfer pathways. *Proc. Natl. Acad. Sci. U S A* **2016,** *113* (29), 8115-20.
50. Bai, S.; Zhang, P.; Antoniou, P.; Skourtis, S. S.; Beratan, D. N., Quantum interferences among Dexter energy transfer pathways. *Faraday Discuss* **2019,** *216* (0), 301-318.
51. Vura-Weis, J.; Abdelwahed, S. H.; Shukla, R.; Rathore, R.; Ratner, M. A.; Wasielewski, M. R., Crossover from single-step tunneling to multistep hopping for molecular triplet energy transfer. *Science* **2010,** *328* (5985), 1547-50.
52. Huang, Z.; Xu, Z.; Huang, T.; Gray, V.; Moth-Poulsen, K.; Lian, T.; Tang, M. L., Evolution from Tunneling to Hopping Mediated Triplet Energy Transfer from Quantum Dots to Molecules. *J Am Chem Soc* **2020,** *142* (41), 17581-17588.
53. Razi Naqvi, K.; Steel, C., Exchange-induced resonance energy transfer. *Chemical Physics Letters* **1970,** *6* (1), 29-32.
54. Lin, S. H., On the Theory of Non-Radiative Transfer of Electronic Excitation. *Proc. R. Soc.*

Lond. A. **1973,** *335* (1600), 51.
55. Davidovich, M. A.; Knox, R. S., On the rate of triplet excitation transfer in the diffusive limit. *Chemical Physics Letters* **1979,** *68* (2-3), 391-394.
56. Orlandi, G.; Monti, S.; Barigelletti, F.; Balzani, V., Triplet Energy-Transfer to Cis and Trans Stilbene - a Quantum-Mechanical Approach. *Chemical Physics* **1980,** *52* (3), 313-319.
57. Serpa, C.; Arnaut, L. G.; Formosinho, S. J.; Naqvi, K. R., Calculation of triplet–triplet energy transfer rates from emission and absorption spectra. The quenching of hemicarcerated triplet biacetyl by aromatic hydrocarbons. *Photochem. Photobiol. Sci.* **2003,** *2* (5), 616-623.
58. Lin, S. H.; Xiao, W. Z.; Dietz, W., Generalized Forster-Dexter theory of photoinduced intramolecular energy transfer. *Phys. Rev. E* **1993,** *47* (5), 3698-3706.
59. Sigman, M. E.; Closs, G. L., Free-Energy and Structure Dependence of Intramolecular Triplet Energy-Transfer in Organic-Model Compounds. *J Phys Chem-Us* **1991,** *95* (13), 5012-5017.
60. Murtaza, Z.; Graff, D. K.; Zipp, A. P.; Worl, L. A.; Jones, W. E.; Bates, W. D.; Meyer, T. J., Energy-Transfer in the Inverted Region - Calculation of Relative Rate Constants by Emission Spectral Fitting. *Journal of Physical Chemistry* **1994,** *98* (41), 10504-10513.
61. Subotnik, J. E.; Vura-Weis, J.; Sodt, A. J.; Ratner, M. A., Predicting accurate electronic excitation transfer rates via marcus theory with Boys or Edmiston-Ruedenberg localized diabatization. *J. Phys. Chem. A* **2010,** *114* (33), 8665-75.
62. Xu, Z.; Huang, Z.; Jin, T.; Lian, T.; Tang, M. L., Mechanistic Understanding and Rational Design of Quantum Dot/Mediator Interfaces for Efficient Photon Upconversion. *Acc. Chem. Res.* **2021,** *54* (1), 70-80.
63. Piland, G. B.; Huang, Z. Y.; Tang, M. L.; Bardeen, C. J., Dynamics of Energy Transfer from CdSe Nanocrystals to Triplet States of Anthracene Ligand Molecules. *J. Phys. Chem. C* **2016,** *120* (11), 5883-5889.
64. Mongin, C.; Garakyaraghi, S.; Razgoniaeva, N.; Zamkov, M.; Castellano, F. N., Direct observation of triplet energy transfer from semiconductor nanocrystals. *Science* **2016,** *351* (6271), 369-72.
65. Xu, Z.; Jin, T.; Huang, Y.; Mulla, K.; Evangelista, F. A.; Egap, E.; Lian, T., Direct triplet sensitization of oligothiophene by quantum dots. *Chem. Sci.* **2019,** *10* (24), 6120-6124.
66. Jin, T.; Lian, T., Trap state mediated triplet energy transfer from CdSe quantum dots to molecular acceptors. *J. Chem. Phys.* **2020,** *153* (7), 074703.
67. Chen, J.; Wu, K.; Rudshteyn, B.; Jia, Y.; Ding, W.; Xie, Z. X.; Batista, V. S.; Lian, T., Ultrafast Photoinduced Interfacial Proton Coupled Electron Transfer from CdSe Quantum Dots to 4,4'-Bipyridine. *J. Am. Chem. Soc.* **2016,** *138* (3), 884-92.
68. Mahboub, M.; Maghsoudiganjeh, H.; Pham, A. M.; Huang, Z. Y.; Tang, M. L., Triplet Energy Transfer from PbS(Se) Nanocrystals to Rubrene: the Relationship between the Upconversion Quantum Yield and Size. *Adv. Funct. Mater.* **2016,** *26* (33), 6091-6097.
69. Huang, Z. Y.; Li, X.; Yip, B. D.; Rubalcava, J. M.; Bardeen, C. J.; Tang, M. L., Nanocrystal Size and Quantum Yield in the Upconversion of Green to Violet Light with CdSe and Anthracene Derivatives. *Chem. Mater.* **2015,** *27* (21), 7503-7507.
70. Rigsby, E. M.; Miyashita, T.; Jaimes, P.; Fishman, D. A.; Tang, M. L., On the size-dependence of CdSe nanocrystals for photon upconversion with anthracene. *The Journal of Chemical Physics* **2020,** *153* (11), 114702.
71. Gray, V.; Allardice, J. R.; Zhang, Z.; Dowland, S.; Xiao, J.; Petty, A. J.; Anthony, J. E.; Greenham, N. C.; Rao, A., Direct vs Delayed Triplet Energy Transfer from Organic Semiconductors to Quantum Dots and Implications for Luminescent Harvesting of Triplet

Excitons. *ACS Nano* **2020,** *14* (4), 4224-4234.
72. Mongin, C.; Moroz, P.; Zamkov, M.; Castellano, F. N., Thermally activated delayed photoluminescence from pyrenyl-functionalized CdSe quantum dots. *Nat. Chem.* **2017,** *10*, 225.
73. He, S.; Han, Y.; Guo, J.; Wu, K., Entropy-Gated Thermally Activated Delayed Emission Lifetime in Phenanthrene-Functionalized CsPbBr3 Perovskite Nanocrystals. *J Phys Chem Lett* **2021,** *12* (35), 8598-8604.
74. He, S.; Han, Y.; Guo, J.; Wu, K., Long-Lived Delayed Emission from CsPbBr3 Perovskite Nanocrystals for Enhanced Photochemical Reactivity. *ACS Energy Letters* **2021,** *6* (8), 2786-2791.
75. Zhu, H.; Song, N.; Lian, T., Controlling charge separation and recombination rates in CdSe/ZnS type I core-shell quantum dots by shell thicknesses. *J. Am. Chem. Soc.* **2010,** *132* (42), 15038-45.
76. Li, X.; Huang, Z.; Zavala, R.; Tang, M. L., Distance-Dependent Triplet Energy Transfer between CdSe Nanocrystals and Surface Bound Anthracene. *J. Phys. Chem. Lett.* **2016,** *7* (11), 1955-9.
77. Xu, Z.; Huang, Z.; Li, C.; Huang, T.; Evangelista, F. A.; Tang, M. L.; Lian, T., Tuning the Quantum Dot (QD)/Mediator Interface for Optimal Efficiency of QD-Sensitized Near-Infrared-to-Visible Photon Upconversion Systems. *ACS Applied Materials & Interfaces* **2020,** *12* (32), 36558-36567.
78. Huang, Z.; Xu, Z.; Mahboub, M.; Li, X.; Taylor, J. W.; Harman, W. H.; Lian, T.; Tang, M. L., PbS/CdS Core-Shell Quantum Dots Suppress Charge Transfer and Enhance Triplet Transfer. *Angew. Chem. Int. Ed.* **2017,** *56* (52), 16583-16587.
79. Luo, X.; Lai, R.; Li, Y.; Han, Y.; Liang, G.; Liu, X.; Ding, T.; Wang, J.; Wu, K., Triplet Energy Transfer from CsPbBr3 Nanocrystals Enabled by Quantum Confinement. *J. Am. Chem. Soc.* **2019,** *141* (10), 4186-4190.
80. He, S.; Lai, R.; Jiang, Q.; Han, Y.; Luo, X.; Tian, Y.; Liu, X.; Wu, K., Engineering Sensitized Photon Upconversion Efficiency via Nanocrystal Wavefunction and Molecular Geometry. *Angew Chem Int Ed Engl* **2020,** *59* (40), 17726-17731.
81. Lai, R.; Liu, Y.; Luo, X.; Chen, L.; Han, Y.; Lv, M.; Liang, G.; Chen, J.; Zhang, C.; Di, D.; Scholes, G. D.; Castellano, F. N.; Wu, K., Shallow distance-dependent triplet energy migration mediated by endothermic charge-transfer. *Nat. Commun.* **2021,** *12* (1), 1532.
82. Becker, M. A.; Vaxenburg, R.; Nedelcu, G.; Sercel, P. C.; Shabaev, A.; Mehl, M. J.; Michopoulos, J. G.; Lambrakos, S. G.; Bernstein, N.; Lyons, J. L.; Stoferle, T.; Mahrt, R. F.; Kovalenko, M. V.; Norris, D. J.; Raino, G.; Efros, A. L., Bright triplet excitons in caesium lead halide perovskites. *Nature* **2018,** *553* (7687), 189-193.
83. Efros, A. L.; Rosen, M., The Electronic Structure of Semiconductor Nanocrystals. *Annual Review of Materials Science* **2000,** *30* (1), 475-521.
84. Luttinger, J. M.; Kohn, W., Motion of Electrons and Holes in Perturbed Periodic Fields. *Physical Review* **1955,** *97* (4), 869-883.
85. Nirmal, M.; Norris, D. J.; Kuno, M.; Bawendi, M. G.; Efros, A. L.; Rosen, M., Observation of the "Dark exciton" in CdSe quantum dots. *Phys. Rev. Lett.* **1995,** *75* (20), 3728-3731.
86. Sercel, P. C.; Efros, A. L., Band-Edge Exciton in CdSe and Other II-VI and III-V Compound Semiconductor Nanocrystals - Revisited. *Nano Lett.* **2018,** *18* (7), 4061-4068.
87. Sercel, P. C.; Lyons, J. L.; Wickramaratne, D.; Vaxenburg, R.; Bernstein, N.; Efros, A. L., Exciton Fine Structure in Perovskite Nanocrystals. *Nano Lett* **2019,** *19* (6), 4068-4077.
88. Bawendi, M. G.; Wilson, W. L.; Rothberg, L.; Carroll, P. J.; Jedju, T. M.; Steigerwald, M. L.; Brus, L. E., Electronic structure and photoexcited-carrier dynamics in nanometer-size CdSe

clusters. *Physical Review Letters* **1990,** *65* (13), 1623-1626.
89. de Mello Donegá, C.; Bode, M.; Meijerink, A., Size- and temperature-dependence of exciton lifetimes in CdSe quantum dots. *Phys. Rev. B* **2006,** *74* (8), 085320.
90. Kang, I.; Wise, F. W., Electronic structure and optical properties of PbS and PbSe quantum dots. *Journal of the Optical Society of America B-Optical Physics* **1997,** *14* (7), 1632-1646.
91. An, J. M.; Franceschetti, A.; Zunger, A., The excitonic exchange splitting and radiative lifetime in PbSe quantum dots. *Nano Lett.* **2007,** *7* (7), 2129-2135.
92. Rossi, D.; Liu, X.; Lee, Y.; Khurana, M.; Puthenpurayil, J.; Kim, K.; Akimov, A. V.; Cheon, J.; Son, D. H., Intense Dark Exciton Emission from Strongly Quantum-Confined CsPbBr3 Nanocrystals. *Nano Letters* **2020,** *20* (10), 7321-7326.
93. Rossi, D.; Qiao, T.; Liu, X.; Khurana, M.; Akimov, A. V.; Cheon, J.; Son, D. H., Size-dependent dark exciton properties in cesium lead halide perovskite quantum dots. *The Journal of Chemical Physics* **2020,** *153* (18), 184703.
94. Tamarat, P.; Bodnarchuk, M. I.; Trebbia, J. B.; Erni, R.; Kovalenko, M. V.; Even, J.; Lounis, B., The ground exciton state of formamidinium lead bromide perovskite nanocrystals is a singlet dark state. *Nat Mater* **2019,** *18* (7), 717-724.
95. Giansante, C.; Infante, I., Surface Traps in Colloidal Quantum Dots: A Combined Experimental and Theoretical Perspective. *The Journal of Physical Chemistry Letters* **2017,** *8* (20), 5209-5215.
96. Chestnoy, N.; Harris, T. D.; Hull, R.; Brus, L. E., Luminescence and photophysics of cadmium sulfide semiconductor clusters: the nature of the emitting electronic state. *The Journal of Physical Chemistry* **1986,** *90* (15), 3393-3399.
97. Pu, C.; Qin, H.; Gao, Y.; Zhou, J.; Wang, P.; Peng, X., Synthetic Control of Exciton Behavior in Colloidal Quantum Dots. *Journal of the American Chemical Society* **2017,** *139* (9), 3302-3311.
98. Fuhr, A. S.; Yun, H. J.; Makarov, N. S.; Li, H.; McDaniel, H.; Klimov, V. I., Light Emission Mechanisms in CuInS2 Quantum Dots Evaluated by Spectral Electrochemistry. *ACS Photonics* **2017,** *4* (10), 2425-2435.
99. Gao, Y.; Peng, X., Photogenerated excitons in plain core CdSe nanocrystals with unity radiative decay in single channel: the effects of surface and ligands. *J Am Chem Soc* **2015,** *137* (12), 4230-5.
100. Jones, M.; Nedeljkovic, J.; Ellingson, R. J.; Nozik, A. J.; Rumbles, G., Photoenhancement of Luminescence in Colloidal CdSe Quantum Dot Solutions. *The Journal of Physical Chemistry B* **2003,** *107* (41), 11346-11352.
101. Hässelbarth, A.; Eychmüller, A.; Weller, H., Detection of shallow electron traps in quantum sized CdS by fluorescence quenching experiments. *Chemical Physics Letters* **1993,** *203* (2), 271-276.
102. Mooney, J.; Krause, M. M.; Saari, J. I.; Kambhampati, P., Challenge to the deep-trap model of the surface in semiconductor nanocrystals. *Physical Review B* **2013,** *87* (8), 081201.
103. Yang, W.; Yang, Y.; Kaledin, A. L.; He, S.; Jin, T.; McBride, J. R.; Lian, T., Surface passivation extends single and biexciton lifetimes of InP quantum dots. *Chemical Science* **2020,** *11* (22), 5779-5789.
104. Jones, M.; Lo, S. S.; Scholes, G. D., Signatures of Exciton Dynamics and Carrier Trapping in the Time-Resolved Photoluminescence of Colloidal CdSe Nanocrystals. *J. Phys. Chem. C* **2009,** *113* (43), 18632-18642.
105. Jones, M.; Lo, S. S.; Scholes, G. D., Quantitative modeling of the role of surface traps in CdSe/CdS/ZnS nanocrystal photoluminescence decay dynamics. *Proc. Natl. Acad. Sci.* **2009,** *106*

(9), 3011-6.
106. Olshansky, J. H.; Balan, A. D.; Ding, T. X.; Fu, X.; Lee, Y. V.; Alivisatos, A. P., Temperature-Dependent Hole Transfer from Photoexcited Quantum Dots to Molecular Species: Evidence for Trap-Mediated Transfer. *ACS Nano* **2017,** *11* (8), 8346-8355.
107. Thomas, A.; Sandeep, K.; Somasundaran, S. M.; Thomas, K. G., How Trap States Affect Charge Carrier Dynamics of CdSe and InP Quantum Dots: Visualization through Complexation with Viologen. *Acs Energy Letters* **2018,** *3* (10), 2368-2375.
108. Wu, K.; Du, Y.; Tang, H.; Chen, Z.; Lian, T., Efficient Extraction of Trapped Holes from Colloidal CdS Nanorods. *J Am Chem Soc* **2015,** *137* (32), 10224-30.
109. Chen, O.; Zhao, J.; Chauhan, V. P.; Cui, J.; Wong, C.; Harris, D. K.; Wei, H.; Han, H.-S.; Fukumura, D.; Jain, R. K.; Bawendi, M. G., Compact high-quality CdSe–CdS core–shell nanocrystals with narrow emission linewidths and suppressed blinking. *Nature Materials* **2013,** *12*, 445.
110. Hanifi, D. A.; Bronstein, N. D.; Koscher, B. A.; Nett, Z.; Swabeck, J. K.; Takano, K.; Schwartzberg, A. M.; Maserati, L.; Vandewal, K.; van de Burgt, Y.; Salleo, A.; Alivisatos, A. P., Redefining near-unity luminescence in quantum dots with photothermal threshold quantum yield. *Science* **2019,** *363* (6432), 1199-1202.
111. Lai, R.; Wu, K., Red-to-blue photon upconversion based on a triplet energy transfer process not retarded but enabled by shell-coated quantum dots. *The Journal of Chemical Physics* **2020,** *153* (11), 114701.
112. Bender, J. A.; Raulerson, E. K.; Li, X.; Goldzak, T.; Xia, P.; Van Voorhis, T.; Tang, M. L.; Roberts, S. T., Surface States Mediate Triplet Energy Transfer in Nanocrystal-Acene Composite Systems. *J. Am. Chem. Soc.* **2018,** *140* (24), 7543-7553.
113. Rigsby, E. M.; Lee, K.; Sun, J.; Fishman, D. A.; Tang, M. L., Primary amines enhance triplet energy transfer from both the band edge and trap state from CdSe nanocrystals. *J. Chem. Phys.* **2019,** *151* (17), 174701.
114. Steiner, U. E.; Ulrich, T., Magnetic field effects in chemical kinetics and related phenomena. *Chem. Rev.* **1989,** *89* (1), 51-147.
115. Wasielewski, M. R., Energy, Charge, and Spin Transport in Molecules and Self-Assembled Nanostructures Inspired by Photosynthesis. *J. Org. Chem.* **2006,** *71* (14), 5051-5066.
116. Chen, K.; Yang, W.; Wang, Z.; Iagatti, A.; Bussotti, L.; Foggi, P.; Ji, W.; Zhao, J.; Di Donato, M., Triplet Excited State of BODIPY Accessed by Charge Recombination and Its Application in Triplet–Triplet Annihilation Upconversion. *The Journal of Physical Chemistry A* **2017,** *121* (40), 7550-7564.
117. Roest, M. R.; Oliver, A. M.; Paddon-Row, M. N.; Verhoeven, J. W., Distance Dependence of Singlet and Triplet Charge Recombination Pathways in a Series of Rigid Bichromophoric Systems. *The Journal of Physical Chemistry A* **1997,** *101* (27), 4867-4871.
118. Gust, D.; Moore, T. A.; Moore, A. L., Mimicking Photosynthetic Solar Energy Transduction. *Accounts of Chemical Research* **2001,** *34* (1), 40-48.
119. Filatov, M. A.; Karuthedath, S.; Polestshuk, P. M.; Savoie, H.; Flanagan, K. J.; Sy, C.; Sitte, E.; Telitchko, M.; Laquai, F.; Boyle, R. W.; Senge, M. O., Generation of Triplet Excited States via Photoinduced Electron Transfer in meso-anthra-BODIPY: Fluorogenic Response toward Singlet Oxygen in Solution and in Vitro. *Journal of the American Chemical Society* **2017,** *139* (18), 6282-6285.
120. Dance, Z. E. X.; Mi, Q.; McCamant, D. W.; Ahrens, M. J.; Ratner, M. A.; Wasielewski, M. R., Time-Resolved EPR Studies of Photogenerated Radical Ion Pairs Separated by p-Phenylene

Oligomers and of Triplet States Resulting from Charge Recombination. *J. Phys. Chem. B* **2006,** *110* (50), 25163-25173.
121. Zhao, Y.; Duan, R.; Zhao, J.; Li, C., Spin–orbit charge transfer intersystem crossing in perylenemonoimide–phenothiazine compact electron donor–acceptor dyads. *Chem. Commun.* **2018,** *54* (87), 12329-12332.
122. Wang, Z.; Zhao, J., Bodipy–Anthracene Dyads as Triplet Photosensitizers: Effect of Chromophore Orientation on Triplet-State Formation Efficiency and Application in Triplet–Triplet Annihilation Upconversion. *Org. Lett.* **2017,** *19* (17), 4492-4495.
123. Filatov, M. A.; Karuthedath, S.; Polestshuk, P. M.; Callaghan, S.; Flanagan, K. J.; Telitchko, M.; Wiesner, T.; Laquai, F.; Senge, M. O., Control of triplet state generation in heavy atom-free BODIPY–anthracene dyads by media polarity and structural factors. *Physical Chemistry Chemical Physics* **2018,** *20* (12), 8016-8031.
124. Weinberg, D. J.; Dyar, S. M.; Khademi, Z.; Malicki, M.; Marder, S. R.; Wasielewski, M. R.; Weiss, E. A., Spin-Selective Charge Recombination in Complexes of CdS Quantum Dots and Organic Hole Acceptors. *J. Am. Chem. Soc.* **2014,** *136* (41), 14513-14518.
125. Luo, X.; Han, Y.; Chen, Z.; Li, Y.; Liang, G.; Liu, X.; Ding, T.; Nie, C.; Wang, M.; Castellano, F. N.; Wu, K., Mechanisms of triplet energy transfer across the inorganic nanocrystal/organic molecule interface. *Nat. Commun.* **2020,** *11* (1), 28.
126. Luo, X.; Liang, G.; Han, Y.; Li, Y.; Ding, T.; He, S.; Liu, X.; Wu, K., Triplet Energy Transfer from Perovskite Nanocrystals Mediated by Electron Transfer. *J. Am. Chem. Soc.* **2020,** *142* (25), 11270-11278.
127. Wang, J.; Ding, T.; Nie, C.; Wang, M.; Zhou, P.; Wu, K., Spin-Controlled Charge Recombination Pathways across the Inorganic/Organic Interface. *J. Am. Chem. Soc.* **2020,** *142* (10), 4723-4731.
128. Zhao, G.; Chen, Z.; Xiong, K.; Liang, G.; Zhang, J.; Wu, K., Triplet energy migration pathways from PbS quantum dots to surface-anchored polyacenes controlled by charge transfer. *Nanoscale* **2021,** *13* (2), 1303-1310.
129. Garakyaraghi, S.; Mongin, C.; Granger, D. B.; Anthony, J. E.; Castellano, F. N., Delayed Molecular Triplet Generation from Energized Lead Sulfide Quantum Dots. *J. Phys. Chem. Lett.* **2017,** *8* (7), 1458-1463.

Chapter 2. Experimental Methods

Reproduced in part with permission from:

Jin, T.; Uhlikova, N.; Xu, Z.; Zhu, Y.; Huang, Y.; Egap, E.; Lian, T., *J. Chem. Phys.* **2019**, 151, 241101. Copyright AIP Publishing 2019;

Jin, T.; Uhlikova, N.; Xu, Z.; Zhu, Y.; Huang, Y.; Egap, E.; Lian, T., *J. Chem. Phys.* **2020**, 152, 214702. Copyright AIP Publishing 2020;

Jin, T.; Lian, T., *J. Chem. Phys.* **2020**, 153, 074703. Copyright AIP Publishing 2020.

2.1 Sample preparation

2.1.1 Reagents:

Cadmium oxide (CdO, 99.5%), selenium powder (Se, 100 mesh, 99.99%), sulfur powder (S, 99.98%), 9-anthracenecarboxylic acid (ACA, 99%), benzoquinone (BQ, 98%), trioctylphosphine oxide (TOPO, 99%), trioctylphosphine (TOP, 97%), methyl viologen dichloride hydrate (MV^{2+}, 98%), phenothiazine (PTZ, 98%), piperidine (> 99.5%), 3Å molecular sieves, sodium hydroxide (> 97%), boron trifluoride diethyl etherate, poly (maleic anhydride-alt-1-octadecene) (PMAO), triethylamine (99%), 2,3-dichloro-5,6-dicyano-p-benzoquinone (98%), 2,4-dimethylpyrrole (97%), methyl 4-formylbenzoate (99%), oleic acid (OA, 90%), 1-octadecene (ODE, 90%), 1-octanethiol (OctSH, 99%), benzene (anhydrous), acetic acid (AcOH, 99.7%), ethyl acetate (EtOAc, HPLC grade), dichloromethane (HPLC grade), hexanes (HPLC grade, >95%) and all other solvents involved were purchased from Sigma-Aldrich. N-octadecylphosphonic acid (ODPA, 99%) was purchased from PCI Synthesis. All chemicals were used without further purification.

2.1.2 Synthesis of modified boron dipyrromethene (BODIPY)

Scheme 2.1: Synthesis of BODIPY (compound 3)

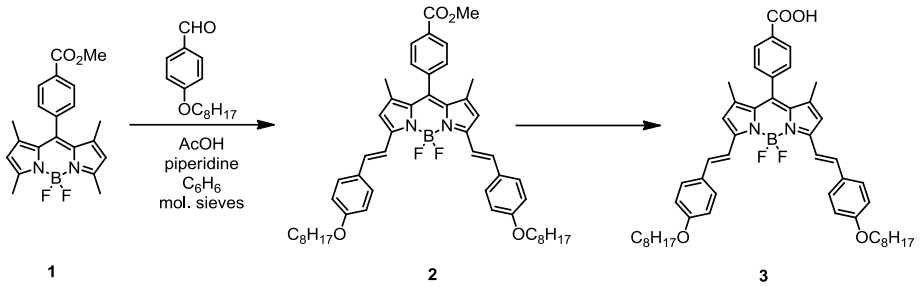

Compound **1** was synthesized according to a previously reported procedure.[1] To synthesize Compound **2**, a mixture of compound **1** (45 mg, 0.12 mmol), 4-(octyloxy)benzaldehyde (110 mg, 0.47 mmol), 80 µL AcOH, 80 µL piperidine, 45 mg 3Å molecular sieves and 2.4 mL benzene were stirred at 80 °C for 24 h, during which the color changed from orange-red to dark green. The reaction mixture was washed with water, extracted with dichloromethane, and dried over anhydrous Na_2SO_4. The crude product was purified by column chromatography (SiO_2, hexanes-EtOAc, gradient) to give **2** as a dark green solid (58 mg, 60%). ^{1}H NMR (500 MHz, $CDCl_3$) δ 8.18 (d, J = 9 Hz, 2H), 7.62 (d, J = 16 Hz, 2H), 7.56 (d, J = 9 Hz, 4H), 7.44 (d, J = 9 Hz, 2H), 7.23 (d, J = 16 Hz, 2H), 6.93 (d, J = 9 Hz, 4H), 6.61 (s, 2H), 4.00 (t, J = 7 Hz, 4H), 3.98 (s, 3H) 1.80 (p, J = 7 Hz, 4H), 1.47 (m, 4H), 1.41 (s, 6H) 1.30 (br, 20H), 0.90 (t, J = 7 Hz, 6H). ^{13}C NMR (500 MHz, $CDCl_3$) δ 166.6, 160.1, 153.1, 141.3, 140.3, 136.3, 132.6, 130.7, 130.2, 129.2, 129.1, 129.0, 117.7, 116.9, 114.8, 68.2, 52.4, 31.8, 29.4, 29.2, 29.2, 26.0, 22.7, 14.8, 14.1.

The conversion from **2** to **3** by basic hydrolysis was carried out according to literature procedures with the following modification.[1] Compound **2** (1 mmol) and sodium hydroxide (3 mmol) were dissolved in THF : water (1 mL : 0.5 mL) and stirred for 24 h at 323K. After cooling, the mixture was acidified to pH = 3–4 by adding a 10% (v/v) aqueous solution of hydrochloric acid. The crude mixture was extracted three times with dichloromethane. The combined organic phases were dried over $MgSO_4$ and the solvent was distilled off under reduced pressure. The crude product was purified by column chromatography to afford compound **3** (molecular formula

$C_{50}H_{59}O_4N_2BF_2$) as a dark green solid (50 % yield). ^{1}H NMR (500 MHz, $CDCl_3$) δ 8.23 (d, J = 8.1 Hz, 2H), 7.57 (d, J = 17.2 Hz, 2H), 7.56 (d, J = 7.0 Hz, 4H), 7.48(d, J = 8.0 Hz, 2H), 7.22 (d, J = 16.1 Hz, 2H), 6.92 (d, J = 8.8 Hz, 4H), 6.62 (s, 2H), 4.01 (t, J = 6.6 Hz, 4H), 1.81 (p, J = 7 Hz,4H), 1.48 (s, 4H), 1.42 (s, 6H) 1.30 (br, 20H), 0.90 (t, J = 7 Hz, 6H)

^{1}H NMR and ^{13}C NMR spectra were obtained on a Bruker 500 spectrometer operated at 500 MHz at room temperature.

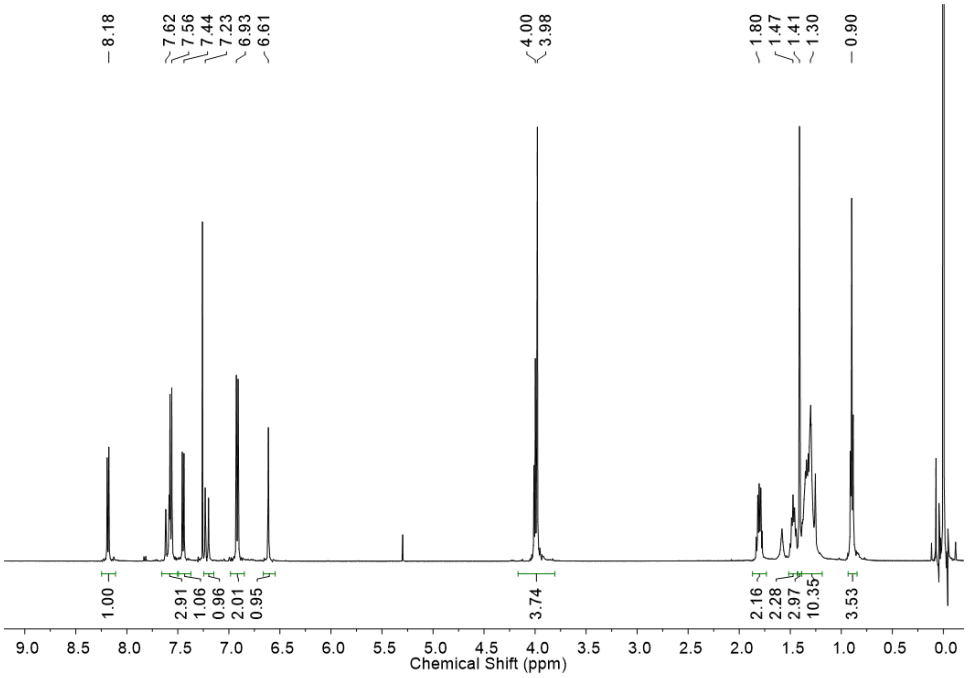

Figure 2.1: ^{1}H NMR spectrum of Compound 2.

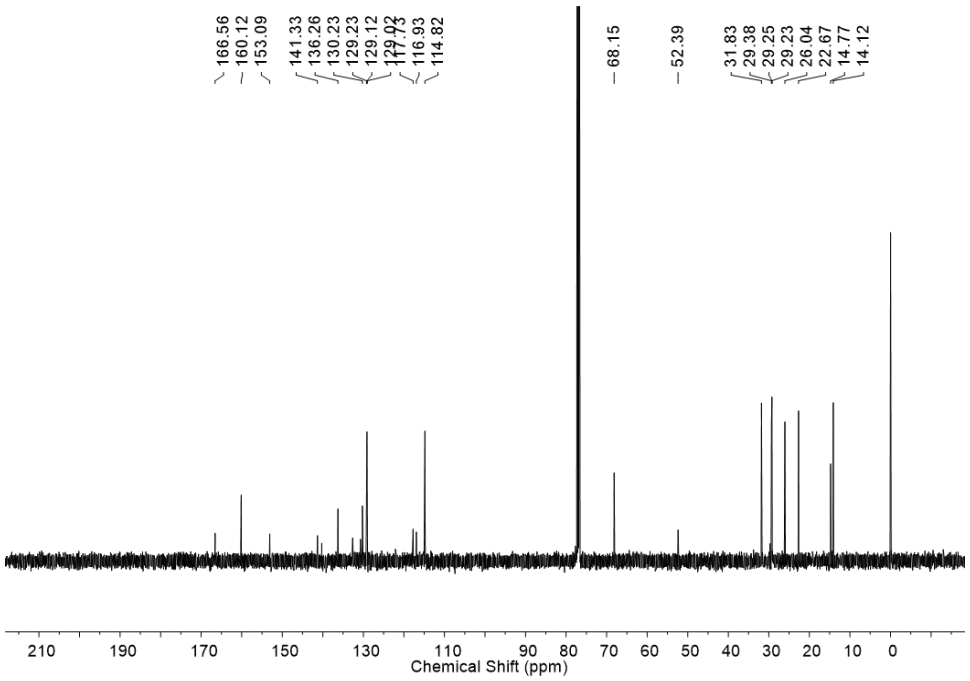

Figure 2.2: ^{13}C NMR spectrum of Compound 2.

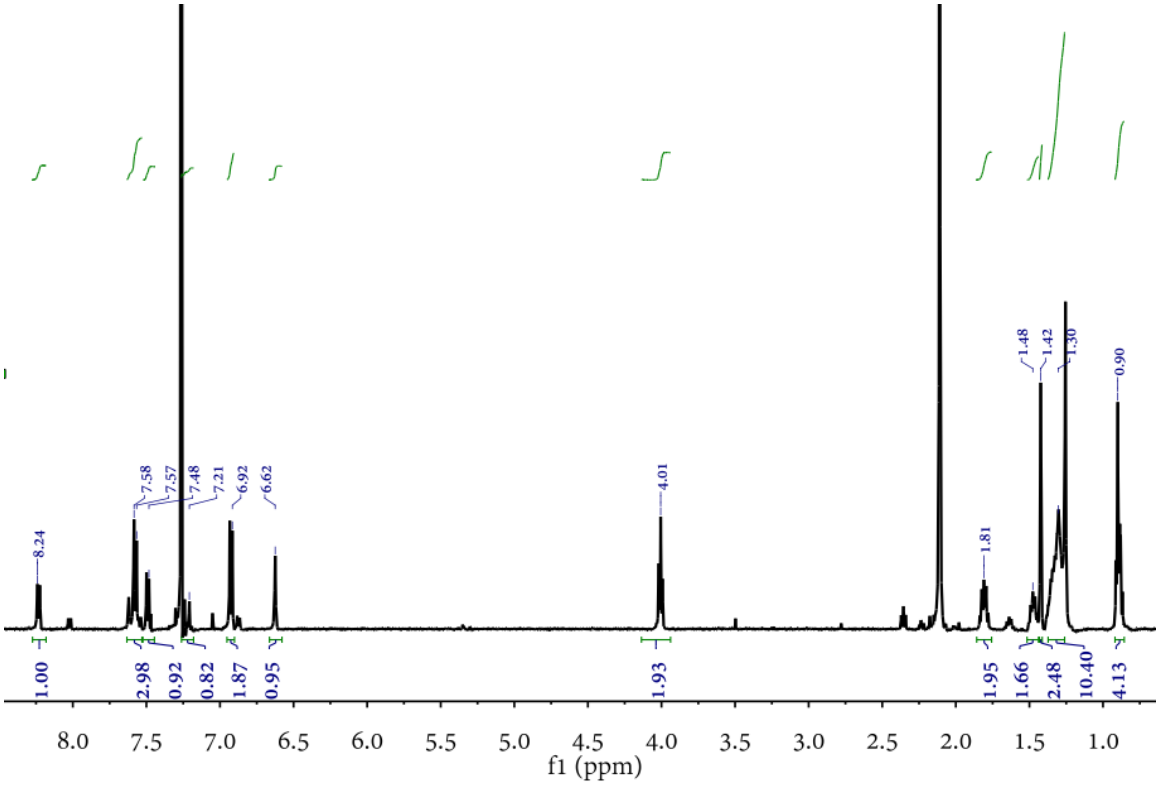

Figure 2.3: ^{1}H NMR spectrum of BODIPY compound (Compound 3).

2.1.3 Synthesis of phosphonic acid capped CdSe quantum dot (QD) and preparation of CdSe-ACA and CdSe-BQ complex

We followed the procedure in previous literature to synthesize phosphonic acid capped CdSe QD.[2] 60 mg CdO, 3 g TOPO and 280 mg ODPA were added to a 25 mL three-neck bottle. The solids were fully mixed under vacuum at 60 ℃ for 30 minutes and then under Argon flow for 10 minutes. The temperature was further increased to 360 ℃ to dissolve CdO. After the solution became colorless, 1 mL TOP was injected. 0.5 mL Se TOP solution containing 60 mg Se was then quickly injected into CdO solution at 360 ℃. The reaction was stopped by intense cool air flow to decrease the temperature once the color of the solution turned from yellow to orange. After the temperature was decreased to 100 ℃, toluene and ethanol were introduced to precipitate the QD. The QD was further washed with toluene and precipitated with ethanol for twice. Finally, the QD was dissolved in hexane with the concentration of 4.2×10^{-5} M and stored in the glove box with argon atmosphere.

The preparation of CdSe-ACA complex was conducted in the glove box. 1 mg ACA powder was added to 1 mL 4.2×10^{-5} M CdSe QD hexane solution. The mixture was ultrasonicated for 2 hours, and the excess undissolved ACA powder was filtered out. The CdSe-ACA complex hexane solution was stored in the glove box for further measurement. The CdSe-BQ complex was prepared with the same method as CdSe-ACA complex.

2.1.4 Synthesis of carboxylic acid capped CdSe QD and preparation of CdSe-BODIPY complex

Phosphonic acid capped CdSe QD was first synthesized following procedures in Section 2.1.3. The obtained CdSe was dissolved in 2 ml of toluene. In order to exchange the capping ligand of CdSe, 30 mg CdO was dissolved in 2.5 ml oleic acid and 3 ml octadecene under argon flow at

270 ℃, into which the CdSe toluene solution was injected at 230 ℃. The mixture was maintained at 230 ℃ for 1 hour. The CdSe was precipitated by adding ethanol and washed twice with toluene and ethanol, and finally was dissolved in toluene in glove box. The concentration of CdSe was determined from UV-vis measurement.[3]

The preparation of CdSe-BODIPY composite was conducted in argon glove box. The synthesized BODIPY powder was dissolved in toluene to reach concentration of 2.6×10^{-4} M. 0.576 ml of BODIPY solution was mixed with 1 ml 3.0×10^{-5} M CdSe solution. The mixture was ultrasonicated for 2 hours before ethanol was added to precipitate CdSe. The precipitation was further dissolved in 1 ml toluene for further measurements.

2.1.5 Synthesis of CdSe/CdS QDs and preparation of CdSe/CdS QD-ACA, CdSe/CdS QD-MV^{2+}, CdSe/CdS QD-PTZ, CdSe/CdS QD-functionalized oligothiophene (T6) complexes

Phosphonic acid capped CdSe QD as CdSe QD core for CdSe/CdS core-shell QD synthesis was first synthesized following procedures in Section 2.1.3. The synthesized QD were finally dissolved in hexane with the concentration of 9.3×10^{-5} M. The CdSe QD solution was stored in a glove box with argon atmosphere for further use.

CdS shell was grown on CdSe QDs by the method reported in previous literature.[2, 4] 0.2 M cadmium oleate ($Cd(OA)_2$) in ODE was prepared as Cd precursor solution. 257 mg CdO, 6.31 mL OA and 3.66 mL ODE were added to a 25-mL three-neck bottle. The mixture was placed in vacuum at 60 ℃ for 20 minutes and then in Argon flow for 10 minutes, after which the temperature was raised to 230 ℃. After the solution turned colorless, the temperature was decreased to and maintained at 110 ℃.0.2 M OctSH in ODE was prepared as S precursor solution by dissolving 0.347 mL OctSH in 9.653 mL ODE through ultrasonication. For the growth of CdS shell, 100 nanomoles CdSe QDs in solution were added to a 25-mL three-neck bottle with 5 mL

ODE. Hexane and oxygen in the mixture were removed by vacuum, after which the temperature of the solution was raised to 240 ℃. Desired amount of Cd and S precursor solutions in two separate syringes were then slowly injected into the CdSe QDs solution at a rate of 3 mL per hour by two syringe pumps. The amount of Cd and S precursor solutions used to achieve growth of certain shell thickness was calculated by estimated CdSe QD core size and the CdS shell lattice constant. After injection of Cd and S solutions, the temperature was further increased to and maintained at 310 ℃ for 10 minutes. Then temperature of the solution was decreased to 100 ℃ with cool air flow, and excess methyl acetate was added to precipitate the CdSe/CdS QDs. The core-shell QDs were further washed with hexane and methyl acetate and finally dispersed in 10 mL hexane or toluene with concentration of ~ 1×10^{-5} M. The core-shell QDs were stored in the glove box for further use.

The CdSe/CdS QD-ACA, CdSe/CdS QD-MV^{2+} and CdSe/CdS QD-PTZ complexes for transient absorption experiment were prepared by adding 1 mg ACA/MV^{2+}/PTZ powder into 1 mL CdSe/CdS QDs so that the amount of acceptor was much larger than that of QDs. The mixture was ultrasonicated for 2 hours, and excess undissolved powders were filtered out. The solvents in the solutions were then removed by air flow, and the complexes were re-dispersed in hexane in the glove box for experiments. For preparation of CdSe/CdS QD-ACA, CdSe/CdS QD-MV^{2+} and CdSe/CdS QD-PTZ complexes for determination of energy/electron/hole transfer rates with varying acceptor concentrations, varying amount of ACA/MV^{2+}/PTZ in toluene solutions (1×10^{-3} M) was added to 1 mL CdSe/CdS QDs toluene solutions. Specifically, the concentration ratios of ACA/PTZ to QDs were determined from UV-vis spectra of the solution, and the concentration ratios of MV^{2+} to QDs were determined from the calculation of amount of MV^{2+} added to the QDs solution and amount of QDs in solution, considering that the UV-vis spectra of MV^{2+} cannot be

well resolved in the spectra window. The solutions were ultrasonicated for 2 hours, and the solvents were removed by air flow. Finally, the complexes along with free acceptors were re-dispersed in toluene in the glove box for transient absorption/time-resolved photoluminescence experiments.

Scheme 2.2: Synthesis of functionalized oligothiophene (3'",4"-dihexyl-[2,2':5',2":5",2'":5'",2"":5"",2""'-sexithiophene]-5-carboxylic acid (T6))

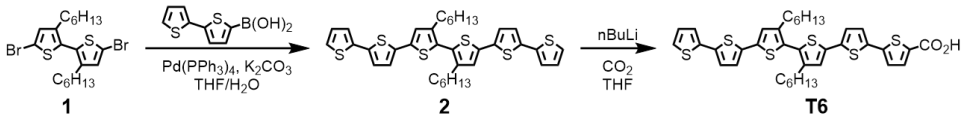

Synthesis of T6 (see Scheme 2.2) was introduced in our previous paper.[5] The obtained T6 was dissolved in toluene with the concentration of 2×10^{-3} M. CdSe/CdS QD-T6 complex was prepared by mixing 0.7 mL QD solution with 0.2 mL T6 solution and ultrasonicating for 2 hours. The QD-T6 complex in solution was then precipitated with ethanol and re-dispersed in 0.7 mL toluene.

To prepare QD and QD T6 complex film samples, 10 mg of Poly (maleic anhydride-alt-1-octadecene) (PMAO) (from Sigma-Aldrich, average M_n of 30000-50000) was added into 0.7 mL QD or QD T6 toluene solution. The mixture was ultrasonicated for 5 minutes to dissolve PMAO, after which the solution was drop-casted onto glass substrate to form the film samples with QD or QD-T6 complex embedded in PMAO.

2.2 Steady state and time-resolved spectroscopy setups

2.2.1 Transient absorption spectroscopy (TA) setups

The femtosecond transient absorption (TA) spectroscopy was built up based on the regenerative amplified Ti: Sapphire femtosecond laser system (Coherent Legend). The output of the laser system is the 800 nm pulse with repetition rate of 1 kHz, pulse energy of 2mJ/pulse and pulse duration of 150 fs. The 800 nm pulse was directed through a 90:10 beam splitter. The 10% was focused onto a 2 mm thick sapphire crystal or a 3 mm thick CaF_2 crystal to generate the white light continuum as femtosecond TA probe. The spectra windows of the probe were 380-650 nm for CaF_2 crystal and 440-900 nm for sapphire crystal. The white light was further directed through a 70:30 beam splitter to generate the signal and reference probe. 1.5 W of the 800 nm pulse was directed to an optical parametric amplifier (OPA) (TORPAS-C from Spectra-Physics). The 550 nm pump pulse was generated by sum frequency generation of the idle output from the OPA and the remaining 800 nm pulse at a BBO crystal. The 500 nm and 520 nm pump pulses were generated by sum frequency generation of the signal output from the OPA and the remaining 800 nm pulse at a BBO crystal. The 650 nm pump pulse was generated through second harmonic generation (SHG) of the signal pulse. The remaining signal/idle pulse was filtered out by a band pass filter. The pump pulse was directed through a 500 Hz chopper, a delay stage and then focused onto the sample with beam diameter of 400 μm. The power density of the pump pulse at the sample was adjusted to be 100 $\mu J/cm^2$/pulse. The signal probe beam was focused onto the sample with beam diameter of 100 μm. The angle of polarization between the pump and the probe at the sample was tuned to be magic angle for excitation of BODIPY experiments. The signal and reference probe beams were finally focused into optical fibers coupled with a visible spectrometer and a CMOS camera with 1024 elements for signal collection. The data was collected and analyzed with the Helios system from Ultrafast Systems, Inc. Instrument response was fit with a Gaussian function from the solvent response. The maximum delay time between pump and probe pulses in

femtosecond TA setup can reach 1.6 ns.

The pump pulse from the femtosecond TA setups can be applied as the pump pulse for nanosecond TA experiments without going through the 500 Hz chopper. The probe pulse for nanosecond TA experiments was generated from a white light continuum laser (STM-2-UV, Leukos) with pulse duration of 0.5 ns and repetition rate of 2 kHz. The data collection and analysis was conducted in EOS system from Ultrafast System, Inc.

Femtosecond near infrared transient absorption spectroscopy experiments were conducted using a regenerative amplified Ti: Sapphire femtosecond laser system (Coherent Astrella) for 800 nm fundamental pulse generation (1 kHz repetition rate, 35 fs pulse duration, 5.5 mJ/pulse). The fundamental pulse was split by an 80:20 beam splitter. The 80% 800 nm pulse was further split by a 50:50 beam splitter in order to pump a visible and near infrared OPA (Light Conversion), respectively. The scheme of generating 650 nm or 500 nm pulse was the same as that in visible TA setup, and it was modulated by a 500 Hz chopper. For the 20% fundamental pulse, 0.2 mJ/pulse was utilized to go through a delay stage and generate NIR probe pulse by focusing the beam onto a sapphire crystal. The angle of polarization between the pump and the probe at the sample was tuned to be magic angle. The power density of the pump beam on the sample was 500 $\mu J/cm^2$. The data collection was conducted in Helios system from Ultrafast Systems, Inc.

The solution samples for the experiments were added to 1 mm thick quartz cuvettes (Starna) and were constantly stirred during TA experiment.

2.2.2 Temperature dependent TA setups

Temperature dependent TA experiments were performed by placing the CdSe/CdS QD or CdSe/CdS QD-T6 film samples into the Janis STVP-100 cryostat. The sample was cooled down by being immersed in helium gas inside the sample chamber. There were two heaters and

temperature sensors in the sample chamber to change and detect the temperature, respectively. One of the temperature sensors was at the top of the sample chamber, and the other one was ~3 cm above the sample in the chamber. Temperatures indicated by the sensors at room temperature were both 298 K. In experiment, sample in the chamber was first immersed in liquid helium, and the temperatures indicated by the sensors were 4.2 K. Temperature then was increased by the heater. The working temperature ranged from ~4 K to 298 K and can be controlled by a temperature controller (Lake Shore Model 335) to ensure that temperatures indicated in both sensors reach the target values. There were four windows (IR grade fused silica) around the sample holder to allow light transmission (170-2500 nm) along all four directions. For temperature dependent TA experiments, the cryostat was placed so that the film sample was at the focal point of the probe beam.

2.2.3 Time-resolved photoluminescence (TRPL) setups

TRPL experiments were based on a mode-locked Ti:Sapphire laser (Tsunami oscillator, Spectra Physics). The wavelength of the output pulse was tuned to be 920 nm. The time duration of the pulse was 100 fs and the repetition rate was 80 MHz. The repetition rate was reduced by a pulse picker (Conoptics) to 20 MHz, 10 MHz and 1.43 MHz for the detection time windows of 50 ns, 100 ns and 700 ns, respectively. The pulse going through the pulse picker was directed to a BBO crystal to generate the 460 nm excitation pulse through second harmonic generation. The remaining 920 nm pulse was filtered out by band pass filters. The 460 nm pulse was directed to the sample, and the emission was collected into a monochromator (Acton Series, Princeton Instruments), by which the band edge exciton emission of the QDs was selected out. The emission going through the monochromator was collected and amplified by a microchannel-plate-photomultiplier tube (Hamamatsu R3809U-51) and analyzed by a time-correlated single photon

counting (TCSPC) board (Becker & Hickel SPC 600). The instrument response function was measured to be a Gaussian function with FWHMs of 62 ps, 110 ps and 626 ps for 50 ns, 100 ns and 700 ns detection time windows, respectively. The absorption at 460 nm, the data collection time and the excitation pulse intensity were controlled to be the same for QDs with and without the acceptors.

2.2.4 Steady state photoluminescence setups

Steady state photoluminescence was performed on Cary Eclipse fluorometer. Emission spectrum of BODIPY was collected with excitation wavelength of 400 nm. 1 cm cuvette was used for measurements. Emission spectrum of carboxylic acid capped CdSe QD was collected with 500 nm excitation light. 1 cm cuvette was used for the measurements. The excitation wavelength was set to be 460 nm, and the emission spectra of CdSe QD and CdSe-ACA complex were collected. For the determination of CdSe QD PL quantum yield, 400 nm excitation light was applied. The excitation wavelength was set to be 400 nm for CdSe core QDs and 510 nm for CdSe/CdS core-shell QDs. The photoluminescence quantum yields of CdSe and CdSe/CdS QDs were determined with Coumarin 153 and Rhodamine 6G as standards, respectively. 1 cm cuvettes were applied for measurements.

2.2.5 Cyclic voltammetry (CV) measurement

Cyclic Voltammetry measurement was performed on a CHI660E electrochemical workstation (CH Instruments). A 3 ml glass cell with air-tight cap was used as the electrochemical cell. Two Pt wires were used as the working electrode and counter electrode, respectively. An Ag wire was selected to be quasi-reference electrode. These electrodes were ultrasonicated in ethanol for 20 minutes before use. Dichloromethane (DCM) solution of 0.26 mM BODIPY and 0.1 M tetrabutylammonium hexafluorophosphate was injected into the electrochemical cell and degassed

by nitrogen for 10 minutes before measurement. The scan rate was set to be 0.1 V/sec. Ferrocene (0.342 V vs. SCE) was used to calibrate the redox potential of BODIPY.

2.3 Reference

1. Hong, X.; Wang, Z.; Yang, J.; Zheng, Q.; Zong, S.; Sheng, Y.; Zhu, D.; Tang, C.; Cui, Y., Silylated BODIPY dyes and their use in dye-encapsulated silica nanoparticles with switchable emitting wavelengths for cellular imaging. *Analyst* **2012,** *137* (18), 4140-4149.
2. Chen, O.; Zhao, J.; Chauhan, V. P.; Cui, J.; Wong, C.; Harris, D. K.; Wei, H.; Han, H.-S.; Fukumura, D.; Jain, R. K.; Bawendi, M. G., Compact high-quality CdSe–CdS core–shell nanocrystals with narrow emission linewidths and suppressed blinking. *Nature Materials* **2013,** *12*, 445.
3. Yu, W. W.; Qu, L. H.; Guo, W. Z.; Peng, X. G., Experimental determination of the extinction coefficient of CdTe, CdSe, and CdS nanocrystals. *Chem. Mater.* **2003,** *15* (14), 2854-2860.
4. Hanifi, D. A.; Bronstein, N. D.; Koscher, B. A.; Nett, Z.; Swabeck, J. K.; Takano, K.; Schwartzberg, A. M.; Maserati, L.; Vandewal, K.; van de Burgt, Y.; Salleo, A.; Alivisatos, A. P., Redefining near-unity luminescence in quantum dots with photothermal threshold quantum yield. *Science* **2019,** *363* (6432), 1199-1202.
5. Xu, Z.; Jin, T.; Huang, Y.; Mulla, K.; Evangelista, F. A.; Egap, E.; Lian, T., Direct triplet sensitization of oligothiophene by quantum dots. *Chem. Sci.* **2019,** *10* (24), 6120-6124.

Chapter 3. On the Coupling Strength of Core-shell Quantum Dot Sensitized Triplet Energy Transfer

3.1 Introduction

Efficient generation of long-lived triplet excited states has been extensively studied during the past decades due to its promising applications in photon-upconversion,[1-5] photodynamic therapy[6-8] and photocatalysis.[9-11] Traditional methods of triplet excited state generation in molecules include intersystem crossing and triplet energy transfer (TET) from molecular sensitizers,[4, 12-13] both of which require intersystem crossing in molecules and suffer from large energy loss due to the large singlet-triplet energy gap in molecules. Recently developed quantum dot (QD) sensitized TET has received intense research interest,[14-18] because it utilizes the unique properties of QDs, including small singlet-triplet energy gap,[19-21] broad absorption spectral range,[22-23] large extinction coefficient[23-24] and tunability in structures and photophysical properties.[25-27] During the past six years, TET sensitized by CdSe,[14, 28-30] CdS,[31] PbS[32-33] and perovskite QDs[34-35] has been successfully developed and incorporated in photon upconversion and photocatalysis.[36-39] Progress has also been made in improving TET efficiency through optimizing QD quantum yield,[40] passivating QD surface,[31, 41] suppressing side reaction pathways[32] and modifying surface ligands.[42]

TET in molecular donor-acceptor systems is well described by Dexter Energy Transfer (DET) involving the simultaneous transfers of an electron and hole.[43-46] The original DET theory was based on Fermi Golden rule with coupling strength given by two-electron exchange integral, which scales with wavefunction overlap and decays exponentially with the distance between the donor

and acceptor.[43, 47] Later research of DET coupling strength emphasized the contribution of one-electron integral terms from TET mediated by charge transfer virtual states.[48-49] Recently, higher energy virtual states including bridge exciton states were proposed to be significant in donor-bridge-acceptor systems with low bridge tunneling barrier and long bridge length.[50-51]

Despite the development of DET theory in molecular donor-acceptor systems, whether the theory can be applied to QD sensitized TET systems is still ambiguous. Time-resolved techniques, including transient absorption spectroscopy (TA) and time-resolved photoluminescence (TRPL), have been applied to probe the dynamics of TET, from which direct Dexter energy transfer (DET) from band edge excitons has been proposed for most QD-acceptor complexes,[14, 34, 52] and TET through charge separated states and trap state intermediates has also been identified for some systems.[53-55]As the critical factor to determine the TET rate, coupling strength of TET has been studied for QD-acceptor systems.[34, 42, 56] The coupling strength can be tuned by varying the QD size,[34] QD ligand length,[42] the molecular spacer length[56-57] or inorganic shell thickness[30-31] between the QD and the acceptor, and it has been demonstrated that the upconversion yield and TET rate decrease with reduced coupling strength in complexes of perovskite-pyrene carboxylic acid,[34] CdSe-phenyl bridge-anthracene,[56] PbS-phenyl bridge-tetracene,[57] PbS/CdS-rubrene,[41] CdSe/Zn(Cd)S-anthracene.[58] However, the rigorous description of the coupling strength and its underlying model have not been well understood. It remains unclear whether TET from QDs is mediated by charge transfer virtual state and can be considered as simultaneous electron and hole transfer from QD. Although the charge transfer virtual state mediated TET has been proposed for QD-acceptor complexes with no intermediate observed before formation of acceptor triplet excited state,[35] there has been no experimental test for the proposed mechanism. These questions concerning TET mechanism would be more of interest for core-shell QDs with more complex

exciton structures, as these QDs have shown better TET performance because of the passivation of surface defects.[31, 41]

In this study, we aim to test whether the TET coupling strength can be modeled with scheme involving charge transfer virtual state, in another word, whether TET can be considered as simultaneous electron and hole transfer in QD-acceptor. CdS shell growth on CdSe core QDs was applied as the approach to systematically vary the coupling strength of TET. The dependence of TET coupling strength on shell thickness was measured and compared to shell thickness dependence of electron and hole transfer coupling strength, with anthracene carboxylic acid (ACA), methyl viologen (MV^{2+}) and phenothiazine (PTZ) as TET, electron transfer and hole transfer acceptors, respectively (Figure 3.1).[27, 59] The experimental result shows a weaker shell thickness dependence of TET coupling strength than expected from the model of charge transfer virtual state mediated TET. Based on the result, we propose that TET from the core-shell QDs may be mediated by virtual exciton states with electron/hole in levels with higher energies than $1S_e$ and $1S_h$ levels.

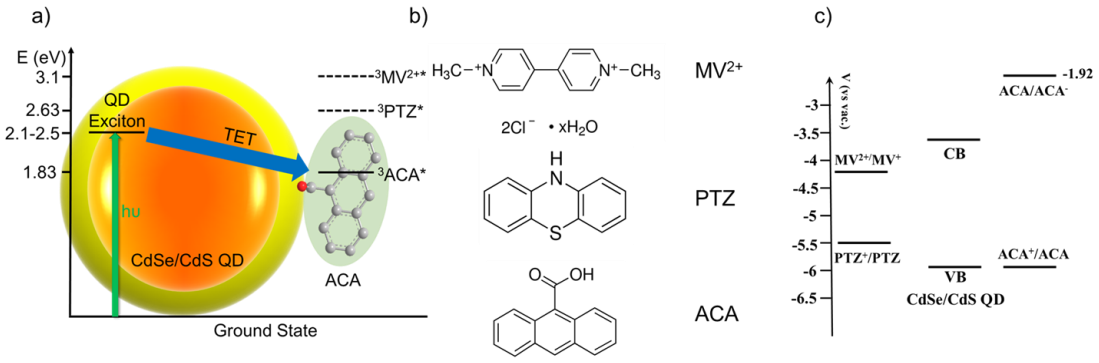

Figure 3.1: The energetics and redox potentials of the CdSe/CdS QDs, triplet energy transfer (TET) acceptor (ACA), electron transfer acceptor (methyl viologen, MV^{2+}) and hole transfer acceptor (phenothiazine, PTZ) in this study. a). Scheme of TET from CdSe/CdS QDs to attached ACA acceptor. Energetics of QD, ^{3}ACA*, $^3MV^{2+}$* and ^{3}PTZ* are shown in the scheme.[60-62] The dashed lines of $^3MV^{2+}$* and ^{3}PTZ* suggest energetically unfavorable TET from QD to MV^{2+} and PTZ,

while the solid line of ^{3}ACA* suggest energetically allowed TET from QD to ACA; b). Molecular structures of MV^{2+}, PTZ and ACA; c). Redox potentials of MV^{2+}, PTZ, ACA and conduction/valence band edge of CdSe/CdS QD.[59, 62-63]

3.2 Results and discussion

3.2.1 Characterization of CdSe/CdS Core-shell QDs

CdSe/CdS core-shell QDs with various shell thicknesses were synthesized following the procedures reported in previous literature.[64] The size distributions of the QDs were measured from transmission electron microscopy (TEM) images, which are shown in Figure 3.2. By fitting diameter histograms with Gaussian functions (shown in Figure 3.3), we determined the average core/shell QD diameters (standard deviation) to be 2.94 (0.49) nm, 3.58 (0.59) nm, 3.90 (0.60) nm, 5.04 (1.00) nm and 5.55 (0.90) nm, corresponding to 0, 0.9, 1.4, 3.1 and 3.8 monolayers (ML) of CdS shell, respectively.[27] These samples are referred to as CdSe/CdS(X ML), where X is the number of CdS monolayers.

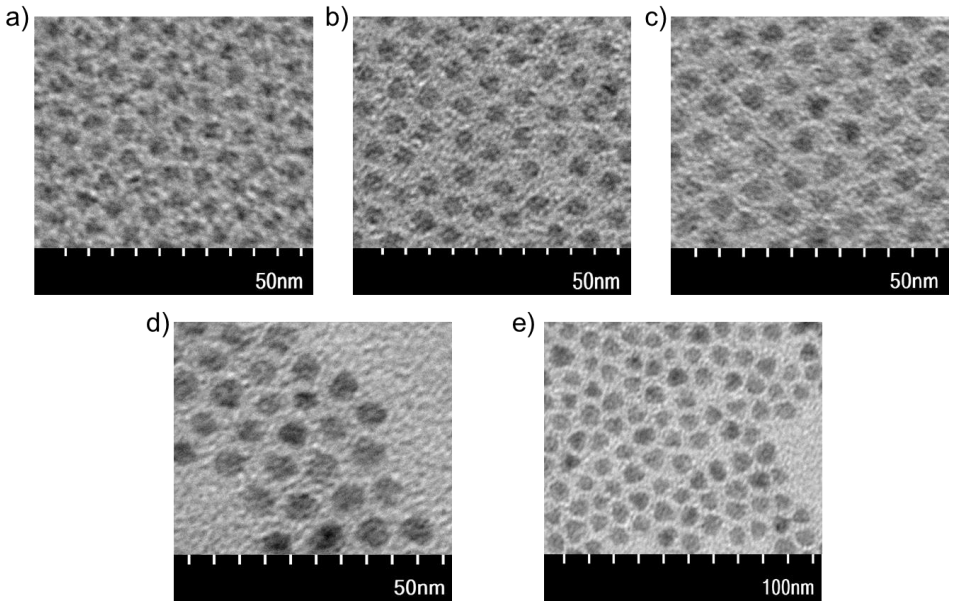

Figure 3.2: Parts of the TEM images of CdSe/CdS core-shell QDs with a). 0, b). 0.9, c). 1,4, d).

3.1 and e). 3.8 monolayers of CdS shell.

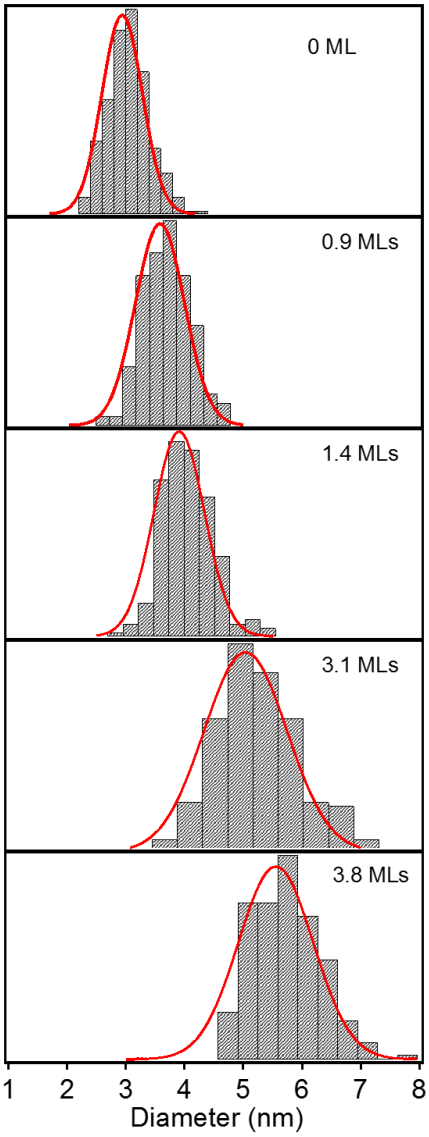

Figure 3.3: Size distributions of the synthesized CdSe QDs and CdSe/CdS core-shell QDs extracted from the TEM images. The red solid lines are the fits to the diameter histograms by Gaussian distribution. The average diameters (standard deviation) of the QDs to be 2.94 (0.49) nm, 3.58 (0.59) nm, 3.90 (0.60) nm, 5.04 (1.00) nm and 5.55 (0.90) nm, corresponding to 0, 0.9, 1.4, 3.1 and 3.8 monolayers of CdS shell, respectively. (1 monolayer = 0.35 nm).[27]

Figure 3.4 shows the UV-vis absorption and photoluminescence (PL) spectra of the synthesized QDs. As shown in Figure 3.4a, with increasing shell thickness, the $1S_h$-$1S_e$ absorption peak shifts from 511 nm to 570 nm, which can be attributed to the extension of the $1S_h$ and/or $1S_e$ wavefunctions into the CdS shell;[25] the intensity of the bulk-like continuous absorption band (400-480 nm) corresponding to the transition between the higher hole levels and the $1S_e$ level (denoted as T band) increases with shell thickness.[27] As shown in Figure 3.4b, the 1S exciton PL emission peak red shifts at larger CdS shell thicknesses from 521 nm for CdSe/CdS (0 ML) to 579 nm for CdSe/CdS (3.8 ML). The PL quantum yields (QYs) for the core-shell QDs increase from 28% in core only QDs to 62 % in CdSe/CdS (1.4 ML) (Figure 3.4c inset), because of the improved passivation of surface trap states of the CdSe core by CdS shell. Further increase of shell thickness leads slight decreases of the PL QY, which is likely caused by increased defects introduced in the synthesis procedure of further growth of CdS shell.

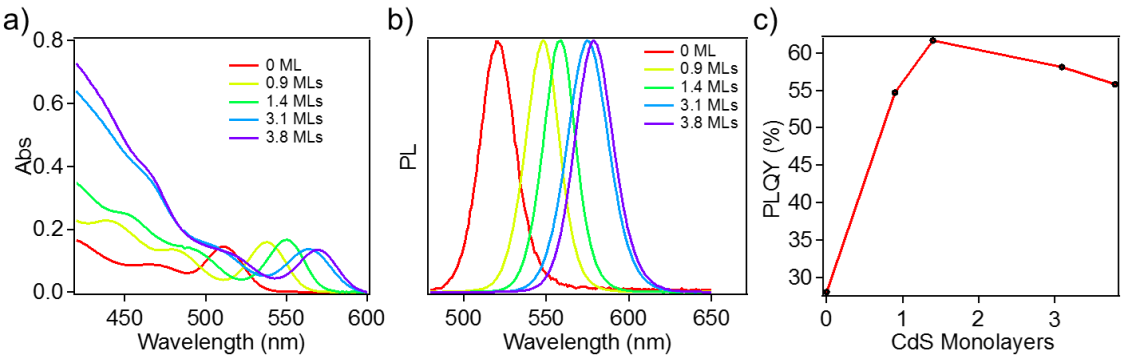

Figure 3.4: Absorption and emission spectra of CdSe/CdS QDs. a). UV-vis absorption spectra and b). steady state PL emission spectra of CdSe/CdS QDs with 0(red) 0.9 (yellow), 1.4 (green), 3.1 (blue) and 3.8 (purple) monolayers of CdS shell. c). PL quantum yields of CdSe/CdS QDs as a function of the CdS shell thickness.

Previous studies have shown that CdSe/CdS QDs of similar core size have a quasi-type II

band alignment, in which the valence band edge of CdSe is higher than CdS and the conduction band edges are degenerate throughout the core and shell.[27] This band alignment can be confirmed by transient absorption study (shown in Figure 3.5). The excitation wavelength in transient absorption study was set at 520 nm for all QD samples so that $1S_h$-$1S_e$ transition for CdSe/CdS (0/0.9/1.4 ML) or $2S_h$-$1S_e$ transition for CdSe/CdS (3.1/3.8 ML) was excited. After the excitation, $1S_h$-$1S_e$ exciton was directly populated in CdSe/CdS (0/0.9/1.4 ML) and populated through hole relaxation from $2S_h$ to $1S_h$ for CdSe/CdS (3.1/3.8 ML). The population of $1S_h$-$1S_e$ exciton results in bleaches at both $1S_h$-$1S_e$ transition and T band, suggesting that the 1S electron wavefunction is delocalized in the entire QD, confirming the quasi-type II band alignment. As shown in Figure 3.5a-e, TA spectra of the QDs contain spectra features of $1S_h$-$1S_e$ transition XB at 511 nm, 535 nm, 554 nm, 570 nm and 573 nm for CdSe/CdS QDs with 0, 0.9, 1.4, 3.1 and 3.8 monolayers of CdS, respectively and the increasing amplitudes of the T band bleach at ~475 nm. The results also show that with increasing shell thickness, the kinetics of $1S_h$-$1S_e$ exciton bleach recovery (Figure 3.5f) become faster and more single exponential, which is attributed to the increasing probability of conduction band electron decay by radiative recombination with the valence band hole compared to the slow nonradiative recombination with trapped holes.[54]

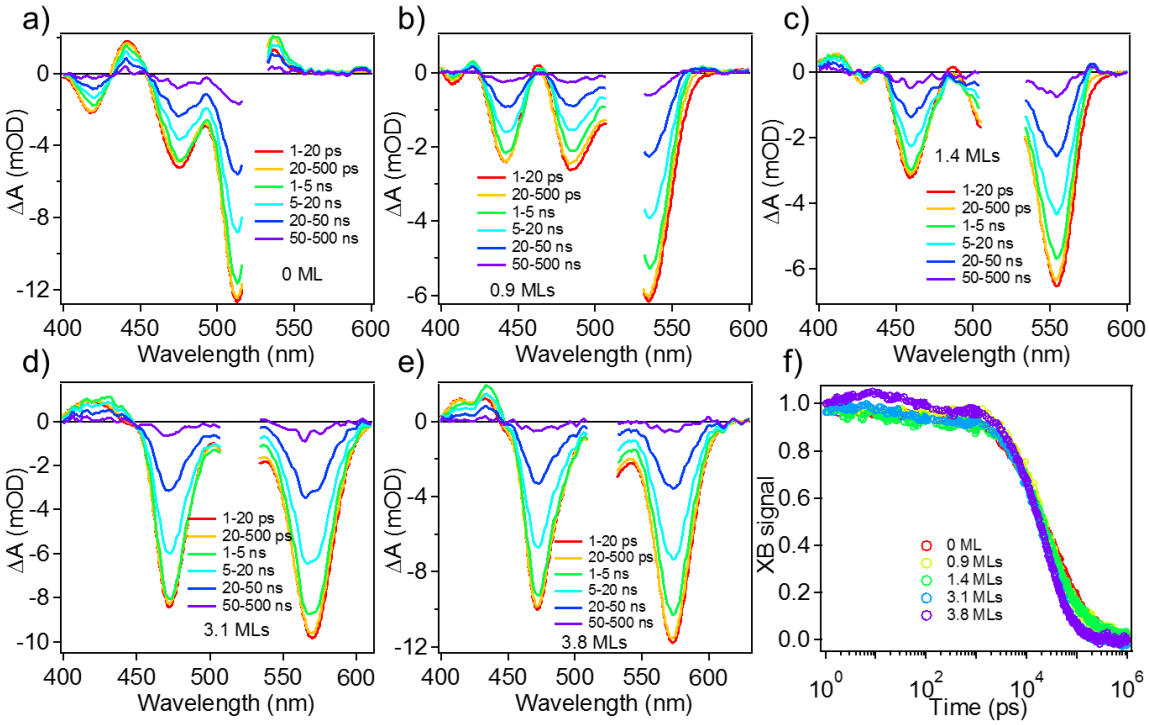

Figure 3.5: TA spectra of the synthesized CdSe/CdS QDs with a). 0, b). 0.9, c). 1.4, d). 3.1 and e). 3.8 monolayers of CdS shell in delay time range of 1 ps – 1 μs. The wavelength of the pump pulse was 520 nm. f). Exciton bleach kinetics of the $1S_h$-$1S_e$ core transition of the QDs.

3.2.2 Core-shell QD sensitized TET

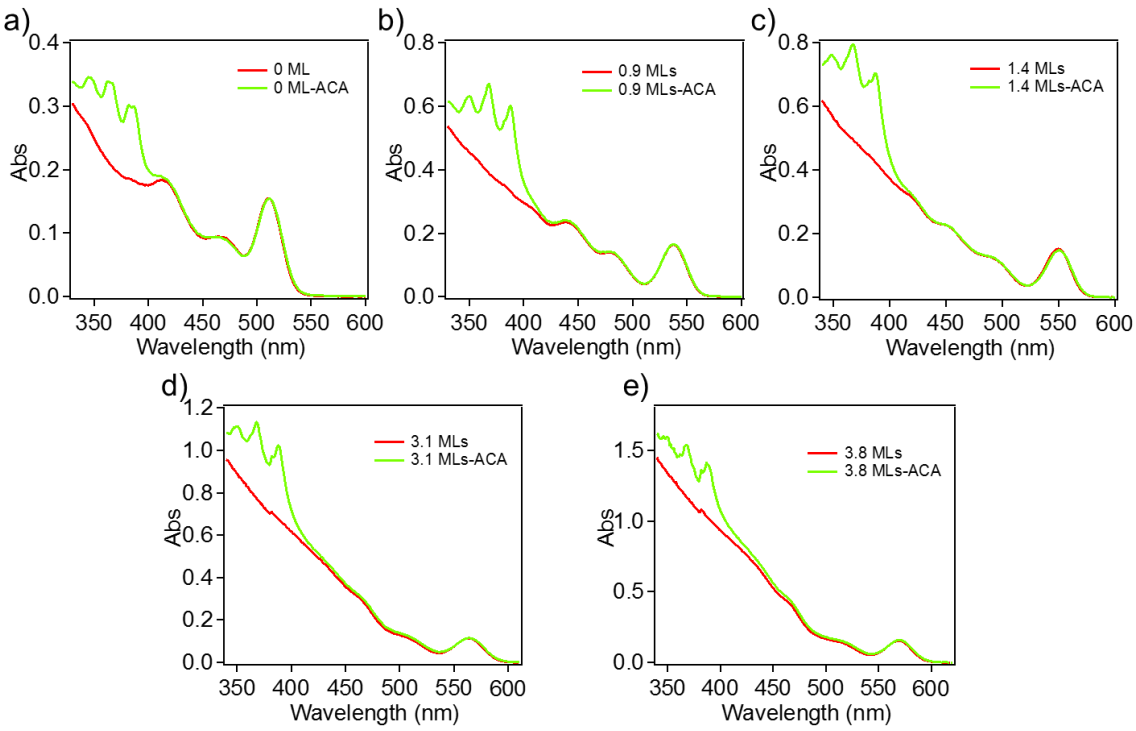

Figure 3.6: UV-vis spectra of CdSe/CdS QDs and CdSe/CdS QD-ACA complexes with a). 0, b). 0.9, c). 1.4, d). 3.1 and e). 3.8 monolayers of CdS shell for TA experiments. The spectra of CdSe/CdS QD-ACA contain absorption of both free ACA in solution and ACA attached to QD surfaces. The concentration ratios of total ACA to QD are 1.7, 5.2, 8.1, 14.4 and 13.1 for CdSe/CdS QDs with 0, 0.9, 1.4, 3.1 and 3.8 monolayers of CdS shell, respectively.

TET from CdSe and CdSe/CdS QDs to 9-anthracene carboxylic acid (ACA) was studied with TA spectroscopy. Comparison of the absorption spectra of QD and QD-ACA complexes in Figure 3.6 shows that the adsorption of ACA has negligible effect on the QD exciton band. TA measurements were conducted with 520 nm pump pulses, which selectively excite the QD exciton transition because of negligible absorptions of ACA at this wavelength. As shown in Figure 3.7 and Figure 3.8, the QD-ACA TA spectra within 1 ns are dominated by QD features, including bleaches of both the $1S_h$-$1S_e$ and T band transition resulted from the state filling of the 1S electron

level.[65-66] The CdSe/CdS (0ML)-ACA complex shows faster decay of the core exciton bleach (XB) signal compared to free QDs without ACA (Figure 3.7a). The faster XB decay is accompanied with the growth of ^{3}ACA* T_1->T_n signal from 420 nm to 450 nm (Figure 3.7d), suggesting TET from the CdSe QD to ACA.[14] With increasing CdS shell thickness, the ^{3}ACA* signal growth can still be observed for all core-shell QDs. The signal amplitude of ^{3}ACA* is larger for core-shell QDs with 0.9 monolayers of CdS than CdSe core-only QDs and slightly decreases with further increase of shell thickness. The observation suggests the initial increase of TET efficiency from QDs after sub-monolayer shell growth and the slight decrease of TET efficiency with further increase of shell thickness. Note that the TA spectra of QD-ACA show no features from cation or anion radicals of ACA, indicating the one-step TET from QDs to ACA instead of sequential charge transfer to form ^{3}ACA*.

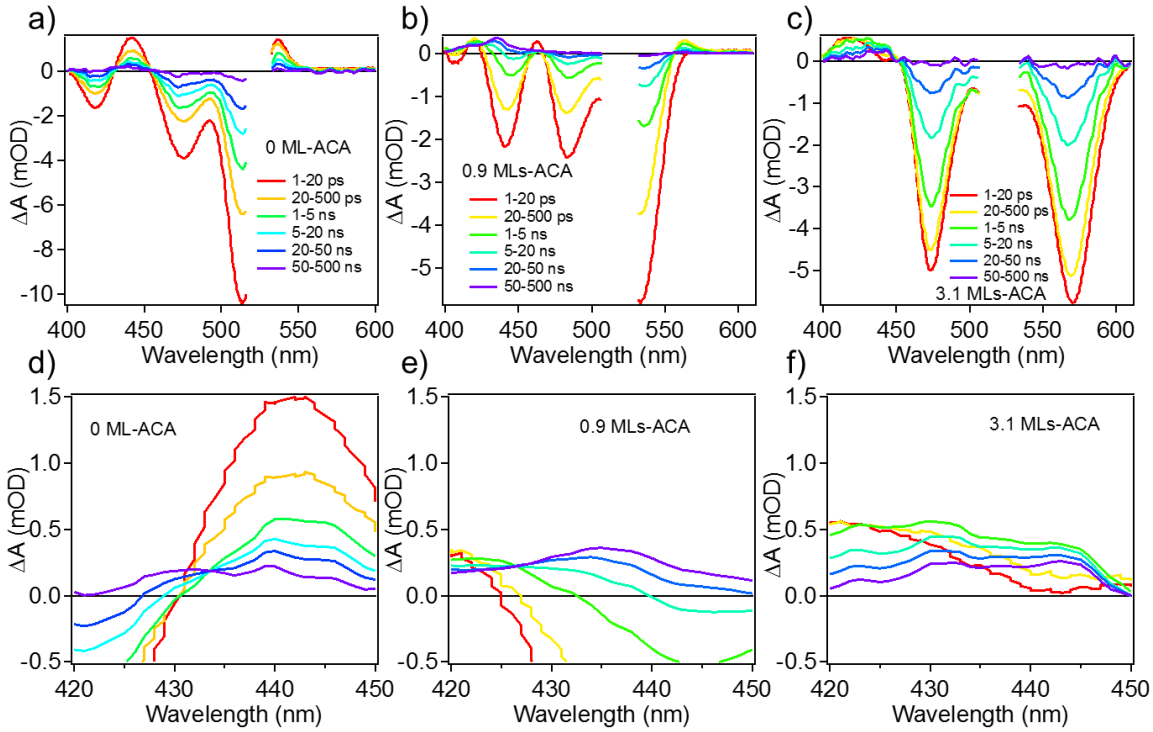

Figure 3.7: Average TA spectra of CdSe/CdS (X ML)-ACA measured 520 nm excitation for a) X=0 ML, b) X= 0.9 ML and c) X = 3.1 ML at indicated delay time windows. d), e) and f) are the

zoom-in figures of a), b) and c) respectively to better resolve the ^{3}ACA* signal in the 420-450 nm region.

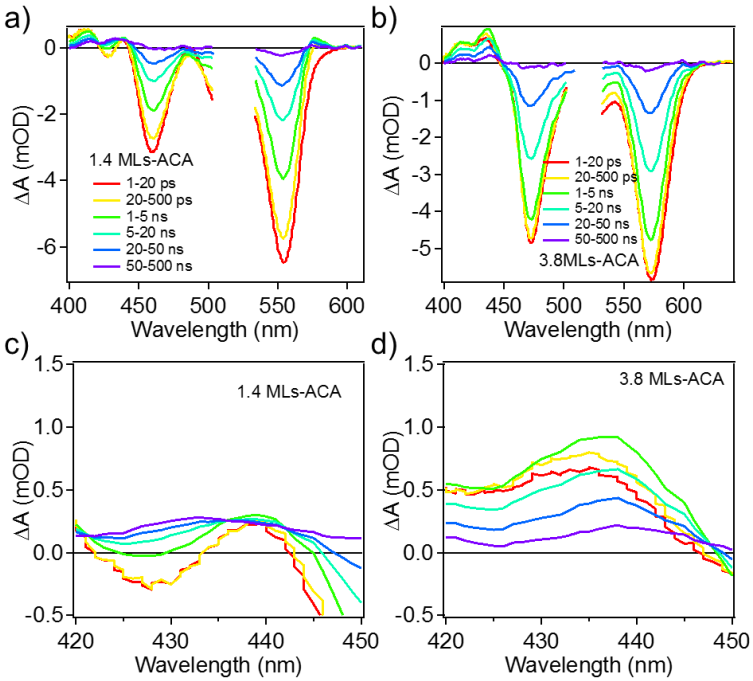

Figure 3.8: TA spectra of CdSe/CdS QD-ACA complexes with a). 1.4 and b). 3.8 monolayers of CdS shell. The delay time range is from 1 ps – 1 μs. The wavelength of the pump pulse was 520 nm. c) and d) shows the zoom-in plot of a) and b) respectively to resolve the ^{3}ACA* T_1->T_n TA signal in range of 400 nm – 450 nm.[14] The ^{3}ACA* signal suggests the triplet energy transfer from CdSe/CdS QDs to ACA.

The kinetics of QD XB ($1S_h$-$1S_e$ transition) and ^{3}ACA* signal growth of QD-ACA complexes are compared in Figure 3.9. The XB kinetics were directly obtained from kinetics at the corresponding XB peak position, while the ^{3}ACA* signal was extracted from averaged kinetics from 430 nm to 435 nm after the subtraction of the QD signal scaled such that the $1S_h$-$1S_e$ XB of the QD, where there is no ^{3}ACA* signal contribution. As shown in Figure 3.9a, the ^{3}ACA* signal in CdSe QD-ACA does not grow until 1 ns, while there is dramatic decrease of XB signal within

1 ns due to electron trapping.[54] After 1 ns, the kinetics of ^{3}ACA* growth matches the kinetics of XB decay of QD-ACA complex, which suggests TET from QD to ACA. The growth of ^{3}ACA* does not end until tens of nanosecond. Compared to CdSe QD-ACA, CdSe/CdS QD-ACA complexes show slight growth of ^{3}ACA* within 1 ns, which ends mostly within 10 ns. This suggests faster apparent TET rates for CdSe/CdS-ACA than CdSe-ACA. For CdSe/CdS QD-ACA complexes, the XB decays faster than that of QDs without ACA due to TET, and the difference between the XB decays is smaller with increasing shell thickness, indicating slower apparent TET rate. The result is consistent with the trend of ^{3}ACA* signal amplitude change in TA spectra, which suggests that the change of TET efficiencies in the studied QD-ACA complexes is mainly attributed to change of TET apparent rates.

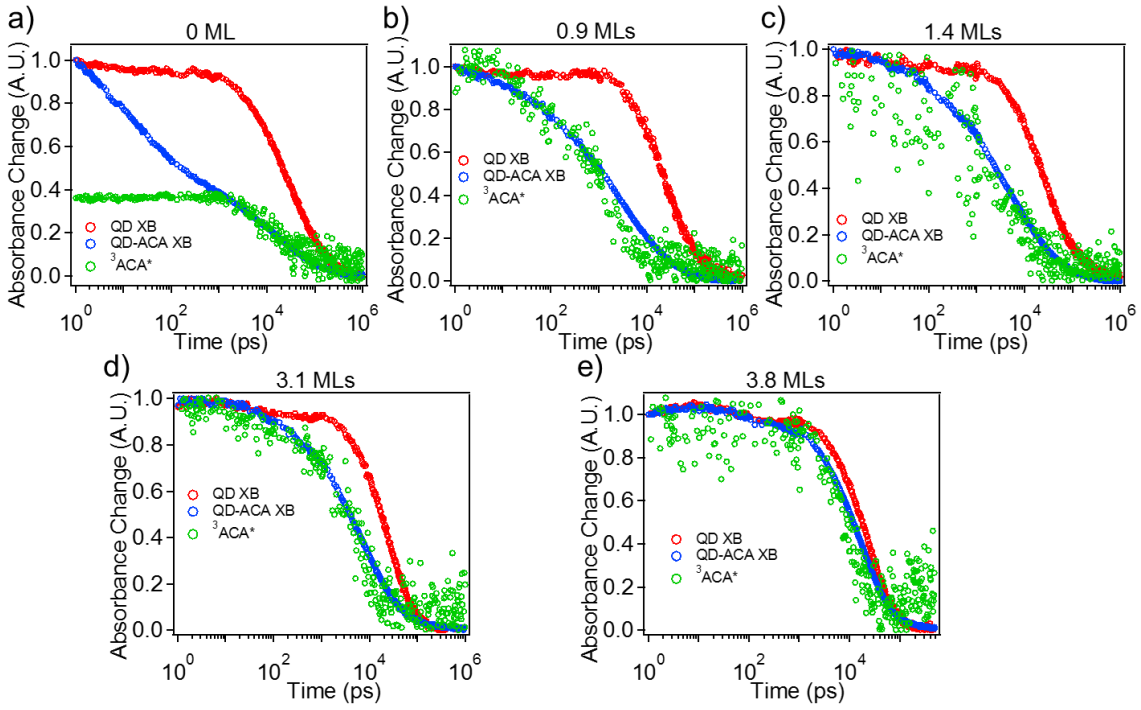

Figure 3.9: Normalized XB kinetics at the core $1S_h$-$1S_e$ transition for QDs (red) and QD-ACA complex (blue) along with ^{3}ACA* signal growth kinetics (green) in time range of 1 ps – 1 μs. a), b), c), d) and e) correspond to CdSe/CdS QDs with 0, 0.9 ,1.4, 3.1 and 3.8 monolayers of CdS

shell, respectively. The ^{3}ACA* growth kinetics were inverted and normalized to 1 in panel b)-e) for better comparison with QD-ACA XB decay. Due to extra XB decay within 1 ns through electron trapping for CdSe QD-ACA, the ^{3}ACA* growth kinetics was inverted and normalized to the XB amplitude after 1ns in panel a).

The apparent TET rate in QD-ACA complexes depends on the number of adsorbed ACA molecules per QD. Thus, in order to compare the TET coupling strength in core-shell QD-ACA complexes with varying shell thickness, TET rates should be measured in complexes with the same number of adsorbed acceptors, which is difficult to do for the following reasons. In the TA experiment, excess of ACA was added to QD hexane solution for ultrasonication. Despite the relatively small solubility of ACA in hexane, it cannot be neglected when determining the number of adsorbed ACA on QD surface from UV-vis spectrum of QD-ACA. The ACA absorption in UV-vis spectrum consists of contributions from both free ACA in solution and ACA attached on QD, and determination of adsorbed ACA number on QD surface from UV-vis spectra is not accurate. Furthermore, the XB kinetics in QDs does not accurately represent the band edge exciton population. For CdSe QDs, VB holes are trapped on surface, and XB kinetics mostly represents the trap exciton dynamics.[54] For CdSe/CdS QDs, there still exist surface trap states, and their contribution to the XB kinetics cannot be neglected, considering the non-unity PL quantum yields of the QDs. Therefore, the QD XB decay and ^{3}ACA* growth kinetics contain the contributions of band edge exciton and trapped exciton populations, which complicate the analysis. It has been show previously that in CdSe-ACA complex, the TET rate from trap excitons is slower than that of band edge excitons and depends on the trap state energy.[54] For the CdSe/CdS-ACA complex, the contribution of deep trap excitons to TET is unknown and is difficult to study due to a lack of

spectra fingerprints of the deep trap excitons in both the photoinduced absorption signal in TA spectra and trap exciton emission in PL spectra.

3.2.3 Shell thickness dependence of TET rate

In order to determine how the TET rate from the band edge state in core-shell QDs to ACA depends on the shell thickness, we turn to TRPL measurement of band edge exciton decay kinetics. First, only the band edge PL signal can be separated from trap state emissions to ensure that only band edge excitons is probed. Second, the TRPL kinetics of core-shell QD-ACA complexes are measured as a function of ACA concentrations, from which the TET rate from QD-ACA with one acceptor (referred to as intrinsic TET rate, k_i) can be determined to allow meaningful comparison of TET rates in different samples. Two detection time windows (100 ns and 700 ns) were applied to resolve the band edge emission kinetics of QD-ACA in early and late time scales, respectively. The instrument response functions of the TRPL were characterized by Gaussian functions with FWHM of 110 ps and 626 ps for 100 ns and 700 ns time windows, respectively. The results are shown in Figure 3.10 and Figure 3.11. With increasing ACA concentrations, QD-ACA complexes show faster band edge PL decay traces and smaller initial PL amplitudes. With thicker CdS shells, the TRPL traces show smaller initial PL amplitude loss and slower decays on the 1 to 100 ns time scale. The initial amplitude recorded by the PL decay reflects the exciton decay within in the < 1 ns time scale. Because the TA measurements above show negligible TET in these complexes within 1 ns, the initial amplitude loss in TRPL decay can be attributed to fast electron trapping induced by ACA adsorption. The slower TEPL decay component can be attributed to TET from the QD to the acceptors, consistent with the formation of the ACA triplet absorption shown by the TA measurement above.

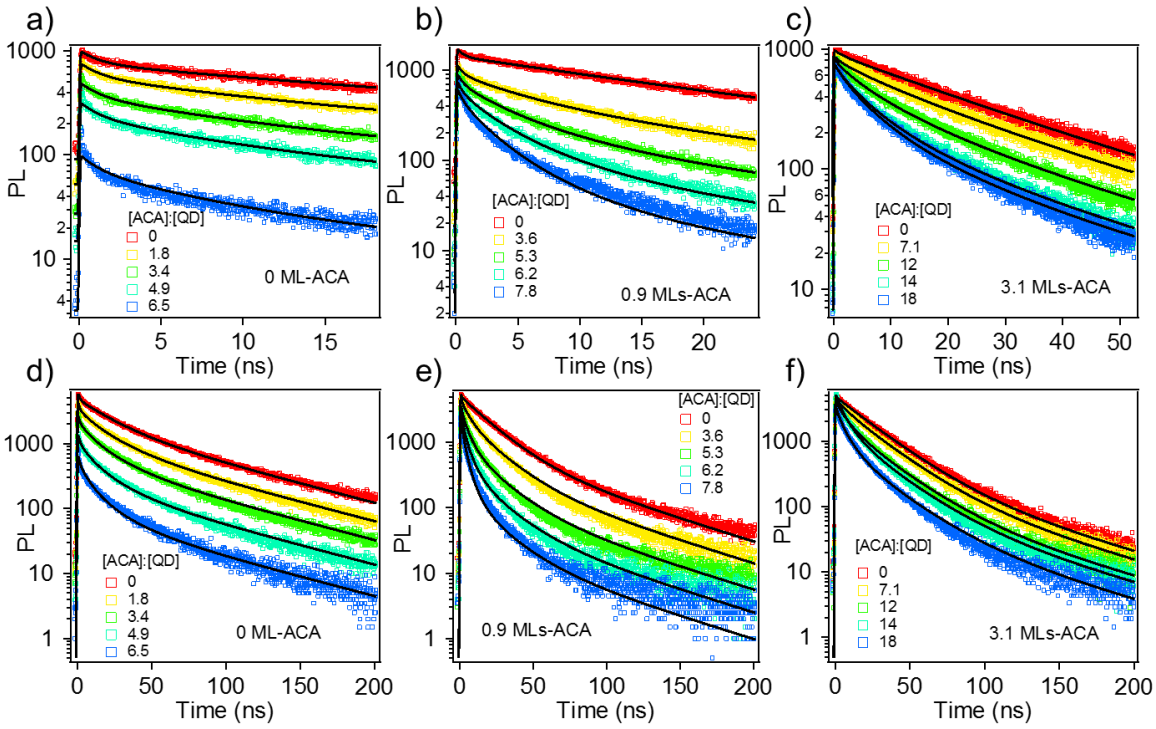

Figure 3.10: TRPL kinetics of a). CdSe QD-ACA, b). CdSe/CdS QD-ACA (0.9 monolayers of CdS) and c). CdSe/CdS QD-ACA (3.1 monolayers of CdS) band edge emission with varying ACA concentrations (colored circles). d), e) and f) are the corresponding TRPL kinetics traces collected in longer detection time window (700 ns). The global fitting curves of the kinetics traces according to Eq. 3.3 and Eq. 3.4 are shown as solid black lines. The excitation wavelength was set as 460 nm due to limitation of the laser for TRPL.

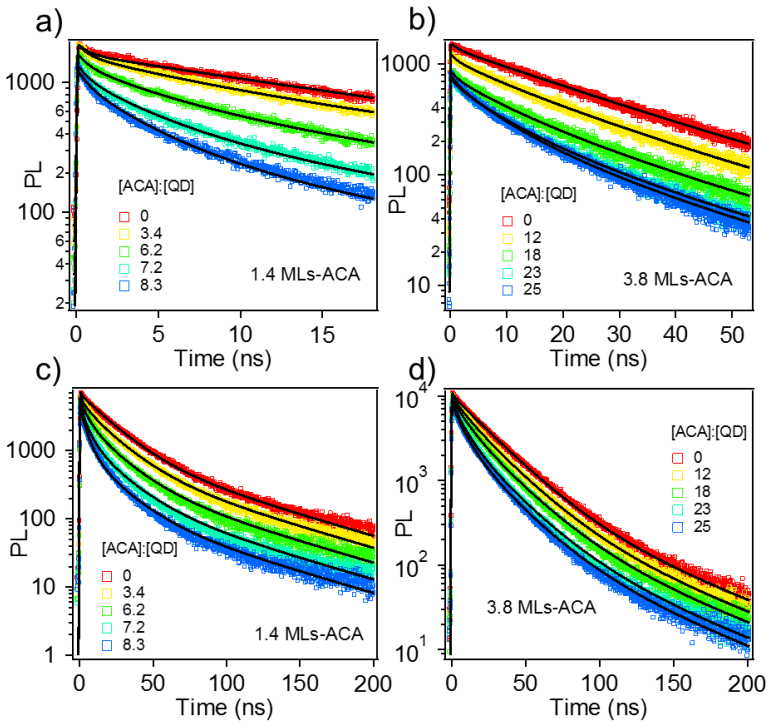

Figure 3.11: TRPL kinetics of a). CdSe/CdS QD-ACA (1.4 monolayers of CdS) and b). CdSe/CdS QD-ACA (3.8 monolayers of CdS) band edge emission with varying ACA concentrations (colored circles). c) and d) are the corresponding TRPL kinetics traces collected in longer detection time window (700 ns). The global fitting curves of the kinetics traces according to Eq. 3.3 and Eq. 3.4 are shown as solid black lines.

In order to fit these TRPL traces to extract the k_i, we assume the Poisson distribution of adsorbed ACA on QD surface:[59]

$$P(n,m) = \frac{m^n e^{-m}}{n!} \qquad \text{Eq. 3.1}$$

where m and n are the average and specific numbers of adsorbed ACA on QDs. The apparent rate of TET to ACA in a QD-ACA complexes with n adsorbed ACA is:[59]

$$k_{app}(n) = nk_i \qquad \text{Eq. 3.2}$$

Accordingly, the TRPL traces of QD-ACA with 700 ns detection time window can be derived as:

$$N(t,m) = bN(0)(\sum_n e^{-nk_i t} P(n,m))S(t) \qquad \text{Eq. 3.3}$$

where N(0) is the initial PL amplitude at time zero, reflecting the initial concentration of excited QDs with a band edge exciton, S(t) is the band edge exciton decay kinetics trace of QDs without ACA, which is described by a three-exponential decay function, and (1-b) is the initial PL amplitude loss due to fast electron trapping that cannot be resolved by our TRPL measurement. In the TRPL traces of QD-ACA with 100 ns time window, the observed signal includes the QD-ACA emission introduced by previous excitation pulses because of the shorter pulse repetition time than the QD exciton lifetime.[59] Therefore, the kinetics traces can be given by:[59]

$$N(t,m) = C\sum_j (bN(0)(\sum_n e^{-nk_i(t+jT_R)} P(n,m))S(t+jT_R)) \qquad \text{Eq. 3.4}$$

where T_R is the pulse repetition time (100 ns), and C is the constant to account for the difference in excitation pulse energies and data acquisition times of TRPL experiments of 100 ns and 700 ns detection time windows. Eq. 3.3 and Eq. 3.4, after convolution with the Gaussian IRF, are used to globally fit the TRPL kinetics traces in Figure 3.10 and Figure 3.11, and the fitting parameters are shown in Table A3.1-Table A3.5 in Appendix 3.1.

3.2.4 Coupling strengths of TET, electron transfer and hole transfer

TET from CdSe/CdS QDs to ACA is considered to proceed with Dexter energy transfer mechanism.[14, 43] The dependence of TET rate (k_i) on coupling strength can be described as:

$$k_i = \frac{2\pi}{\hbar}|V|^2 FCWD \quad \text{Eq. 3.5}$$

where $|V|$ and FCWD are the coupling strength for TET and the Frank-Condon overlap weighted density of states, respectively.[43] In molecular donor-acceptor systems, the TET coupling strength consists of two-electron exchange integral and one-electron integral term from the charge transfer virtual state:

$$V \approx \frac{2T_{ET}T_{HT}}{\Delta E} - Z \qquad \text{Eq. 3.6}$$

where T_{ET}, T_{HT} and Z are the electron transfer coupling strength, hole transfer coupling strength and exchange integral, respectively, and ΔE is the energy difference between the charge transfer virtual state and the donor excited state.[48] The first term is considered to be dominant in Eq. 3.6 for molecular donor-acceptor systems,[49] and Z is approximately proportional to the product of T_{ET} and T_{HT} when the wavefunction is localized compared to the donor and acceptor distance.[47] Under these circumstances, the TET coupling strength can be predicted from the electron and hole transfer coupling matrix elements, which decrease exponentially with the donor-acceptor distance. To test the relationship between TET coupling strength and electron/hole transfer coupling strength in CdSe/CdS QD system, we also measured the intrinsic electron/hole transfer rates (k_i) as function of CdS shell thickness (with details in Appendix 3.2 and Appendix 3.3), from which the shell thickness dependence of the electron/hole transfer coupling strength can be extracted.[25] MV^{2+} and PTZ were selected as electron and hole acceptor, respectively. k_i of electron/hole transfer from core-shell QDs to MV^{2+}/PTZ were determined from fitting of $1S_h$-$1S_e$ XB kinetics in TA and band edge emission kinetics in TRPL with increasing loading of MV^{2+} and PTZ, respectively (Figure A3.2 and Figure A3.5). The results are shown in Table A3.6-A3.11 in Appendix 3.2 and Appendix 3.3.

As shown in Eq. 3.5, one has to calculate FCWD in order to extract the coupling strength for electron/hole transfer and TET from the corresponding k_is measured from experiments. FCWD of electron/hole transfer from CdSe/CdS QDs to acceptors can be calculated with Auger-assisted model.[63, 67] For electron transfer:

$$k_{ET,i} = \frac{2\pi}{\hbar}|V|^2_{ET} FCWD = \frac{2\pi}{\hbar}|V|^2_{ET} R^2 \int_0^\infty \frac{E}{\sqrt{4\pi\lambda k_b T}} \exp\left[-\frac{(\lambda+\Delta G+E)^2}{4\lambda k_b T}\right] dE \quad \text{Eq. 3.7}$$

where $|V|_{ET}$ is the coupling strength for electron transfer from QDs, R is the radius of the QD.[63] For hole transfer:

$$k_{HT,i} = \frac{2\pi}{\hbar}|V|^2{}_{HT}FCWD = \frac{2\pi}{\hbar}|V|^2{}_{HT}\sum_{i=0} g_i \frac{1}{\sqrt{4\pi\lambda k_b T}} \exp\left[-\frac{(\lambda+\Delta G+E_i)^2}{4\lambda k_b T}\right] \quad \text{Eq. 3.8}$$

where $|V|_{HT}$ is the coupling strength for hole transfer, and g_i is the degeneracy of the upper conduction band level with excess energy of E_i compared to $1S_e$ level.[67] For TET, FCWD can be calculated with conventional Marcus model:[68]

$$k_{TET,i} = \frac{2\pi}{\hbar}|V|^2{}_{TET}FCWD = \frac{2\pi}{\hbar}|V|^2{}_{TET}\frac{1}{\sqrt{4\pi\lambda k_b T}} \exp\left[-\frac{(\lambda+\Delta G)^2}{4\lambda k_b T}\right] \quad \text{Eq. 3.9}$$

In order to calculate ΔG for electron/hole transfer and TET, we applied the effective mass approximation (EMA) method to calculate the energies of electron, hole and exciton in CdSe/CdS QDs. Details for calculation are shown in Appendix 3.4. The calculated energies of electron/hole at the corresponding 1S, 1D, 1P and 2S levels as well as the $1S_h$-$1S_e$ exciton energies for CdSe/CdS QDs are shown in Table A3.13-A3.14 in Appendix 3.4. The calculated $1S_h$-$1S_e$ exciton energies agree with those measured from UV-vis spectra, which confirms the fidelity of the EMA calculation. Reorganization energies of the acceptors for the three processes were calculated based on B3LYP/6-31++G(d,p) level of theory with details in Appendix 3.5. The reorganization energy of solvent and QD was estimated as 100 meV for all three processes.[69-70] With the results from calculation, redox potentials of MV^{2+} and PTZ and triplet excited state energy of ACA shown in Figure 3.1, the change of FCWD for electron/hole transfer and TET as QD shell thickness increases can be obtained. The experimentally measured rates of the three processes were scaled to reflect the shell thickness dependent coupling strength as:

$$k'_r = \frac{k_{i_r}}{FCWD_r} FCWD_{r=0} \propto |V|^2 \quad \text{Eq. 3.10}$$

where r is the shell thickness of QDs. The obtained k's (coupling strength) as function of shell thickness are shown in Figure 3.12. The measured coupling strengths for electron/hole transfer and TET overall decrease exponentially with shell thickness. The trend was fit with:

$$k' = Ae^{-\beta r} \ or \ ln(k') = a - \beta r \quad \text{Eq. 3.11}$$

where β is the exponential decay coefficient. β obtained from the fitting is (0.016 ± 0.011) $Å^{-1}$ for TET, (0.234 ± 0.060) $Å^{-1}$ for electron transfer and (0.130 ± 0.011) $Å^{-1}$ for hole transfer. Surprisingly, the β for TET is smaller than the sum of βs for electron/hole transfer, and β value for hole transfer is also surprisingly smaller than that of electron transfer because of the expected lower hole charge density than electron charge density at the surface of CdSe/CdS core/shell QDs.[27] If the coupling strength of TET from CdSe/CdS QDs to the acceptor is proportional to product of T_{ET} and T_{HT} as in molecular donor-acceptor systems, then β for TET is expected to be equal to the sum of βs for electron/hole transfer.[46] The weak dependence of TET rates on shell thickness compared to electron/hole transfer suggests that TET from CdSe/CdS core-shell QDs cannot be depicted by simple Dexter energy transfer from band edge excitons.

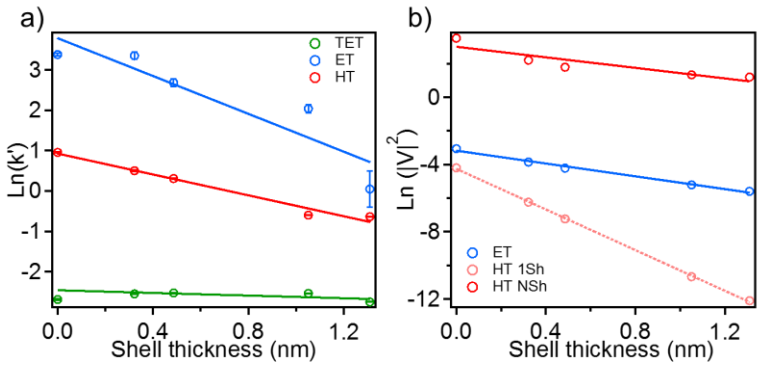

Figure 3.12: Coupling strength of electron/hole/energy transfer from experimental measurement and calculation. a) Change of k' (proportional to coupling strength) for TET (green), electron transfer (ET) (blue) and hole transfer (HT) (red) from CdSe/CdS core/shell QDs to the corresponding acceptors as a function of the shell thickness. The solid lines are the fittings assuming exponential decrease of k' with increasing shell thickness. b) Predicted coupling strength change for electron transfer from $1S_e$ surface wavefunction density (blue), hole transfer from $1S_h$ surface wavefunction density (pink) and hole transfer from the model involving NS_h virtual states

(red). The lines are the fitting assuming exponential decrease of coupling strength with shell thickness. Note that the predicted coupling strength values from calculation do not represent the absolute values because of the undetermined proportionality between coupling strength and surface wavefunction density and only the trend should be considered here.

To further rationalize the measured shell thickness dependences of the electron/hole/energy transfer coupling strengths, we compared the measured coupling strength to those predicted by EMA calculation. In our previous research, it was proposed that the coupling strength for electron/hole transfer can be modeled by wavefunction overlap between the QD and the acceptors.[25] In shell thickness dependence studies, the overlap is proportional to electron/hole surface charge density because of the non-dependence of acceptor wavefunction on the QD shell thickness. Although the coupling strength of electron/hole transfer in Auger assisted model is also related to electron-hole Coulomb interaction,[63] the Coulomb interaction change is relatively small for CdSe/CdS QDs in this study compared to the measured coupling strength change (see Table A3.13) and thus will be neglected for simplicity. Figure 3.12b shows the calculated electron/hole transfer coupling strength change as function of shell thickness from $1S_e$ and $1S_h$ surface charge density (see Table A3.15). The calculated coupling strength decreases exponentially with shell thickness for electron/hole transfer, and the βs from fitting are (0.190 ± 0.010) $Å^{-1}$ for electron transfer and (0.605 ± 0.007) $Å^{-1}$ for hole transfer. The calculation result is consistent with experimental one for electron transfer. However, the calculated coupling strength change for hole transfer from $1S_h$ surface charge density dramatically deviates from experimental results. Because involvement of only $1S_h$ state cannot account for the measured hole transfer coupling strength, we herein propose that hole transfer from CdSe/CdS QDs may be mediated by virtual states. The

inclusion of virtual states has been proposed for molecular donor-bridge-acceptor systems, in which the localized bridge virtual states with higher energies can couple to wavefunctions of the donor and acceptor and thus facilitate the through-bond electron transfer. Such a mechanism has been referred to as super-exchange mechanism.[71-74] In our study of CdSe/CdS QD, higher energy virtual states may also be involved in hole transfer from QDs to acceptor. These states can be higher energy hole states, as suggested by radial distribution functions (RDF) of hole states in the EMA calculation. As shown in Figure A3.6, the wavefunctions of higher hole states (NS_h) extend more to QD surface compared to $1S_h$ state, which is more localized in the CdSe core, and thus has more overlap with the wavefunctions of the acceptor. Therefore, these higher energy hole states could serve as virtual states to mediate hole transfer if their energies are close to that of $1S_h$ level. In this scenario, the coupling strength of hole transfer can be described as:

$$V = \sum_i \frac{h_{1Sh-Xi} h_{Xi-A}}{\Delta E_i} \quad \text{Eq. 3.12}$$

where h_{1Sh-Xi} is the coupling strength between $1S_h$ state to higher energy hole state X_i; h_{Xi-A} is the coupling between state X_i and the acceptor, and ΔE_i is the energy difference between $1S_h$ and X_i.[72] Within the framework of triplet exciton interactions in QDs,[75] h_{1Sh-Xi} can be calculated as a Coulomb integral between the $1S_h$-$1S_e$ and X_i-$1S_e$ excitons. The element $|h_{Xi-A}|^2$ can be assumed proportional to the surface charge density of X_i, with additional computational details provided in Appendix 3.4 and Table A3.16. Because of the formal treatment of these QDs as spherical particles and the resulting angular momentum conservation condition, only $X_i = NS_h$ states (N=2,3…) can couple to the $1S_h$ state. The calculated hole transfer coupling strength with Eq. 3.12 overall decreases exponentially with the shell thickness and shows much weaker dependence on shell thickness compared to that calculated from the $1S_h$ surface charge density, as shown in Figure 3.12b. The fitting of the trend with Eq. 3.11 yields β of (0.157 ± 0.042) Å^{-1}, which

is in reasonable agreement with the experiment value of (0.130 ± 0.011) $Å^{-1}$. One should note that the prerequisite for higher energy virtual state involvement in electron/hole transfer is the small energy difference between the virtual state and the donor state ($1S_e$ or $1S_h$), as indicated in Eq. 3.12. For electron transfer from CdSe/CdS QD, because the energy difference between $1S_e$ and NS_e (> 1 eV for the first few CdS ML) is larger than that for the hole, we do not consider this process to be mediated by higher energy virtual states, and surface charge density of $1S_e$ is adequate to describe the shell thickness dependent coupling strength.

We now turn to discussion of the measured TET coupling strength, which shows much weaker dependence on shell thickness compared to those of electron/hole transfer. From previous discussion, it can be derived that the TET coupling strength from CdSe/CdS QDs to molecular acceptors is described by wavefunction overlap of $1S_e$/$1S_h$ and LUMO/HOMO of the acceptor if the coupling strength is dominated by two-electron exchange integral that couples the QD $1S_h$-$1S_e$ exciton and molecular triplet excited state (<QD*|V|T*> shown as green arrow in Figure 3.13) or by one-electron integrals that only involve charge transfer virtual states (<QD*|V|CT> and <CT|V|T*> shown as blue arrows in Figure 3.13):

$$|V|^2{}_{TET} \approx C'|<\Psi_{1Se}|\Psi_{LUMO}>|^2|<\Psi_{1Sh}|\Psi_{HOMO}>|^2 \propto (|\Psi_{1Se}|^2\,|\Psi_{1Sh}|^2)|_{surface} \quad \text{Eq. 3.13}$$

where C' is a constant. Then TET coupling strength is expected to drop exponentially with shell thickness, and β is expected to be (0.190+0.605=0.795) $Å^{-1}$ from the calculation result of $1S_h$ and $1S_e$ surface wavefunction density. Apparently, this model is not consistent with the experimental result. The experimental result also cannot be accounted for by the recently proposed endothermic charge-transfer mediated TET, considering that β for TET is smaller than β for electron/hole transfer.[62] Our previous discussion of coupling strength for hole transfer has included other virtual states with hole in higher energy levels. These virtual states may also be nonnegligible in TET

from QD, as shown in red arrows in Figure 3.13. The contribution of higher QD virtual states to TET coupling strength would then involve <QD*|V|X*> and <X*|V|T*>, where X* is the virtual exciton states shown in Figure 3.13. The first term can be described as the Coulomb integral between the $1S_h$-$1S_e$ exciton and NS_h-$1S_e$ exciton. The second term is a two-electron exchange integral similar to <QD*|V|T*>. Actually, similar conclusion has been invoked in molecular systems for TET. Previous research has demonstrated the involvement of bridge exciton virtual state mediated TET in molecular donor-bridge-acceptor systems, especially for the low bridge tunneling barrier and long bridge length.[50] The calculation showed the weaker dependence of TET coupling mediated by bridge exciton on bridge length than TET coupling mediated by charge transfer state, which is consistent with the result in this study. Further detailed evaluations of the coupling strength of higher energy virtual state mediated TET from CdSe/CdS QD require more sophisticated calculation method, thus are out of the scope of this article and await future research in the field.

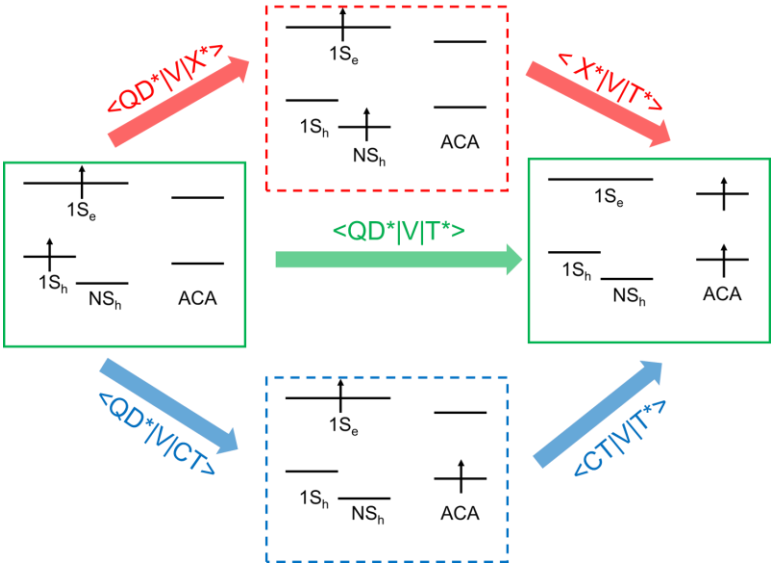

Figure 3.13: Potential models to account for coupling strength of TET from CdSe/CdS QDs to ACA. TET may be mediated by virtual exciton states with electron/hole in higher energy levels

(shown as red arrows). The direct two-electron coupling between initial and final states are shown as green arrow, and TET with charge transfer virtual state is shown as blue arrows.

3.3 Conclusion

In summary, we have tested whether the coupling strength of core-shell QD sensitized TET can be described by the model of TET involving charge transfer virtual state and whether the process can be considered as simultaneous electron and hole transfer. By varying the CdS shell thickness in CdSe/CdS QDs and extracting the shell thickness dependent coupling strength of TET from QDs to molecular acceptor from the measured TET rates, we have demonstrated the exponential decrease of TET coupling strength with increasing shell thickness, and the exponential decay factor or damping coefficient β is (0.016 ± 0.011) $Å^{-1}$, which is smaller than the sum of βs for extracted coupling strength of electron transfer ((0.234 ± 0.060) $Å^{-1}$) and hole transfer ((0.130 ± 0.011) $Å^{-1}$) from QDs. The weak shell thickness dependence of TET coupling strength from QDs is not consistent with the model of charge transfer virtual state mediated TET. We propose that other high energy virtual exciton states may be involved for core-shell QD sensitized TET. Our finding suggests that the unique exciton structures of QDs can enable new TET pathways other than ones in molecular counterparts, which may be applied to further improve the efficiency of TET from QDs in future research.

Appendix 3.1

Fittings of TRPL Kinetics of CdSe/CdS QDs-ACA

Eq. 3.3 and Eq. 3.4 in the main text were applied to global fit the TRPL kinetics traces of CdSe/CdS QD-ACA. In TRPL experiments, the wavelength of the excitation pulse was set as 460 nm due to limitation of the laser for TRPL. The excitation pulse would inevitably excite the T band transition in CdSe/CdS QDs. According to our previous research, the generated hole after excitation would either be trapped to surface or relax to $1S_h$ level localized in the core in much shorter time compared to TET process.[27] Here we only probed the band edge emission kinetics, thus the TRPL kinetics traces mainly show TET from band edge excitons. In the global fitting of the kinetics traces in Eq. 3.3 and Eq. 3.4, the summations of n were performed until n = 20, considering that the average numbers of adsorbed ACA on QD surface in TRPL experiments are expected to be smaller than 20, and the probability of QD with more than 20 adsorbed ACA, which follows Poisson distribution (Eq. 3.1 in the main text), is negligible.[28] The summations of j in Eq. 3.4 were performed until j = 10 because the lifetime of the QD TRPL signal is smaller than 1000 ns, and the contribution of the excitation pulse arriving 1000 ns before the time of signal detection to the QD TRPL signal of 100 ns detection time window is negligible. TRPL kinetics traces of QDs without ACA can be fit with three-exponential function convoluted with the Gaussian IRF, and the parameters of the fitting were fixed for fitting of the kinetics traces of QD-ACA. The rates of TET from QD to one ACA molecule (k_i) were controlled to the same for QD-ACA with varying ACA concentrations, and m and b in Eq. 3.3 and Eq. 3.4 were controlled to be the same for kinetics traces in 100 ns and 700 ns detection time windows of QD-ACA with specific ACA concentration. The fitting result is shown in Table A3.1-Table A3.5.

Table A3.1: Parameters of global fitting of TRPL kinetics traces of CdSe QD-ACA in Figure 3.10a and Figure 3.10d. a_i and τ_i (i = 1, 2, 3) are the parameters in three-exponential function to fit the kinetics traces of QD without ACA.

[ACA]:[QD]	0	1.8	3.4	4.9	6.5
a_1	$(1.80 \pm 0.02) \times 10^3$				
τ_1 (ns)	1.19 ± 0.02				
a_2	$(2.99 \pm 0.02) \times 10^3$				
τ_2 (ns)	20.1 ± 0.2				
a_3	$(1.91 \pm 0.02) \times 10^3$				
τ_3 (ns)	72.9 ± 0.5				
m	0	0.328 ± 0.003	0.548 ± 0.004	0.732 ± 0.009	1.13 ± 0.02
k_i (ns^{-1})	0.0677 ± 0.0010				
b	1	0.721 ± 0.001	0.461 ± 0.001	0.232 ± 0.001	0.112 ± 0.001
C	0.136 ± 0.001				

Table A3.2: Parameters of global fitting of TRPL kinetics traces of CdSe/CdS QD (0.9 monolayers of CdS)-ACA in Figure 3.10b and Figure 3.10e.

[ACA]:[QD]	0	3.6	5.3	6.2	7.8
a_1	$(1.37 \pm 0.03) \times 10^3$				
τ_1 (ns)	0.457 ± 0.013				
a_2	$(4.34 \pm 0.02) \times 10^3$				
τ_2 (ns)	18.8 ± 0.1				
a_3	754 ± 22				

τ_3 (ns)	62.3 ± 1.0				
m	0	0.711 ± 0.003	1.37 ± 0.01	1.98 ± 0.01	2.76 ± 0.02
k_i (ns^{-1})	0.119 ± 0.001				
b	1	0.943 ± 0.002	0.724 ± 0.002	0.594 ± 0.002	0.508 ± 0.002
C	0.268 ± 0.001				

Table A3.3: Parameters of global fitting of TRPL kinetics traces of CdSe/CdS QD (1.4 monolayers of CdS)-ACA in Figure 3.11a and Figure 3.11c.

[ACA]:[QD]	0	3.4	6.2	7.2	8.3
a_1	$(1.49 \pm 0.03) \times 10^3$				
τ_1 (ns)	0.654 ± 0.021				
a_2	$(5.77 \pm 0.02) \times 10^3$				
τ_2 (ns)	19.0 ± 0.1				
a_3	$(1.00 \pm 0.03) \times 10^3$				
τ_3 (ns)	69.4 ± 1.1				
m	0	0.275 ± 0.003	0.715 ± 0.004	1.13 ± 0.01	1.52 ± 0.01
k_i (ns^{-1})	0.117 ± 0.001				
b	1	0.880 ± 0.002	0.828 ± 0.002	0.716 ± 0.002	0.670 ± 0.002
C	0.233 ± 0.001				

Table A3.4: Parameters of global fitting of TRPL kinetics traces of CdSe/CdS QD (3.1 monolayers of CdS)-ACA in Figure 3.10c and Figure 3.10f.

[ACA]:[QD]	0	7.1	12	14	18

a_1	387 ± 14				
τ_1 (ns)	1.56 ± 0.09				
a_2	$(4.44 \pm 0.02) \times 10^3$				
τ_2 (ns)	23.8 ± 0.1				
a_3	320 ± 28				
τ_3 (ns)	74.9 ± 3.3				
m	0	0.231 ± 0.003	0.714 ± 0.004	1.17 ± 0.01	1.52 ± 0.01
k_i (ns^{-1})	0.0825 ± 0.0007				
b	1	0.933 ± 0.002	0.860 ± 0.002	0.790 ± 0.003	0.703 ± 0.002
C	0.184 ± 0.001				

Table A3.5: Parameters of global fitting of TRPL kinetics traces of CdSe/CdS QD (3.8 monolayers of CdS)-ACA in Figure 3.11b and Figure 3.11d.

[ACA]:[QD]	0	12	18	23	25
a_1	$(1.23 \pm 0.02) \times 10^3$				
τ_1 (ns)	1.34 ± 0.03				
a_2	$(9.61 \pm 0.03) \times 10^3$				
τ_2 (ns)	23.4 ± 0.1				
a_3	780 ± 36				
τ_3 (ns)	65.6 ± 1.4				
m	0	0.270 ± 0.002	0.519 ± 0.002	0.832 ± 0.003	1.02 ± 0.01
k_i (ns^{-1})	0.0622 ± 0.0004				
b	1	0.954 ± 0.001	0.912 ± 0.001	0.819 ± 0.001	0.789 ± 0.001

C	0.130 ± 0.001

Appendix 3.2

Determination of Rates of Electron Transfer from CdSe/CdS QDs to Methyl Viologen (MV^{2+})

MV^{2+} was applied as the electron transfer acceptor for determination of the shell thickness dependent electron transfer rate. As shown in Figure A3.1, electron transfer from CdSe/CdS QDs to MV^{2+} can be well resolved in TA spectra. For CdSe-MV^{2+}, charge separated state feature consisting of MV^{+} radical absorption signal from 550 nm to 700 nm and derivative-like feature due to Stark effect is almost instantaneously formed after excitation of the QDs, suggesting ultrafast electron transfer from QDs to MV^{2+}.[27] The formation of charge separated state signal is slower with increasing shell thickness, and the relative signal amplitude of MV^{2+} radical is smaller with the growth of CdS shell, which indicates the slower and less efficient electron transfer from the core-shell QDs.

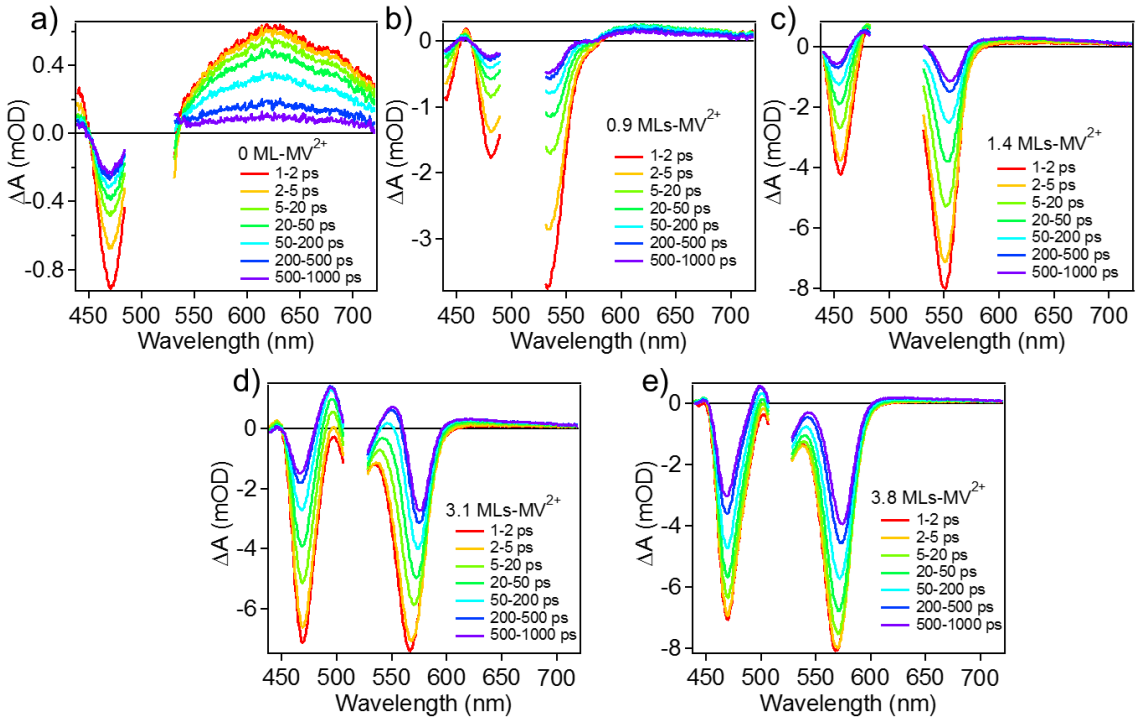

Figure A3.1: TA spectra of CdSe/CdS QD-MV^{2+} with a). 0, b). 0.9, c). 1.4, d). 3.1 and e). 3.8

monolayers of CdS shell in time range of 1 ps – 1 ns. The amount of the MV^{2+} was excess compared to that of QDs. The wavelength of the pump pulse was 520 nm.

In order to determine the rates of electron transfer from QDs to one MV^{2+}, we extracted and fit the XB kinetics ($1S_h$-$1S_e$ transition of the core) of the QD-MV^{2+} with varying loading amount of MV^{2+}. As shown in Figure A3.2, with increasing loading amount of MV^{2+}, the XB kinetics show faster decay within the time range of the plots before reaching saturation due to change of apparent electron transfer rate from the change in numbers of adsorbed MV^{2+} on QD surface. It is assumed that the numbers of adsorbed MV^{2+} on QD surface follow Poisson distribution:

$$P(n,m) = \frac{m^n e^{-m}}{n!} \qquad \text{Eq. A3.1}$$

where m and n are the average and specific numbers of adsorbed MV^{2+} on QDs, respectively.[76] The apparent rate of electron transfer is proportional to n as:

$$k_{app} = nk_i \qquad \text{Eq. A3.2}$$

where k_{app} and k_i are the apparent rate of electron transfer and the rate of electron transfer from QD to one acceptor, respectively. Different from TA spectra of QD with excess MV^{2+} in Figure A3.1, the signal amplitudes of the charge separated state spectra in experiments to determine the k_i are much smaller compared to those of the QD excited state spectra because of the smaller amount of MV^{2+} added to the QD solutions, as indicated by negligible red-shift of the XB peaks and small MV^{+} radical signal amplitudes shown in Figure A3.3. Therefore, the XB kinetics in Figure A3.2 are dominated by signal from state filling of $1S_e$ electron level that is proportional to conduction band edge electron populations. Accordingly, the XB kinetics can be derived as:

$$XB(t) = XB(0)(\sum_n e^{-nk_i t} P(n,m))S(t) \quad \text{Eq. A3.3}$$

where S(t) is the XB kinetics of QDs without MV^{2+} in the form of two-exponential or three-

exponential function. In order to better fit the XB kinetics of the CdSe/CdS QD-MV^{2+}, two components of the electron transfer rates were applied:

$$XB(t) = XB(0)[\sum_n (b_1 e^{-nk_{i1}t} + b_2 e^{-nk_{i2}t})P(n,m)]S(t) \quad \text{Eq. A3.4}$$

Eq. A3.3 and Eq. A3.4 convoluted with IRF in TA were applied to fit the XB kinetics of CdSe QD-MV^{2+} and CdSe/CdS QD-MV^{2+}, respectively. The summations in the equations were performed until n = 20, considering that the average numbers of adsorbed MV^{2+} are expected to be much smaller than 20 for samples in Figure A3.2, and P(n,m) is negligible when n is larger than 20. The fitting results are shown in Figure A3.2 and Table A3.6-Table A3.10. For CdSe/CdS QDs, the averaged k_i for electron transfer were calculated as:

$$k = \frac{(b_1 k_{i1} + b_2 k_{i2})}{(b_1 + b_2)} \quad \text{Eq. A3.5}$$

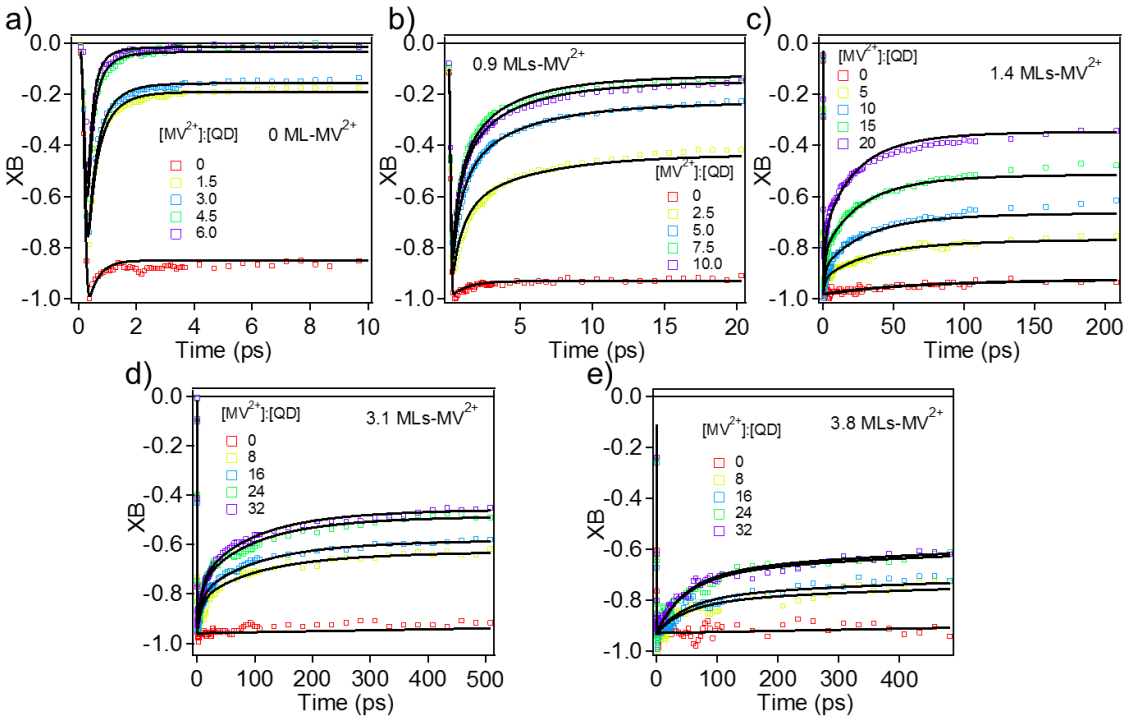

Figure A3.2: XB kinetics ($1S_h$-$1S_e$ core transition) of CdSe/CdS QD-MV^{2+} with varying amount of MV^{2+} added to QD solution for determination of k_i for electron transfer. a)-e) correspond to CdSe/CdS QDs with 0, 0.9, 1.4, 3.1 and 3.8 monolayers of CdS shell. The wavelength of the pump

pulse was 520 nm.

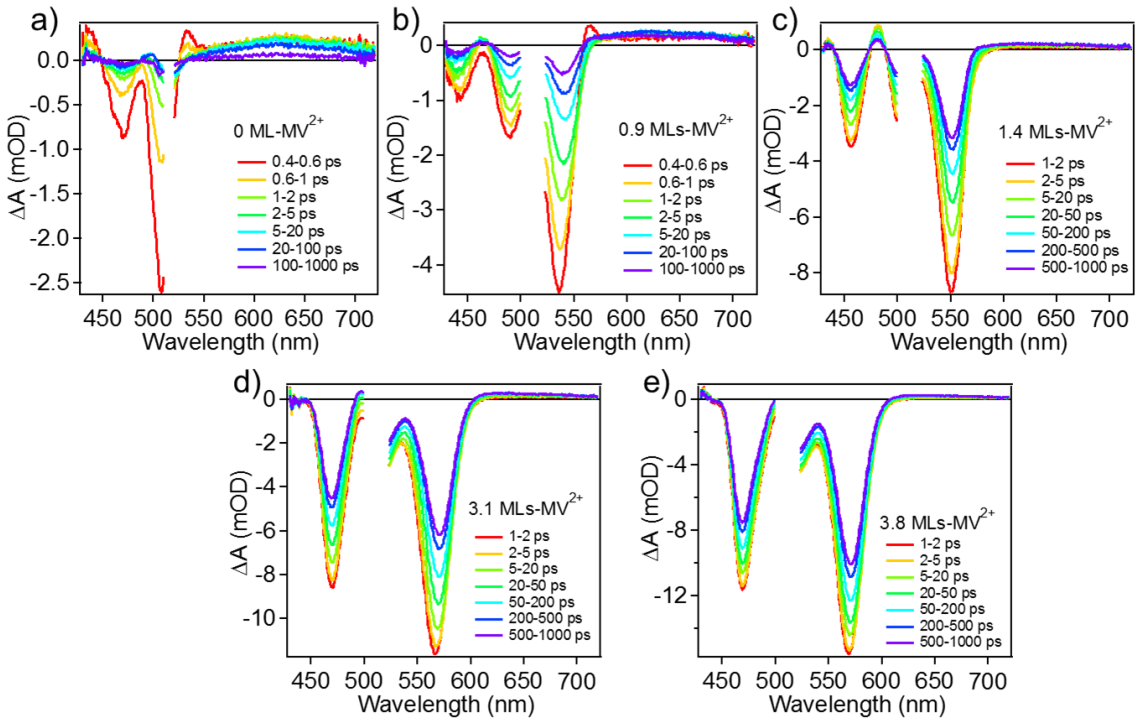

Figure A3.3: TA spectra of CdSe/CdS QD-MV^{2+} with a). 0, b). 0.9, c). 1.4, d). 3.1 and e). 3.8 monolayers CdS shell in TA experiments of determination of k_i for electron transfer from QDs. The ratios of MV^{2+} to QDs were 1.5, 10, 20, 32 and 32 from a) to e). The wavelength of the pump pulse was 520 nm.

Table A3.6: Parameters of global fitting of XB kinetics traces of CdSe QD-MV^{2+} in Figure A3.2. a_i and τ_i (i = 1, 2, 3) are the parameters in three-exponential function to fit the kinetics traces of QD without MV^{2+}.

[MV^{2+}]:[QD]	0	1.5	3.0	4.5	6.0
a_1	0.218 ± 0.016				
τ_1 (ps)	0.370 ± 0.037				

a_2	0.395 ± 0.008				
τ_2 (ns)	13.0 ± 0.4				
a_3	0.389 ± 0.008				
τ_3 (ns)	104 ± 2				
m	0	1.49 ± 0.02	1.68 ± 0.03	3.21 ± 0.10	4.03 ± 0.16
k_i (ps^{-1})	1.46 ± 0.05				

Table A3.7: Parameters of global fitting of XB kinetics traces of CdSe/CdS QD (0.9 monolayers of CdS)-MV^{2+} in Figure A3.2.

$[MV^{2+}]$:[QD]	0	2.5	5.0	7.5	10.0
a_1	0.101 ± 0.007				
τ_1 (ps)	1.12 ± 0.21				
a_2	0.649 ± 0.010				
τ_2 (ns)	20.3 ± 0.4				
a_3	0.249 ± 0.010				
τ_3 (ns)	149 ± 7				
m	0	0.760 ± 0.011	1.39 ± 0.02	1.84 ± 0.03	2.00 ± 0.04
b_1	0.530 ± 0.028				
k_{i1} (ps^{-1})	1.15 ± 0.09				
b_2	0.470 ± 0.028				
k_{i2} (ps^{-1})	0.152 ± 0.016				

Table A3.8: Parameters of global fitting of XB kinetics traces of CdSe/CdS QD (1.4 monolayers

of CdS)-MV^{2+} in Figure A3.2.

$[MV^{2+}]$:[QD]	0	5	10	15	20
a_1	0.047 ± 0.004				
τ_1 (ps)	13.6 ± 3.0				
a_2	0.729 ± 0.007				
τ_2 (ns)	24.9 ± 0.4				
a_3	0.218 ± 0.007				
τ_3 (ns)	223 ± 9				
m	0	0.186 ± 0.005	0.331 ± 0.007	0.589 ± 0.009	0.983 ± 0.015
b_1	0.368 ± 0.014				
k_{i1} (ps^{-1})	0.740 ± 0.070				
b_2	0.632 ± 0.013				
k_{i2} (ps^{-1})	0.0314 ± 0.0020				

Table A3.9: Parameters of global fitting of XB kinetics traces of CdSe/CdS QD (3.1 monolayers of CdS)-MV^{2+} in Figure A3.2.

$[MV^{2+}]$:[QD]	0	8	16	24	32
a_1	0.689 ± 0.044				
τ_1 (ns)	18.7 ± 1.0				
a_2	0.311 ± 0.044				
τ_2 (ns)	70.1 ± 7.0				
m	0	0.395 ± 0.015	0.473 ± 0.017	0.655 ± 0.023	0.714 ± 0.025
b_1	0.406 ± 0.037				

k_{i1} (ps^{-1})	0.119 ± 0.020
b_2	0.594 ± 0.036
k_{i2} (ps^{-1})	0.0844 ± 0.0014

Table A3.10: Parameters of global fitting of XB kinetics traces of CdSe/CdS QD (3.8 monolayers of CdS)-MV^{2+} in Figure A3.2.

$[MV^{2+}]$:[QD]	0	8	16	24	32
a_1	0.531 ± 0.063				
τ_1 (ns)	14.4 ± 1.2				
a_2	0.469 ± 0.063				
τ_2 (ns)	47.0 ± 3.9				
m	0	0.201 ± 0.092	0.237 ± 0.109	0.407 ± 0.198	0.425 ± 0.208
b_1	0.684 ± 0.130				
k_{i1} (ps^{-1})	0.0187 ± 0.0082				
b_2	0.316 ± 0.130				
k_{i2} (ps^{-1})	$(2.615 \pm 0.918) \times 10^{-3}$				

Appendix 3.3

Determination of Rates of Hole Transfer from CdSe/CdS QDs to Phenothiazine (PTZ)

Shell thickness dependent rates of hole transfer from CdSe/CdS QDs were studied with PTZ as the hole acceptor. As shown in Figure A3.4, the TA spectra of CdSe/CdS QDs adsorbed with excess PTZ show formation of derivative-like features due to Stark effect from charge separation and show no faster decay of $1S_h$-$1S_e$ XB in range of 500 nm to 600 nm, suggesting hole transfer from QDs to PTZ considering that XB in CdSe/CdS QDs is mainly attributed to state filling of 1S electron level.[59] One should note that the PTZ^+ radical signal at around 520 nm overlaps with the QD excited state spectra and charge separated state spectra and cannot be well resolved in TA spectra because of its small amplitude.

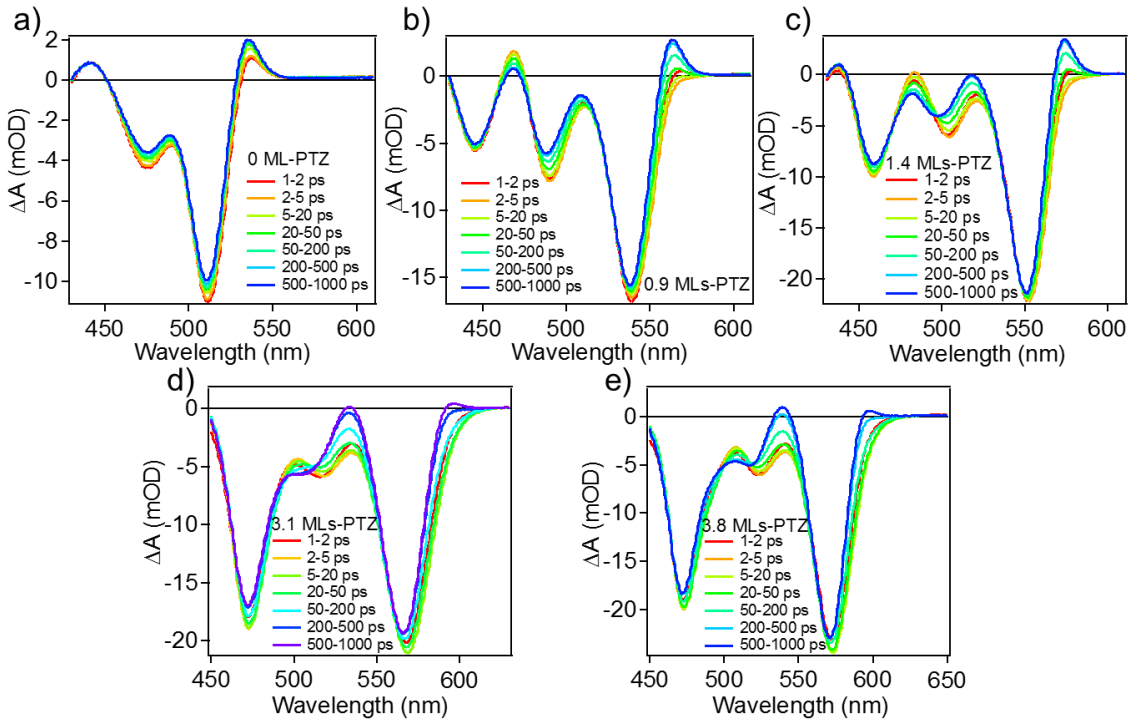

Figure A3.4: TA spectra of CdSe/CdS QD-PTZ with a). 0, b). 0.9, c). 1.4, d). 3.1 and e). 3.8 monolayers of CdS shell in time range of 1 ps – 1 ns. The amount of the PTZ was excess compared to that of QDs. The wavelength of the pump pulse was 400 nm.

Because XB signal of the core-shell QDs in TA mainly consists of state filling of conduction band edge electron, we turned to TRPL measurement when determining rates of hole transfer from QDs to one PTZ (k_i). The excitation wavelength was set as 460 nm due to limitation of the laser for TRPL. Despite the inevitable excitation of T band transition by 460 nm, the hole generated by excitation will either be trapped or relax to $1S_h$ level of the QD in much shorter time compared to the instrument response of the TRPL measurement. Because only band edge emission was monitored in TRPL, holes in deep trap states would not be detected in TRPL. Therefore, the TRPL kinetics mainly show the dynamics of hole transfer from $1S_h$ level to PTZ. In order to determine the k_i of hole transfer, we measured the TRPL kinetics with varying loading amount of PTZ and extracted the k_i of hole transfer from global fitting, which is similar to the determination of k_i for triplet energy transfer and electron transfer in the study. Because of the relatively fast hole transfer, the detection time window for TRPL was set as 50 ns, with FWHM of 62 ps for the Gaussian IRF. With the assumption of Poisson distribution of the numbers of adsorbed PTZ, TRPL kinetics of QD-PTZ can be derived in a similar manner to Eq. 3.4 in the main text. The expression is:

$$N(t,m) = \sum_j (N(0)(\sum_n e^{-nk_i(t+jT_R)} P(n,m)) S(t+jT_R)) \quad \text{Eq. A3.6}$$

where S(t) is the TRPL kinetics of the free QD without PTZ, and T_R is the repetition time of the pulse.[59] The summations of j and n were performed until j = 10 and n = 20. The fitting result is shown in Figure A3.5 and Table A3.11.

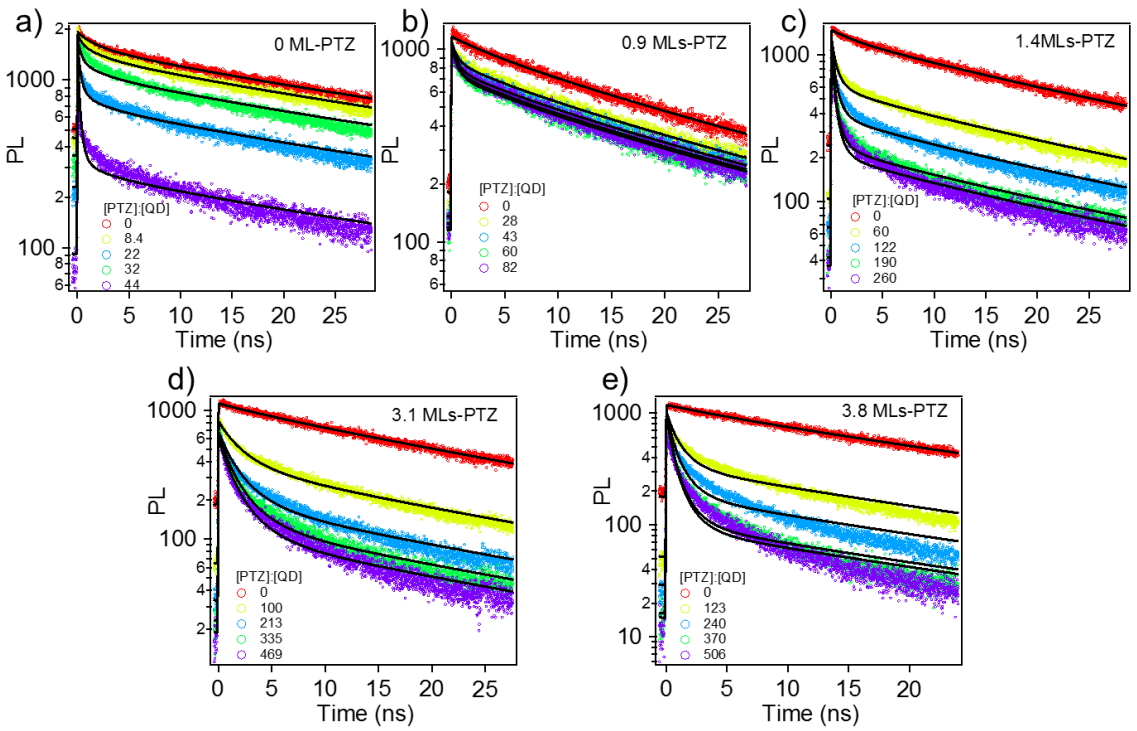

Figure A3.5: TRPL kinetics at band edge emission peaks of CdSe/CdS QDs-PTZ with a). 0, b). 0.9, c). 1.4, d). 3.1 and e). 3.8 monolayers of CdS shell and varying PTZ to QD ratios. The detection time window was 50 ns. The global fitting curves of the kinetics traces are shown as black solid lines.

Table A3.11: Parameters of global fitting of TRPL kinetics traces of CdSe/CdS QD-PTZ in **Figure A3.5**. The parameters of S(t) are the same as those in fitting of TRPL kinetics traces of CdSe/CdS QD-ACA and thus are not shown in the table. m_i (i=0, 1, 2, 3, 4) refer to average numbers of adsorbed PTZ on QD surface with increasing concentrations of PTZ added to QD solution.

Monolayers of CdS shell	0	0.9	1.4	3.1	3.8
m_0	0	0	0	0	0

m_1	0.122 ± 0.001	0.287 ± 0.001	0.835 ± 0.002	1.00 ± 0.01	1.23 ± 0.01
m_2	0.364 ± 0.002	0.377 ± 0.001	1.28 ± 0.01	1.63 ± 0.01	1.81 ± 0.01
m_3	0.796 ± 0.002	0.425 ± 0.001	1.75 ± 0.01	1.95 ± 0.01	2.40 ± 0.01
m_4	1.72 ± 0.01	0.451 ± 0.001	1.88 ± 0.01	2.17 ± 0.01	2.49 ± 0.01
k_i (ns^{-1})	2.60 ± 0.04	1.78 ± 0.03	1.58 ± 0.01	0.684 ± 0.004	0.683 ± 0.004

Appendix 3.4

Single-band Effective Mass Calculation for Electron/hole Energies and Wavefunctions of Core-shell QDs

Table A3.12. Material parameters used in the EMA calculations: m_0 is the electron mass; e_r the medium dielectric; V_e and V_h are conduction and valence band edges respectively.

	CdSe	CdS	hexane
m_e^* / m_0	0.13	0.21	1
m_h^* / m_0	0.45	0.80	1
e_r	10	8.9	1.8819
V_e / eV	-4.0	-3.78	0
V_h / eV	-5.7	-6.29	-8.4

The material parameters for bulk wurtzite CdSe and CdS used in the present EMA calculations are those reported elsewhere[77] and are given in **Table A3.12**. Calculation of electron/hole orbitals requires numerically solving the coupled Schrödinger-Poisson equations for a single exciton in the initial state:[77-79] for the electron in $1S_e$ orbital,

$$\left\{-\frac{\hbar^2}{2}\nabla\cdot[\frac{1}{m_e^*}\nabla]+V_e(\mathbf{r})+\frac{1}{2}\Phi_e^{\text{ind}}(\mathbf{r})+\Phi_h(\mathbf{r})\right\}1S_e(\mathbf{r})=E_e 1S_e(\mathbf{r}) \quad \text{Eq. A3.7a}$$

$$\nabla\cdot e_r\nabla F_e(\mathbf{r})=4\rho\left|1S_e(\mathbf{r})\right|^2 . \quad \text{Eq. A3.7b}$$

and for the hole in $1S_h$ orbital,

$$\left\{-\frac{\hbar^2}{2}\nabla\cdot[\frac{1}{m_h^*}\nabla]+V_h(\mathbf{r})+\frac{1}{2}\Phi_h^{\text{ind}}(\mathbf{r})+\Phi_e(\mathbf{r})\right\}1S_h(\mathbf{r})=E_h 1S_h(\mathbf{r}) \quad \text{Eq. A3.8a}$$

$$\nabla \cdot \varepsilon_r \nabla F_h(\mathbf{r}) = -4\pi \left|1S_h(\mathbf{r})\right|^2, \qquad \text{Eq. A3.8b}$$

and corresponding equations for all final state excitons ($1S_h$,NS_e) and (MS_h,$1S_e$) for the various N and M values of the excited S-orbitals. The curly brackets in 1a and 2a contain, respectively, the effective mass kinetic energy terms, the band potentials for electron and hole, the electrostatic source potentials due to hole and electron, and the self-induced electron and hole potentials with the proper factor of 1/2.[77, 80] The Poisson equations are solved subject to the condition that the inner and outer potentials match at the surface boundary.[78-79] We note that the outer potential in the surrounding environment (presently an organic solvent), at a point sufficiently far from the QD, is given by $\varepsilon_{\text{outside}}^{-1} \int d\mathbf{r}' |1S_e(\mathbf{r}')|^2 / |\mathbf{r}' - \mathbf{r}|$, for the electron, with the corresponding expression for the hole, where $\varepsilon_{\text{outside}}$ is the dielectric constant of the medium outside the quantum dot, presently hexane (see **Table A3.12**). The surface, defined by all points with the dot center as the origin satisfying $x^2 + y^2 + z^2 = R_{\max}^2$ at which the inner and outer potentials are matched, coincides with the surface beyond which the wavefunction is made to vanish, which in the present study is a distance DR from the outer surface of a quantum dot, i.e. $R_{\max}=R_{\text{core}}+L+\Delta R$, where R_{core} is the radius of the CdSe core, L is the CdS shell thickness, and DR = 1 nm. This sets the necessary boundary conditions for the differential equations 7b, 8b.

The differential operators, wavefunctions and electrostatic potentials are recovered using a contracted, infinite order, discrete variable representation (DVR) method described in detail previously.[78] We construct a uniform isotropic Cartesian grid with $\Delta x = \Delta y = \Delta z$ and retain the points within the cutoff radius $R_{\max}$. The above conditions define the coupled matrix equations: (*i*) the eigenvalue equations (7a,8a) for the wavefunctions, which are solved using Davidson's subspace expansion,[81] and (*ii*) linear equations (7b,8b) for the electrostatic potentials, which are

solved using a generic linear conjugate gradient algorithm.

The induced potentials F_e^{ind}, F_h^{ind} are derived from the source potentials F_e, F_h by integrating the induced surface polarization density[82] over all interfacial (CdSe/solvent, CdSe/CdS and CdS/solvent) surfaces *I*,

$$\Phi_e^{\mathrm{ind}}(\mathbf{r}) = \frac{1}{4\pi}\sum_I \frac{\varepsilon_{out}^I - \varepsilon_{in}^I}{\varepsilon_{out}^I} \oint \frac{\vec{\nabla}\Phi_e(\mathbf{r})\big|_{in} \cdot \hat{n}_{out}^{in}(\mathbf{r}_I)}{|\mathbf{r}-\mathbf{r}_I|} dA_I \quad , \qquad \text{Eq. A3.9a}$$

$$\Phi_h^{\mathrm{ind}}(\mathbf{r}) = \frac{1}{4\pi}\sum_I \frac{\varepsilon_{out}^I - \varepsilon_{in}^I}{\varepsilon_{out}^S} \oint \frac{\vec{\nabla}\Phi_h(\mathbf{r})\big|_{in} \cdot \hat{n}_{out}^{in}(\mathbf{r}_I)}{|\mathbf{r}-\mathbf{r}_I|} dA_I \quad . \qquad \text{Eq. A3.9b}$$

By the convention used in deriving equations (A3) the dielectric constants e_{in}^I and e_{out}^I are measured on either side of the interface along the surface norm $\hat{n}_{out}^{in}$ pointing from inside to outside; the potential gradient is evaluated just inside the interfacial surface. With these definitions, the coupled equation systems A3.7-3.9 are solved to self-consistency. Typically, convergence of the wavefunction to 10^{-7} is reached after a few iterations. For the case of an excited state calculation, the Hamiltonians in A3.7a, A3.8a are transformed to yield the sought excited state to be the ground state, i.e. by applying a shift to the Hamiltonian matrix (the DVR matrix representation of the quantity in the curly brackets in A3.7a and A3.8a), and squaring the result: $\mathbf{H} \Rightarrow (\mathbf{H} - \lambda \mathbf{I})^2$. The transformed matrix shares the same eigenvectors as the original, while scanning over a sufficiently wide range of λ yields the desired excited states. The result of the EMA calculation is shown below.

Table A3.13: Calculation result of $1S_e$ electron energy (E_{1Se}), $1S_h$ hole energy (E_{1Sh}), electron-hole Coulomb interaction (<e-h>), $1S_h$-$1S_e$ exciton energy ($E_{1Sh\text{-}1Se}$) and the measured $1S_h$-$1S_e$ exciton energy from UV-vis spectra shown in Figure 3.4 ($E_{1Sh\text{-}1Se}$ from UV-vis) for the studied CdSe/CdS QDs. $1S_h$-$1S_e$ exciton energy can be calculated as: $E_{1Sh\text{-}1Se} = E_{1Se} - E_{1Sh} - \langle e\text{-}h \rangle$.

Monolayers of CdS shell	E_{1Se} (eV)	E_{1Sh} (eV)	<e-h> (eV)	$E_{1Sh-1Se}$ (eV)	$E_{1Sh-1Se}$ from UV-vis (eV)
0	-3.79	-5.62	-0.55	2.39	2.42
0.9	-3.86	-5.64	-0.46	2.24	2.30
1.4	-3.87	-5.65	-0.43	2.21	2.25
3.1	-3.91	-5.69	-0.34	2.12	2.19
3.8	-3.91	-5.71	-0.31	2.11	2.18

Table A3.14: Calculation result of energies of higher electron/hole levels (1P, 1D and 2S) for the studied CdSe/CdS QDs.

Monolayers of CdS shell	E_{1Pe} (eV)	E_{1De} (eV)	E_{2Se} (eV)	E_{1Ph} (eV)	E_{1Dh} (eV)	E_{2Sh} (eV)
0	-3.05	-2.12	-1.35	-5.91	-6.27	-6.44
0.9	-3.33	-2.69	-2.12	-5.87	-6.15	-6.31
1.4	-3.41	-2.89	-2.42	-5.88	-6.15	-6.29
3.1	-3.58	-3.26	-3.10	-5.90	-6.14	-6.24
3.8	-3.61	-3.35	-3.26	-5.92	-6.15	-6.23

Table A3.15: Calculation result of surface charge density (ρ) of electron in $1S_e$ level and hole in $1S_h$ level of the studied CdSe/CdS QDs.

Monolayers of CdS shell	ρ $1S_e$	ρ $1S_h$
0	4.69×10^{-2}	1.50×10^{-2}
0.9	2.21×10^{-2}	1.94×10^{-3}

1.4	1.47×10^{-2}	7.19×10^{-4}
3.1	5.42×10^{-3}	2.31×10^{-5}
3.8	3.69×10^{-3}	5.51×10^{-6}

Table A3.16: Calculation result of energies of the bound S_h hole states (E_{NSh}), coupling elements of NS_h to $1S_h$ (J_{1N}) and the corresponding surface charge densities of these states (ρ) in the studied CdSe/CdS QDs.

Monolayers of CdS shell	E_{2Sh} (eV) (J_{12}) ρ	E_{3Sh} (eV) (J_{13}) ρ	E_{4Sh} (eV) (J_{14}) ρ	E_{5Sh} (eV) (J_{15}) ρ	E_{6Sh} (eV) (J_{16}) ρ
0	-6.44 (16.4) 5.67×10^{-2}	-7.82 (2.0) 1.81×10^{-1}	-8.39 (1.8) 9.17×10^{-1}	non-bound	non-bound
0.9	-6.31 (14.9) 1.33×10^{-2}	-7.28 (0.6) 9.88×10^{-2}	-8.20 (1.4) 3.79×10^{-1}	non-bound	non-bound
1.4	-6.29 (13.5) 9.05×10^{-3}	-7.02 (1.1) 7.77×10^{-2}	-7.93 (1.1) 1.50×10^{-1}	-8.44 (0.04) 8.77×10^{-1}	non-bound
3.1	-6.24 (9.9) 4.35×10^{-3}	-6.54 (4.0) 1.95×10^{-2}	-7.21 (0.3) 5.55×10^{-2}	-7.89 (0.5) 9.80×10^{-2}	non-bound
3.8	-6.23 (8.5) 3.16×10^{-3}	-6.47 (4.7) 1.22×10^{-2}	-6.97 (0.8) 3.97×10^{-2}	-7.61 (0.2) 6.32×10^{-2}	-8.21 (0.5) 2.00×10^{-1}

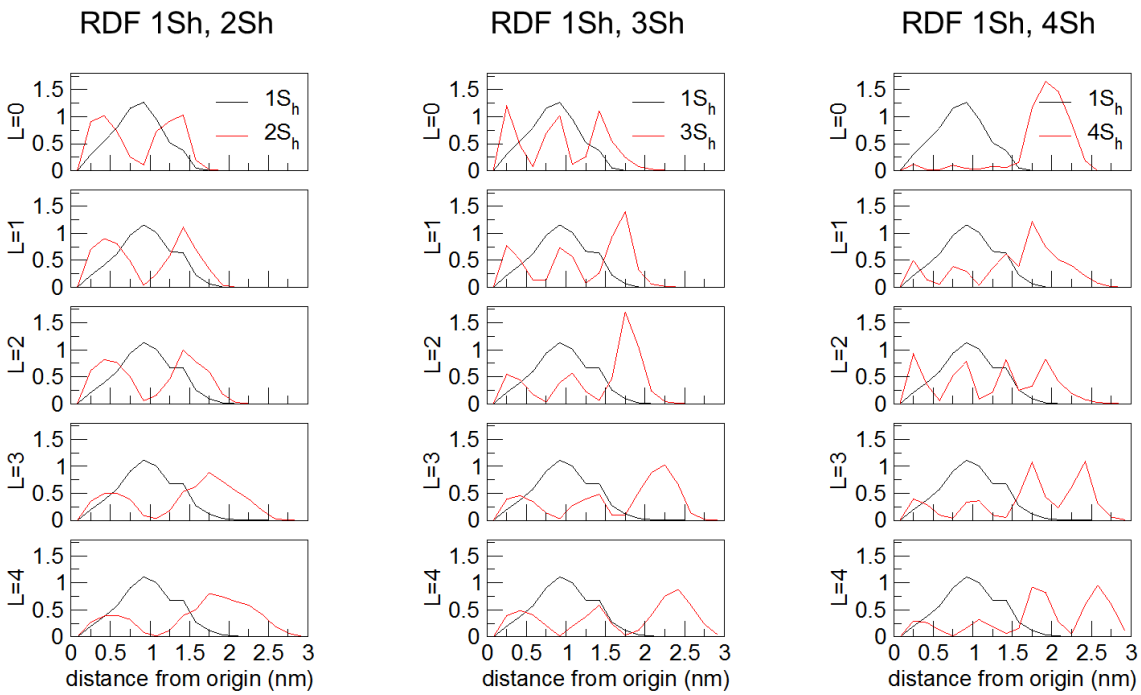

Figure A3.6: Radial distribution function (RDF) of NS_h (N=1,2,3,4) hole states in CdSe/CdS core-shell QDs with different monolayers of CdS shell. Visual inspection of the curves and node placement of the excited states helps interpret the coupling strength between the $1S_h$ and NS_h orbitals.

Appendix 3.5

Calculation of Reorganization Energies of the Acceptors for Electron/hole/energy Transfer

The acceptor (ACC) component of reorganization energy λ_{ACC} is defined as the difference between the energy of ACC^* at the equilibrium geometry of ACC, i.e. electron/hole/triplet-exciton acceptor's initial state, and the energy of ACC^* at the equilibrium geometry of ACC^*, its final state. For this we use the B3LYP functional[83-84] with a 6-31++G(d,p) basis as implemented in Gaussian 09.[85] The calculated values for each of the acceptor's reorganization energy are λ_{MV} = 300, λ_{PTZ} = 87 , λ_{ACA} = 317 meV. Tables A3.17-A3.19 summarize the geometries of the three acceptor molecules before and after ET/HT/TET.

Table A3.17a. $MV^+@MV^{2+}$ Cartesian coordinates in Å before ET. E(ROB3LYP) = -575.026131509 E_h

Atom	X	Y	Z
C	0.743468	0.005678	0.003632
C	1.469384	1.130968	-0.415856
C	2.854860	1.102843	-0.404640
C	2.850409	-1.093547	0.429638
C	1.466439	-1.120429	0.432076
C	-0.743468	0.005678	-0.003634
C	-1.469383	1.130968	0.415854
C	-2.854859	1.102843	0.404639
C	-2.850409	-1.093547	-0.429639

C	-1.466439	-1.120428	-0.432078
H	0.977239	2.027024	-0.776499
H	3.453386	1.944645	-0.729893
H	3.448700	-1.935504	0.757262
H	0.970047	-2.014364	0.792483
H	-0.977238	2.027024	0.776497
H	-3.453386	1.944645	0.729893
H	-3.448701	-1.935504	-0.757262
H	-0.970048	-2.014364	-0.792486
C	5.012661	-0.021137	-0.019195
H	5.380987	-0.457938	0.908846
H	5.336150	-0.619355	-0.873295
H	5.381976	0.997920	-0.116656
C	-5.012661	-0.021138	0.019199
H	-5.336148	-0.619350	0.873304
H	-5.381976	0.997921	0.116654
H	-5.380989	-0.457945	-0.908838
N	3.524877	0.004474	0.012384
N	-3.524877	0.004474	-0.012384

Table A3.17b. MV^+ Cartesian coordinates in Å after ET, E(ROB3LYP) = -575.037331083 E_h

Atom	X	Y	Z
C	0.716380	0.001480	0.000196

C	1.487728	1.204486	-0.049535
C	2.842913	1.178742	-0.046558
C	2.843690	-1.172368	0.054182
C	1.489839	-1.200788	0.051243
C	-0.716386	0.001480	-0.000195
C	-1.487732	1.204485	0.049535
C	-2.842911	1.178741	0.046558
C	-2.843687	-1.172367	-0.054182
C	-1.489843	-1.200787	-0.051243
H	1.017674	2.177402	-0.103676
H	3.435480	2.083664	-0.090655
H	3.440524	-2.075120	0.098466
H	1.020318	-2.174232	0.103582
H	-1.017680	2.177401	0.103677
H	-3.435478	2.083662	0.090654
H	-3.440521	-2.075118	-0.098466
H	-1.020324	-2.174231	-0.103581
C	5.007470	-0.013092	-0.007486
H	5.380579	-0.574470	0.852499
H	5.368478	-0.475417	-0.930321
H	5.377827	1.009904	0.049067
C	-5.007465	-0.013092	0.007486
H	-5.368473	-0.475403	0.930329

H	-5.377823	1.009903	-0.049083
H	-5.380575	-0.574483	-0.852490
N	3.538694	0.005358	0.007830
N	-3.538690	0.005358	-0.007831

Table A3.18a. PTZ^{+}@PTZ Cartesian coordinates in Å before HT, E(UB3LYP) = -915.421871567 E_h

Atom	X	Y	Z
C	0.000000	3.817857	0.391670
C	0.000000	2.672027	1.193331
C	0.000000	1.394353	0.628365
C	0.000000	1.250683	-0.772160
C	0.000000	2.406081	-1.569244
C	0.000000	3.678765	-0.996550
C	-0.000000	-1.250683	-0.772160
C	-0.000000	-1.394353	0.628365
C	-0.000000	-2.672027	1.193331
H	0.000000	-2.770529	2.275654
C	-0.000000	-3.817857	0.391670
C	-0.000000	-3.678765	-0.996550
C	-0.000000	-2.406081	-1.569244
H	0.000000	4.800436	0.852429
H	0.000000	2.770529	2.275654

H	0.000000	2.298266	-2.651796
H	0.000000	4.553696	-1.639595
H	-0.000000	0.000000	-2.397464
H	-0.000000	-4.800436	0.852429
H	-0.000000	-4.553696	-1.639595
H	-0.000000	-2.298266	-2.651796
N	-0.000000	0.000000	-1.388783
S	0.000000	-0.000000	1.746286

Table A3.18b. PTZ^{+} Cartesian coordinates in Å after HT, E(UB3LYP) = -915.425032857 E_h

Atom	X	Y	Z
C	-3.783009	-0.404636	-0.000279
C	-2.657286	-1.213743	-0.000095
C	-1.373207	-0.638632	0.000112
C	-1.238924	0.775079	0.000185
C	-2.396340	1.583603	-0.000049
C	-3.649450	0.999896	-0.000298
C	1.238935	0.775043	0.000127
C	1.373165	-0.638671	0.000057
C	2.657310	-1.213749	-0.000063
H	2.759666	-2.294724	-0.000002
C	3.782997	-0.404657	-0.000229
C	3.649459	0.999924	-0.000325

C	2.396361	1.583586	-0.000100
H	-4.769492	-0.855750	-0.000387
H	-2.759731	-2.294708	-0.000093
H	-2.291053	2.665147	-0.000087
H	-4.534077	1.627870	-0.000565
H	0.000009	2.392748	0.001003
H	4.769519	-0.855694	-0.000283
H	4.534136	1.627816	-0.000584
H	2.290951	2.665120	-0.000122
N	0.000028	1.378001	0.000600
S	-0.000012	-1.721381	0.000167

Table A3.19a. ACA(T1@S0) Cartesian coordinates in Å before TET, E(UB3LYP) = -728.050532890 E_h

Atom	X	Y	Z
C	-2.205387	-4.092461	-0.027470
C	-0.835814	-4.065349	-0.030656
C	-0.121679	-2.824678	-0.025901
C	-0.855935	-1.578745	-0.033010
C	-2.287924	-1.658404	-0.019635
C	-2.935132	-2.868859	-0.016209
C	1.276506	-2.800315	-0.009757
C	-0.132523	-0.358799	-0.005801

C	1.286092	-0.343688	0.040870
C	1.997309	-1.602285	0.021418
C	3.428700	-1.604136	0.035922
H	3.942243	-2.561989	0.021018
C	4.135583	-0.431114	0.065496
C	3.440054	0.812304	0.082926
C	2.068154	0.858178	0.072360
H	1.820177	-3.742532	-0.016300
H	-2.737830	-5.038951	-0.028244
H	-0.262256	-4.988654	-0.030586
H	-2.870413	-0.746367	-0.018042
H	-4.021015	-2.894855	-0.004231
H	5.221492	-0.442757	0.076203
H	4.005273	1.739555	0.109354
H	1.565000	1.815752	0.107022
C	-0.851049	0.953121	-0.003206
O	-0.649551	1.868650	0.772466
O	-1.769959	1.067117	-0.999316
H	-2.166058	1.951002	-0.906201

Table A3.19b. ACA(T1) Cartesian coordinates in Å after TET, E(UB3LYP) = -728.062168929 E_h

Atom	X	Y	Z

C	-2.244347	-4.086373	-0.008574
C	-0.841751	-4.041757	-0.091246
C	-0.145081	-2.821816	-0.085494
C	-0.880339	-1.585453	-0.032923
C	-2.276430	-1.663617	0.077082
C	-2.956254	-2.900439	0.088051
C	1.279182	-2.795327	-0.106834
C	-0.138740	-0.324521	-0.042448
C	1.321335	-0.320108	0.054943
C	2.016936	-1.580199	-0.007126
C	3.420547	-1.598016	0.030987
H	3.930761	-2.556321	-0.021246
C	4.168568	-0.411055	0.131621
C	3.504867	0.803727	0.195329
C	2.093647	0.847659	0.155923
H	1.821222	-3.735760	-0.155746
H	-2.757879	-5.043240	-0.013459
H	-0.273478	-4.966133	-0.153803
H	-2.860985	-0.756636	0.145102
H	-4.038967	-2.909806	0.167037
H	5.253352	-0.454441	0.159593
H	4.059760	1.733387	0.276344
H	1.597822	1.806263	0.219765

C	-0.842282	0.970193	-0.160891
O	-0.515589	2.018530	0.379765
O	-1.929757	0.942885	-0.986725
H	-2.282065	1.849112	-0.984537

3.4 Reference

1. Kozlov, D. V.; Castellano, F. N., Anti-Stokes delayed fluorescence from metal–organic bichromophores. *Chemical Communications* **2004,** (24), 2860-2861.
2. Zhao, W.; Castellano, F. N., Upconverted Emission from Pyrene and Di-tert-butylpyrene Using Ir(ppy)3 as Triplet Sensitizer. *J. Phys. Chem. A* **2006,** *110* (40), 11440-11445.
3. Zhao, J.; Ji, S.; Guo, H., Triplet–triplet annihilation based upconversion: from triplet sensitizers and triplet acceptors to upconversion quantum yields. *RSC Advances* **2011,** *1* (6), 937-950.
4. Singh-Rachford, T. N.; Castellano, F. N., Photon upconversion based on sensitized triplet–triplet annihilation. *Coord. Chem. Rev.* **2010,** *254* (21-22), 2560-2573.
5. Fan, C.; Wu, W.; Chruma, J. J.; Zhao, J.; Yang, C., Enhanced Triplet–Triplet Energy Transfer and Upconversion Fluorescence through Host–Guest Complexation. *Journal of the American Chemical Society* **2016,** *138* (47), 15405-15412.
6. Majumdar, P.; Nomula, R.; Zhao, J., Activatable triplet photosensitizers: magic bullets for targeted photodynamic therapy. *J. Mater. Chem. C* **2014,** *2* (30), 5982-5997.
7. Li, X. S.; Kolemen, S.; Yoon, J.; Akkaya, E. U., Activatable Photosensitizers: Agents for Selective Photodynamic Therapy. *Adv. Funct. Mater.* **2017,** *27* (5), 1604053.
8. Zhao, J.; Wu, W.; Sun, J.; Guo, S., Triplet photosensitizers: from molecular design to applications. *Chemical Society Reviews* **2013,** *42* (12), 5323-5351.
9. Welin, E. R.; Le, C.; Arias-Rotondo, D. M.; McCusker, J. K.; MacMillan, D. W. C., Photosensitized, energy transfer-mediated organometallic catalysis through electronically excited nickel(II). *Science* **2017,** *355* (6323), 380.
10. Kim, T.; McCarver, S. J.; Lee, C.; MacMillan, D. W. C., Sulfonamidation of Aryl and Heteroaryl Halides through Photosensitized Nickel Catalysis. *Angew. Chem. Int. Ed.* **2018,** *57* (13), 3488-3492.
11. Strieth-Kalthoff, F.; James, M. J.; Teders, M.; Pitzer, L.; Glorius, F., Energy transfer catalysis mediated by visible light: principles, applications, directions. *Chem. Soc. Rev.* **2018,** *47* (19), 7190-7202.
12. Yogo, T.; Urano, Y.; Ishitsuka, Y.; Maniwa, F.; Nagano, T., Highly Efficient and Photostable Photosensitizer Based on BODIPY Chromophore. *Journal of the American Chemical Society* **2005,** *127* (35), 12162-12163.
13. Marian, C. M., Spin–orbit coupling and intersystem crossing in molecules. *WIREs Computational Molecular Science* **2012,** *2* (2), 187-203.
14. Mongin, C.; Garakyaraghi, S.; Razgoniaeva, N.; Zamkov, M.; Castellano, F. N., Direct observation of triplet energy transfer from semiconductor nanocrystals. *Science* **2016,** *351* (6271), 369-72.
15. Huang, Z.; Li, X.; Mahboub, M.; Hanson, K. M.; Nichols, V. M.; Le, H.; Tang, M. L.; Bardeen, C. J., Hybrid Molecule-Nanocrystal Photon Upconversion Across the Visible and Near-Infrared. *Nano Lett* **2015,** *15* (8), 5552-7.
16. Huang, Z.; Tang, M. L., Designing Transmitter Ligands That Mediate Energy Transfer between Semiconductor Nanocrystals and Molecules. *J. Am. Chem. Soc.* **2017,** *139* (28), 9412-9418.
17. Wu, M.; Congreve, D. N.; Wilson, M. W. B.; Jean, J.; Geva, N.; Welborn, M.; Van Voorhis, T.; Bulović, V.; Bawendi, M. G.; Baldo, M. A., Solid-state infrared-to-visible upconversion sensitized by colloidal nanocrystals. *Nat. Photon.* **2015,** *10*, 31-34.

18. Nishimura, N.; Allardice, J. R.; Xiao, J.; Gu, Q.; Gray, V.; Rao, A., Photon upconversion utilizing energy beyond the band gap of crystalline silicon with a hybrid TES-ADT/PbS quantum dots system. *Chem. Sci.* **2019,** *10* (18), 4750-4760.
19. de Mello Donegá, C.; Bode, M.; Meijerink, A., Size- and temperature-dependence of exciton lifetimes in CdSe quantum dots. *Phys. Rev. B* **2006,** *74* (8), 085320.
20. Efros, A. L.; Rosen, M.; Kuno, M.; Nirmal, M.; Norris, D. J.; Bawendi, M., Band-edge exciton in quantum dots of semiconductors with a degenerate valence band: Dark and bright exciton states. *Phys. Rev. B* **1996,** *54* (7), 4843-4856.
21. Scholes, G. D.; Rumbles, G., Excitons in nanoscale systems. *Nat. Mater.* **2006,** *5* (9), 683-96.
22. Chen, O.; Zhao, J.; Chauhan, V. P.; Cui, J.; Wong, C.; Harris, D. K.; Wei, H.; Han, H.-S.; Fukumura, D.; Jain, R. K.; Bawendi, M. G., Compact high-quality CdSe–CdS core–shell nanocrystals with narrow emission linewidths and suppressed blinking. *Nature Materials* **2013,** *12*, 445.
23. Yu, W. W.; Qu, L. H.; Guo, W. Z.; Peng, X. G., Experimental determination of the extinction coefficient of CdTe, CdSe, and CdS nanocrystals. *Chem. Mater.* **2003,** *15* (14), 2854-2860.
24. Moreels, I.; Lambert, K.; Smeets, D.; De Muynck, D.; Nollet, T.; Martins, J. C.; Vanhaecke, F.; Vantomme, A.; Delerue, C.; Allan, G.; Hens, Z., Size-dependent optical properties of colloidal PbS quantum dots. *ACS Nano* **2009,** *3* (10), 3023-30.
25. Zhu, H.; Song, N.; Lian, T., Controlling charge separation and recombination rates in CdSe/ZnS type I core-shell quantum dots by shell thicknesses. *J. Am. Chem. Soc.* **2010,** *132* (42), 15038-45.
26. Zhu, H.; Song, N.; Lian, T., Wave Function Engineering for Ultrafast Charge Separation and Slow Charge Recombination in Type II Core/Shell Quantum Dots. *Journal of the American Chemical Society* **2011,** *133* (22), 8762-8771.
27. Zhu, H.; Song, N.; Rodríguez-Córdoba, W.; Lian, T., Wave Function Engineering for Efficient Extraction of up to Nineteen Electrons from One CdSe/CdS Quasi-Type II Quantum Dot. *J. Am. Chem. Soc.* **2012,** *134* (9), 4250-4257.
28. Xu, Z.; Jin, T.; Huang, Y.; Mulla, K.; Evangelista, F. A.; Egap, E.; Lian, T., Direct triplet sensitization of oligothiophene by quantum dots. *Chem. Sci.* **2019,** *10* (24), 6120-6124.
29. De Roo, J.; Huang, Z.; Schuster, N. J.; Hamachi, L. S.; Congreve, D. N.; Xu, Z.; Xia, P.; Fishman, D. A.; Lian, T.; Owen, J. S.; Tang, M. L., Anthracene Diphosphate Ligands for CdSe Quantum Dots; Molecular Design for Efficient Upconversion. *Chem. Mater.* **2020,** *32* (4), 1461-1466.
30. He, S.; Lai, R.; Jiang, Q.; Han, Y.; Luo, X.; Tian, Y.; Liu, X.; Wu, K., Engineering Sensitized Photon Upconversion Efficiency via Nanocrystal Wavefunction and Molecular Geometry. *Angew Chem Int Ed Engl* **2020,** *59* (40), 17726-17731.
31. Gray, V.; Xia, P.; Huang, Z.; Moses, E.; Fast, A.; Fishman, D. A.; Vullev, V. I.; Abrahamsson, M.; Moth-Poulsen, K.; Lee Tang, M., CdS/ZnS core-shell nanocrystal photosensitizers for visible to UV upconversion. *Chem. Sci.* **2017,** *8* (8), 5488-5496.
32. Huang, Z.; Xu, Z.; Mahboub, M.; Li, X.; Taylor, J. W.; Harman, W. H.; Lian, T.; Tang, M. L., PbS/CdS Core-Shell Quantum Dots Suppress Charge Transfer and Enhance Triplet Transfer. *Angew. Chem. Int. Ed.* **2017,** *56* (52), 16583-16587.
33. Papa, C. M.; Garakyaraghi, S.; Granger, D. B.; Anthony, J. E.; Castellano, F. N., TIPS-pentacene triplet exciton generation on PbS quantum dots results from indirect sensitization. *Chem. Sci.* **2020,** *11* (22), 5690-5696.
34. Luo, X.; Lai, R.; Li, Y.; Han, Y.; Liang, G.; Liu, X.; Ding, T.; Wang, J.; Wu, K., Triplet

Energy Transfer from CsPbBr3 Nanocrystals Enabled by Quantum Confinement. *J. Am. Chem. Soc.* **2019,** *141* (10), 4186-4190.
35. Luo, X.; Han, Y.; Chen, Z.; Li, Y.; Liang, G.; Liu, X.; Ding, T.; Nie, C.; Wang, M.; Castellano, F. N.; Wu, K., Mechanisms of triplet energy transfer across the inorganic nanocrystal/organic molecule interface. *Nat. Commun.* **2020,** *11* (1), 28.
36. Jiang, Y.; Weiss, E. A., Colloidal Quantum Dots as Photocatalysts for Triplet Excited State Reactions of Organic Molecules. *J. Am. Chem. Soc.* **2020,** *142* (36), 15219-15229.
37. Jiang, Y.; Wang, C.; Rogers, C. R.; Kodaimati, M. S.; Weiss, E. A., Regio- and diastereoselective intermolecular [2+2] cycloadditions photocatalysed by quantum dots. *Nat. Chem.* **2019,** *11* (11), 1034-1040.
38. Mase, K.; Okumura, K.; Yanai, N.; Kimizuka, N., Triplet sensitization by perovskite nanocrystals for photon upconversion. *Chem. Commun.* **2017,** *53* (59), 8261-8264.
39. Nienhaus, L.; Wu, M.; Bulovic, V.; Baldo, M. A.; Bawendi, M. G., Using lead chalcogenide nanocrystals as spin mixers: a perspective on near-infrared-to-visible upconversion. *Dalton Trans* **2018,** *47* (26), 8509-8516.
40. Huang, Z.; Xu, Z.; Mahboub, M.; Liang, Z.; Jaimes, P.; Xia, P.; Graham, K. R.; Tang, M. L.; Lian, T., Enhanced Near-Infrared-to-Visible Upconversion by Synthetic Control of PbS Nanocrystal Triplet Photosensitizers. *J. Am. Chem. Soc.* **2019,** *141* (25), 9769-9772.
41. Mahboub, M.; Huang, Z.; Tang, M. L., Efficient Infrared-to-Visible Upconversion with Subsolar Irradiance. *Nano Lett.* **2016,** *16* (11), 7169-7175.
42. Nienhaus, L.; Wu, M.; Geva, N.; Shepherd, J. J.; Wilson, M. W. B.; Bulovic, V.; Van Voorhis, T.; Baldo, M. A.; Bawendi, M. G., Speed Limit for Triplet-Exciton Transfer in Solid-State PbS Nanocrystal-Sensitized Photon Upconversion. *ACS Nano* **2017,** *11* (8), 7848-7857.
43. L. J. Dexter, D., A Theory of Sensitized Luminescence in Solid. *J. Chem. Phys.* **1953,** *21*, 836-850.
44. Lin, S. H., On the Theory of Non-Radiative Transfer of Electronic Excitation. *Proc. R. Soc. Lond. A.* **1973,** *335* (1600), 51.
45. Sigman, M. E.; Closs, G. L., Free-Energy and Structure Dependence of Intramolecular Triplet Energy-Transfer in Organic-Model Compounds. *J Phys Chem-Us* **1991,** *95* (13), 5012-5017.
46. Closs, G. L.; Johnson, M. D.; Miller, J. R.; Piotrowiak, P., A Connection between Intramolecular Long-Range Electron, Hole, and Triplet Energy Transfers. *J. Am. Chem. Soc.* **1989,** *111* (10), 3751-3753.
47. Bai, S.; Zhang, P.; Beratan, D. N., Predicting Dexter Energy Transfer Interactions from Molecular Orbital Overlaps. *J. Phys. Chem. C* **2020,** *124* (35), 18956-18960.
48. Harcourt, R. D.; Scholes, G. D.; Ghiggino, K. P., Rate expressions for excitation transfer. II. Electronic considerations of direct and through–configuration exciton resonance interactions. *J. Chem. Phys.* **1994,** *101* (12), 10521-10525.
49. Scholes, G. D.; Harcourt, R. D.; Ghiggino, K. P., Rate expressions for excitation transfer. III. An ab initio study of electronic factors in excitation transfer and exciton resonance interactions. *J. Chem. Phys.* **1995,** *102* (24), 9574-9581.
50. Skourtis, S. S.; Liu, C.; Antoniou, P.; Virshup, A. M.; Beratan, D. N., Dexter energy transfer pathways. *Proc. Natl. Acad. Sci. U S A* **2016,** *113* (29), 8115-20.
51. Bai, S.; Zhang, P.; Antoniou, P.; Skourtis, S. S.; Beratan, D. N., Quantum interferences among Dexter energy transfer pathways. *Faraday Discuss* **2019,** *216* (0), 301-318.
52. Piland, G. B.; Huang, Z. Y.; Tang, M. L.; Bardeen, C. J., Dynamics of Energy Transfer from CdSe Nanocrystals to Triplet States of Anthracene Ligand Molecules. *J. Phys. Chem. C* **2016,** *120*

(11), 5883-5889.
53. Jin, T.; Uhlikova, N.; Xu, Z.; Zhu, Y.; Huang, Y.; Egap, E.; Lian, T., Competition of Dexter, Förster, and charge transfer pathways for quantum dot sensitized triplet generation. *J. Chem. Phys.* **2020,** *152* (21), 214702.
54. Jin, T.; Lian, T., Trap state mediated triplet energy transfer from CdSe quantum dots to molecular acceptors. *J. Chem. Phys.* **2020,** *153* (7), 074703.
55. Han, Y.; He, S.; Luo, X.; Li, Y.; Chen, Z.; Kang, W.; Wang, X.; Wu, K., Triplet Sensitization by "Self-Trapped" Excitons of Nontoxic CuInS2 Nanocrystals for Efficient Photon Upconversion. *J. Am. Chem. Soc.* **2019,** *141* (33), 13033-13037.
56. Li, X.; Huang, Z.; Zavala, R.; Tang, M. L., Distance-Dependent Triplet Energy Transfer between CdSe Nanocrystals and Surface Bound Anthracene. *J. Phys. Chem. Lett.* **2016,** *7* (11), 1955-9.
57. Xu, Z.; Huang, Z.; Li, C.; Huang, T.; Evangelista, F. A.; Tang, M. L.; Lian, T., Tuning the Quantum Dot (QD)/Mediator Interface for Optimal Efficiency of QD-Sensitized Near-Infrared-to-Visible Photon Upconversion Systems. *ACS Applied Materials & Interfaces* **2020,** *12* (32), 36558-36567.
58. Huang, Z. Y.; Xia, P.; Megerdich, N.; Fishman, D. A.; Vullev, V. I.; Tang, M. L., ZnS Shells Enhance Triplet Energy Transfer from CdSe Nanocrystals for Photon Upconversion. *ACS Photonics* **2018,** *5* (8), 3089-3096.
59. Huang, J. E.; Huang, Z. Q.; Jin, S. Y.; Lian, T. Q., Exciton Dissociation in CdSe Quantum Dots by Hole Transfer to Phenothiazine. *Journal of Physical Chemistry C* **2008,** *112* (49), 19734-19738.
60. Jockusch, S.; Yagci, Y., The active role of excited states of phenothiazines in photoinduced metal free atom transfer radical polymerization: singlet or triplet excited states? *Polymer Chemistry* **2016,** *7* (39), 6039-6043.
61. Peon, J.; Tan, X.; Hoerner, J. D.; Xia, C.; Luk, Y. F.; Kohler, B., Excited State Dynamics of Methyl Viologen. Ultrafast Photoreduction in Methanol and Fluorescence in Acetonitrile. *The Journal of Physical Chemistry A* **2001,** *105* (24), 5768-5777.
62. Lai, R.; Liu, Y.; Luo, X.; Chen, L.; Han, Y.; Lv, M.; Liang, G.; Chen, J.; Zhang, C.; Di, D.; Scholes, G. D.; Castellano, F. N.; Wu, K., Shallow distance-dependent triplet energy migration mediated by endothermic charge-transfer. *Nat. Commun.* **2021,** *12* (1), 1532.
63. Zhu, H.; Yang, Y.; Hyeon-Deuk, K.; Califano, M.; Song, N.; Wang, Y.; Zhang, W.; Prezhdo, O. V.; Lian, T., Auger-assisted electron transfer from photoexcited semiconductor quantum dots. *Nano Lett* **2014,** *14* (3), 1263-9.
64. Hanifi, D. A.; Bronstein, N. D.; Koscher, B. A.; Nett, Z.; Swabeck, J. K.; Takano, K.; Schwartzberg, A. M.; Maserati, L.; Vandewal, K.; van de Burgt, Y.; Salleo, A.; Alivisatos, A. P., Redefining near-unity luminescence in quantum dots with photothermal threshold quantum yield. *Science* **2019,** *363* (6432), 1199.
65. Huang, J.; Huang, Z.; Yang, Y.; Zhu, H.; Lian, T., Multiple Exciton Dissociation in CdSe Quantum Dots by Ultrafast Electron Transfer to Adsorbed Methylene Blue. *Journal of the American Chemical Society* **2010,** *132* (13), 4858-4864.
66. Grimaldi, G.; Geuchies, J. J.; van der Stam, W.; du Fosse, I.; Brynjarsson, B.; Kirkwood, N.; Kinge, S.; Siebbeles, L. D. A.; Houtepen, A. J., Spectroscopic Evidence for the Contribution of Holes to the Bleach of Cd-Chalcogenide Quantum Dots. *Nano Lett* **2019,** *19* (5), 3002-3010.
67. Olshansky, J. H.; Balan, A. D.; Ding, T. X.; Fu, X.; Lee, Y. V.; Alivisatos, A. P., Temperature-Dependent Hole Transfer from Photoexcited Quantum Dots to Molecular Species: Evidence for

Trap-Mediated Transfer. *ACS Nano* **2017,** *11* (8), 8346-8355.
68. Xu, Z.; Huang, Z.; Jin, T.; Lian, T.; Tang, M. L., Mechanistic Understanding and Rational Design of Quantum Dot/Mediator Interfaces for Efficient Photon Upconversion. *Acc. Chem. Res.* **2021,** *54* (1), 70-80.
69. Cui, S.-C.; Tachikawa, T.; Fujitsuka, M.; Majima, T., Solvent-Polarity Dependence of Electron-Transfer Kinetics in a CdSe/ZnS Quantum Dot−Pyromellitimide Conjugate. *The Journal of Physical Chemistry C* **2010,** *114* (2), 1217-1225.
70. Wang, J.; Ding, T.; Gao, K.; Wang, L.; Zhou, P.; Wu, K., Marcus inverted region of charge transfer from low-dimensional semiconductor materials. *Nature Communications* **2021,** *12* (1), 6333.
71. Ratner, M. A., Bridge-assisted electron transfer: effective electronic coupling. *The Journal of Physical Chemistry* **1990,** *94* (12), 4877-4883.
72. McConnell, H. M., Intramolecular Charge Transfer in Aromatic Free Radicals. *The Journal of Chemical Physics* **1961,** *35* (2), 508-515.
73. Albinsson, B.; Mårtensson, J., Long-range electron and excitation energy transfer in donor–bridge–acceptor systems. *Journal of Photochemistry and Photobiology C: Photochemistry Reviews* **2008,** *9* (3), 138-155.
74. Gosztola, D.; Wang, B.; Wasielewski, M. R., Factoring through-space and through-bond contributions to rates of photoinduced electron transfer in donor—spacer—acceptor molecules. *Journal of Photochemistry and Photobiology A: Chemistry* **1996,** *102* (1, Supplement 1), 71-80.
75. Kaledin, A. L.; Lian, T.; Hill, C. L.; Musaev, D. G., An All-Atom Theory of Electron Transfer at Nanocrystal/Molecule Interfaces: A Hybrid LCAO/DFT Approach. *The Journal of Physical Chemistry C* **2021,** *125* (9), 5116-5126.
76. Chen, J.; Wu, K.; Rudshteyn, B.; Jia, Y.; Ding, W.; Xie, Z. X.; Batista, V. S.; Lian, T., Ultrafast Photoinduced Interfacial Proton Coupled Electron Transfer from CdSe Quantum Dots to 4,4'-Bipyridine. *J. Am. Chem. Soc.* **2016,** *138* (3), 884-92.
77. Jia, Y.; Chen, J.; Wu, K.; Kaledin, A.; Musaev, D. G.; Xie, Z.; Lian, T., Enhancing photo-reduction quantum efficiency using quasi-type II core/shell quantum dots. *Chemical Science* **2016,** *7* (7), 4125-4133.
78. Kaledin, A. L.; Lian, T.; Hill, C. L.; Musaev, D. G., An Infinite Order Discrete Variable Representation of an Effective Mass Hamiltonian: Application to Exciton Wave Functions in Quantum Confined Nanostructures. *Journal of Chemical Theory and Computation* **2014,** *10* (8), 3409-3416.
79. Kaledin, A. L.; Lian, T.; Hill, C. L.; Musaev, D. G., A Hybrid Quantum Mechanical Approach: Intimate Details of Electron Transfer between Type-I CdSe/ZnS Quantum Dots and an Anthraquinone Molecule. *The Journal of Physical Chemistry B* **2015,** *119* (24), 7651-7658.
80. Allan, G.; Delerue, C.; Lannoo, M.; Martin, E., Hydrogenic impurity levels, dielectric constant, and Coulomb charging effects in silicon crystallites. *Physical Review B* **1995,** *52* (16), 11982-11988.
81. Davidson, E. R., The iterative calculation of a few of the lowest eigenvalues and corresponding eigenvectors of large real-symmetric matrices. *Journal of Computational Physics* **1975,** *17* (1), 87-94.
82. Jackson, J. D., *Classical electrodynamics*. Wiley: New York, 1962.
83. Becke, A. D., Density-functional exchange-energy approximation with correct asymptotic behavior. *Physical Review A* **1988,** *38* (6), 3098-3100.
84. Lee, C.; Yang, W.; Parr, R. G., Development of the Colle-Salvetti correlation-energy formula

into a functional of the electron density. *Physical Review B* **1988,** *37* (2), 785-789.
85. Frisch, M. J. T., G. W.; Schlegel, H. B.; Scuseria, G. E.; Robb, M. A.; Cheeseman, J. R.; Scalmani, G.; Barone, V.; Mennucci, B.; Petersson, G. A.; Nakatsuji, H.; Caricato, M.; Li, X.; Hratchian, H. P.; Izmaylov, A. F.; Bloino, J.; Zheng, G.; Sonnenberg, J. L.; Hada, M.; Ehara, M.; Toyota, K.; Fukuda, R.; Hasegawa, J.; Ishida, M.; Nakajima, T.; Honda, Y.; Kitao, O.; Nakai, H.; Vreven, T.; Montgomery, J. A., Jr.; Peralta, J. E.; Ogliaro, F.; Bearpark, M.; Heyd, J. J.; Brothers, E.; Kudin, K. N.; Staroverov, V. N.; Kobayashi, R.; Normand, J.; Raghavachari, K.; Rendell, A.; Burant, J. C.; Iyengar, S. S.; Tomasi, J.; Cossi, M.; Rega, N.; Millam, M. J.; Klene, M.; Knox, J. E.; Cross, J. B.; Bakken, V.; Adamo, C.; Jaramillo, J.; Gomperts, R.; Stratmann, R. E.; Yazyev, O.; Austin, A. J.; Cammi, R.; Pomelli, C.; Ochterski, J. W.; Martin, R. L.; Morokuma, K.; Zakrzewski, V. G.; Voth, G. A.; Salvador, P.; Dannenberg, J. J.; Dapprich, S.; Daniels, A. D.; Farkas, Ö.; Foresman, J. B.; Ortiz, J. V.; Cioslowski, J.; Fox, D. J., Gaussian 09, Revision D.01. *Gaussian, Inc., Wallingford CT* **2009**.

Chapter 4. Bright State Sensitized Triplet Energy Transfer from Quantum Dot to Molecular Acceptor Revealed by Temperature Dependent Energy Transfer Dynamics

This work has been submitted to Nano Letters and is under review.

4.1 Introduction

Molecular triplet state generation has received extensive research interest because of its wide applications in photodynamic therapy,[1-2] photon up-conversion[3-5] and photocatalytic organic reactions.[6-7] Traditional approaches for triplet excited state formation include intersystem crossing of target molecules and triplet energy transfer (TET) from molecular sensitizers. Both approaches involve intersystem crossing from singlet excited states generated by light absorption, a process with large energy loss because of the relatively large energy gap between molecular singlet and triplet states.[5] Recently, quantum dot (QD) sensitized TET[8-11] has been developed as a promising route for triplet excited state generation because of the unique advantages of QD sensitizers, including large extinction coefficients,[12-13] tunable absorption from visible to near and mid-infrared regions,[14-15] and small bright and dark state energy difference.[16-17] So far, TET from QDs to molecular acceptors has been demonstrated for QD sensitizers including CdSe,[18-19] PbS,[20] InP,[21] CdS[22] and $CsPbBr_3$ perovskite[8] and has been integrated into photon up-conversion[23-26] and photocatalytic organic synthesis[27-28]. The TET mechanisms from QD sensitizers to molecular acceptors have also been studied as it is a key step to determine the overall efficiency of up-conversion or photocatalysis systems.[29] Inspired by TET and other triplet excited state generation schemes in molecular donor-acceptor systems, similar mechanisms have been proposed for TET in QD-acceptor complexes, which include direct TET mediated by charge transfer virtual states[18,

[30-33] and TET mediated by sequential charge transfer with charge separated state intermediate.[34-35]

While unique properties of QDs have been utilized to improve the TET efficiency of QD-acceptor complexes, their influences on mechanisms of QD sensitized TET have rarely been discussed. Molecule-to-molecule TET through direct Dexter mechanism involves optically forbidden triplet excited states of the donor and acceptor molecules. In QDs, because of strong spin-orbit coupling, spin is no longer a good quantum number, and bright and dark exciton states resulted from the bound conduction band (CB) edge electron and valence band (VB) edge hole pair are determined by their total angular momentum. These degenerate bright and dark exciton states are further split by electron-hole exchange and QD shape or lattice asymmetry to form band edge exciton fine structures.[16, 36-40] For example, in CdSe QDs with a wurtzite crystal structure, the two-fold degenerate $1S_{1/2}$ electron level and four-fold degenerate $1S_{3/2}$ hole level forms 8 exciton states with total angular momentum of 0, 1, 2, respectively, that are further split according to their angular momentum projection along the wurtzite hexagonal axis (z axis) to form exciton fine structures with a manifold of bright and dark states spanning an energy range of a few to tens of meVs.[16] These bright and dark states have mixtures of electron spin singlet and triplet characters and it is unclear and has not been demonstrated experimentally how QD band edge exciton fine structure affects the TET process from the QD sensitizer to molecular acceptors. Such ambiguity in QD sensitized TET mechanisms could impede further optimization of the TET efficiency. Therefore, detailed examination of the effect of exciton fine structure on QD sensitized TET is necessary.

In this paper, we systematically tune the relative population of bright and dark states in CdSe/CdS core/shell QDs by varying the temperature and study its effect on the TET dynamics from the QD to attached triplet acceptors with transient absorption (TA) spectroscopy. We use a

functionalized oligothiophene (3'",4"-dihexyl-[2,2':5',2":5",2'":5'",2"":5"",2""'-sexithiophene]-5-carboxylic acid (T6)) (shown in Figure 4.1a) as the acceptor following a previous report of efficient TET in CdSe-T6 complexes.[19] With increasing population of dark states at lower temperature, kinetics of triplet excited states of T6 show slower growth. Further kinetics analysis shows that TET from the bright states to T6 is higher than that from the dark states. The bright states contribution to TET can be attributed to the wavefunction components with triplet-state-like spin characters, resulting in non-zero TET transition probability.

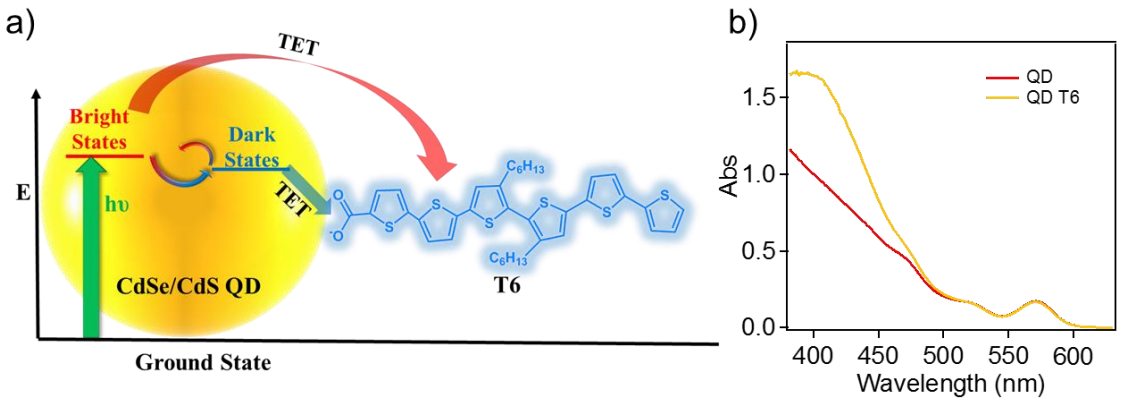

Figure 4.1: a). Photophysical processes (arrows) in CdSe/CdS QD-T6 complex following QD excitation. The QD bright state generated by excitation can relax to the dark state, and both bright and dark states can undergo triplet energy transfer (TET) to T6. b). UV-vis absorption spectra of free QDs (red) and QD-T6 complexes (orange) embedded in polymer films at room temperature.

4.2 Results and discussion

4.2.1 Bright and dark state equilibrium in CdSe/CdS QDs

CdSe/CdS core-shell QDs and T6 molecules were synthesized according to procedures from previous literature,[19, 41] and the preparations of QD-T6 complexes dispersed in toluene or

embedded in a polymer matrix on the surface of glass substrate are described in Section 2.1.5 and Figure 4.2. CdSe/CdS core/shell QDs instead of bare CdSe QDs were selected as the sensitizer because of their low trap state population, which may also contribute to triplet energy transfer and complicate the analysis.[41-42] The UV-vis absorption spectra of the QD and QD-T6 complexes are shown in Figure 4.1b. The $1S_h$-$1S_e$ absorption peak of the QD is centered at 570 nm and shows negligible shift after T6 adsorption. The QD-T6 spectrum shows an additional peak centered at 400 nm due to the T6 S_0-S_1 absorption.[19] The surrounding temperature of the QD-T6 complex was tuned by placing the film sample into a Janis STVP-100 cryostat (more details in Section 2.2.2). Figure 4.3 shows the absorption spectra of QD and QD T6 at the applied temperatures. The absorption spectra were obtained from calculating the absorbance of the sample at each wavelength from the signal and reference probe intensities in TA experiments. The reference probe spectra were first scaled to reach the same intensity at 700 nm as signal probe spectra, because there is supposed to be zero absorbance for QD and QD T6 at 700 nm. Then the absorbance of the sample can be calculated as:

$$Abs = lg \frac{I_{signal}}{I_{reference}} \qquad \text{Eq. 4.1}$$

where I_{signal} and $I_{reference}$ are the intensities of signal probe and scaled reference probe at each wavelength. As is shown in Figure 4.3, there is a tail in spectra from 570 nm to 650 nm, which is due to the scattering of the signal probe by the sample or cryostat. In additional, because of the weak probe intensity at wavelengths below 450 nm, absorbance spectra below 450 nm cannot be well resolved. As is shown in the figure, when temperature is decreased from room temperature to 40 K, the $1S_h$-$1S_e$ exciton peaks of the QD and QD-T6 both blue-shift to 550 nm, consistent with previous observations.[43] However, in temperature regime of 5-40 K, there is negligible $1S_h$-$1S_e$ absorption peak shift of QD and QD-T6, indicating negligible change of the QD to T6 TET driving

force in this temperature range. $1S_h$-$1S_e$ transition energy (E(T)) extracted from the absorption peak positions in a) and b) as function of temperature for CdSe/CdS QD and CdSe/CdS QD T6 complex are plotted in panel c). E(T) of the QD and QD T6 complex show consistent change with increasing temperature. The trend can be well fit with the Varshini model:

$$E\ (T) = E(0) - \frac{\alpha T^2}{\beta + T} \qquad \text{Eq. 4.2}$$

where E(0) is the $1S_h$-$1S_e$ transition energy at 0 K, α is constant, and β is comparable to the Debye temperature.[44] The fitting yields E(0) = (2.26 ± 0.01) eV, α = (3.95 ± 0.56)×10^{-4} eV/K and β = (120 ± 55) K, which are in agreement with the values reported in previous literature and thus suggest the validity of the applied temperature at the sample.[45]

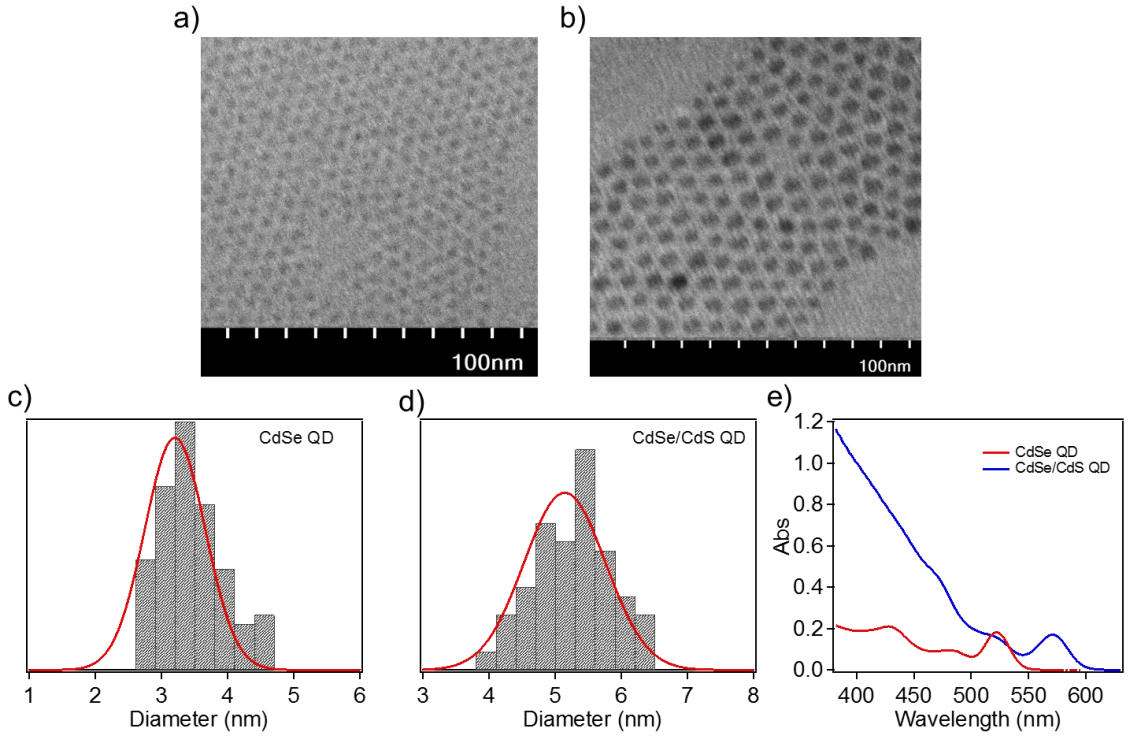

Figure 4.2: Characterization of CdS shell growth to form CdSe/CdS core-shell QD. a) and b). Parts of the TEM images of CdSe core QD and CdSe/CdS core-shell QD, respectively. c) and d). Size distributions of the synthesized CdSe QD and CdSe/CdS QD extracted from a) and b). The

red solid lines are the fits of the diameter histograms by Gaussian distribution. The average diameters (standard deviations) of the QDs are 3.20 (0.65) nm for core QD and 5.14 (0.87) nm for CdSe/CdS QD, suggesting shell thickness to be 0.97 nm. e). UV-vis absorption spectra of CdSe QD (red) and CdSe/CdS QD (blue). The red shift of $1S_h$-$1S_e$ absorption peak and emergence of bulk-like absorption band (380-480 nm) corresponding to transition from higher hole levels and the 1Se level in core-shell QD suggest successful growth of CdS shell.[41]

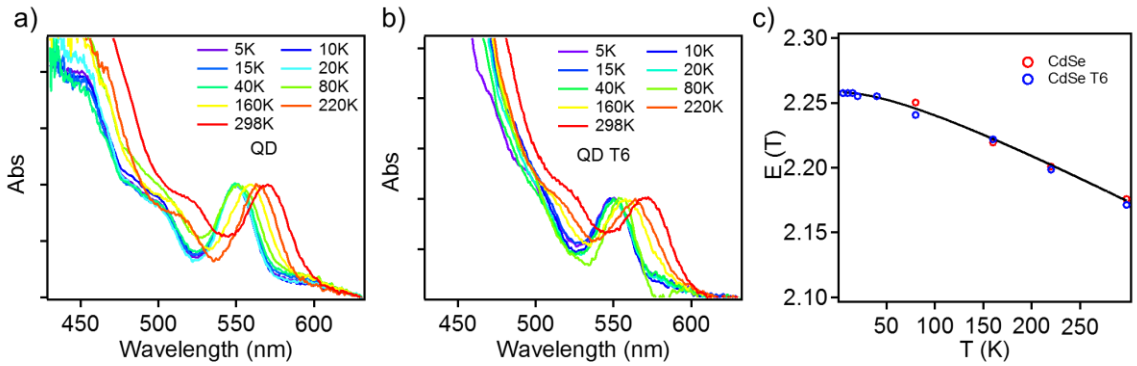

Figure 4.3: Absorption spectra of a). CdSe/CdS QD and b). CdSe/CdS QD T6 complex at temperatures from 5 K to 298 K. c). $1S_h$-$1S_e$ transition energy (E(T)) extracted from the absorption peak positions in a) and b) as function of temperature for CdSe/CdS QD (red circles) and CdSe/CdS QD T6 complex (blue circles). The black line is the fitting of $1S_h$-$1S_e$ transition energy of CdSe/CdS QD as function of temperature with the Varshni model.

Thermal equilibrium of bright and dark states in free CdSe/CdS QDs was studied with temperature dependent TA spectroscopy. TA spectra of QDs at room temperature with 550 nm pulse excitation (Figure 4.4a) show the exciton bleach (XB) of $1S_h$-$1S_e$ transition at 570 nm and the transition from higher hole levels to the $1S_e$ level (denoted as T band) at 473 nm, respectively, similar to previous reports.[46] As temperature decreases from room temperature to 40 K, XB peaks

of $1S_h$-$1S_e$ transition and T band blue shift to ~550 nm and 459 nm, respectively, along with decrease of the peak line-width, as shown in Figure 4.4b and Figure 4.5. In temperature regime of 5-40 K, the position and linewidth of the XB peaks show negligible changes. The result is consistent with the QD UV-vis spectra change as function of temperature and can be rationalized by decreasing lattice expansion and exciton-phonon coupling with decreasing temperature.[43, 47-48] As shown in Figure 4.4c, the $1S_h$-$1S_e$ XB kinetics show slower decay from 40 K to 5 K, which can be attributed to increasing population of dark state with longer lifetime at lower temperature,[49-51] consistent with previous reports of temperature dependent photoluminescence lifetimes of CdSe QDs.[50] Compared to XB kinetics at 40 K, XB kinetics at 298 K shows slower decay from 1 ps to 10 ns and faster decay from 10 ns to 1 μs. The difference is attributed to not only bright-dark state population change but also the change in trap state population from 40 K to 298 K.[52-54] For this reason, our analysis is focused on the temperature dependent changes from 40 to 5 K, which can be attributed to changes in bright and dark state populations with negligible effects caused by change of trap states.[50] Note that XB decay is dominated by decay of bright/dark states to ground states instead of other nonradiative pathways because of the high photoluminescence quantum yield of QD in this temperature regime.[50]

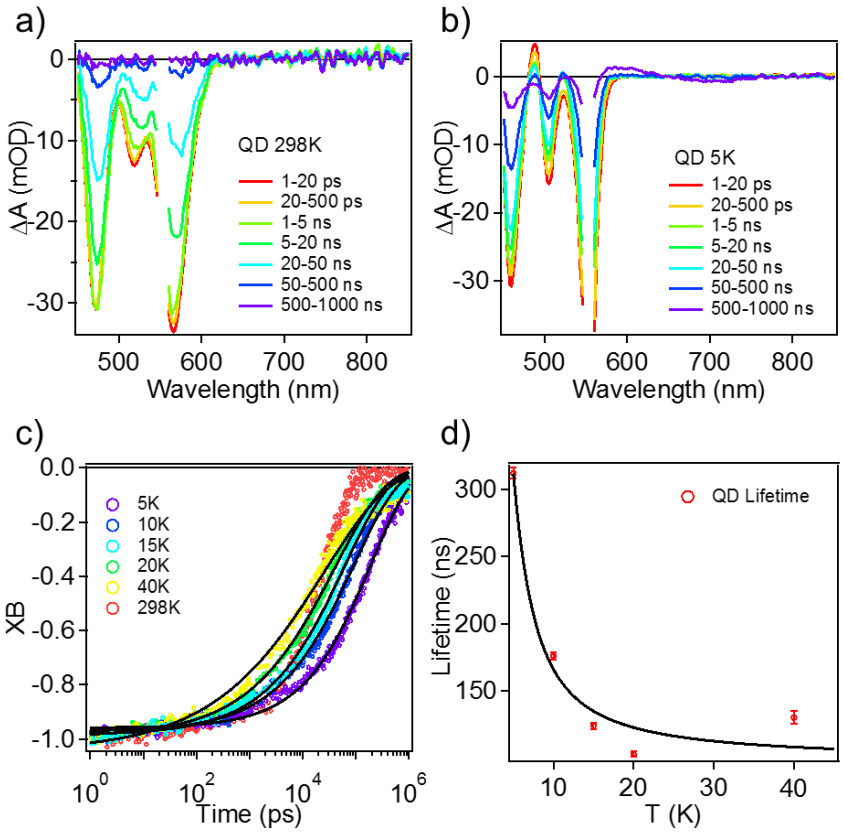

Figure 4.4: Temperature dependent TA spectra and kinetics of free CdSe/CdS QDs measured with 550 nm pulse excitation. Average TA spectra of QDs at a) 298 K and b) 5K at indicated delay time window; c) Comparison of $1S_h$-$1S_e$ XB kinetics of QDs at indicated temperatures from 5 to 298 K(open symbols) and their fits to stretched exponential function (black solid lines). d) Average lifetime of $1S_h$-$1S_e$ XB recovery kinetics as function of temperature (open symbols) and fit to the model of thermal equilibrium between bright and dark states (black solid line). Details of the model are described in the main text.

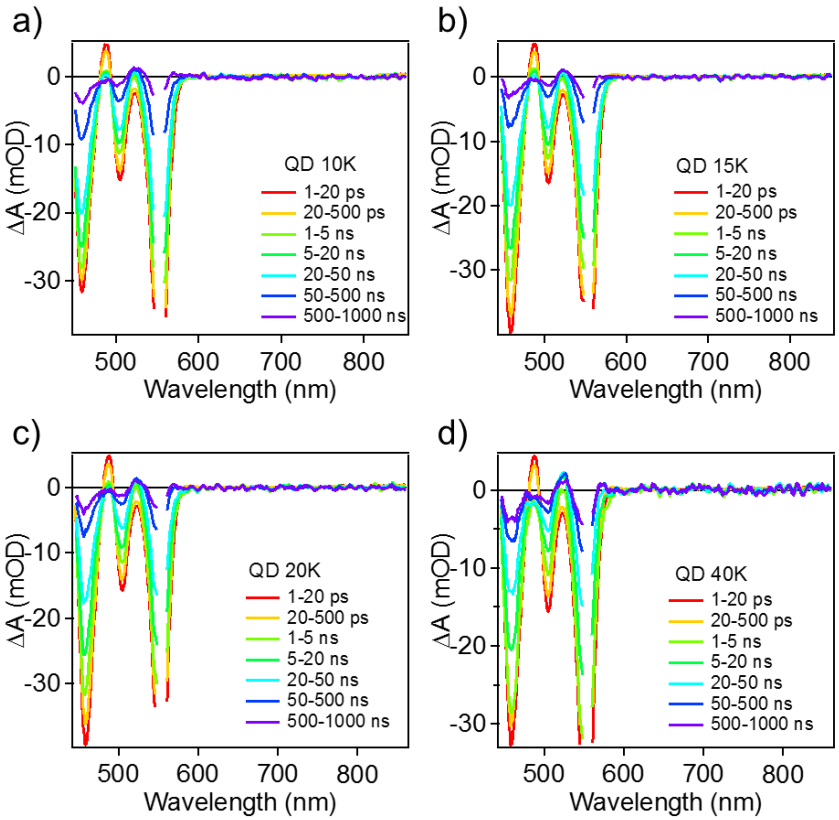

Figure 4.5: TA spectra of free CdSe/CdS QD with 550 nm pump pulse excitation at a). 10 K; b). 15 K; c). 20 K and d). 40 K. The delay time window is 1 ps to 1 μs. Because of the overlap between exciton bleach (XB) of the QD at low temperatures and the scattering of the 550 nm pump pulse, the center of the XB peak cannot be well resolved.

XB kinetics from 5 K to 40 K can be well fit with stretched exponential function, as shown in Eq. 4.3.

$$A\,(t) = A_0 e^{-(\frac{t}{\tau_k})^{\beta}} \qquad \text{Eq. 4.3}$$

In Eq. 4.3, A(t) and A0 are signal amplitudes at time t and t=0 respectively, τ_k and β are the time constant and stretching exponent of the stretch exponential function. The fitting parameters are listed in Table A4.1 in Appendix 4.1. Average lifetime of XB kinetics can be calculated from

fitting parameters according to:

$$< \tau >= \frac{\tau_k}{\beta} \Gamma(\frac{1}{\beta}) \qquad \text{Eq. 4.4}$$

where Γ is the gamma function.[55] Average XB decay lifetime as function of temperature is plotted in Figure 4.4d. Based on a kinetics model involving forward and backward transfer from bright to dark states in QD (more specifically $\pm 1^L$ bright states and ±2 dark states) and their decays to ground state,[50] temperature dependent average XB decay lifetime can be fit as:

$$\frac{1}{<\tau>} = \frac{\frac{1}{\tau_b} e^{-\frac{E}{kT}} + \frac{1}{\tau_d}}{e^{-\frac{E}{kT}} + 1} \qquad \text{Eq. 4.5}$$

where <τ> is the average lifetime of XB kinetics; τ_b and τ_d is the decay time constants from bright and dark states to ground state, respectively; E is the energy difference between bright and dark states, and k is the Boltzmann constant. (More details in Appendix 4.1 and Figure A4.1). Herein, it is assumed that contribution of bright state to XB is as large as that of dark state based on a simplified fine structure model described in Appendix 4.1 and Figure A4.1. The fitting yields E = (1.21 ± 0.55) meV; τ_b = (46.5 ± 7.0) ns and τ_d = (486 ± 117) ns. The result agrees with findings of temperature dependent QD photoluminescence experiment in previous literature.[49-51, 56-57] For example, it has been reported that the dark exciton lifetime decreases from ~1.4 ms to ~ 0.3 ms when the CdSe QD diameter increases from 1.7 nm to 6.3 nm.[50] In summary, equilibrium between bright and dark states ($\pm 1^L$ and ±2, respectively) in CdSe/CdS QD can be tuned by temperature.

4.2.2 Temperature dependent TET from CdSe/CdS QD

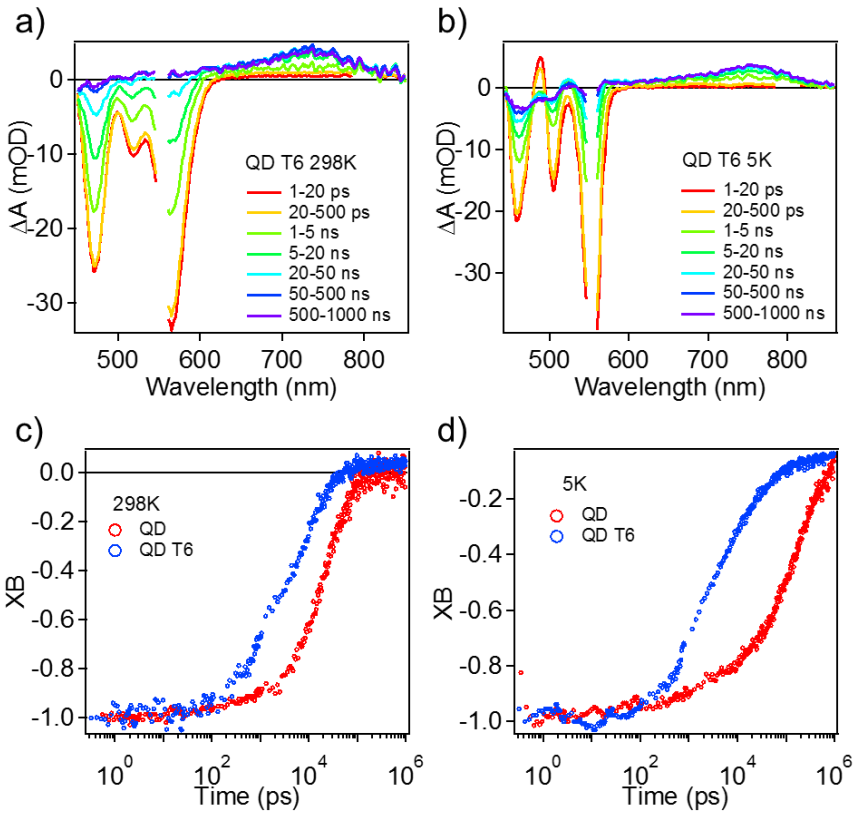

Figure 4.6: a) and b). TA spectra of QD T6 complex from 1 ps to 1 μs with 550 nm excitation at 298 K and 5 K, respectively. c) and d). Comparison of $1S_h$-$1S_e$ XB kinetics of QD in QD-T6 complex (blue) and in free QD (red) at 298 K and 5 K, respectively.

Temperature dependent TET from CdSe/CdS QDs to attached T6 was studied with TA spectroscopy (Figure 4.6). Because there is no absorption of T6 at 550 nm (see Figure 4.1b), QD can be selectively excited with 550 nm pump pulse, as confirmed in Figure 4.7. As shown in Figure 4.6a and 4.6b and Figure 4.8, TA spectra of QD-T6 complexes at all temperatures show the same spectral features as those of free QDs at corresponding temperatures from 1 to 20 ps, indicative of QD exciton generation. The TA spectra show growth of an additional broad positive peak at 600 nm to 850 nm due to the T6 T_1-T_n absorption[19] along with decay of QD XB signal on the 500 ps to 500 ns time scale, indicative of formation of T6 T_1 state (well-defined spin state) by TET from

QD. With a temperature decrease from 298 K to 40 K, the T_1->T_n peak of T6 shows a slight decrease of maximum peak amplitude and slight red shift with peak maxima from 735 nm to 755 nm, while negligible peak shift is observed in 5-40 K. The peak shift may be attributed to aggregation of adsorbed T6 molecule at low temperature.[58] The $1S_h$-$1S_e$ XB signal in QD-T6 complexes recovers faster than free QDs after ~ 100 ps, as shown in Figure 4.6c, 4.6d and Figure A4.2 in Appendix 4.2, consistent with TET from the QD to T6. XB decay kinetics of QD-T6 complexes is consistent with kinetics of T6 triplet signal growth, as shown in Figure A4.3 in Appendix 4.2, suggesting direct Dexter type TET from QD to T6 without other intermediates. This also agrees with previous report of direct Dexter type TET from CdSe QDs to adsorbed T6 molecules.[19]

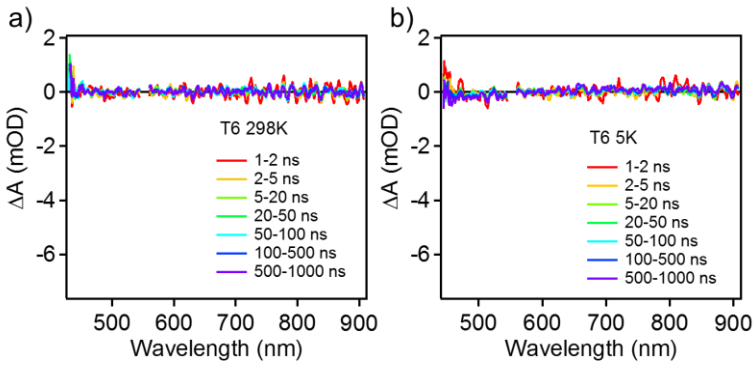

Figure 4.7: TA spectra of free T6 film sample with 550 nm excitation at a). 298 K and b). 5 K. The delay time window is 1ns to 1000 ns. The spectra show no signal for T6, suggesting that 550 nm pump pulse cannot directly excite T6.

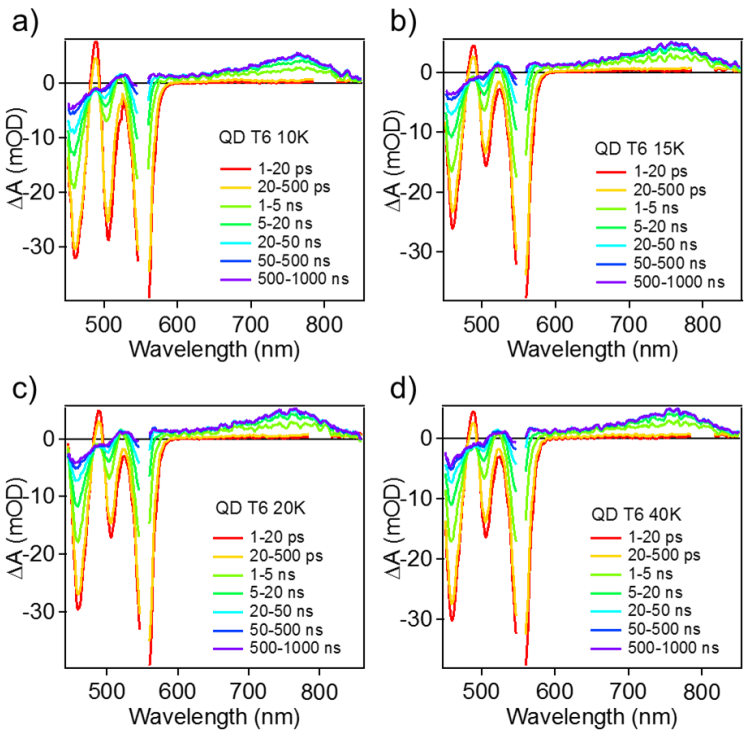

Figure 4.8: TA spectra of free CdSe/CdS QD T6 complex film sample with 550 nm pump pulse excitation at a). 10 K; b). 15 K; c). 20 K and d). 40 K. The delay time window is 1 ps to 1 μs.

Temperature dependent TET from QD to T6 is further demonstrated in T6 triplet signal growth kinetics extracted from TA. The kinetics can be obtained by averaging kinetics from 700-800 nm of QD T6 TA spectra and is shown in Figure 4.9a and Figure 4.9b. Because of negligible QD signal amplitude in this regime, the kinetics solely represents the growth of T6 triplet excited state population. As shown in Figure 4.9a, T6 triplet state mainly grows from 100 ps to 100 ns and show relatively small difference for increasing temperature from 5 K to 40 K. The small difference can be better resolved in kinetics plot in Figure 4.9b and Figure A4.4 in Appendix 4.2. The kinetics shows almost no dependence on temperature in delay time range of 1-5 ns but shows slightly slower T6 triplet growth with decreasing temperature in delay time range of 10-100 ns. The difference is manifested from 5 K to 10 K and is not obvious for higher temperature, coinciding

with change of thermal equilibrium between bright/dark states with temperature. The result is consistent with slower $1S_h$-$1S_e$ XB decay with increasing temperature (shown in Figure A4.5 in Appendix 4.2). Therefore, TET from QD to T6 is influenced by temperature and is related to bright and dark states equilibrium. To better rationalize the result, we applied the kinetics model in Figure 4.9c to fit the T6 triplet growth kinetics. The kinetics model involves intrinsic decay of bright/dark states of QD to ground state, exchange between bright/dark states and potential TET from both bright and dark states to T6 triplet excited state. Considering the large energy difference between QD exciton and T6 triplet excited states ($\Delta E = 0.41$ eV),[19] at the low applied temperatures, back energy transfer from T6 to QD is neglected. Based on the model (with more details in Appendix 4.3), T6 triplet excited state growth can be described as:

$$[T] = N_{B0}k_{bt}\left(\frac{B+\lambda_1}{(\lambda_1-\lambda_2)}\frac{e^{\lambda_1 t}-1}{\lambda_1} - \frac{B+\lambda_2}{(\lambda_1-\lambda_2)}\frac{e^{\lambda_2 t}-1}{\lambda_2}\right) + N_{B0}k_{dt}\left(\frac{k_r}{(\lambda_1-\lambda_2)}\frac{e^{\lambda_1 t}-1}{\lambda_1} - \frac{k_r}{(\lambda_1-\lambda_2)}\frac{e^{\lambda_2 t}-1}{\lambda_2}\right) \quad \text{Eq. 4.6a}$$

where

$$B = k_r e^{-\frac{E}{kT}} + k_d + k_{dt} \quad \text{Eq. 4.6b}$$

N_{B0} is the bright state population at t = 0, and λ_1 and λ_2 ($\lambda_1 > \lambda_2$) are the solutions for the following equation:

$$\lambda^2 + \left(k_b + k_{bt} + k_r + k_d + k_{dt} + k_r e^{-\frac{E}{kT}}\right)\lambda + \left(k_b + k_{bt} + k_r\right)\left(k_d + k_{dt} + k_r e^{-\frac{E}{kT}}\right) - {k_r}^2 e^{-\frac{E}{kT}} = 0 \quad \text{Eq. 4.6c}$$

Because in Dexter energy transfer framework, rate of TET from donor (D) to acceptor (A) follows Fermi's golden rule:

$$k_{TET} = \frac{2\pi}{\hbar}|V|^2_{TET} FCWD \quad \text{Eq. 4.7}$$

where $|V|_{TET}$ is the coupling strength and FCWD is the overlap integral of the Frank-Condon weighted density of states.[59] Coupling strength for TET is described by wavefunction overlap and

thus is temperature independent for bright and dark states. FCWD can be described by spectra overlap between T_1->S_0 transition of the donor and S_0->T_1 transition of the acceptor and is temperature dependent.[59-60] Additional term u(T) was added to the fitting to account for changes of k_{bt} and k_{dt} from 5 K to 40 K by change in FCWD as:

$$k_{bt\ or\ dt}(T) = k_{bt\ or\ dt}(5\ K) \cdot u(T) = k_{bt\ or\ dt}(5\ K) \cdot \frac{FCWD\ (T)}{FCWD\ (5\ K)} \qquad \text{Eq. 4.8}$$

Herein u(T) is assumed to be the same for bright and dark states because of the small energy difference between these states.[16] Figure 4.9b and Figure A4.4 show the fitting result, which yields TET rate from bright states to be (0.492 ± 0.011) ns^{-1}, TET rate from dark states to be (0.0271 ± 0.0014) ns^{-1} at 5 K and u (T) to be 1.00, 1.00, 0.99 and 1.04 for T = 10, 15, 20 and 40 K, respectively. The negligible change of FCWD from 5 to 40 K further supports that change in TET growth kinetics is mainly due to change in bright/dark state equilibrium. This is consistent with negligible spectra shift and line broadening for both QD and T6 triplet signal from 5 K to 40 K in TA spectra of QD T6 complex, suggesting little change in FCWD with temperature. The faster TET from bright states than from dark states is surprising. Actually, as shown in Figure A4.6 in Appendix 4.3, T6 triplet growth would be faster with decreasing temperature if TET was solely transferred from dark states based on the kinetics model, which contradicts the experimental observation. Therefore, current experimental result suggests the significant contribution of TET from bright states of QD to attached acceptor.

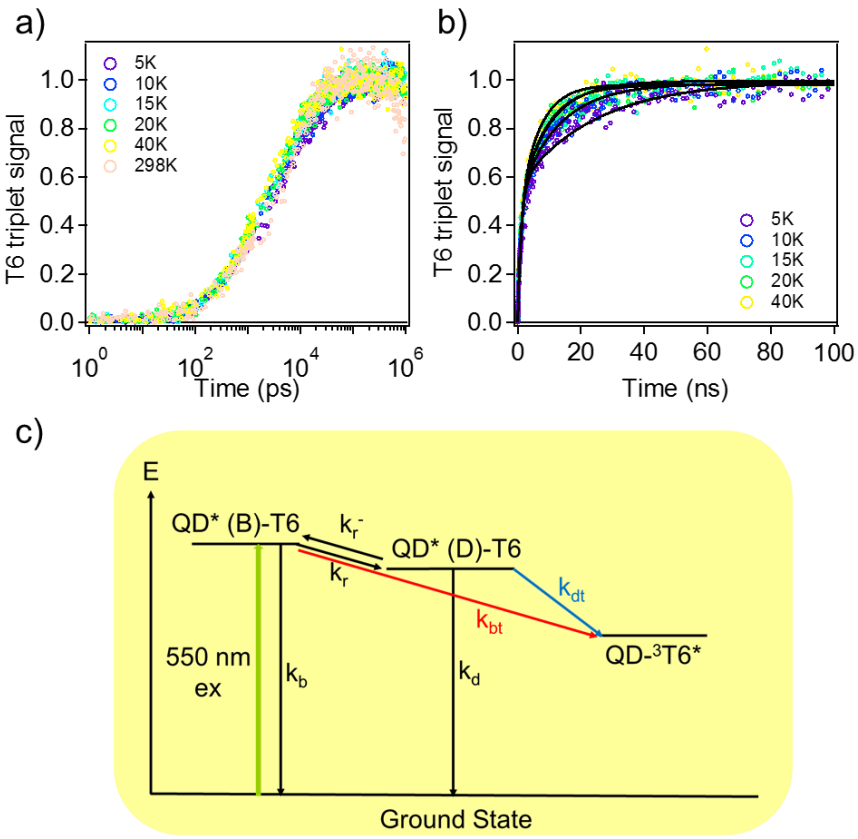

Figure 4.9: Temperature dependent T6 triplet signal (T_1->T_n induced absorption) growth kinetics and the corresponding kinetics model. a) T6 triplet signal growth kinetics from 1 ps to 1 μs in temperature regime of 5 K (purple) to 40 K (yellow) and at 298 K (light pink) plotted in log scale; b). T6 triplet signal growth kinetics from 1 ps to 100 ns in temperature regime of 5 K to 40 K plotted in linear scale. The fitting of the kinetics based on the kinetics model is shown as black solid lines. c). Kinetics model for fitting the T6 triplet signal growth. The model considers the intrinsic decay of bright ($\pm 1^L$) and dark states (± 2) of QD to ground state (black arrows), forward and backward transfer from bright state to dark state (black arrows) and TET from bright and dark state to form T6 triplet (red and blue arrows, respectively).

4.2.3 Discussion

The non-zero rate of TET from bright state of QD can be accounted for by evaluating spin characters of bright/dark states in QD and TET rate expression. With the wavefunction expressions of doubly degenerate $1S_e$ electron states of CdSe/CdS QD and fourfold degenerate $1S_{3/2}$ hole states (shown as Eq. A4.6-A4.8 in Appendix 4.4),[16] the wavefunctions of 0^L, $\pm1^U$, 0^U, $\pm1^L$ and ±2 states can be calculated by considering the asymmetry of QD shape and lattice and electron-hole exchange interaction and shown as Eq. A4.10a-e, which were demonstrated in previous literature.[16] By separating out the spin wavefunctions of the electron and hole, exciton states wavefunctions can be generally written as:

$$\Psi_X(\boldsymbol{r_e}, \boldsymbol{r_h}) = c_X{}^{(1)}\varphi_X{}^{(1)}(\boldsymbol{r_e}, \boldsymbol{r_h})|\uparrow\rangle_e\,|\uparrow\rangle_h + c_X{}^{(2)}\varphi_X{}^{(2)}(\boldsymbol{r_e}, \boldsymbol{r_h})|\uparrow\rangle_e\,|\downarrow\rangle_h +$$

$$c_X{}^{(3)}\varphi_X{}^{(3)}(\boldsymbol{r_e}, \boldsymbol{r_h})|\downarrow\rangle_e\,|\uparrow\rangle_h + c_X{}^{(4)}\varphi_X{}^{(4)}(\boldsymbol{r_e}, \boldsymbol{r_h})|\downarrow\rangle_e\,|\downarrow\rangle_h \qquad \text{Eq. 4.9}$$

where $\varphi_X{}^{(i)}(\boldsymbol{r_e}, \boldsymbol{r_h})$ is the part of the wavefunctions of exciton state X involving real space coordinates and consists of envelope functions and Bloch functions with real space coordinates, and $c_X{}^{(i)}$ is the corresponding constant. Therefore, specifically for CdSe/CdS QD, all exciton states consist of components with the same and opposite electron/hole spin projections, as shown in Figure 4.10, although spin of electron and hole in QD is not good quantum number because of the angular momentum coupling. Note that this characteristic of QD bright/dark state wavefunctions differs from many molecular sensitizers with well-defined singlet and triplet excited states, but shares some similarity with organometallic sensitizers with strong S_0-T_1 transitions caused by strong spin-orbit coupling.[61-64]

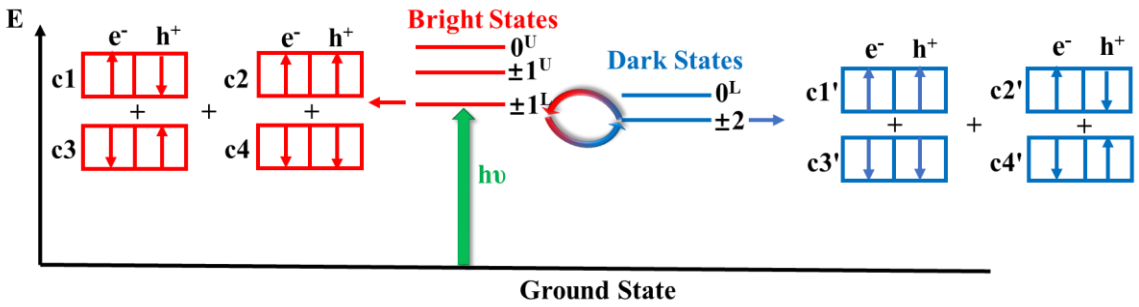

Figure 4.10: Diagram of bright and dark states in CdSe/CdS QD. The lowest dark states are ±2 states while the lowest bright states are ±1 states. Wavefunctions of these states all consist of components with the same and opposite electron/hole spin projections.

With the wavefunctions of bright/dark states of QD, rate of TET from QD can be evaluated. Because of similar FCWD in rates of TET from bright and dark states due to small energy difference between these states, coupling strength is the factor resulting in difference of TET rate of bright and dark states. In Dexter's formula for TET, coupling strength is described as two-electron exchange integral:

$$|V| \propto \langle \varphi_{HO}^{D}(1)\varphi_{LU}^{A}(2) \left|\frac{e^2}{r_{12}}\right| \varphi_{LU}^{D}(2)\varphi_{HO}^{A}(1)\rangle \langle \chi_{HO}^{D}(1)|\chi_{HO}^{A}(1)\rangle\langle \chi_{LU}^{D}(2)|\chi_{LU}^{A}(2)\rangle \quad \text{Eq. 4.10}$$

where HO and LU stand for HOMO and LUMO orbital, and χ is the spin wavefunction (either $|\uparrow>$ or $|\downarrow>$).[59] Eq. 4.10 can be applied to evaluate exchange integral for TET from QD to T6, where $\varphi_{\pm 2,\pm 1}{}^{(i)}(\boldsymbol{r_e}, \boldsymbol{r_h})$ in Eq. 4.9 are included in integral for real space coordinates, and $|\uparrow(\downarrow)>_{e/h}$ are included in spin integral term. When considering the triplet excited state of the T6 with the same spin of electrons in HOMO and LUMO, integral in Eq. 4.10 for TET from QD to T6 will be non-zero only if spin projections of electron and hole are the same. Because both bright and dark states contain components with the same electron and hole spin projections, as shown in Eq. 4.9 and Figure 4.10, the exchange integrals involving QD exciton and T6 triplet

excited state orbitals are non-zero for both bright and dark states. The analysis is consistent with experimental results that both bright and dark states of QD could undergo TET to form T6 triplet excited state. The difference between TET rates from the bright and dark states can be attributed to the difference in their triplet component amplitudes and the wavefunction overlaps between the QD spin-triplet components and T6 triplet state. More quantitative evaluation of the expected TET rate differences from these states is difficult and will not be conducted in this work due to the lack of information of the exact values of constants in Equation A4.10, T6 triplet state wavefunction and the geometry of T6 on QD. Similar analysis could be conducted, and same conclusion could be reached for other terms of coupling strength involving charge transfer virtual states. TET pathways with charge transfer virtual states have been considered to outcompete direct Dexter energy transfer described by two-electron exchange integral.[32, 65] In this scenario, one-electron integral for electron/hole transfer should be evaluated, in which the same spin integral terms $\langle \chi_{HO}^{D}(1)|\chi_{HO}^{A}(1)\rangle$ and $\langle \chi_{LU}^{D}(2)|\chi_{LU}^{A}(2)\rangle$ will be included. Therefore, the conclusion that bright and dark states both can undergo TET in CdSe/CdS QD is still valid for TET pathways involving virtual states.

4.3 Conclusion

In summary, we demonstrate the TET in CdSe/CdS core/shell QD-functionalized oligothiophene complex sensitized by both bright and dark states through analysis of dependence of TET dynamics on temperature, which could shift equilibrium between bright and dark states. Non-zero TET rate of bright and dark states can be rationalized by considering the electron and hole spin projections in wavefunctions of QD, with components of the same electron/hole spin projections bringing about non-zero TET probability. The conclusion is applicable to various TET pathways involving direct two-electron exchange Dexter energy transfer and charge transfer

virtual state mediated TET. Similar analysis may also be applied to other QDs, including PbS and $CsPbBr_3$ QDs. Our finding suggests that simple analogy between bright/dark states in QDs and singlet/triplet excited states in molecules cannot be made, and the mechanisms for QD sensitized TET should be treated differently in certain aspects compared to mechanisms for TET in molecular donor-acceptor complexes.

Appendix 4.1

Fitting of Temperature Dependent Exciton Bleach (XB) Kinetics of Free CdSe/CdS QD

Table A4.1: Results for free QD XB fitting with stretched exponential functions.

T (K)	τ_k (ns)	β
5	195 ± 2	0.575 ± 0.005
10	92.0 ± 1.0	0.513 ± 0.005
15	61.7 ± 1.0	0.499 ± 0.006
20	41.4 ± 0.7	0.450 ± 0.005
40	29.3 ± 0.6	0.381 ± 0.004

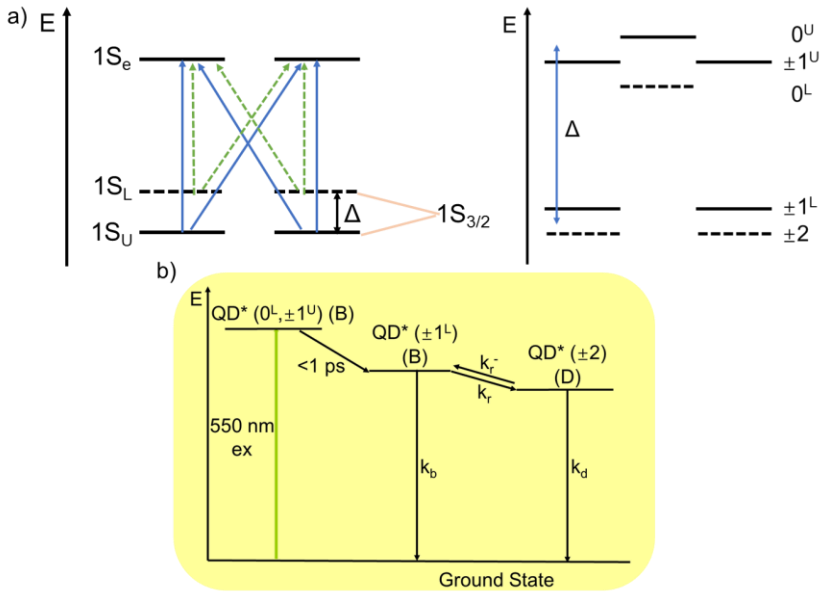

Figure A4.1: a). Simplified model for analyzing the relative contribution of bright and dark states in QD to XB. In the model, $1S_{3/2}$ four-fold degenerate hole levels are split into $1S_L$ and $1S_U$ sublevels by asymmetry of the the QD shape and lattice. $1S_L$-to-$1S_e$ transitions (shown as green dashed arrows) with small oscillator strength are assumed to be mixture of $\pm1^L$ and ±2 exciton

states (shown in right panel), while $1S_U$-to-$1S_e$ transitions (shown as blue solid arrows) with large oscillator strength are assumed to be mixture of 0^L, $\pm1^U$ and 0^U exciton states. In the right panel, the solid lines and dashed lines are bright and dark states in CdSe/CdS QDs, respectively. b). Kinetics model for fitting temperature dependent XB average lifetimes of free QD. Relaxation from the initially populated 0^L and $\pm1^U$ states to lowest bright $\pm1^L$ states is not considered in the kinetics equation because it proceeds within 1 ps.

In order to fit the temperature dependent average lifetime of XB of free QD, we first analyze the relative contribution of bright and dark states to XB based on a simple modified model from previous literature.[66] Because of the high photoluminescence quantum yield of CdSe/CdS core-shell QD, especially at low temperature,[50] only band edge excitons instead of trap states are considered. Under the effective mass approximation framework, the lowest $1S_e$ electron level in CdSe/CdS QD is twofold degenerate, while the lowest $1S_{3/2}$ hole levels are four-fold degenerate.[16] The asymmetry of non-spherical shape and wurtzite lattice of the QD splits the eightfold degenerate exciton levels into $1S_L$ and $1S_U$ sub-levels with the energy splitting Δ to be about 20 meV,[16, 67] as shown in Figure A4.1a. In a simplified model applied to account for state filling effect,[68] further splitting of these sub-levels into 0^L, $\pm1^U$, 0^U, $\pm1^L$ and ±2 states resulting from electron-hole exchange interaction is not considered to avoid complication. Within this scheme, the transitions from $1S_L$ to $1S_e$ are assumed to be mixture of $\pm1^L$ and ±2 exciton states with small and zero oscillator strength, respectively.[16, 40] As a result, the absorption of pump and probe pulses by the $1S_L$-to-$1S_e$ transitions can be neglected. The transitions from $1S_U$ to $1S_e$ are assumed to be mixture of 0^L, $\pm1^U$ and 0^U exciton states.[16, 40] Because of the large oscillator strength of 0^L and $\pm1^U$ states, the $1S_U$-to-$1S_e$ transitions contribute mostly to absorption of the pump and probe pulses in

the TA experiments. In TA experiments of QD in temperature regime of 5 K to 40 K, the pump pulse induced the $1S_U$-to-$1S_e$ transition, and the hole in $1S_U$ level would relax to $1S_L$ level within 1 ps,[69] resulting in population of $\pm1^L$ bright states, after which the ±2 dark states would be populated by relaxation from $\pm1^L$ bright states.[70] Due to relatively large energy difference between $1S_L$ to $1S_U$ level and the low temperature,[68-69] back transfer of hole from $1S_L$ to $1S_U$ through thermal equilibrium can be neglected, and only equilibrium between $\pm1^L$ bright states and ±2 dark states as well as their corresponding decay to ground state will be considered in XB kinetics analysis after 1 ps. Because both $\pm1^L$ and ±2 states correspond to $1S_L$-to-$1S_e$ transition with low oscillator strength in the scheme in Figure A4.1a, the hole state filling effect of these states to XB of the QD will not be considered. On the other hand, there will be one electron filled in $1S_e$ level when either $\pm1^L$ or ±2 states are populated, contributing to XB of the QD from the electron state filling effect, and it can be assumed that the contribution of $\pm1^L$ bright states to XB is approximately the same as that of ±2 dark states.

We then consider the kinetics model for fitting the temperature dependent average lifetime of XB, as shown in Figure A4.1b. The model considers the decay of QD bright and dark states to ground state and the exchange between bright and dark states. The differential equations for bright and dark states of free QD can be written as:

$$\frac{dN_B}{dt} = -k_b N_B - k_r N_B + k_r e^{-\frac{E}{kT}} N_D \qquad \text{Eq. A4.1a}$$

$$\frac{dN_D}{dt} = -k_d N_D + k_r N_B - k_r e^{-\frac{E}{kT}} N_D \qquad \text{Eq. A4.1b}$$

where N_B and N_D are the populations of bright and dark states, respectively; k_b ($1/\tau_b$) and k_d ($1/\tau_d$) are the decay rates of bright and dark states to ground state; k_r is the decay rate of bright states to form dark states; E is the energy difference between bright and dark states, and k is the Boltzmann constant. Then, it can be derived that:

$$\frac{d\,XB}{dt} \propto \frac{d(N_B+N_D)}{dt} = -k_b N_B - k_d N_D = -k_{QD}(N_B + N_D) \propto -k_{QD} XB \quad \text{Eq. A4.2}$$

where XB is the XB intensity, and k_{QD} is the effective decay rate for XB. For free QD, it can be assumed that bright and dark states are in thermal equilibrium[50]:

$$\frac{N_B}{N_D} = e^{-\frac{E}{kT}} \quad \text{Eq. A4.3}$$

After plugging Eq. A4.3 into Eq. A4.2, we could obtain the XB decay rate shown as Eq. 4.5.

Appendix 4.2

Kinetics Comparison of XB of QD and QD T6 and T6 triplet growth of QD T6 at Applied Temperatures

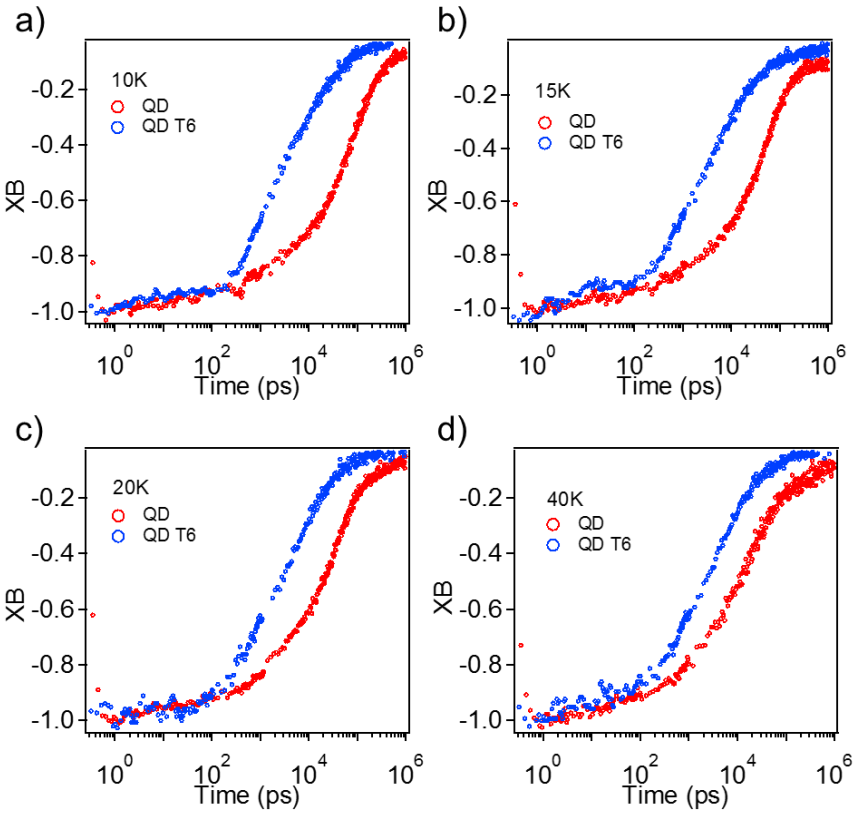

Figure A4.2: Comparison between $1S_h$-$1S_e$ XB kinetics of free QD (red) and QD T6 complex (blue) with 550 nm excitation at a). 10 K; b). 15 K; c). 20 K; d). 40 K.

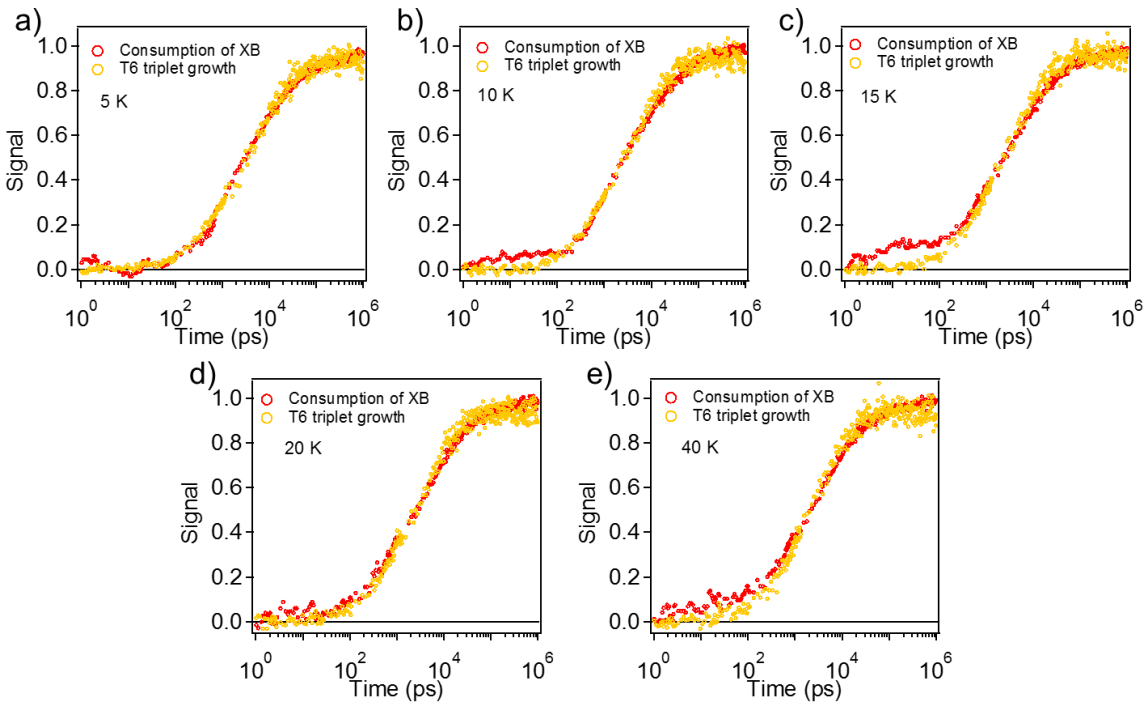

Figure A4.3: Comparison between $1S_h$-$1S_e$ XB decay or consumption (red, with "Consumption of XB" at 0 representing no XB decay and at 1 representing complete XB decay) and T6 triplet growth (yellow) of QD T6 complex at a). 5 K; b). 10 K; c). 15 K; d). 20 K; e). 40 K.

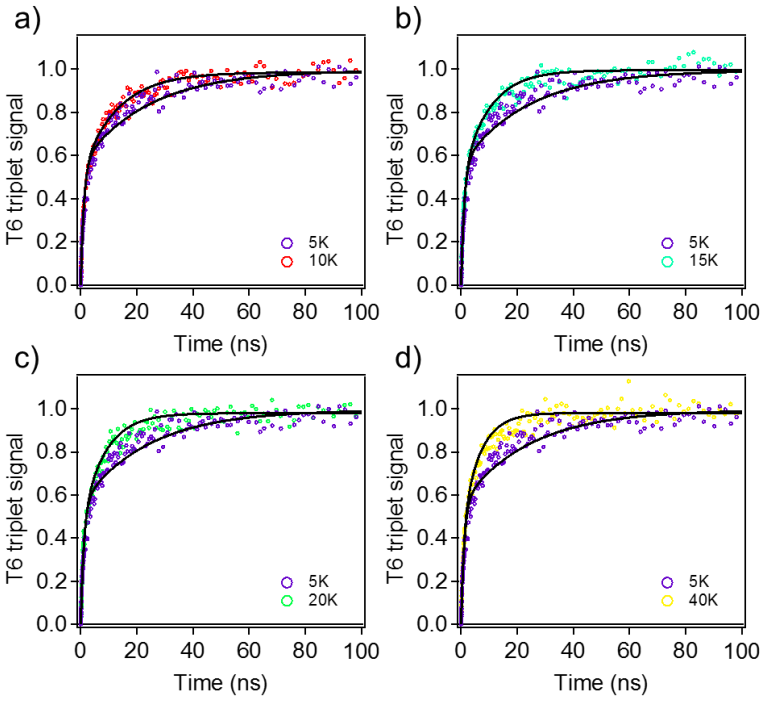

Figure A4.4: Comparison between T6 triplet growth kinetics at a). 5 K (purple) and 10 K (red); b). 5 K (purple) and 15 K (light blue); c). 5 K (purple) and 20 K (green); d). 5 K (purple) and 40 K (yellow). Black solid lines show the global fits of the T6 triplet growth kinetics according to kinetics model in Figure 4.9c and Appendix 4.3.

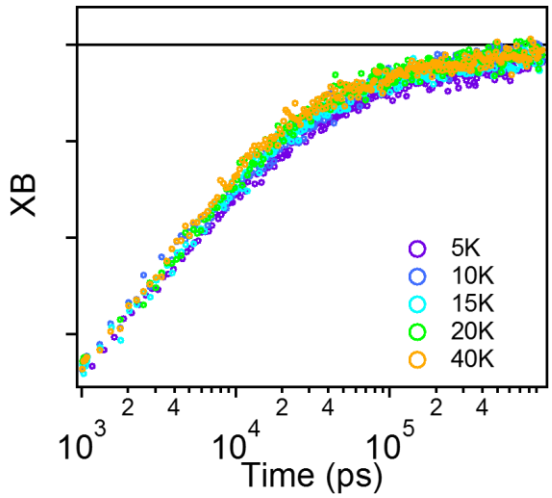

Figure A4.5: Comparison of $1S_h$-$1S_e$ XB of QD T6 complex with 550 nm excitation at temperatures from 5 K (purple) to 40 K (orange).

Appendix 4.3

Fitting of Temperature Dependent T6 Triplet Excited State Growth Kinetics

With the kinetics model shown in Figure 4.9c in the main text, differential equations of bright states ($\pm1^L$) population N_B, dark state (±2) population N_D and T6 triplet excited state population [T] can be written as:

$$\frac{dN_B}{dt} = -(k_b + k_{bt})N_B - k_r N_B + k_r e^{-\frac{E}{kT}} N_D \quad \text{Eq. A4.4a}$$

$$\frac{dN_D}{dt} = -(k_d + k_{dt})N_D + k_r N_B - k_r e^{-\frac{E}{kT}} N_D \quad \text{Eq. A4.4b}$$

$$\frac{d[T]}{dt} = k_{dt} N_D + k_{bt} N_B \quad \text{Eq. A4.4c}$$

Here additional terms for TET from bright states (k_{bt}) and from dark states (k_{dt}) were added to equations of bright and dark states population compared to Eq. A4.1. Decay of triplet excited states of T6 to ground state is neglected in Eq. A4.4 because the process is much slower compared to TET.[19] With the boundary condition that at t = 0, $N_B = N_{B0}$, ND = 0, [T] = 0, the solution of Eq. A4.4 can be solved mathematically. The result is:

$$N_B = N_{B0}\left(\frac{B+\lambda_1}{\lambda_1-\lambda_2} e^{\lambda_1 t} - \frac{B+\lambda_2}{\lambda_1-\lambda_2} e^{\lambda_2 t}\right) \quad \text{Eq. A4.5a}$$

$$N_D = N_{B0}\left(\frac{k_r}{\lambda_1-\lambda_2} e^{\lambda_1 t} - \frac{k_r}{\lambda_1-\lambda_2} e^{\lambda_2 t}\right) \quad \text{Eq. A4.5b}$$

$$[T] = N_{B0} k_{bt}\left(\frac{B+\lambda_1}{(\lambda_1-\lambda_2)} \frac{e^{\lambda_1 t}-1}{\lambda_1} - \frac{B+\lambda_2}{(\lambda_1-\lambda_2)} \frac{e^{\lambda_2 t}-1}{\lambda_2}\right) + N_{B0} k_{dt}\left(\frac{k_r}{(\lambda_1-\lambda_2)} \frac{e^{\lambda_1 t}-1}{\lambda_1} - \frac{k_r}{(\lambda_1-\lambda_2)} \frac{e^{\lambda_2 t}-1}{\lambda_2}\right)$$

Eq. A4.5c

where the values of B, λ_1 and λ_2 are shown in Eq. 4.6 in the main text. Additional term u(T) was added to account for the change of FCWD in k_{bt} and k_{dt} with change in temperature, as shown in Eq. 4.8 in the main text. Eq. A4.5c and Eq. 4.8 were applied for global fitting T6 triplet kinetics

traces in Figure 4.9b. The values of k_b, k_d and E were from the fitting of temperature dependent average lifetime of free QD XB. The global fitting result is shown in Figure 4.9b in main text and Figure A4.4. From the fitting we obtained k_{bt} (5 K)= (0.492 ± 0.011) ns^{-1}; k_{dt} (5 K) = (0.0271 ± 0.0014) ns^{-1},k_r = (0.368 ± 0.016) ns^{-1} and u (T) to be 1.00, 1.00, 0.99 and 1.04 for T = 10, 15, 20 and 40 K, respectively. In order to verify the global fitting result, T6 triplet kinetics were plotted with different combinations of k_{bt} and k_{dt}, as shown in Figure A4.6. In the plots, the values of the rest parameters were from the global fitting results. As shown in Figure A4.6, only when rate of TET from bright states is non-zero and is larger than rate of TET from dark states can the simulated temperature dependent triplet growth kinetics match the experimental observations.

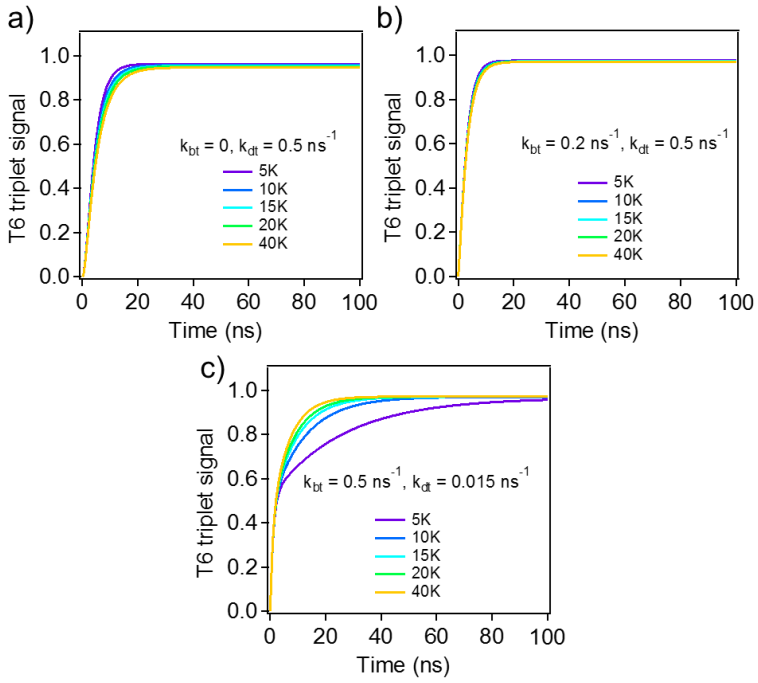

Figure A4.6: Simulated T6 triplet excited state growth kinetics at temperatures from 5 K (purple) to 40 K (orange). The TET rates in the simulation are a). k_{bt} = 0, k_{dt} = 0.5 ns^{-1}; b). k_{bt} = 0.2 ns^{-1}, k_{dt} = 0.5 ns^{-1}; c). k_{bt} = 0.5 ns^{-1}, k_{dt} = 0.015 ns^{-1}.

Appendix 4.4

Similar to bare CdSe quantum dot, wavefunctions of electron/hole levels of CdSe/CdS QD can be described by effective mass approximation framework.[16] Considering the electron/hole levels at conduction/valence band edge, the wavefunctions of doubly degenerate $1S_e$ electron state of the QD are:

$$\varphi_{\uparrow(\downarrow)}(\boldsymbol{r}) = \xi_e(\boldsymbol{r})|S> |\uparrow(\downarrow)> \quad \text{Eq. A4.6}$$

where $\xi_e(\boldsymbol{r})$ is the envelope function, $|S> |\uparrow(\downarrow)>$ is the Bloch function of the conduction band including the spin wavefunction. The wavefunctions of fourfold degenerate $1S_{3/2}$ hole state characterized by total angular momentum M (±3/2, ±1/2) are[71-72]:

$$\varphi_M(\boldsymbol{r}) = 2\sum_{l=0,2} R_l(\boldsymbol{r})(-1)^{M-3/2} \sum_{m+\mu=M} C(l,m,M,\mu) Y_{l,m} u_\mu \quad \text{Eq. A4.7}$$

where $R_l(\boldsymbol{r})$ is the radial function; C (l, m, M, μ) is the Wigner 3j symbol factor; $Y_{l,m}$ are spherical harmonic functions; and u_μ are the Block functions of the valence band edge:

$$u_{3/2} = \frac{1}{\sqrt{2}}(X+iY)|\uparrow>, \quad u_{-3/2} = \frac{i}{\sqrt{2}}(X-iY)|\downarrow>$$

$$u_{1/2} = \frac{i}{\sqrt{6}}[(X+iY)|\downarrow> -2Z|\uparrow>], \; u_{-1/2} = \frac{1}{\sqrt{6}}[(X-iY)|\uparrow> +2Z|\downarrow>] \quad \text{Eq. A4.8}$$

As is shown in Eq. A4.7 and A4.8, each hole wavefunction contains contribution from both $|\uparrow>$ and $|\downarrow>$ spin wavefunctions because of the strong spin-orbit coupling and coupling between angular momentums of Bloch function and envelope function.[71] The $1S_h$-$1S_e$ exciton wavefunction is:

$$\Psi(\boldsymbol{r_e}, \boldsymbol{r_h}) = \varphi_{\uparrow(\downarrow)}(\boldsymbol{r_e})\varphi_M(\boldsymbol{r_h}) \quad \text{Eq. A4.9}$$

In the presence of hexagonal lattice structure, crystal shape asymmetry and electron-hole exchange interaction, the eightfold degenerate exciton is split into 5 sublevels characterized by the exciton total angular momentum F.[16] The wavefunctions of these exciton states are:[16]

$$\Psi_{-2}(\boldsymbol{r_e},\boldsymbol{r_h}) = \Psi_{\downarrow,-\frac{3}{2}}(\boldsymbol{r_e},\boldsymbol{r_h}) = -2\xi_e(\boldsymbol{r_e})|S> |\downarrow>_e \{R_0(\boldsymbol{r_h})C\left(0,0,-\frac{3}{2},-\frac{3}{2}\right)Y_{0,0}\frac{i}{\sqrt{2}}(X -$$

$$iY)|\downarrow>_h + R_2(\boldsymbol{r_h})C\left(2,-2,-\frac{3}{2},\frac{1}{2}\right)Y_{2,-2}\frac{i}{\sqrt{6}}[(X+iY)|\downarrow>_h - 2Z|\uparrow>_h] +$$

$$R_2(\boldsymbol{r_h})C\left(2,-1,-\frac{3}{2},-\frac{1}{2}\right)Y_{2,-1}\frac{1}{\sqrt{6}}[(X-iY)|\uparrow>_h + 2Z|\downarrow>_h] +$$

$$R_2(\boldsymbol{r_h})C\left(2,0,-\frac{3}{2},-\frac{3}{2}\right)Y_{2,0}\frac{i}{\sqrt{2}}(X-iY)|\downarrow>_h\} \quad \text{Eq. A4.10a}$$

$$\Psi_2(\boldsymbol{r_e},\boldsymbol{r_h}) = \Psi_{\uparrow,\frac{3}{2}}(\boldsymbol{r_e},\boldsymbol{r_h}) = 2\xi_e(\boldsymbol{r_e})|S> |\uparrow>_e \{R_0(\boldsymbol{r_h})C\left(0,0,\frac{3}{2},\frac{3}{2}\right)Y_{0,0}\frac{1}{\sqrt{2}}(X+iY)|\uparrow>_h +$$

$$R_2(\boldsymbol{r_h})C\left(2,2,\frac{3}{2},-\frac{1}{2}\right)Y_{2,2}\frac{1}{\sqrt{6}}[(X-iY)|\uparrow>_h + 2Z|\downarrow>_h] + R_2(\boldsymbol{r_h})C\left(2,1,\frac{3}{2},\frac{1}{2}\right)Y_{2,1}\frac{i}{\sqrt{6}}[(X +$$

$$iY)|\downarrow>_h - 2Z|\uparrow>_h] + R_2(\boldsymbol{r_h})C\left(2,0,\frac{3}{2},\frac{3}{2}\right)Y_{2,0}\frac{1}{\sqrt{2}}(X+iY)|\uparrow>_h\} \quad \text{Eq. A4.10b}$$

$$\Psi_1^{U,L}(\boldsymbol{r_e},\boldsymbol{r_h}) = \mp iC^+\Psi_{\uparrow,\frac{1}{2}}(\boldsymbol{r_e},\boldsymbol{r_h}) + C^-\Psi_{\downarrow,\frac{3}{2}}(\boldsymbol{r_e},\boldsymbol{r_h}) = \pm 2iC^+\xi_e(\boldsymbol{r_e})|S> |\uparrow$$

$$>_e \left\{R_0(\boldsymbol{r_h})C\left(0,0,\frac{1}{2},\frac{1}{2}\right)Y_{0,0}\frac{i}{\sqrt{6}}[(X+iY)|\downarrow>_h - 2Z|\uparrow>_h] + R_2(\boldsymbol{r_h})C\left(2,2,\frac{1}{2},-\frac{3}{2}\right)Y_{2,2}\frac{i}{\sqrt{2}}(X -\right.$$

$$iY)|\downarrow>_h + R_2(\boldsymbol{r_h})C\left(2,1,\frac{1}{2},-\frac{1}{2}\right)Y_{2,1}\frac{1}{\sqrt{6}}[(X-iY)|\uparrow>_h + 2Z|\downarrow>_h] +$$

$$R_2(\boldsymbol{r_h})C\left(2,-1,\frac{1}{2},\frac{3}{2}\right)Y_{2,-1}\frac{1}{\sqrt{2}}(X+iY)|\uparrow>_h + R_2(\boldsymbol{r_h})C\left(2,0,\frac{1}{2},\frac{1}{2}\right)Y_{2,0}\frac{i}{\sqrt{6}}[(X+iY)|\downarrow>_h -$$

$$\left.2Z|\uparrow>_h]\right\} + 2C^-\xi_e(\boldsymbol{r_e})|S> |\downarrow>_e \{R_0(\boldsymbol{r_h})C\left(0,0,\frac{3}{2},\frac{3}{2}\right)Y_{0,0}\frac{1}{\sqrt{2}}(X+iY)|\uparrow>_h +$$

$$R_2(\boldsymbol{r_h})C\left(2,2,\frac{3}{2},-\frac{1}{2}\right)Y_{2,2}\frac{1}{\sqrt{6}}[(X-iY)|\uparrow>_h + 2Z|\downarrow>_h] + R_2(\boldsymbol{r_h})C\left(2,1,\frac{3}{2},\frac{1}{2}\right)Y_{2,1}\frac{i}{\sqrt{6}}[(X +$$

$$iY)|\downarrow>_h - 2Z|\uparrow>_h] + R_2(\boldsymbol{r_h})C\left(2,0,\frac{3}{2},\frac{3}{2}\right)Y_{2,0}\frac{1}{\sqrt{2}}(X+iY)|\uparrow>_h\} \quad \text{Eq. A4.10c}$$

$$\Psi_{-1}^{U,L}(\boldsymbol{r_e},\boldsymbol{r_h}) = \mp iC^-\Psi_{\uparrow,-\frac{3}{2}}(\boldsymbol{r_e},\boldsymbol{r_h}) + C^+\Psi_{\downarrow,-\frac{1}{2}}(\boldsymbol{r_e},\boldsymbol{r_h}) = \pm 2iC^-\xi_e(\boldsymbol{r_e})|S> |\uparrow$$

$$>_e \left\{R_0(\boldsymbol{r_h})C\left(0,0,-\tfrac{3}{2},-\tfrac{3}{2}\right)Y_{0,0}\tfrac{i}{\sqrt{2}}(X-iY)|\downarrow>_h + R_2(\boldsymbol{r_h})C\left(2,-2,-\tfrac{3}{2},\tfrac{1}{2}\right)Y_{2,-2}\tfrac{i}{\sqrt{6}}[(X+$$

$$iY)|\downarrow>_h - 2Z|\uparrow>_h] + R_2(\boldsymbol{r_h})C\left(2,-1,-\tfrac{3}{2},-\tfrac{1}{2}\right)Y_{2,-1}\tfrac{1}{\sqrt{6}}[(X-iY)|\uparrow>_h + 2Z|\downarrow>_h] +$$

$$R_2(\boldsymbol{r_h})C\left(2,0,-\tfrac{3}{2},-\tfrac{3}{2}\right)Y_{2,0}\tfrac{i}{\sqrt{2}}(X-iY)|\downarrow>_h\Big\} + 2C^{+}\xi_e(\boldsymbol{r_e})|S>|\downarrow$$

$$>_e \left\{R_0(\boldsymbol{r_h})C\left(0,0,-\tfrac{1}{2},-\tfrac{1}{2}\right)Y_{0,0}\tfrac{1}{\sqrt{6}}[(X-iY)|\uparrow>_h + 2Z|\downarrow>_h] +\right.$$

$$R_2(\boldsymbol{r_h})C\left(2,-2,-\tfrac{1}{2},\tfrac{3}{2}\right)Y_{2,-2}\tfrac{1}{\sqrt{2}}(X+iY)|\uparrow>_h + R_2(\boldsymbol{r_h})C\left(2,-1,-\tfrac{1}{2},\tfrac{1}{2}\right)Y_{2,-1}\tfrac{i}{\sqrt{6}}[(X+iY)|\downarrow$$

$$>_h - 2Z|\uparrow>_h] + R_2(\boldsymbol{r_h})C\left(2,1,-\tfrac{1}{2},-\tfrac{3}{2}\right)Y_{2,1}\tfrac{i}{\sqrt{2}}(X-iY)|\downarrow>_h +$$

$$R_2(\boldsymbol{r_h})C\left(2,0,-\tfrac{1}{2},-\tfrac{1}{2}\right)Y_{2,0}\tfrac{1}{\sqrt{6}}[(X-iY)|\uparrow>_h + 2Z|\downarrow>_h]\Big\} \quad \text{Eq. A4.10d}$$

$$\Psi_0^{U,L}(\boldsymbol{r_e},\boldsymbol{r_h}) = \tfrac{1}{\sqrt{2}}\left[\mp i\Psi_{\uparrow,-\frac{1}{2}}(\boldsymbol{r_e},\boldsymbol{r_h}) + \Psi_{\downarrow,\frac{1}{2}}(\boldsymbol{r_e},\boldsymbol{r_h})\right] = \mp\sqrt{2}i\xi_e(\boldsymbol{r_e})|S>|\uparrow$$

$$>_e \left\{R_0(\boldsymbol{r_h})C\left(0,0,-\tfrac{1}{2},-\tfrac{1}{2}\right)Y_{0,0}\tfrac{1}{\sqrt{6}}[(X-iY)|\uparrow>_h + 2Z|\downarrow>_h] +\right.$$

$$R_2(\boldsymbol{r_h})C\left(2,-2,-\tfrac{1}{2},\tfrac{3}{2}\right)Y_{2,-2}\tfrac{1}{\sqrt{2}}(X+iY)|\uparrow>_h + R_2(\boldsymbol{r_h})C\left(2,-1,-\tfrac{1}{2},\tfrac{1}{2}\right)Y_{2,-1}\tfrac{i}{\sqrt{6}}[(X+iY)|\downarrow$$

$$>_h - 2Z|\uparrow>_h] + R_2(\boldsymbol{r_h})C\left(2,1,-\tfrac{1}{2},-\tfrac{3}{2}\right)Y_{2,1}\tfrac{i}{\sqrt{2}}(X-iY)|\downarrow>_h +$$

$$R_2(\boldsymbol{r_h})C\left(2,0,-\tfrac{1}{2},-\tfrac{1}{2}\right)Y_{2,0}\tfrac{1}{\sqrt{6}}[(X-iY)|\uparrow>_h + 2Z|\downarrow>_h]\Big\} - \sqrt{2}\xi_e(\boldsymbol{r_e})|S>|\downarrow$$

$$>_e \left\{R_0(\boldsymbol{r_h})C\left(0,0,\tfrac{1}{2},\tfrac{1}{2}\right)Y_{0,0}\tfrac{i}{\sqrt{6}}[(X+iY)|\downarrow>_h - 2Z|\uparrow>_h] + R_2(\boldsymbol{r_h})C\left(2,2,\tfrac{1}{2},-\tfrac{3}{2}\right)Y_{2,2}\tfrac{i}{\sqrt{2}}(X-\right.$$

$$iY)|\downarrow>_h + R_2(\boldsymbol{r_h})C\left(2,1,\tfrac{1}{2},-\tfrac{1}{2}\right)Y_{2,1}\tfrac{1}{\sqrt{6}}[(X-iY)|\uparrow>_h + 2Z|\downarrow>_h] +$$

$$R_2(\boldsymbol{r_h})C\left(2,-1,\tfrac{1}{2},\tfrac{3}{2}\right)Y_{2,-1}\tfrac{1}{\sqrt{2}}(X+iY)|\uparrow>_h + R_2(\boldsymbol{r_h})C\left(2,0,\tfrac{1}{2},\tfrac{1}{2}\right)Y_{2,0}\tfrac{i}{\sqrt{6}}[(X+iY)|\downarrow>_h -$$

$$\left.2Z|\uparrow>_h]\right\} \quad \text{Eq. A4.10e}$$

where:

$$C^{\pm} = \sqrt{\frac{\sqrt{f^2+d} \pm f}{2\sqrt{f^2+d}}} \quad \text{Eq. A4.10f}$$

$$f = (-2\eta + \Delta)/2 \quad \text{Eq. A4.10g}$$

$$d = 3\eta^2 \quad \text{Eq. A4.10h}$$

$$\eta = \left(\frac{a_{ex}}{a}\right)^3 \hbar\omega_{ST}\chi(\beta) \quad \text{Eq. A4.10i}$$

Δ is the energy splitting of degenerate hole levels due to asymmetry of QD shape and lattice; $\hbar\omega_{ST}$ describes the energy splitting of exciton states due to electron-hole exchange interaction; a_{ex} is the bulk exciton Bohr radius; a is the size of the QD; $\chi(\beta)$ is the dimensionless function in terms of electron/hole radial wavefunctions.[16] Note that antisymmetrizing operator to convert product of electron and hole wavefunctions to Slater determinant should be added to Eq. A4.9 and Eq. A4.10a-e but was not shown in the expressions for simplification. It is obvious from Equation Eq. A4.10a-e that all exciton states in CdSe/CdS QDs can be written is the form of Eq. 4.9 in the main text, which consist of components with the same and opposite electron/hole spin projections.

4.4 Reference

1. Majumdar, P.; Nomula, R.; Zhao, J., Activatable triplet photosensitizers: magic bullets for targeted photodynamic therapy. *J. Mater. Chem. C* **2014,** *2* (30), 5982-5997.
2. Li, X. S.; Kolemen, S.; Yoon, J.; Akkaya, E. U., Activatable Photosensitizers: Agents for Selective Photodynamic Therapy. *Adv. Funct. Mater.* **2017,** *27* (5), 1604053.
3. Islangulov, R. R.; Kozlov, D. V.; Castellano, F. N., Low power upconversion using MLCT sensitizers. *Chem. Commun.* **2005,** (30), 3776-3778.
4. Zhao, W.; Castellano, F. N., Upconverted Emission from Pyrene and Di-tert-butylpyrene Using Ir(ppy)3 as Triplet Sensitizer. *J. Phys. Chem. A* **2006,** *110* (40), 11440-11445.
5. Singh-Rachford, T. N.; Castellano, F. N., Photon upconversion based on sensitized triplet–triplet annihilation. *Coord. Chem. Rev.* **2010,** *254* (21-22), 2560-2573.
6. Kim, T.; McCarver, S. J.; Lee, C.; MacMillan, D. W. C., Sulfonamidation of Aryl and Heteroaryl Halides through Photosensitized Nickel Catalysis. *Angew. Chem. Int. Ed.* **2018,** *57* (13), 3488-3492.
7. Strieth-Kalthoff, F.; James, M. J.; Teders, M.; Pitzer, L.; Glorius, F., Energy transfer catalysis mediated by visible light: principles, applications, directions. *Chem. Soc. Rev.* **2018,** *47* (19), 7190-7202.
8. Luo, X.; Lai, R.; Li, Y.; Han, Y.; Liang, G.; Liu, X.; Ding, T.; Wang, J.; Wu, K., Triplet Energy Transfer from CsPbBr3 Nanocrystals Enabled by Quantum Confinement. *J. Am. Chem. Soc.* **2019,** *141* (10), 4186-4190.
9. Mongin, C.; Garakyaraghi, S.; Razgoniaeva, N.; Zamkov, M.; Castellano, F. N., Direct observation of triplet energy transfer from semiconductor nanocrystals. *Science* **2016,** *351* (6271), 369-72.
10. Mahboub, M.; Maghsoudiganjeh, H.; Pham, A. M.; Huang, Z. Y.; Tang, M. L., Triplet Energy Transfer from PbS(Se) Nanocrystals to Rubrene: the Relationship between the Upconversion Quantum Yield and Size. *Adv. Funct. Mater.* **2016,** *26* (33), 6091-6097.
11. Gray, V.; Allardice, J. R.; Zhang, Z.; Dowland, S.; Xiao, J.; Petty, A. J.; Anthony, J. E.; Greenham, N. C.; Rao, A., Direct vs Delayed Triplet Energy Transfer from Organic Semiconductors to Quantum Dots and Implications for Luminescent Harvesting of Triplet Excitons. *ACS Nano* **2020,** *14* (4), 4224-4234.
12. Yu, W. W.; Qu, L. H.; Guo, W. Z.; Peng, X. G., Experimental determination of the extinction coefficient of CdTe, CdSe, and CdS nanocrystals. *Chem. Mater.* **2003,** *15* (14), 2854-2860.
13. Cademartiri, L.; Montanari, E.; Calestani, G.; Migliori, A.; Guagliardi, A.; Ozin, G. A., Size-Dependent Extinction Coefficients of PbS Quantum Dots. *J. Am. Chem. Soc.* **2006,** *128* (31), 10337-10346.
14. Ma, Y.; Zhang, Y.; Yu, W. W., Near infrared emitting quantum dots: synthesis, luminescence properties and applications. *J. Mater. Chem. C* **2019,** *7* (44), 13662-13679.
15. Hudson, M. H.; Chen, M.; Kamysbayev, V.; Janke, E. M.; Lan, X.; Allan, G.; Delerue, C.; Lee, B.; Guyot-Sionnest, P.; Talapin, D. V., Conduction Band Fine Structure in Colloidal HgTe Quantum Dots. *ACS Nano* **2018,** *12* (9), 9397-9404.
16. Efros, A. L.; Rosen, M.; Kuno, M.; Nirmal, M.; Norris, D. J.; Bawendi, M., Band-edge exciton in quantum dots of semiconductors with a degenerate valence band: Dark and bright exciton states. *Phys. Rev. B* **1996,** *54* (7), 4843-4856.
17. Scholes, G. D.; Rumbles, G., Excitons in nanoscale systems. *Nat. Mater.* **2006,** *5* (9), 683-96.
18. Piland, G. B.; Huang, Z. Y.; Tang, M. L.; Bardeen, C. J., Dynamics of Energy Transfer from

CdSe Nanocrystals to Triplet States of Anthracene Ligand Molecules. *J. Phys. Chem. C* **2016,** *120* (11), 5883-5889.
19. Xu, Z.; Jin, T.; Huang, Y.; Mulla, K.; Evangelista, F. A.; Egap, E.; Lian, T., Direct triplet sensitization of oligothiophene by quantum dots. *Chem. Sci.* **2019,** *10* (24), 6120-6124.
20. Huang, Z.; Xu, Z.; Mahboub, M.; Li, X.; Taylor, J. W.; Harman, W. H.; Lian, T.; Tang, M. L., PbS/CdS Core-Shell Quantum Dots Suppress Charge Transfer and Enhance Triplet Transfer. *Angew. Chem. Int. Ed.* **2017,** *56* (52), 16583-16587.
21. Lai, R.; Sang, Y.; Zhao, Y.; Wu, K., Triplet Sensitization and Photon Upconversion Using InP-Based Quantum Dots. *J. Am. Chem. Soc.* **2020,** *142* (47), 19825-19829.
22. Gray, V.; Xia, P.; Huang, Z.; Moses, E.; Fast, A.; Fishman, D. A.; Vullev, V. I.; Abrahamsson, M.; Moth-Poulsen, K.; Lee Tang, M., CdS/ZnS core-shell nanocrystal photosensitizers for visible to UV upconversion. *Chem. Sci.* **2017,** *8* (8), 5488-5496.
23. Okumura, K.; Mase, K.; Yanai, N.; Kimizuka, N., Employing Core-Shell Quantum Dots as Triplet Sensitizers for Photon Upconversion. *Chem. Eur. J.* **2016,** *22* (23), 7721-6.
24. Wu, M.; Congreve, D. N.; Wilson, M. W. B.; Jean, J.; Geva, N.; Welborn, M.; Van Voorhis, T.; Bulović, V.; Bawendi, M. G.; Baldo, M. A., Solid-state infrared-to-visible upconversion sensitized by colloidal nanocrystals. *Nat. Photon.* **2015,** *10*, 31-34.
25. Okumura, K.; Yanai, N.; Kimizuka, N., Visible-to-UV Photon Upconversion Sensitized by Lead Halide Perovskite Nanocrystals. *Chem. Lett.* **2019,** *48* (11), 1347-1350.
26. Xia, P.; Raulerson, E. K.; Coleman, D.; Gerke, C. S.; Mangolini, L.; Tang, M. L.; Roberts, S. T., Achieving spin-triplet exciton transfer between silicon and molecular acceptors for photon upconversion. *Nat. Chem.* **2020,** *12* (2), 137-144.
27. Jiang, Y.; Weiss, E. A., Colloidal Quantum Dots as Photocatalysts for Triplet Excited State Reactions of Organic Molecules. *J. Am. Chem. Soc.* **2020,** *142* (36), 15219-15229.
28. Jiang, Y.; Wang, C.; Rogers, C. R.; Kodaimati, M. S.; Weiss, E. A., Regio- and diastereoselective intermolecular [2+2] cycloadditions photocatalysed by quantum dots. *Nat. Chem.* **2019,** *11* (11), 1034-1040.
29. Xu, Z.; Huang, Z.; Jin, T.; Lian, T.; Tang, M. L., Mechanistic Understanding and Rational Design of Quantum Dot/Mediator Interfaces for Efficient Photon Upconversion. *Acc. Chem. Res.* **2021,** *54* (1), 70-80.
30. Li, X.; Huang, Z.; Zavala, R.; Tang, M. L., Distance-Dependent Triplet Energy Transfer between CdSe Nanocrystals and Surface Bound Anthracene. *J. Phys. Chem. Lett.* **2016,** *7* (11), 1955-9.
31. Luo, X.; Han, Y.; Chen, Z.; Li, Y.; Liang, G.; Liu, X.; Ding, T.; Nie, C.; Wang, M.; Castellano, F. N.; Wu, K., Mechanisms of triplet energy transfer across the inorganic nanocrystal/organic molecule interface. *Nat. Commun.* **2020,** *11* (1), 28.
32. Harcourt, R. D.; Scholes, G. D.; Ghiggino, K. P., Rate expressions for excitation transfer. II. Electronic considerations of direct and through–configuration exciton resonance interactions. *J. Chem. Phys.* **1994,** *101* (12), 10521-10525.
33. Bai, S.; Zhang, P.; Beratan, D. N., Predicting Dexter Energy Transfer Interactions from Molecular Orbital Overlaps. *J. Phys. Chem. C* **2020,** *124* (35), 18956-18960.
34. Luo, X.; Liang, G.; Han, Y.; Li, Y.; Ding, T.; He, S.; Liu, X.; Wu, K., Triplet Energy Transfer from Perovskite Nanocrystals Mediated by Electron Transfer. *J. Am. Chem. Soc.* **2020,** *142* (25), 11270-11278.
35. Lai, R.; Liu, Y.; Luo, X.; Chen, L.; Han, Y.; Lv, M.; Liang, G.; Chen, J.; Zhang, C.; Di, D.; Scholes, G. D.; Castellano, F. N.; Wu, K., Shallow distance-dependent triplet energy migration

mediated by endothermic charge-transfer. *Nat. Commun.* **2021,** *12* (1), 1532.
36. Becker, M. A.; Vaxenburg, R.; Nedelcu, G.; Sercel, P. C.; Shabaev, A.; Mehl, M. J.; Michopoulos, J. G.; Lambrakos, S. G.; Bernstein, N.; Lyons, J. L.; Stoferle, T.; Mahrt, R. F.; Kovalenko, M. V.; Norris, D. J.; Raino, G.; Efros, A. L., Bright triplet excitons in caesium lead halide perovskites. *Nature* **2018,** *553* (7687), 189-193.
37. An, J. M.; Franceschetti, A.; Zunger, A., The excitonic exchange splitting and radiative lifetime in PbSe quantum dots. *Nano Lett.* **2007,** *7* (7), 2129-2135.
38. Kane, R. S.; Cohen, R. E.; Silbey, R., Theoretical Study of the Electronic Structure of PbS Nanoclusters. *J Phys Chem-Us* **1996,** *100* (19), 7928-7932.
39. Shabaev, A.; Mehl, M. J.; Efros, A. L., Energy band structure of CuInS2 and optical spectra of CuInS2 nanocrystals. *Phys. Rev. B* **2015,** *92* (3), 035431.
40. Sercel, P. C.; Efros, A. L., Band-Edge Exciton in CdSe and Other II-VI and III-V Compound Semiconductor Nanocrystals - Revisited. *Nano Lett.* **2018,** *18* (7), 4061-4068.
41. Hanifi, D. A.; Bronstein, N. D.; Koscher, B. A.; Nett, Z.; Swabeck, J. K.; Takano, K.; Schwartzberg, A. M.; Maserati, L.; Vandewal, K.; van de Burgt, Y.; Salleo, A.; Alivisatos, A. P., Redefining near-unity luminescence in quantum dots with photothermal threshold quantum yield. *Science* **2019,** *363* (6432), 1199.
42. Jin, T.; Lian, T., Trap state mediated triplet energy transfer from CdSe quantum dots to molecular acceptors. *J. Chem. Phys.* **2020,** *153* (7), 074703.
43. Ortner, G.; Schwab, M.; Bayer, M.; Pässler, R.; Fafard, S.; Wasilewski, Z.; Hawrylak, P.; Forchel, A., Temperature dependence of the excitonic band gap in InxGa1-xAs/GaAs self-assembled quantum dots. *Phys. Rev. B* **2005,** *72* (8), 085328.
44. Varshni, Y. P., Temperature dependence of the energy gap in semiconductors. *Physica* **1967,** *34* (1), 149-154.
45. Joshi, A.; Narsingi, K. Y.; Manasreh, M. O.; Davis, E. A.; Weaver, B. D., Temperature dependence of the band gap of colloidal CdSe ⁄ ZnS core/shell nanocrystals embedded into an ultraviolet curable resin. *Applied Physics Letters* **2006,** *89* (13), 131907.
46. Zhu, H.; Song, N.; Rodríguez-Córdoba, W.; Lian, T., Wave Function Engineering for Efficient Extraction of up to Nineteen Electrons from One CdSe/CdS Quasi-Type II Quantum Dot. *J. Am. Chem. Soc.* **2012,** *134* (9), 4250-4257.
47. Mack, T. G.; Jethi, L.; Kambhampati, P., Temperature Dependence of Emission Line Widths from Semiconductor Nanocrystals Reveals Vibronic Contributions to Line Broadening Processes. *J. Phys. Chem. C* **2017,** *121* (51), 28537-28545.
48. O'Donnell, K. P.; Chen, X., Temperature dependence of semiconductor band gaps. *Appl. Phys. Lett.* **1991,** *58* (25), 2924-2926.
49. Labeau, O.; Tamarat, P.; Lounis, B., Temperature dependence of the luminescence lifetime of single CdSe/ZnS quantum dots. *Phys. Rev. Lett.* **2003,** *90* (25 Pt 1), 257404.
50. de Mello Donegá, C.; Bode, M.; Meijerink, A., Size- and temperature-dependence of exciton lifetimes in CdSe quantum dots. *Phys. Rev. B* **2006,** *74* (8), 085320.
51. Nirmal, M.; Norris, D. J.; Kuno, M.; Bawendi, M. G.; Efros, A. L.; Rosen, M., Observation of the "Dark exciton" in CdSe quantum dots. *Phys. Rev. Lett.* **1995,** *75* (20), 3728-3731.
52. Gaponenko, M. S.; Lutich, A. A.; Tolstik, N. A.; Onushchenko, A. A.; Malyarevich, A. M.; Petrov, E. P.; Yumashev, K. V., Temperature-dependent photoluminescence of PbS quantum dots in glass: Evidence of exciton state splitting and carrier trapping. *Phys. Rev. B* **2010,** *82* (12), 125320.
53. Jones, M.; Lo, S. S.; Scholes, G. D., Quantitative modeling of the role of surface traps in

CdSe/CdS/ZnS nanocrystal photoluminescence decay dynamics. *Proc. Natl. Acad. Sci.* **2009,** *106* (9), 3011-6.
54. Jones, M.; Lo, S. S.; Scholes, G. D., Signatures of Exciton Dynamics and Carrier Trapping in the Time-Resolved Photoluminescence of Colloidal CdSe Nanocrystals. *J. Phys. Chem. C* **2009,** *113* (43), 18632-18642.
55. Zatryb, G.; Podhorodecki, A.; Misiewicz, J.; Cardin, J.; Gourbilleau, F., On the nature of the stretched exponential photoluminescence decay for silicon nanocrystals. *Nanoscale Res. Lett.* **2011,** *6* (1), 106-106.
56. Crooker, S. A.; Barrick, T.; Hollingsworth, J. A.; Klimov, V. I., Multiple temperature regimes of radiative decay in CdSe nanocrystal quantum dots: Intrinsic limits to the dark-exciton lifetime. *Appl. Phys. Lett.* **2003,** *82* (17), 2793-2795.
57. Kim, D.; Okazaki, K.; Nakayama, M., Temperature dependence of the energy transfer of exciton states in bilayer structures of CdSe/ZnS quantum dots. *Phys. Rev. B* **2009,** *80* (4), 045322.
58. Jin, T.; Uhlikova, N.; Xu, Z.; Zhu, Y.; Huang, Y.; Egap, E.; Lian, T., Enhanced triplet state generation through radical pair intermediates in BODIPY-quantum dot complexes. *J. Chem. Phys.* **2019,** *151* (24), 241101.
59. L. J. Dexter, D., A Theory of Sensitized Luminescence in Solid. *J. Chem. Phys.* **1953,** *21*, 836-850.
60. Lin, S. H., On the Theory of Non-Radiative Transfer of Electronic Excitation. *Proc. R. Soc. Lond. A.* **1973,** *335* (1600), 51.
61. Sasaki, Y.; Amemori, S.; Kouno, H.; Yanai, N.; Kimizuka, N., Near infrared-to-blue photon upconversion by exploiting direct S–T absorption of a molecular sensitizer. *J. Mater. Chem. C* **2017,** *5* (21), 5063-5067.
62. Sasaki, Y.; Oshikawa, M.; Bharmoria, P.; Kouno, H.; Hayashi-Takagi, A.; Sato, M.; Ajioka, I.; Yanai, N.; Kimizuka, N., Near-Infrared Optogenetic Genome Engineering Based on Photon-Upconversion Hydrogels. *Angew. Chem. Int. Ed.* **2019,** *58* (49), 17827-17833.
63. Wei, Y.; Zheng, M.; Chen, L.; Zhou, X.; Liu, S., Near-infrared to violet triplet–triplet annihilation fluorescence upconversion of Os(ii) complexes by strong spin-forbidden transition. *Dalton Trans.* **2019,** *48* (31), 11763-11771.
64. Amemori, S.; Sasaki, Y.; Yanai, N.; Kimizuka, N., Near-Infrared-to-Visible Photon Upconversion Sensitized by a Metal Complex with Spin-Forbidden yet Strong S0–T1 Absorption. *J. Am. Chem. Soc.* **2016,** *138* (28), 8702-8705.
65. Scholes, G. D.; Harcourt, R. D.; Ghiggino, K. P., Rate expressions for excitation transfer. III. An ab initio study of electronic factors in excitation transfer and exciton resonance interactions. *J. Chem. Phys.* **1995,** *102* (24), 9574-9581.
66. Grimaldi, G.; Geuchies, J. J.; van der Stam, W.; du Fosse, I.; Brynjarsson, B.; Kirkwood, N.; Kinge, S.; Siebbeles, L. D. A.; Houtepen, A. J., Spectroscopic Evidence for the Contribution of Holes to the Bleach of Cd-Chalcogenide Quantum Dots. *Nano Lett* **2019,** *19* (5), 3002-3010.
67. Shabaev, A.; Rodina, A. V.; Efros, A. L., Fine structure of the band-edge excitons and trions in CdSe/CdS core/shell nanocrystals. *Physical Review B* **2012,** *86* (20), 205311.
68. Klimov, V. I., Spectral and dynamical properties of multiexcitons in semiconductor nanocrystals. *Annu Rev Phys Chem* **2007,** *58* (1), 635-73.
69. Klimov, V. I.; Mikhailovsky, A. A.; Xu, S.; Malko, A.; Hollingsworth, J. A.; Leatherdale, C. A.; Eisler, H. J.; Bawendi, M. G., Optical Gain and Stimulated Emission in Nanocrystal Quantum Dots. *Science* **2000,** *290* (5490), 314-317.
70. Kim, J.; Wong, C. Y.; Scholes, G. D., Exciton fine structure and spin relaxation in

semiconductor colloidal quantum dots. *Acc Chem Res* **2009,** *42* (8), 1037-46.
71. Sercel, P. C.; Vahala, K. J., Analytical formalism for determining quantum-wire and quantum-dot band structure in the multiband envelope-function approximation. *Physical Review B* **1990,** *42* (6), 3690-3710.
72. Efros, A. L., Luminescence polarization of CdSe microcrystals. *Physical Review B* **1992,** *46* (12), 7448-7458.

Chapter 5. Trap State Mediated Triplet Energy Transfer from CdSe Quantum Dots to Molecular Acceptors

5.1 Introduction

Photon up-conversion has found promising application in solar energy harvesting and in biological imaging.[1-3] In triplet-triplet annihilation (TTA) based photon up-conversion systems,[4-6] triplet energy transfer (TET) from a sensitizer to a triplet acceptor is a key efficiency-limiting-step and has been extensively studied in the past two decades, especially in the molecular donor-acceptor complexes.[7-11] Recently, colloidal semiconductor nanocrystal sensitizer-organic molecule acceptor hybrid structures have received intense interest in TTA applications because of the large extinction coefficient,[12-13] broad absorption range[14] and small bright/dark state energy difference[15-16] of the nanocrystal sensitizers compared to traditional organometallic compounds. During the past five years, TET in hybrid structures using CdSe,[17-19] PbS[20-25] and perovskite[26-28] quantum dots (QDs) has been reported, and TET pathways via direct Dexter energy transfer and sequential charge transfer have been identified.[18, 29-35]

Unlike molecular triplet sensitizers, most nanocrystals have inherent surface defects that lead to the presence of trap states below the bandgap. For nanocrystals with low photoluminescence quantum yields (PLQYs), trap states play an important, often dominating, role in the dynamics of excitons.[36-37] Despite the prevalence of trap states, their roles in the TET process in QD/acceptor complexes have not been explicitly discussed until recently and remain poorly understood.[38-40]

While some studies have revealed that passivation of surface defects in CdSe or CdS QDs by inorganic shell growth enhances TTA efficiencies,[41-42] other studies of $CuInS_2$ QDs,[38] amine capped CdSe QDs[39] and PbS QDs[43] suggest that trap states could also undergo TET. A lack of clear understanding of the roles of defects in QDs can be attributed in part to a poor understanding of the nature of trap states and their energetics and to a lack of clear spectroscopic signatures of trapped excitons.[37, 44-46]

Herein, we report a detailed mechanistic study of TET from trap states in phosphonic acid capped CdSe QDs to 9-anthracene carboxylic acid (ACA) acceptors with transient absorption spectroscopy (TA) and time-resolved photoluminescence (TRPL). We show that trap states in CdSe QD have a broad distribution of energies. Upon adsorption of ACA, both band edge and trap excitons undergo direct TET to form ACA triplet state (^{3}ACA*), as shown in Figure 5.1.[47-48] Using TA spectroscopy and TRPL, we directly measure the TET rates and efficiencies from both the band edge exciton and trap exciton states. We discuss the dependence of these TET rates and efficiencies on the energy of the excitons and the relative contributions of both band edge and trap excitons to the overall TET process in CdSe-ACA complexes.

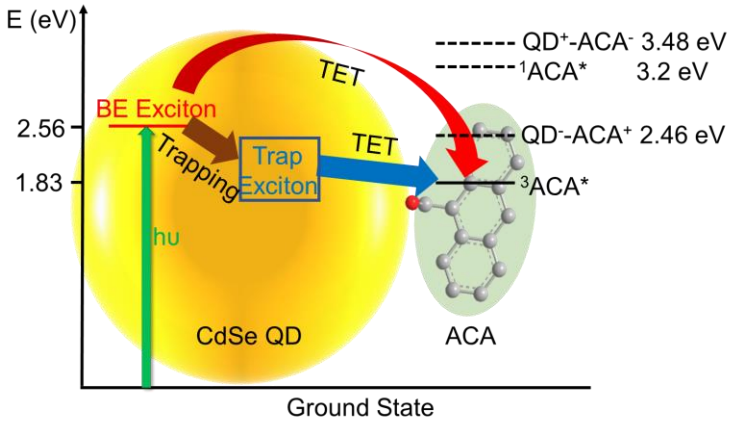

Figure 5.1: Photophysical processes (arrows) and energetics of relevant states (solid lines) in CdSe-ACA complexes. QD band edge (BE) excitons can undergo direct triplet energy transfer

(TET) to ACA (red arrow) to form ACA triplet excited state (^{3}ACA*) or rapid trapping to form trap excitons (black arrow) followed by TET to ACA (blue arrow). The energetics of states, including those not involved in TET (dashed lines), are calculated from experimental results and from Ref. 41-42.

5.2 Results and discussion

5.2.1 Steady state absorption and photoluminescence spectra of CdSe QD and CdSe QD-ACA

CdSe QDs with phosphonic acid ligand were synthesized according to previous literature procedures and further details can be found in Section 2.1.3.[49] As shown in Figure 5.2a, the $1S_{3/2}$-$1S_e$ absorption peak of the QD is centered at 2.56 eV in the UV-vis absorption spectrum.[50] QD-9-ACA complexes were prepared by ultrasonicating excess ACA powder in the hexane solution of QD, followed by filtering out undissolved ACA powder. The UV-vis absorption spectrum of the obtained CdSe-ACA complex solution (Figure 5.2a) shows a progression of ACA absorption peaks centered at 3.78 eV, 3.60 eV, 3.42 eV and 3.24 eV respectively, in addition to the absorption of the QD. The latter shows negligible shift after the adsorption of ACA. From the UV-vis spectrum, the ratio of the total ACA molecules, including bound to QD or free in solution, to QDs is estimated to be 5.1:1.0.

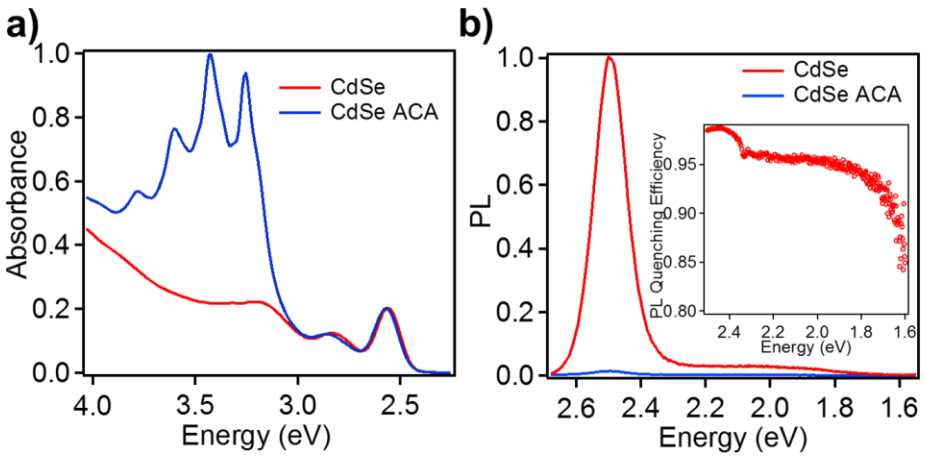

Figure 5.2: Quenching of band edge and trap exciton emission in QD-ACA complexes. a). UV-vis absorption spectra of free CdSe QD (red) and CdSe-ACA complex (blue). b). Steady state PL spectra of free CdSe QD (red) and CdSe-ACA complex (blue). Inset: PL quenching efficiency of QD-ACA as a function emission energy.

Figure 5.2b shows the steady state photoluminescence (PL) spectra of free CdSe QDs and CdSe-ACA complexes. The free CdSe QD PL spectrum mainly consists of the band edge exciton emission peak centered at 2.49 eV and a broad trap state emission extending from the band edge to 1.6 eV. The width of latter has been attributed to the wide distribution of trap state energy and/or the strong electron- phonon coupling of trap state transition.[44, 51] As will be described below, our TRPL results are more consistent with a model in which the width is dominated by the distribution of trap state energies. Within this model, the PL emission wavelength/energy represents approximately the corresponding exciton state energy. Coumarin 153 was applied as standard for determination of CdSe QD PL quantum yield.[52] CdSe QD and Coumarin 153 were dissolved in hexane and ethanol, respectively. A series of CdSe and Coumarin 153 solution with absorbance of 0.2, 0.4, 0.6, 0.8 at 400 nm were prepared. Steady state PL spectra were collected for these solutions, and integrated PL intensities were calculated and plotted as function of absorbance, as

shown in Figure 5.3. Quantum yield of CdSe QD was determined as:

$$\Phi_{QD} = \Phi_{Coumarin} \frac{Grad_{QD}}{Grad_{Coumarin}} \left(\frac{\eta_{hexane}}{\eta_{ethanol}}\right)^2 = (11.7 \pm 0.7)\ \% \qquad \text{Eq. 5.1}$$

where Φ, Grad and η are the quantum yield, gradient or slope of the PL vs. absorbance graph and refractive index of the solvent, respectively. Upon the adsorption of excess ACA, there is a dramatic quenching of both the band edge and trap state exciton emission, which is consistent with a previous report of TET from both band edge and trap exciton states in amine capped CdSe QDs/ACA complexes.[39] Interestingly, the PL quenching efficiency (shown in the inset of Figure 5.2b) decreases from 98% to 84% with decreasing emission energy, indicating that the TET rate and efficiency are dependent on exciton energy for both band edge and trapped excitons.

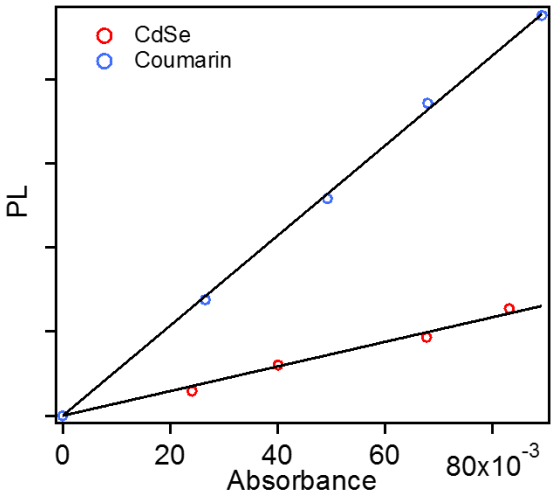

Figure 5.3: Integrated photoluminescence of free CdSe QD and Coumarin 153 as a function of absorbance. The wavelength of excitation light is 400 nm.

5.2.2 Transient absorption spectra of CdSe QD and CdSe QD-ACA

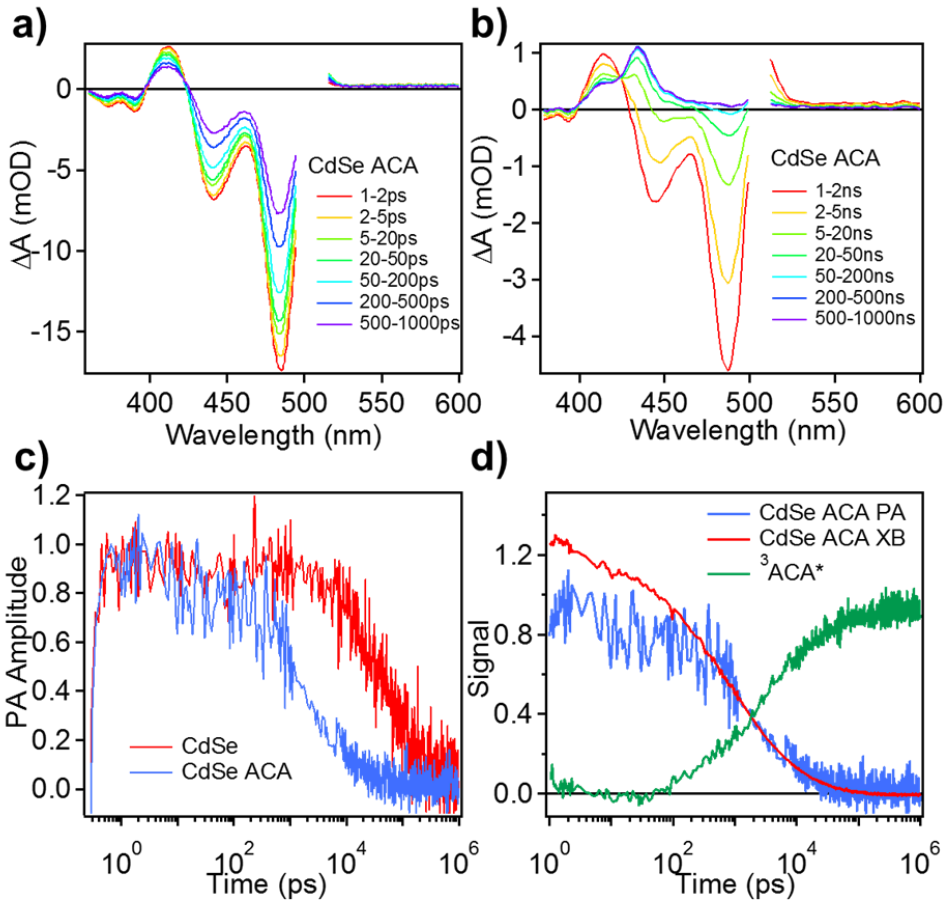

Figure 5.4: TA spectra and kinetics of CdSe-ACA with pump pulse wavelength of 500 nm. a). TA spectra of CdSe-ACA in delay time window of 1 ps – 1 ns. b). TA spectra of CdSe-ACA in delay time window of 1 ns - 1μs. c). Comparison of PA signal kinetics of free CdSe QD (red) and CdSe-ACA complex (blue) in time range of 0.1 ps – 1 μs. The kinetics were obtained by averaging kinetics of the PA band from 530 nm to 600 nm. d). Comparison of XB signal decay (red), PA signal decay (blue) and ^{3}ACA* signal growth (green) of CdSe-ACA in delay time window of 1 ps – 1 μs. The XB kinetics was extracted from kinetics at 485 nm. The kinetics of ^{3}ACA* signal was obtained from kinetics at 434 nm with subtraction of the QD signal contribution.

To provide direct evidence of TET to ACA and the participation of trap states, we measured TA spectra of CdSe-ACA complexes (Figure 5.4a and b) and free CdSe QDs (Figure 5.5a and b)

with selective excitation of the QD at 500 nm. The TA spectra of free QDs (Figure 5.5a &b) show two main QD features: a 1S exciton bleach (XB) centered at 485 nm, caused by the state filling of conduction band 1S electron level, and a much smaller broad photoinduced absorption (PA) band ranging from 530 nm to 600 nm, attributed to the absorption of trapped holes.[53-55] This assignment is further supported by comparison of the PA and XB signals in QD and QD-benzoquinone complexes. In order to confirm whether the PA signal in TA spectra of CdSe QD is due to electron or hole transition, we compare the TA spectra of free CdSe QD (Figure 5.5a &b) and CdSe-benzoquinone (CdSe-BQ) complexes (Figure 5.5c), in which BQ is the electron acceptor for CdSe.[56] Within the first 10 ps, the XB decay in CdSe-BQ complexes is much faster than free CdSe QDs (Figure 5.5d**)**, QD, which suggests fast electron transfer from CdSe to BQ, while there is negligible change in PA signal kinetics (Figure 5.5e**)**. From 10 ps to 1 ns, the PA decay in CdSe-BQ complexes is much faster than free QDs, which can be attributed mainly to the charge recombination processes following the fast electron transfer to BQ (> 80% completed within 10 ps). The results suggest that PA signal in CdSe can be attributed to hole transitions. Because of the low quantum yield of CdSe QDs due to dominating hole trap states,[57-58] the PA signal can be assigned to trapped hole absorptions, which is consistent with previous reports.[55-56] As a result, the decay of the PA signal of free QDs, overlapping with the XB kinetics from 1 ns to 1 μs (shown in Figure 5.5f), mainly reflects the kinetics of charge recombination of trapped hole and CB edge electron. The fast growth of the PA signal suggests a fast hole trapping process (within 1 ps). Because there is no fast decay component of XB within 1 ns in free CdSe QD (Figure 5.5a & c), the electron trap states can be neglected, and the trap states are mainly due to trapped holes, which is consistent with previous reports.[36, 57-58] Because of much faster hole trapping than band edge exciton radiative decay rate, for QDs with hole traps, the band edge exciton decays by hole trapping

to form trap excitons, and band edge emission comes from small percentage of QDs (~ 11%) with negligible hole traps.[59]

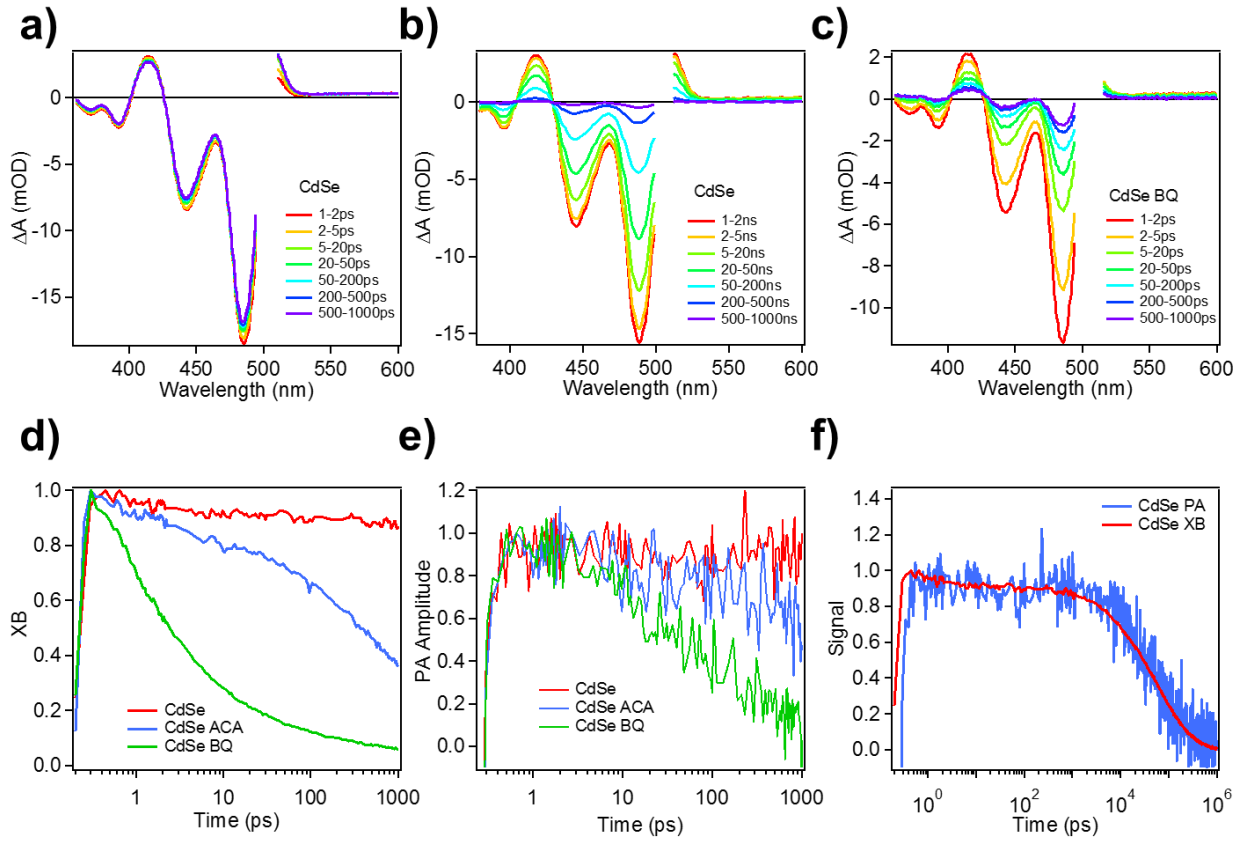

Figure 5.5: Assignment of PA signal in TA spectra of CdSe QD. a) and b). TA spectra of free CdSe QD in delay time window of a). 1 ps – 1 ns; b). 1 ns – 1 μs. c). TA spectra of CdSe-BQ complex in delay time window of 1 ps – 1 ns. d) Comparison of XB kinetics of free CdSe QD (red), CdSe-BQ complex (green) and CdSe-ACA complex (blue) in delay time window of 1 ps- 1 ns. The XB kinetics was extracted from kinetics at 485 nm in TA spectra. e). Comparison of PA kinetics of free CdSe QD (red), CdSe-BQ complex (green) and CdSe-ACA complex (blue) in the same delay time window. The PA kinetics was obtained by averaging kinetics of the PA band from 530 nm to 600 nm. f). Comparison of XB (red) and PA (blue) kinetics of free CdSe QD in delay time window of 1 ps – 1 μs.

In the delay time range of 1 - 100 ps, the TA spectra of the QD-ACA complex show negligible spectral shape change (Figure 5.4a), a similar PA signal decay (Figure 5.4c**),** and a faster XB decay **(**Figure 5.5d**)** compared to the free QD sample. Therefore, the faster decay of XB signal in CdSe-ACA complexes at this time range can only be attributed to electron trapping in the QD induced by ACA adsorption. In the time range of 100 ps – 1 μs, the TA spectra of the complex show a growth of long-lived ^{3}ACA* T_1->T_n absorption signal from 400 nm to 480 nm (Figure 5.4b**)**, indicating the presence of TET from the CdSe QD to ACA. Because there is no spectral signal of ACA cation or anion radicals observed in TA spectra in the time range of 1 ps – 1 μs, electron or hole transfer from QD to ACA can be excluded, and ^{3}ACA* is formed through one-step (direct) triplet energy transfer from the QD instead of through sequential charge transfer. Comparison of TA kinetics show that both XB and PA signals decay faster in QD-ACA complexes than free QDs (Figure 5.4c, and Figure 5.5d and Figure 5.4d), and the kinetics of QD XB and PA signal decay and ^{3}ACA* signal growth in QD-ACA complexes agree well with each other in this time range **(**Figure 5.4d**)**. The agreement of the kinetics of conduction band edge electron (XB), trapped hole (PA) and ^{3}ACA* provide direct evidence for triplet energy transfer from trapped excitons to ACA. Although XB should contain contribution of band edge exciton decay, its contribution is relatively small, considering the low PLQY of QD (11.7 %). Therefore, TET in CdSe-ACA complexes is dominated by TET from trap excitons.

5.2.3 Wavelength dependent time-resolved photoluminescence of CdSe QD and CdSe QD-ACA

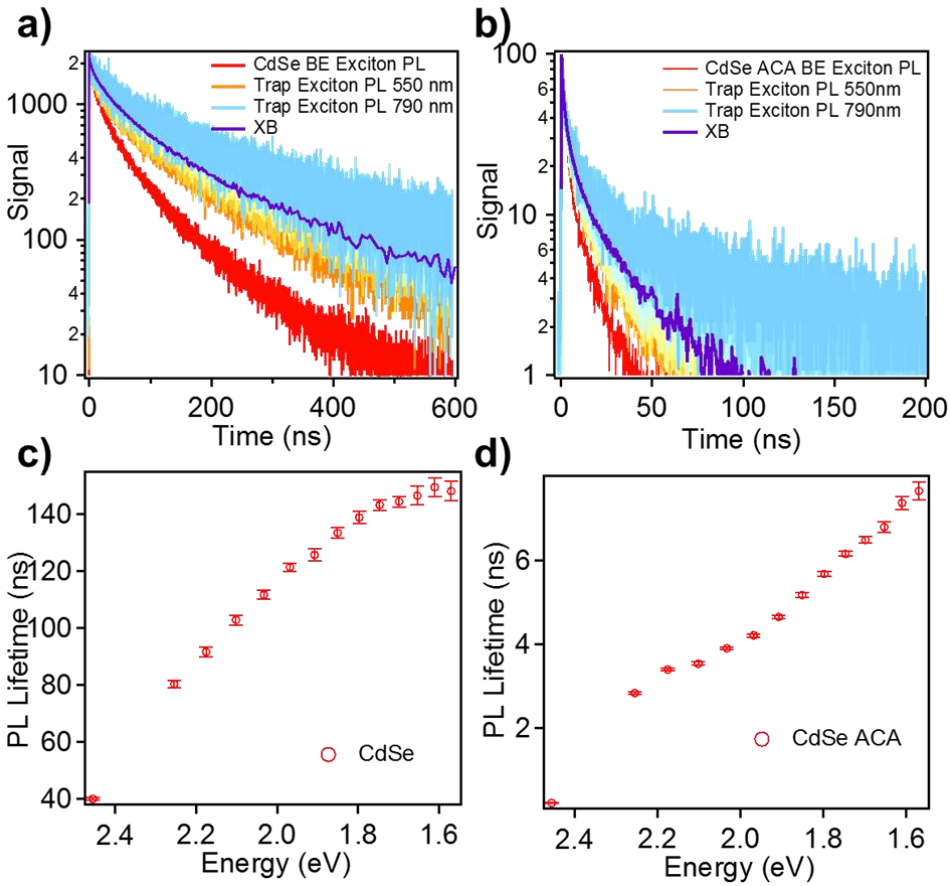

Figure 5.6: TRPL kinetics of a). CdSe QD and b). CdSe-ACA complex at various detection wavelengths and the calculated average exciton lifetime from TRPL results as function of exciton energies in c) CdSe QD and d). CdSe-ACA. In a) and b), the red lines are the TRPL kinetics of band edge (BE) exciton detected at 505 nm. The TRPL kinetics traces of trap states detected from 550 nm to 790 nm with detection wavelength interval of 20 nm are shown as the line series with colors evolving from orange to blue. The purple lines are the XB kinetics in TA spectra. In c) and d), the exciton energies are converted from detection wavelengths of the corresponding TRPL kinetics traces.

To investigate how TET rate depends on the energy of the exciton, we also measured PL decay as a function of emission wavelength. As shown in Figure 5.6a**,** the lifetime of the band edge

exciton of free QD, measured at the peak of steady state PL spectrum (505 nm), is the shortest among all exciton states. For the broad trap state PL band, the PL lifetime increases with increasing wavelength. The result is more consistent with a model that the width of the trap state emission in CdSe QD is due to a distribution of trapped hole energy.[46, 51] For trap holes with different energies, the rate of recombination with the conduction band electron may be different, leading to wavelength dependent PL lifetimes. If the broad trap state emission results from one single trap state that is strongly coupled with phonons, we would expect that the PL lifetimes are the same throughout the entire trap state emission band, which is not consistent with our observation. A comparison of the PL decay kinetics with the XB kinetics measured by TA show that the XB decay lies near the middle of the wavelength dependent PL kinetics traces **(**Figure 5.6a**)**. This is consistent with the fact that the XB signal probes the conduction band edge electron population, and its lifetime is the averaged of all band edge and trap exciton states, regardless of the energy of the hole.

The instrument response function of the time-resolved PL measurement can be characterized by a Gaussian function with a FWHM of 620 ps. The kinetics at all wavelengths show an instrument response time limited rise. We fit all the kinetics traces after 1 ns with stretched exponential functions:

$$A\,(t) = A_0 e^{-(\frac{t}{\tau_k})^{\beta}} \qquad \text{Eq. 5.2}$$

The average lifetime of each TRPL kinetics trace can be calculated from the fitting parameters to represent the exciton lifetime at the corresponding energy:

$$< \tau >= \frac{\tau_k}{\beta} \Gamma(\frac{1}{\beta}) \qquad \text{Eq. 5.3}$$

where Γ is the gamma function.[60] The results are shown in Figure 5.6c and Table 5.1. Compared to free CdSe QD, the PL decay kinetics traces is faster for CdSe-ACA complexes at all

wavelengths (Figure 5.7). According to the TA measurement above, at time scale of 1 ns – 1 μs, exciton quenching in CdSe-ACA complexes can be attributed to TET from the QD to ACA. The PL decay kinetics of CdSe-ACA were also fit with stretched exponential functions in a similar manner as those of free QDs. Specifically, because the populations of excitons with the same energy are the same at t = 0 for CdSe QD and CdSe-ACA if the absorption at the excitation wavelength, excitation intensity and data collection time are the same for the two samples, we keep the amplitude term A_0 in stretched exponential function to fit kinetics in CdSe-ACA complex the same as that in free CdSe QD. The function for fitting kinetics in CdSe-ACA is written as:

$$A_{CdSe-ACA}(t) = A_0 e^{-(\frac{t}{\tau_{k\,CdSe-ACA}})^{\beta_{CdSe-ACA}}} \qquad \text{Eq. 5.4}$$

The fitting result of τ_k and β is shown in Table 5.1. From the result in Table 5.1, the average lifetime, TET rate and TET efficiency could be calculated and the calculated PL lifetime as a function of exciton energy is plotted in Figure 5.6d, which shows increasing PL lifetime with decreasing exciton energy.

Table 5.1: Parameters in stretched exponential functions (shown in Eq. 5.2 and Eq. 5.4) applied to fit the TRPL kinetics of excitons with corresponding energies in CdSe QD and CdSe-ACA complex.

	CdSe QD		CdSe ACA	
Energy (eV)	τ_k (ns)	β	τ_k (ns)	β
2.45	26.0±0.2	0.588±0.002	(2.18±0.02) ×10^{-3}	0.205±0.001
2.25	47.4±0.6	0.551±0.005	0.744±0.004	0.381±0.001
2.18	53.6±0.7	0.548±0.006	1.09±0.01	0.411±0.001
2.10	62.2±0.7	0.560±0.006	1.10±0.01	0.405±0.001

2.03	68.8±0.8	0.567±0.003	1.23±0.01	0.407±0.001
1.97	77.7±0.8	0.584±0.003	1.28±0.01	0.401±0.001
1.91	83.6±0.9	0.601±0.008	1.32±0.01	0.392±0.001
1.85	89.2±1.1	0.603±0.004	1.32±0.01	0.378±0.001
1.80	94.6±1.3	0.612±0.005	1.33±0.01	0.367±0.001
1.75	100±1	0.625±0.005	1.41±0.01	0.365±0.001
1.70	100±1	0.622±0.005	1.27±0.01	0.348±0.001
1.65	101±2	0.615±0.006	1.21±0.01	0.340±0.002
1.61	107±2	0.635±0.007	1.13±0.01	0.326±0.002
1.57	103±2	0.621±0.007	1.05±0.02	0.317±0.002

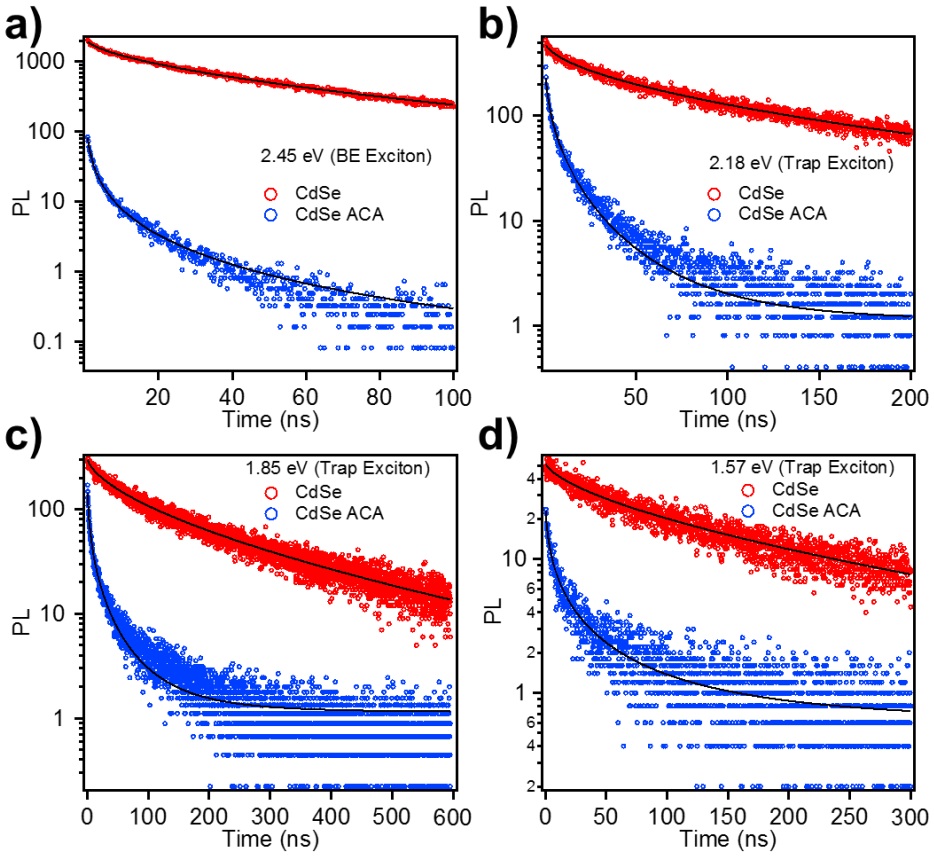

Figure 5.7: Comparison of TRPL kinetics of excitons in CdSe QD (red) and CdSe-ACA complex (blue) with energies of a). 2.45 eV (band edge (BE) exciton); b). 2.18 eV (trap exciton); c). 1.85 eV (trap exciton); d). 1.57 eV (trap exciton). The energies were calculated from the corresponding detection wavelengths of TRPL kinetics traces, which are good representations of exciton energies if Stoke shift is small, and the broad emission band of trap states is due to wide distribution of trap exciton energies. The black lines are the fitting of the kinetics traces with stretched exponential functions. The figure shows faster decay of exciton populations for both BE excitons and trap excitons in CdSe-ACA than in CdSe QD, indicating contribution of both BE excitons and trap excitons to TET from CdSe to ACA.

5.2.4 Triplet energy transfer rate and efficiency from band edge exciton and trap states

With the measured average PL lifetime of free CdSe QDs ($< \tau_{CdSe} >$) and CdSe-ACA complexes ($< \tau_{CdSe-ACA} >$), the apparent TET rate (k_{TET}) and efficiency (η) are calculated as:

$$k_{TET} = \frac{1}{<\tau_{CdSe-ACA}>} - \frac{1}{<\tau_{CdSe}>} \qquad \text{Eq. 5.5}$$

$$\eta = \frac{k_{TET}}{\left(\frac{1}{<\tau_{CdSe-ACA}>}\right)} \qquad \text{Eq. 5.6}$$

The calculated TET rate and efficiency are plotted as a function of emission energy (or the corresponding exciton energy) in Figure 5.8a and b, respectively. Both TET rates and efficiencies decrease with exciton energy. The calculated TET efficiencies are consistent with that measured from the steady state PL quenching (as shown in inset of Figure 5.2b), which further supports the analysis of the PL decay results. The estimated TET rate of the band edge exciton is 13-37 times faster than trap excitons (Figure 5.8a). The TET rate of band edge excitons may be overestimated because the quenching caused by electron trapping process induced by the adsorption of ACA is

also included in the calculation.

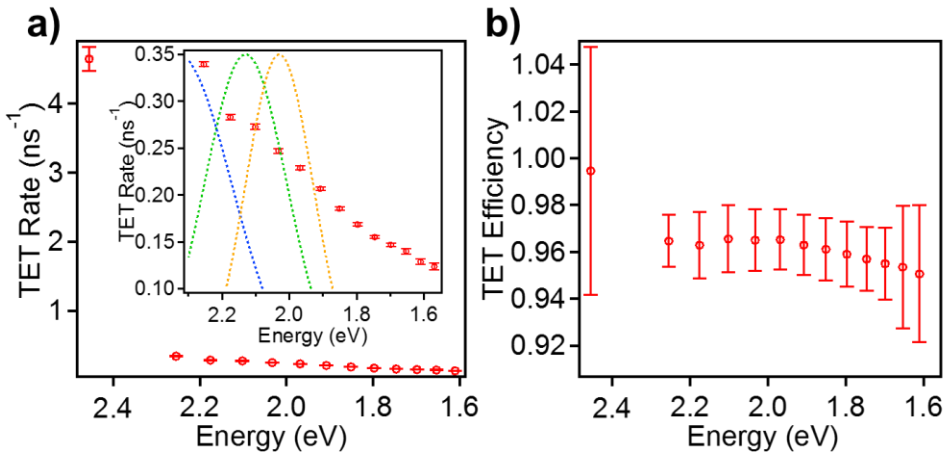

Figure 5.8: Calculated a). TET rate and b). TET efficiency as function of exciton energies from TRPL kinetics traces. The zoom-in figure of Figure 5.8a is shown as the inset. The orange, green and blue dash lines in the inset correspond to the curves of Eq. 5.7 with coupling strengths to be the same for all trap states and reorganization energies of 0.2 eV, 0.3 eV and 0.5 eV, respectively.

Dependence of TET rates on driving force can be described by:

$$k_{TET} = A|V|^2 e^{-[\frac{(\Delta G+\lambda)^2}{4\lambda k_B T}]} \qquad \text{Eq. 5.7}$$

where $|V|$, ΔG and λ are the coupling strength, driving force and reorganization energy, respectively.[61-62] Here the coupling strength depends on the overlap of both the electron and hole wavefunctions in the donor and acceptor. While both the band edge and trap exciton states involve the conduction band electron, their hole wavefunctions are different. The band edge exciton involves delocalized valence band edge hole level, and the trap exciton involves localized trapped holes. As a result, the electronic coupling strength for TET from the band edge exciton state is likely larger than that of the trapped exciton.[29, 58, 63] In addition, the energy of band edge exciton is higher than that of trap state, resulting in higher driving force for TET. Among the trap exciton

states, the observed TET rate increases with the exciton energy, varying by a factor of 3 over a range of 0.7 eV. This likely reflects the change of coupling strength and driving force for TET from different trap exciton states. Shown in insets of Figure 5.8a are driving force dependent TET rates calculated using Eq. 5.7 assuming energy independent coupling strength and reorganization energy of 0.2, 0.3 and 0.5eV. The observed driving force dependence of trap state TET rates may be consistent with the behavior in the Marcus normal region, in which larger driving force results in larger TET rate, if the reorganization energy significantly exceeds 0.5 eV.[64] It is also possible that both the coupling strength and reorganization energy vary for different trap states, giving rise to the observed trend. More quantitative analysis of the TET rates and their trends awaits future computational studies.

Finally, as shown in Figure 5.8b, the TET efficiencies of both band edge and trapped excitons are high, approaching 100%. Although the TET rates from trapped excitons are slower than band edge excitons, TET efficiencies from trapped excitons are still very high because of their long lifetimes. Because of the low PLQY ((11.7 ± 0.7) %) of the CdSe QDs, the majority of band edge excitons undergo fast trapping process to form trap excitons with a wide distribution of energies. As a result, trapped excitons dominate the overall TET process from CdSe QDs to ACA.

5.3 Conclusion

We have studied the contribution of trapped exciton to the triplet energy transfer in CdSe-ACA complexes. Comparison of the static PL spectra of free CdSe QDs and CdSe-ACA complexes shows that both band edge and trap state exciton emissions of CdSe QDs are quenched by the addition of ACA. Transient absorption study of the CdSe-ACA complexes provides direct evidence of ACA triplet state formation by direct Dexter energy transfer. PL decay studies show that the rate of TET from band edge exciton is 13-37 times faster than trapped excitons, and among

trapped excitons, the TET rate decreases at smaller trapped exciton energy. The band edge exciton transfer efficiency approaches 100% because of the fast TET rate. However, because the longer intrinsic trap exciton lifetimes, the TET efficiency from trapped excitons are also high, >95%, despite their relatively slower TET rate. Interestingly, because of small PLQY in CdSe QDs, most excitons (> 88% in this study) undergo rapid hole trapping to form trapped excitons. As a result, trapped excitons play a dominating role in the overall triplet energy transfer from the QD to ACA. Our finding highlights the importance of trapped excitons in nanocrystal sensitized triplet energy transfer systems.

5.4 Reference

1. Wohnhaas, C.; Mailänder, V.; Dröge, M.; Filatov, M. A.; Busko, D.; Avlasevich, Y.; Baluschev, S.; Miteva, T.; Landfester, K.; Turshatov, A., Triplet–Triplet Annihilation Upconversion Based Nanocapsules for Bioimaging Under Excitation by Red and Deep-Red Light. *Macromolecular Bioscience* **2013,** *13* (10), 1422-1430.
2. Lin, Y. L.; Koch, M.; Brigeman, A. N.; Freeman, D. M. E.; Zhao, L.; Bronstein, H.; Giebink, N. C.; Scholes, G. D.; Rand, B. P., Enhanced sub-bandgap efficiency of a solid-state organic intermediate band solar cell using triplet-triplet annihilation. *Energy & Environmental Science* **2017,** *10* (6), 1465-1475.
3. Schulze, T. F.; Schmidt, T. W., Photochemical upconversion: present status and prospects for its application to solar energy conversion. *Energy & Environmental Science* **2015,** *8* (1), 103-125.
4. Singh-Rachford, T. N.; Castellano, F. N., Photon upconversion based on sensitized triplet–triplet annihilation. *Coord. Chem. Rev.* **2010,** *254* (21-22), 2560-2573.
5. Islangulov, R. R.; Kozlov, D. V.; Castellano, F. N., Low power upconversion using MLCT sensitizers. *Chem. Commun.* **2005,** (30), 3776-3778.
6. Nishimura, N.; Gray, V.; Allardice, J. R.; Zhang, Z.; Pershin, A.; Beljonne, D.; Rao, A., Photon Upconversion from Near-Infrared to Blue Light with TIPS-Anthracene as an Efficient Triplet–Triplet Annihilator. *ACS Materials Letters* **2019,** *1* (6), 660-664.
7. Schmidt, T. W.; Castellano, F. N., Photochemical Upconversion: The Primacy of Kinetics. *The Journal of Physical Chemistry Letters* **2014,** *5* (22), 4062-4072.
8. Lin, S. H., On the Theory of Non-Radiative Transfer of Electronic Excitation. *Proc. R. Soc. Lond. A.* **1973,** *335* (1600), 51.
9. Sigman, M. E.; Closs, G. L., Free-Energy and Structure Dependence of Intramolecular Triplet Energy-Transfer in Organic-Model Compounds. *J Phys Chem-Us* **1991,** *95* (13), 5012-5017.
10. Harcourt, R. D.; Scholes, G. D.; Ghiggino, K. P., Rate expressions for excitation transfer. II. Electronic considerations of direct and through–configuration exciton resonance interactions. *J.*

Chem. Phys. **1994,** *101* (12), 10521-10525.
11. Skourtis, S. S.; Liu, C.; Antoniou, P.; Virshup, A. M.; Beratan, D. N., Dexter energy transfer pathways. *Proc. Natl. Acad. Sci. U S A* **2016,** *113* (29), 8115-20.
12. Cademartiri, L.; Montanari, E.; Calestani, G.; Migliori, A.; Guagliardi, A.; Ozin, G. A., Size-Dependent Extinction Coefficients of PbS Quantum Dots. *J. Am. Chem. Soc.* **2006,** *128* (31), 10337-10346.
13. Yu, W. W.; Qu, L. H.; Guo, W. Z.; Peng, X. G., Experimental determination of the extinction coefficient of CdTe, CdSe, and CdS nanocrystals. *Chem. Mater.* **2003,** *15* (14), 2854-2860.
14. Jasieniak, J.; Califano, M.; Watkins, S. E., Size-dependent valence and conduction band-edge energies of semiconductor nanocrystals. *ACS Nano* **2011,** *5* (7), 5888-902.
15. Efros, A. L.; Rosen, M.; Kuno, M.; Nirmal, M.; Norris, D. J.; Bawendi, M., Band-edge exciton in quantum dots of semiconductors with a degenerate valence band: Dark and bright exciton states. *Phys. Rev. B* **1996,** *54* (7), 4843-4856.
16. Scholes, G. D.; Rumbles, G., Excitons in nanoscale systems. *Nat. Mater.* **2006,** *5* (9), 683-96.
17. Piland, G. B.; Huang, Z. Y.; Tang, M. L.; Bardeen, C. J., Dynamics of Energy Transfer from CdSe Nanocrystals to Triplet States of Anthracene Ligand Molecules. *J. Phys. Chem. C* **2016,** *120* (11), 5883-5889.
18. Mongin, C.; Garakyaraghi, S.; Razgoniaeva, N.; Zamkov, M.; Castellano, F. N., Direct observation of triplet energy transfer from semiconductor nanocrystals. *Science* **2016,** *351* (6271), 369-72.
19. Xu, Z.; Jin, T.; Huang, Y.; Mulla, K.; Evangelista, F. A.; Egap, E.; Lian, T., Direct triplet sensitization of oligothiophene by quantum dots. *Chem. Sci.* **2019,** *10* (24), 6120-6124.
20. Mahboub, M.; Maghsoudiganjeh, H.; Pham, A. M.; Huang, Z. Y.; Tang, M. L., Triplet Energy Transfer from PbS(Se) Nanocrystals to Rubrene: the Relationship between the Upconversion Quantum Yield and Size. *Adv. Funct. Mater.* **2016,** *26* (33), 6091-6097.
21. Huang, Z.; Xu, Z.; Mahboub, M.; Li, X.; Taylor, J. W.; Harman, W. H.; Lian, T.; Tang, M. L., PbS/CdS Core-Shell Quantum Dots Suppress Charge Transfer and Enhance Triplet Transfer. *Angew. Chem. Int. Ed.* **2017,** *56* (52), 16583-16587.
22. Kroupa, D. M.; Arias, D. H.; Blackburn, J. L.; Carroll, G. M.; Granger, D. B.; Anthony, J. E.; Beard, M. C.; Johnson, J. C., Control of Energy Flow Dynamics between Tetracene Ligands and PbS Quantum Dots by Size Tuning and Ligand Coverage. *Nano Lett.* **2018,** *18* (2), 865-873.
23. Wu, M.; Congreve, D. N.; Wilson, M. W. B.; Jean, J.; Geva, N.; Welborn, M.; Van Voorhis, T.; Bulović, V.; Bawendi, M. G.; Baldo, M. A., Solid-state infrared-to-visible upconversion sensitized by colloidal nanocrystals. *Nat. Photon.* **2015,** *10*, 31-34.
24. Huang, Z.; Xu, Z.; Mahboub, M.; Liang, Z.; Jaimes, P.; Xia, P.; Graham, K. R.; Tang, M. L.; Lian, T., Enhanced Near-Infrared-to-Visible Upconversion by Synthetic Control of PbS Nanocrystal Triplet Photosensitizers. *J. Am. Chem. Soc.* **2019,** *141* (25), 9769-9772.
25. Nishimura, N.; Allardice, J. R.; Xiao, J.; Gu, Q.; Gray, V.; Rao, A., Photon upconversion utilizing energy beyond the band gap of crystalline silicon with a hybrid TES-ADT/PbS quantum dots system. *Chem. Sci.* **2019,** *10* (18), 4750-4760.
26. Mase, K.; Okumura, K.; Yanai, N.; Kimizuka, N., Triplet sensitization by perovskite nanocrystals for photon upconversion. *Chem. Commun.* **2017,** *53* (59), 8261-8264.
27. Okumura, K.; Yanai, N.; Kimizuka, N., Visible-to-UV Photon Upconversion Sensitized by Lead Halide Perovskite Nanocrystals. *Chem. Lett.* **2019,** *48* (11), 1347-1350.
28. Han, Y.; Luo, X.; Lai, R.; Li, Y.; Liang, G.; Wu, K., Visible-Light-Driven Sensitization of Naphthalene Triplets Using Quantum-Confined CsPbBr3 Nanocrystals. *J. Phys. Chem. Lett.* **2019,**

10 (7), 1457-1463.
29. Li, X.; Huang, Z.; Zavala, R.; Tang, M. L., Distance-Dependent Triplet Energy Transfer between CdSe Nanocrystals and Surface Bound Anthracene. *J. Phys. Chem. Lett.* **2016,** *7* (11), 1955-9.
30. Luo, X.; Lai, R.; Li, Y.; Han, Y.; Liang, G.; Liu, X.; Ding, T.; Wang, J.; Wu, K., Triplet Energy Transfer from CsPbBr3 Nanocrystals Enabled by Quantum Confinement. *J. Am. Chem. Soc.* **2019,** *141* (10), 4186-4190.
31. Nienhaus, L.; Wu, M.; Geva, N.; Shepherd, J. J.; Wilson, M. W. B.; Bulovic, V.; Van Voorhis, T.; Baldo, M. A.; Bawendi, M. G., Speed Limit for Triplet-Exciton Transfer in Solid-State PbS Nanocrystal-Sensitized Photon Upconversion. *ACS Nano* **2017,** *11* (8), 7848-7857.
32. Luo, X.; Han, Y.; Chen, Z.; Li, Y.; Liang, G.; Liu, X.; Ding, T.; Nie, C.; Wang, M.; Castellano, F. N.; Wu, K., Mechanisms of triplet energy transfer across the inorganic nanocrystal/organic molecule interface. *Nat. Commun.* **2020,** *11* (1), 28.
33. Garakyaraghi, S.; Mongin, C.; Granger, D. B.; Anthony, J. E.; Castellano, F. N., Delayed Molecular Triplet Generation from Energized Lead Sulfide Quantum Dots. *J. Phys. Chem. Lett.* **2017,** *8* (7), 1458-1463.
34. Jin, T.; Uhlikova, N.; Xu, Z.; Zhu, Y.; Huang, Y.; Egap, E.; Lian, T., Competition of Dexter, Förster, and charge transfer pathways for quantum dot sensitized triplet generation. *J. Chem. Phys.* **2020,** *152* (21), 214702.
35. Xia, P.; Raulerson, E. K.; Coleman, D.; Gerke, C. S.; Mangolini, L.; Tang, M. L.; Roberts, S. T., Achieving spin-triplet exciton transfer between silicon and molecular acceptors for photon upconversion. *Nat. Chem.* **2020,** *12* (2), 137-144.
36. Califano, M.; Franceschetti, A.; Zunger, A., Temperature Dependence of Excitonic Radiative Decay in CdSe Quantum Dots: The Role of Surface Hole Traps. *Nano Letters* **2005,** *5* (12), 2360-2364.
37. Jones, M.; Lo, S. S.; Scholes, G. D., Quantitative modeling of the role of surface traps in CdSe/CdS/ZnS nanocrystal photoluminescence decay dynamics. *Proc. Natl. Acad. Sci.* **2009,** *106* (9), 3011-6.
38. Han, Y.; He, S.; Luo, X.; Li, Y.; Chen, Z.; Kang, W.; Wang, X.; Wu, K., Triplet Sensitization by "Self-Trapped" Excitons of Nontoxic CuInS2 Nanocrystals for Efficient Photon Upconversion. *J. Am. Chem. Soc.* **2019,** *141* (33), 13033-13037.
39. Rigsby, E. M.; Lee, K.; Sun, J.; Fishman, D. A.; Tang, M. L., Primary amines enhance triplet energy transfer from both the band edge and trap state from CdSe nanocrystals. *J. Chem. Phys.* **2019,** *151* (17), 174701.
40. Mahboub, M.; Xia, P.; Van Baren, J.; Li, X.; Lui, C. H.; Tang, M. L., Midgap States in PbS Quantum Dots Induced by Cd and Zn Enhance Photon Upconversion. *ACS Energy Lett.* **2018,** *3* (4), 767-772.
41. Gray, V.; Xia, P.; Huang, Z.; Moses, E.; Fast, A.; Fishman, D. A.; Vullev, V. I.; Abrahamsson, M.; Moth-Poulsen, K.; Lee Tang, M., CdS/ZnS core-shell nanocrystal photosensitizers for visible to UV upconversion. *Chem. Sci.* **2017,** *8* (8), 5488-5496.
42. Mahboub, M.; Huang, Z.; Tang, M. L., Efficient Infrared-to-Visible Upconversion with Subsolar Irradiance. *Nano Lett.* **2016,** *16* (11), 7169-7175.
43. Bender, J. A.; Raulerson, E. K.; Li, X.; Goldzak, T.; Xia, P.; Van Voorhis, T.; Tang, M. L.; Roberts, S. T., Surface States Mediate Triplet Energy Transfer in Nanocrystal-Acene Composite Systems. *J. Am. Chem. Soc.* **2018,** *140* (24), 7543-7553.
44. Mooney, J.; Krause, M. M.; Saari, J. I.; Kambhampati, P., Challenge to the deep-trap model

of the surface in semiconductor nanocrystals. *Physical Review B* **2013,** *87* (8), 081201.
45. Jones, M.; Lo, S. S.; Scholes, G. D., Signatures of Exciton Dynamics and Carrier Trapping in the Time-Resolved Photoluminescence of Colloidal CdSe Nanocrystals. *J. Phys. Chem. C* **2009,** *113* (43), 18632-18642.
46. Hässelbarth, A.; Eychmüller, A.; Weller, H., Detection of shallow electron traps in quantum sized CdS by fluorescence quenching experiments. *Chemical Physics Letters* **1993,** *203* (2), 271-276.
47. Barraza-Jimenez, D.; Flores-Hidalgo, A.; Glossman-Mitnik, D., Theoretical analysis of anthracene and its carbonyl and carboxyl derivatives using DFT and TD-DFT. *Journal of Molecular Structure: THEOCHEM* **2009,** *894* (1), 64-70.
48. Zhu, H. M.; Lian, T. Q., Wavefunction engineering in quantum confined semiconductor nanoheterostructures for efficient charge separation and solar energy conversion. *Energy & Environmental Science* **2012,** *5* (11), 9406-9418.
49. Chen, O.; Zhao, J.; Chauhan, V. P.; Cui, J.; Wong, C.; Harris, D. K.; Wei, H.; Han, H.-S.; Fukumura, D.; Jain, R. K.; Bawendi, M. G., Compact high-quality CdSe–CdS core–shell nanocrystals with narrow emission linewidths and suppressed blinking. *Nature Materials* **2013,** *12*, 445.
50. Ekimov, A. I.; Hache, F.; Schanne-Klein, M. C.; Ricard, D.; Flytzanis, C.; Kudryavtsev, I. A.; Yazeva, T. V.; Rodina, A. V.; Efros, A. L., Absorption and intensity-dependent photoluminescence measurements on CdSe quantum dots: assignment of the first electronic transitions. *J. Opt. Soc. Am. B* **1993,** *10* (1), 100-107.
51. Jones, M.; Nedeljkovic, J.; Ellingson, R. J.; Nozik, A. J.; Rumbles, G., Photoenhancement of Luminescence in Colloidal CdSe Quantum Dot Solutions. *The Journal of Physical Chemistry B* **2003,** *107* (41), 11346-11352.
52. Rurack, K.; Spieles, M., Fluorescence Quantum Yields of a Series of Red and Near-Infrared Dyes Emitting at 600−1000 nm. *Analytical Chemistry* **2011,** *83* (4), 1232-1242.
53. Huang, J. E.; Huang, Z. Q.; Jin, S. Y.; Lian, T. Q., Exciton Dissociation in CdSe Quantum Dots by Hole Transfer to Phenothiazine. *Journal of Physical Chemistry C* **2008,** *112* (49), 19734-19738.
54. Huang, J.; Huang, Z.; Yang, Y.; Zhu, H.; Lian, T., Multiple Exciton Dissociation in CdSe Quantum Dots by Ultrafast Electron Transfer to Adsorbed Methylene Blue. *Journal of the American Chemical Society* **2010,** *132* (13), 4858-4864.
55. Schnitzenbaumer, K. J.; Labrador, T.; Dukovic, G., Impact of Chalcogenide Ligands on Excited State Dynamics in CdSe Quantum Dots. *J. Phys. Chem. C* **2015,** *119* (23), 13314-13324.
56. Wu, K.; Zhu, H.; Liu, Z.; Rodríguez-Córdoba, W.; Lian, T., Ultrafast Charge Separation and Long-Lived Charge Separated State in Photocatalytic CdS–Pt Nanorod Heterostructures. *Journal of the American Chemical Society* **2012,** *134* (25), 10337-10340.
57. Gómez-Campos, F. M.; Califano, M., Hole Surface Trapping in CdSe Nanocrystals: Dynamics, Rate Fluctuations, and Implications for Blinking. *Nano Letters* **2012,** *12* (9), 4508-4517.
58. Giansante, C.; Infante, I., Surface Traps in Colloidal Quantum Dots: A Combined Experimental and Theoretical Perspective. *The Journal of Physical Chemistry Letters* **2017,** *8* (20), 5209-5215.
59. Ebenstein, Y.; Mokari, T.; Banin, U., Fluorescence quantum yield of CdSe/ZnS nanocrystals investigated by correlated atomic-force and single-particle fluorescence microscopy. *Applied Physics Letters* **2002,** *80* (21), 4033-4035.
60. Zatryb, G.; Podhorodecki, A.; Misiewicz, J.; Cardin, J.; Gourbilleau, F., On the nature of the

stretched exponential photoluminescence decay for silicon nanocrystals. *Nanoscale Res. Lett.* **2011,** *6* (1), 106-106.
61. Subotnik, J. E.; Vura-Weis, J.; Sodt, A. J.; Ratner, M. A., Predicting accurate electronic excitation transfer rates via marcus theory with Boys or Edmiston-Ruedenberg localized diabatization. *J Phys Chem A* **2010,** *114* (33), 8665-8675.
62. Serpa, C.; Arnaut, L. G.; Formosinho, S. J.; Naqvi, K. R., Calculation of triplet–triplet energy transfer rates from emission and absorption spectra. The quenching of hemicarcerated triplet biacetyl by aromatic hydrocarbons. *Photochem. Photobiol. Sci.* **2003,** *2* (5), 616-623.
63. L. J. Dexter, D., A Theory of Sensitized Luminescence in Solid. *J. Chem. Phys.* **1953,** *21*, 836-850.
64. Huang, Z. Y.; Li, X.; Yip, B. D.; Rubalcava, J. M.; Bardeen, C. J.; Tang, M. L., Nanocrystal Size and Quantum Yield in the Upconversion of Green to Violet Light with CdSe and Anthracene Derivatives. *Chem. Mater.* **2015,** *27* (21), 7503-7507.

Chapter 6. Enhanced Triplet State Generation through Radical Pair Intermediates in BODIPY-Quantum Dot Complexes

Reproduced in part with permission from: Jin, T.; Uhlikova, N.; Xu, Z.; Zhu, Y.; Huang, Y.; Egap, E.; Lian, T., *J. Chem. Phys.* **2019**, 151, 241101. Copyright AIP Publishing 2019

6.1 Introduction

Because of long lifetimes of triplet excitons,[1-3] extensive research efforts have been devoted to the efficient generation and harvesting of triplet excited states and their application in photodynamic therapy,[4-6] bioimaging,[7-8] photocatalysis[9-11] and photon upconversion.[12-14] Traditional methods for efficiently generating triplet excited states include intersystem crossing by heavy atom enhanced spin-orbit coupling[15-16] and energy transfer from organometallic triplet sensitizers,[17-20] Recently, quantum dots (QDs) have been shown to be excellent triplet sensitizers,[21-27] owing to their large extinction coefficients,[28-29] tunable band structures[30-33] and small bright/dark state energy difference.[34-36] Excitons can be transferred from QDs to molecular acceptors through Dexter energy transfer,[21, 37-38] and significant progress has been made in understanding triplet sensitization mechanisms and improving their efficiencies.[26, 39-40]

More recently, QD sensitized triplet formation has also been suggested to go through charge transfer intermediate states, but the nature of the spin states in these charge separated radical pairs has not been carefully examined.[41-43] In molecular donor-acceptor or host-guest complexes, triplet excited states can be generated through a charge transfer intermediate,[44-48] by radical pair intersystem crossing (RP-ISC)[49-50] or spin-orbit coupling mechanism (SOCT-ISC).[51-52] Charge separated states between QDs and adsorbed molecules often decay by charge recombination to

form singlet ground state, implying that these radical pairs are likely in their spin singlet state .[31, 33, 53] In a recent study of thiol-modified bis(diarylamino)4,4′-biphenyl (TPD) attached on CdS QDs, it was demonstrated that electron transfer from TPD to CdS forms charge separated states (with an oxidized TPD and trapped electron in CdS) that undergo charge recombination to generate both TPD ground state and triplet excited state.[54] EPR studies revealed that the charge separated intermediates consist of spin-correlated singlet and triplet radical pairs, suggesting that these hybrid QD-adsorbate complexes may be a novel platform for spintronics applications.[55-56] However, because of strong spin-orbit coupling in QDs,[36] it remains unclear whether such spin correlated radical pair is a general characteristics and whether the spin states can be effectively controlled and selected.

In this chapter we demonstrate that in CdSe QD-modified BODIPY (shown as Compound 3 in Scheme 2.1) complexes, long lived triplet excited state of BODIPY can be generated by visible light excitation of BODIPY with 27% quantum efficiency. The triplet excited state is formed through a charge separated state immediate consisted of a conduction band (CB) electron in the QD and an oxidized BODIPY radical cation (Figure 6.1).

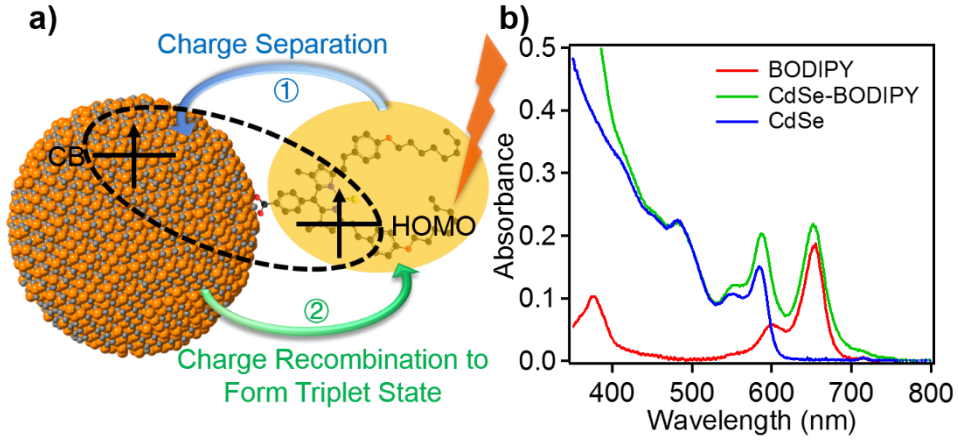

Figure 6.1: a) Scheme of photophysical processes in CdSe-BODIPY when BODIPY is excited, with radical pair as intermediate b) UV-vis absorption spectra of CdSe-BODIPY (green), CdSe

(blue) and BODIPY (red) in a 1 mm pathlength cell.

6.2 Results and discussion

6.2.1 Sample preparation and optical properties

CdSe QDs with $Cd(oleate)_2$ surface ligand and modified BODIPY with carboxylic acid anchoring group were synthesized following reported procedures[23, 57] (see Section 2.1.2, Section 2.1.4 and Figure 2.1-2.3 for ^{1}H and ^{13}C NMR spectra). Figure 6.1b shows the UV-vis absorption spectra of BODIPY, CdSe quantum dots and their complex. The S_0-S_1 absorption peak of BODIPY lies at 656 nm, with a shoulder peak at 600 nm corresponding to the 0-1 vibrational band of the same transition.[58] Because of further conjugation induced by benzene rings attached to the main body of the BODIPY structure, the S_0-S_1 peak is red-shifted by around 150 nm compared to unmodified BODIPY molecules.[8] Upon adsorption onto CdSe QDs, the absorption spectrum shows additional features in the range from 700 nm to 750 nm, which can be attributed to the aggregation of BODIPY molecules on the QD surface.[59] The adsorption of BODIPY does not affect the lowest energy $1S_{3/2}$-$1S_e$ exciton transition of the CdSe QD, centered at 584 nm.[60] Because there is no absorption of CdSe at 656 nm, selective excitation of BODIPY can be achieved in this wavelength region.

6.2.2 Transient absorption spectra of free BODIPY

The transient absorption spectra of BODIPY at indicated delay times after 650 nm excitation are shown in Figure 6.2a. Optical excitation generates BODIPY singlet excited state (^{1}BODIPY*), which results in the ground state bleach (GSB) signal centered at 656 nm. The negative peak centered at 740 nm is attributed to the stimulated emission (SE) of ^{1}BODIPY* given that its position matches that of BODIPY steady state fluorescence. The TA spectra also contain positive

bands (induced absorption, IA) ranging from 430 to 600 nm and from 800 to 913 nm, which are attributed to the transition from the first (S_1) to higher singlet excited states (S_1->S_n) of BODIPY. [61] The TA spectra show the simultaneous decay of the amplitudes of ground state (GSB) and singlet excited state (SE and IA) features with clear isosbestic points and no change of spectral shape, which suggests that the only decay channel of ^{1}BODIPY* is to regenerate the ground state, and there is negligible formation of triplet excited state of BODIPY (^{3}BODIPY*) through intersystem crossing (ISC). The kinetics of ^{1}BODIPY* decay can be well fit by convolution with a single exponential decay function with a time constant of (4.20±0.09) ns, as shown in Figure 6.2b and Table 6.1**.**

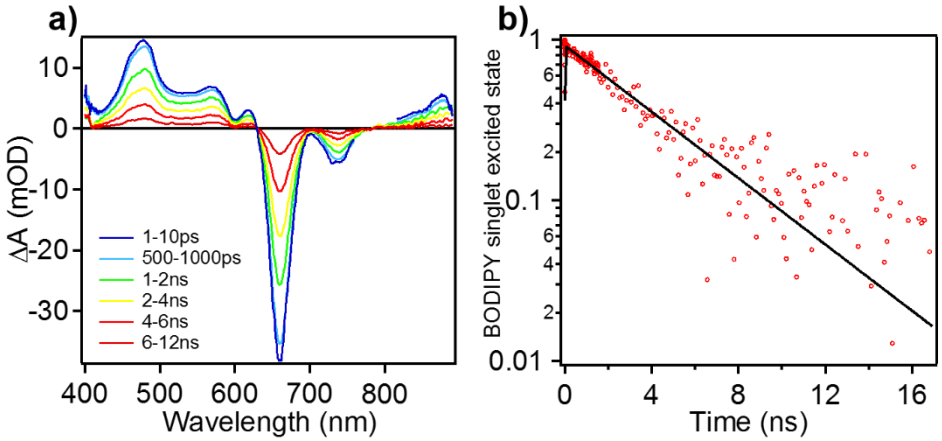

Figure 6.2: Transient absorption spectra and kinetics of free BODIPY in toluene. a) Transient absorption spectra at indicated delay times after 650 nm excitation. b) Transient kinetics of BODIPY singlet excited state monitored at 656 nm (red circles) and its fit to single exponential decay (black line).

Table 6.1: Fitting parameters for kinetics traces of ^{1}BODIPY* in Figure 6.2b. T_0 is the time zero value in the fitting. $1/k_0$ is the time constant of single exponential decay function.

Parameters	Value
Irf_FWHM	0.150 (ps)
T_0	0.020±0.009 (ps)
$1/k_0$	4.20±0.09 (ns)

6.2.3 Transient absorption spectra of BODIPY-QD complex

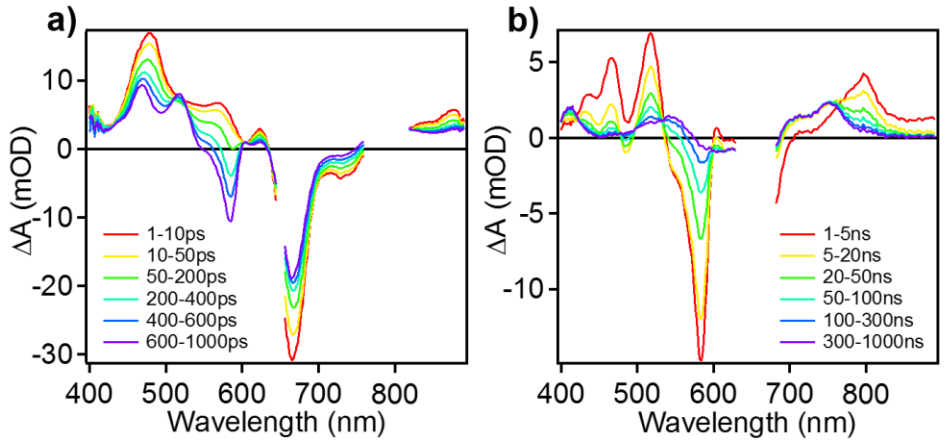

Figure 6.3: Transient absorption spectra of BODIPY-CdSe QD complexes measured with 650 nm excitation in delay time ranges of a) 1-1000 ps and b)1-1000 ns.

Femtosecond transient absorption spectra of BODIPY-CdSe QD at indicated delay times after 650 nm excitation are shown in Figure 6.3a. Since the 650 nm pump pulse selectively excites BODIPY to its singlet excited state, the initial spectra at 1-10 ps are similar to isolated BODIPY molecules in solution (Figure 6.2a), showing well resolved features of GSB, SE and IA (S_1->S_n). Note that because of the aggregation of BODIPY on the QD surface, there is slightly more overlap between GSB and SE features at this initial time range. Interestingly, from 10 to 1000 ps, the decay

of ^{1}BODIPY* signal leads to the growth of the QD 1S exciton bleach centered at 584 nm and a positive peak centered at around 800 nm. The positive peak is not resolved at <1 ns because of the saturation of the probe pulse at 800 nm but can be well observed at > 1 ns using a different probe light source (see Figure 6.3b). Because the 1S exciton bleach, resembling those of photoexcited CdSe QDs (see Figure 6.4), has been shown to be mainly caused by the state filling of the conduction band 1S level,[62-63] its growth suggests either energy or electron transfer from the ^{1}BODIPY* to CdSe QD.[38] The fluorescence spectrum peak of BODIPY is at 665 nm, and there is no CdSe QD absorption at region of 600-800 nm (see Figure 6.5 and Figure 6.1b). Therefore, there is no spectral overlap for energy transfer from BODIPY to CdSe QD, and energy transfer can be excluded.[38, 64] The remaining possibility is electron transfer, which generates a charge separated (CS) state $BODIPY^{+\cdot}$-$QD^{-\cdot}$. This process is consistent with the energy level alignment of CdSe QD and BODIPY. Figure 6.6a shows the cyclic voltammetry curve of BODIPY in DCM. Oxidation and reduction potentials of BODIPY were calculated by averaging reversible oxidation peaks at 0.579 V and 0.626 V and reduction peaks at -1.234 V and -1.164 V (vs. SCE). The conduction and valance band edge of CdSe QD was calculated to be -0.593 V and 1.500 V (vs. NHE) from literature.[65] The energy alignment of CdSe QD and BODIPY is shown in Figure 6.6b. Conduction band edge position of CdSe QD and reduction potential of BODIPY allow the electron transfer from BODIPY to CdSe QD. The positive peak at around 800 nm from 50-1000 ps in Figure 6.3 can thus be assigned to absorption of BODIPY cation radicals ($BODIPY^{+\cdot}$).[66]

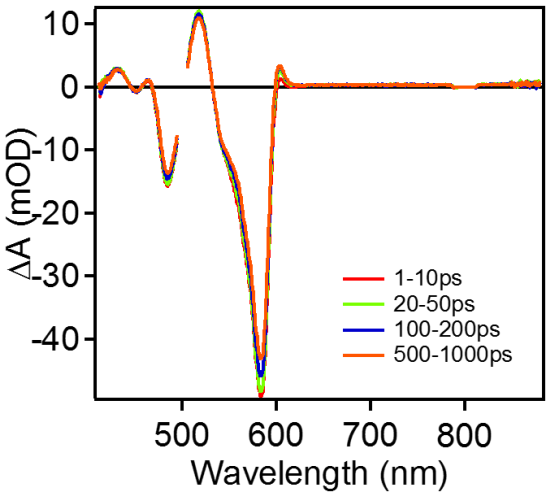

Figure 6.4: Femtosecond transient absorption spectra of CdSe QDs at indicated delay times after 500 nm excitation.

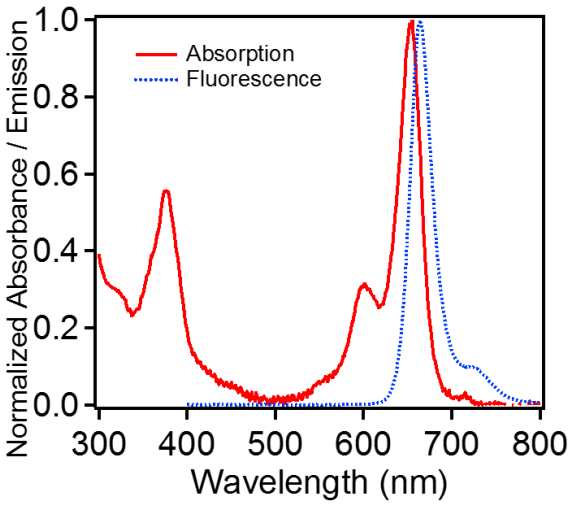

Figure 6.5: Absorption and emission spectra of BODIPY. The extinction coefficient of BODIPY at 656 nm in absorption spectrum is determined to be ε =91800 $L \cdot mol^{-1} \cdot cm^{-1}$. The excitation wavelength for the fluorescence spectrum measurement is 400 nm.

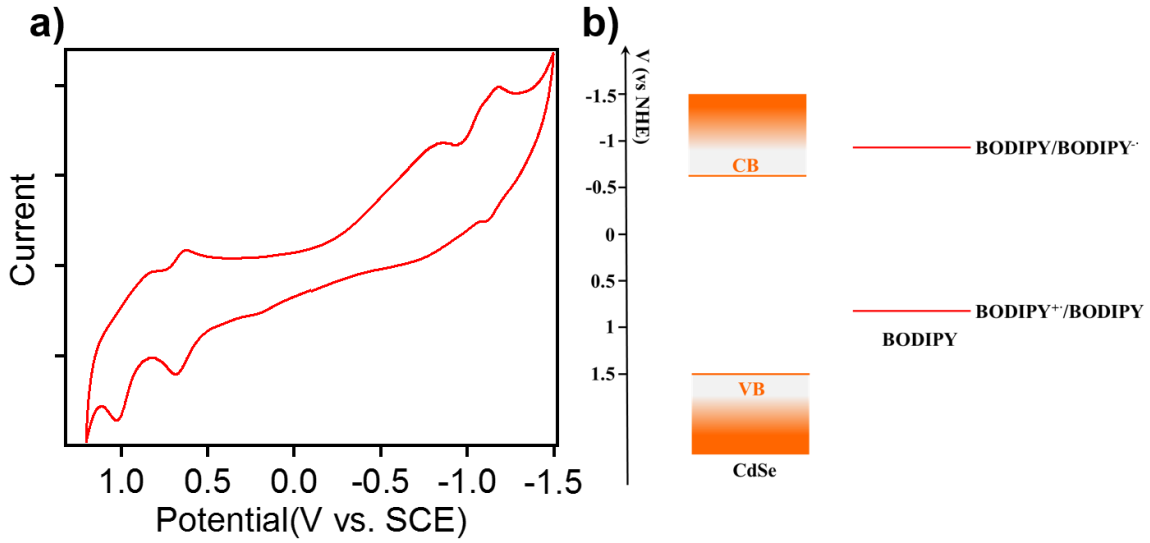

Figure 6.6: a) Cyclic voltammetry curve of BODIPY in DCM solution. b) Energy alignment of CdSe quantum dot and BODIPY.

Further spectra evolutions in the 1ns -1μs time scale are shown in Figure 6.3b. In these spectra, the positive peak of $BODIPY^{+\cdot}$ centered at 797 nm can be well resolved. The amplitude of charge separated state signal reaches maximum at 1-5 ns, and then decays within 100 ns. The decay of CS state leads to the formation of a new species with three positive peaks centered at 412 nm, 570 nm and 750 nm. Its signal amplitude reaches maximum at ~100 ns and, as shown in Figure 6.7, its decay kinetics can be fit with a single exponential function with a time constant of (20.0±0.3) μs. Because this signal is long-lived, and there are no remaining spectral features of the QD, it can only be assigned to BODIPY triplet excited state (^{3}BODIPY*) formed by back electron transfer from the $QD^{-\cdot}$ to $BODIPY^{+\cdot}$. The positive absorption peaks in the TA spectra can be attributed to the T_1->T_n absorption bands of ^{3}BODIPY*. This assignment is further confirmed by the faster decay of the signal when the system was exposed to oxygen (Figure 6.8).

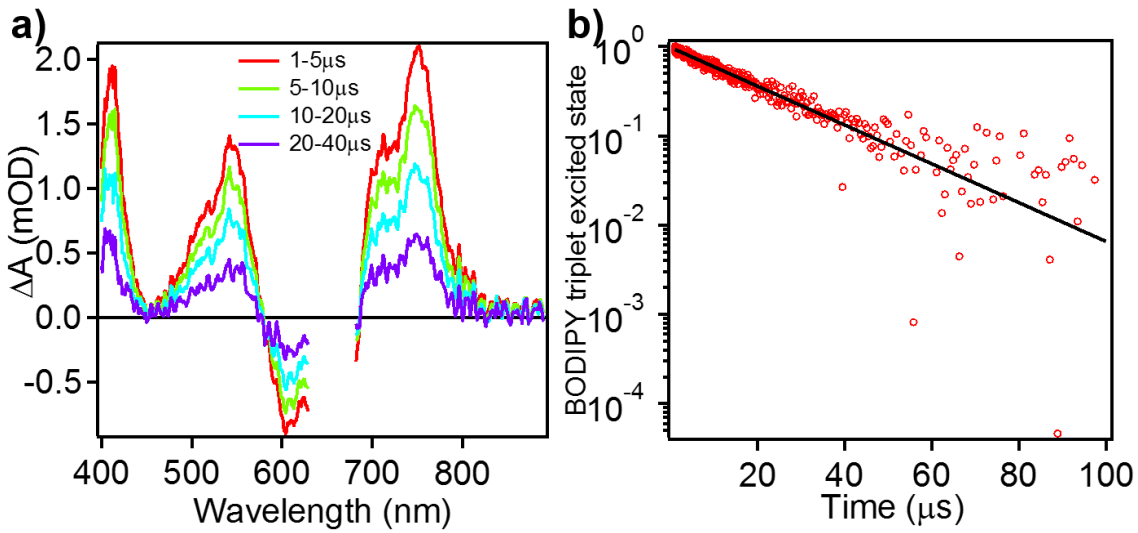

Figure 6.7: a) Transient absorption spectra of CdSe QD-BODIPY complex in time range of 1 μs to 40 μs. The wavelength of the pump pulse was 650 nm. The spectra shape is the same as TA spectra of CdSe-BODIPY complex in time range of 300 ns to 1000 ns. From the main text, the only remaining species in this time range is ^{3}BODIPY*. b) Kinetics trace of ^{3}BODIPY* in time range of 1 μs to 100 μs (red circles), which can be fit with single exponential function with time constant of (20.0±0.3) μs (shown as the black line).

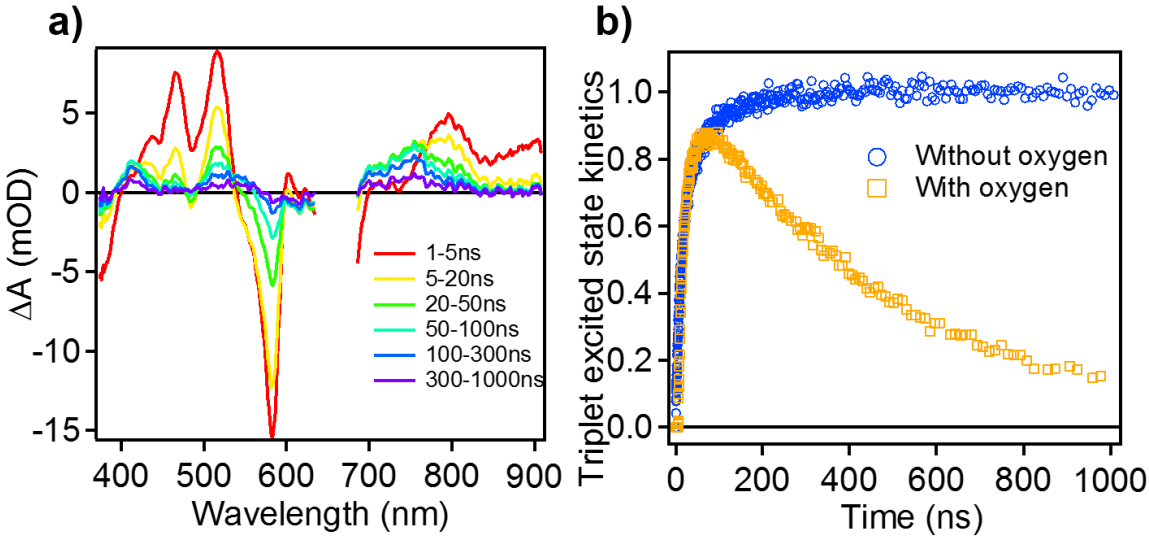

Figure 6.8: a). Transient absorption spectra of BODIPY-CdSe QD complexes measured with 650 nm excitation in delay time range of 1-1000 ns with exposure of oxygen. As shown in the figure,

the same ^{3}BODIPY* signal is formed, but decays faster than that without exposure of oxygen. b). Corresponding ^{3}BODIPY* kinetics in BODIPY-CdSe complexes with and without exposure to oxygen.

6.2.4 Spectra and kinetics analysis

In order to fully understand the competing processes and mechanism for ^{3}BODIPY* generation, we further analyze the TA spectra of BODIPY-CdSe QD from 10 ps to 1000 ns, which are the combination of ^{1}BODIPY*, ^{3}BODIPY* and CS state signals. The spectra of ^{1}BODIPY* can be obtained independently from the TA spectra of free ^{1}BODIPY* and the spectra of ^{3}BODIPY* is obtained from the TA spectra of BODIPY-QD at long delay time, when only ^{3}BODIPY* exists. Multivariate Curve Resolution-Alternating Least Squares (MCR) method was applied to extract the CS spectrum.[67] The detailed principle and algorithm of MCR were introduced in other literatures.[67-68] Here, the number of species was set to 3 (^{1}BODIPY*, ^{3}BODIPY* and charge separated state). Instead of using CdSe QD-BODIPY TA spectra at early delay time (1-10 ps) as ^{1}BODIPY* spectrum, which does not resolve the signal well at range of 400-430 nm, ^{1}BODIPY* spectrum can be obtained by averaging spectra in Figure 6.2a from 1 ns to 5 ns, and ^{3}BODIPY* spectrum can be obtained by averaging spectra in Figure 6.7 from 5 μs to 20 μs. The spectra of these two species were set as initial guesses and fixed during iteration. Non-negativity of the concentration was added as another constraint. Charge separated state spectrum was obtained after 100 times of iteration. The fitting result is shown in Figure 6.9a. As expected, the resulting CS spectrum shows the features of QD exciton bleach and BODIPY cation radical absorption. The CS spectrum can also be obtained by subtraction of ^{1}BODIPY* spectrum signal from TA spectrum of CdSe-BODIPY (shown in Figure 6.3a). Specifically, Because the kinetics at the range of 890-900 nm is exclusively from ^{1}BODIPY*, and there is negligible population of

^{3}BODIPY* at time range of 1-100 ps, the CS state spectrum can also be obtained by subtraction of ^{1}BODIPY* spectrum signal from TA spectrum of CdSe-BODIPY at 100 ps. As shown in Figure 6.10, the resulting CS state spectrum agrees well with that obtained from MCR fitting, showing features of CdSe exciton bleach and BODIPY cation radical absorption signal. This proves the validity of the CS spectrum obtained from MCR analysis. Note that because of the saturated probe pulse intensity at range of 760-800 nm for TA spectrum at 100 ps, the BODIPY cation radical signal is not well resolved in the CS state spectrum obtained from the subtraction method.

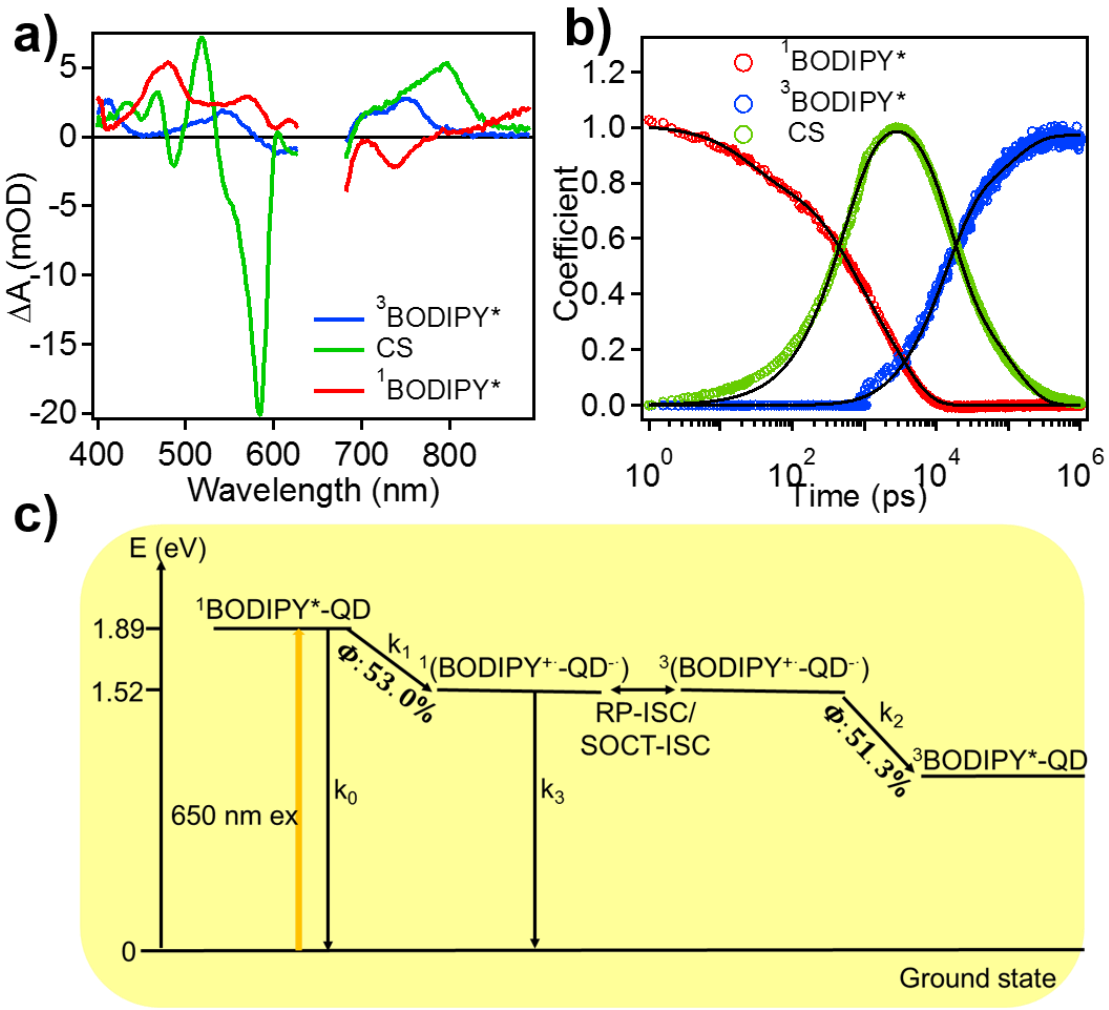

Figure 6.9: Spectra and kinetics of the involved species and processes. a) Spectra of ^{1}BODIPY*

(red line), ^{3}BODIPY* (blue line) and CS state (green line) as basis to obtain kinetics traces of each species. b) Normalized kinetics traces of ^{1}BODIPY* (red circles), ^{3}BODIPY* (blue circles) and CS state (green circles) from 1 ps to 1 μs obtained from linear regression analysis. The black lines are fitting curves of the kinetics traces according to the model in Figure 6.9c. c) Model for fitting kinetics traces in Figure 6.9b. The efficiencies of initial charge separation to form charge separated state and charge recombination to form ^{3}BODIPY* are shown in the figure.

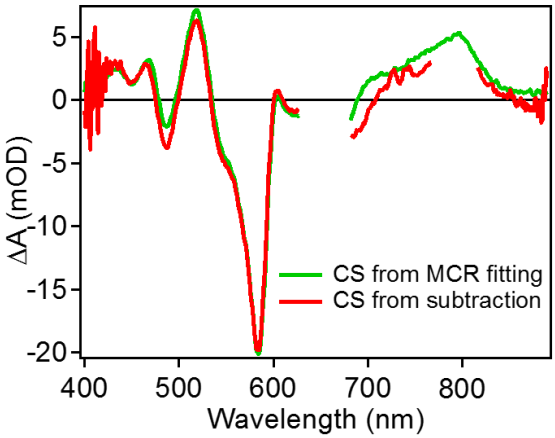

Figure 6.10: Comparison of CS state spectrum obtained by MCR fitting (shown as the green solid line) and by subtraction method (shown as the red solid line).

The kinetics for each species can be obtained from linear regression. The obtained CS spectrum from MCR was combined with ^{1}BODIPY* and ^{3}BODIPY* spectra to form basis, and the kinetics of each species was obtained by fitting spectra at each time point with linear regression.

$$xA(\lambda) + yB(\lambda) + zC(\lambda) = D(\lambda) \qquad \text{Eq. 6.1}$$

Here $A(\lambda)$, $B(\lambda)$, $C(\lambda)$ and $D(\lambda)$ are the spectra of ^{1}BODIPY*, ^{3}BODIPY*, CS state and original data, respectively. x, y and z are the coefficients for each species at each time point. Note that the extinction coefficients of each species at specific wavelengths in TAS are unknown. Therefore, the exact concentration of each species is unknown and will not be discussed. The result

of linear regression is shown in Figure 6.9b. Furthermore, ^{1}BODIPY* kinetics can be determined independently at near infrared (NIR) spectral region where spectral overlap is negligible. Figure 6.11a shows the NIR transient absorption spectra of BODIPY-CdSe QD with excitation of BODIPY. The initial spectrum from 1-10 ps has only contribution of ^{1}BODIPY* since there is almost no growth of CS state in this time range. The positive peaks are the transitions of S1->Sn. At later delay times, when the CS state is populated, there is no spectral shape change besides the decay of the amplitude of signal, indicating that there is no signal of CS state in this spectral range. This agrees with CS spectra obtained from MCR analysis, where there is negligible contribution of CS at range of 890-900 nm. In addition, there is no signal contribution from ^{3}BODIPY*, as indicated in ^{3}BODIPY* spectrum. Therefore, the decay of amplitudes of signal in 890-900 nm or NIR range can represent the kinetics of ^{1}BODIPY*. As shown in Figure 6.11b, the obtained ^{1}BODIPY* kinetics from 890-900 nm and NIR regions agree well with results from linear regression. The kinetics of other species can also be extracted independently by subtraction at isosbestic points. Kinetics of CS state can be extracted from kinetics of combination spectra at 580 nm. At this wavelength, there is no ^{3}BODIPY* contribution, thus CS state kinetics can be extracted by subtraction of ^{1}BODIPY* from total signal. The result is shown in Figure 6.11b and agrees with that from linear regression. Kinetics of ^{3}BODIPY* can be obtained from kinetics at 535 nm, where there is no contribution of CS state. After subtracting contribution of ^{1}BODIPY* from the total signal, kinetics of ^{3}BODIPY* was obtained (shown in Figure 6.11b), which also agrees with result from linear regression. All these comparison supports the results from MCR and linear regression analysis. The kinetics obtained from linear regression (shown in Figure 6.9b) shows that there is an initial fast decay of ^{1}BODIPY* with little growth of CS state from 1 to 10 ps, which can be attributed to nonradiative decay induced by partial aggregation of BODIPY, as mentioned above.[59]

At later delay time ranges, the kinetics traces show the decay of ^{1}BODIPY* within 10 ns, which leads to the corresponding growth of CS state, and the decay of CS state at longer delay times produces of ^{3}BODIPY*.

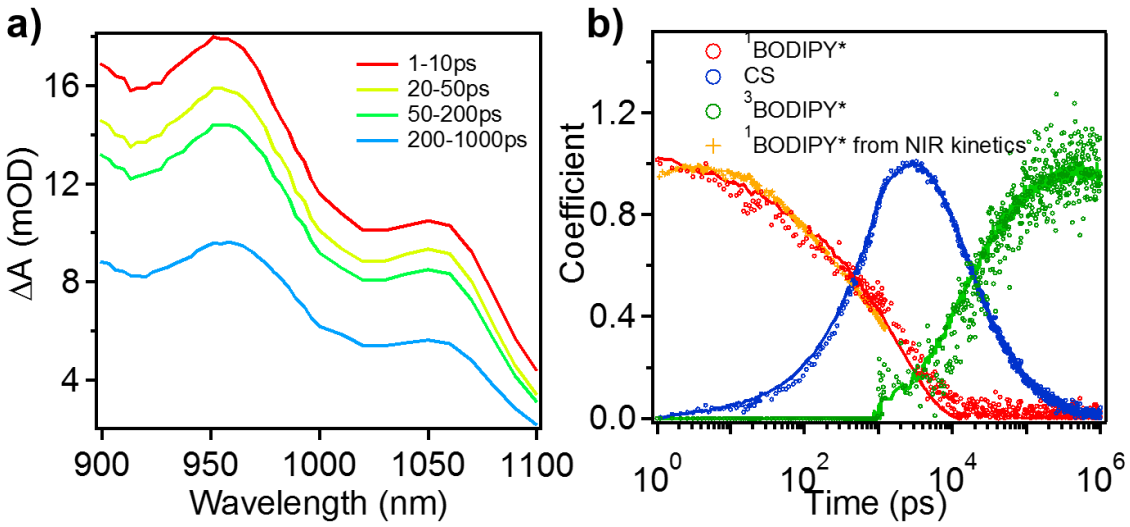

Figure 6.11: a) Near infrared transient absorption spectra of CdSe QD-BODIPY in the time range of 1 ps to 1000 ps. The wavelength of the pump pulse was 650 nm. b) Comparison of normalized kinetics traces of involved species obtained by different methods. The red, green and blue solid lines are kinetics of ^{1}BODIPY*, CS state and ^{3}BODIPY* obtained from linear regression, respectively. The red, green and blue dots are kinetics of ^{1}BODIPY*, CS state and ^{3}BODIPY* obtained from kinetics at 890-900 nm, 580 nm and 535 nm, respectively. The yellow dots are the kinetics of ^{1}BODIPY* obtained from Figure 6.11a.

The three kinetics traces were globally fit according to the kinetics model shown in Figure 6.9c. We fit the kinetics of ^{1}BODIPY*, ^{3}BODIPY* and CS state at time range of 1 ps-1 μs, when the charge recombination takes place. In this range, decay of the ^{3}BODIPY* is negligible, considering its decay time constant of (20.0±0.3) μs. With the attachment of QD, there is additional charge transfer pathway for the decay of ^{1}BODIPY*, and population of ^{1}BODIPY* can be written

as:

$$[S] = \sum_{i=1}^{2} a_i[S]_0 e^{-(k_0+k_{1i})t} + a_3[S]_0 e^{-k_{01}t} + a_4[S]_0\, e^{-k_0 t} \qquad \text{Eq. 6.2}$$

Here, to account for the heterogeneous distribution of BODIPY binding to surface of QD,[69] we have assumed two configurations in the first term, in which a_i and k_{1i} are the percentage and electron transfer rate constant of each configuration, and k_0 is the intrinsic decay rate of isolated ^{1}BODIPY*. a_3 (k_{01}) and a_4 (k_0) are the percentage (decay rate constant) of aggregated BODIPY on QD surface and free BODIPY in solution, respectively, which decay by reforming the ground state only.[59] We have assumed that the partially aggregated BODIPY and free BODIPY in solution do not contribute to charge separated state formation. CS state can be populated by charge transfer and depleted by charge recombination, as described in Eq. 6.3:

$$\frac{d[CS]_i}{dt} = k_{1i}[S]_i - (k_{2i} + k_{3i})[CS]_i \qquad \text{Eq. 6.3}$$

where k_{2i} and k_{3i} are the rates for charge recombination to the ^{3}BODIPY* and ground state, respectively. Substituting Eq. 6.4

$$[S]_i = a_i[S]_0 e^{-(k_0+k_{1i})t} \quad \text{Eq. 6.4}$$

into Eq. 6.3, we can obtain equation for CS state population:

$$[CS] = \sum_{i=1}^{2}[CS]_i = \sum_{i=1}^{2} \frac{a_i[S]_0 k_{1i}}{k_0+k_{1i}-k_{2i}-k_{3i}} [e^{-(k_{2i}+k_{3i})t} - e^{-(k_0+k_{1i})t}] \qquad \text{Eq. 6.5}$$

^{3}BODIPY* can only be obtained by charge recombination from CS state, its kinetics equation is:

$$\frac{d[T]_i}{dt} = k_{2i}[CS]_i \qquad \text{Eq. 6.6}$$

The concentration of triplet state is:

$$[\mathrm{T}] = \sum_{i=1}^{2}[T]_i = \sum_{i=1}^{2} \frac{a_i[S]_0 k_{1i} k_{2i}}{k_0+k_{1i}-k_{2i}-k_{3i}} \left[\frac{1-e^{-(k_{2i}+k_{3i})t}}{k_{2i}+k_{3i}} + \frac{e^{-(k_0+k_{1i})t}-1}{k_0+k_{1i}}\right] \qquad \text{Eq. 6.7}$$

We applied Eq. 6.2, Eq. 6.5 and Eq. 6.7 to global fit the kinetics of the three species. The global fitting result is shown in Figure 6.9b and Table 6.2.

Table 6.2: Global fitting parameters for kinetics traces of ^{1}BODIPY*, CS state and ^{3}BODIPY* in Figure 6.9b. a_1 and a_2 are the percentages of the BODIPY bound to CdSe QD surface in the two configurations. a_3 and a_4 are the percentages of partially aggregated BODIPY and other free BODIPY in solution. k_{0i} is the rate of ^{1}BODIPY* decay to ground state. k_{1i} is the rate of electron transfer from BODIPY to CdSe QD. k_{2i} and k_{3i} are the rates of charge recombination to form ^{3}BODIPY* and ground state, respectively. The reported time constants are the reciprocals of the corresponding rates.

i	a_i	$1/k_{0i}$ (ps)	$1/k_{1i}$ (ps)	$1/k_{2i}$ (ps)	$1/k_{3i}$ (ps)
1	0.466±0.073	4.20×10^3	$(1.03\pm0.03)\times10^4$	$(2.52\pm0.02)\times10^5$	$(1.88\pm0.01)\times10^5$
2	0.320±0.005	4.20×10^3	569±10	$(2.30\pm0.09)\times10^4$	$(2.86\pm0.01)\times10^4$
3	0.176±0.004	23.8±1.4			
4	0.037±0.007	4.20×10^3			

From the obtained rate constants, the efficiency of each step can be calculated from branching ratio:

$$\Phi_j = \sum_{i=1}^{2} \frac{a_i k_j}{k_j + k_{other}} \qquad \text{Eq. 6.8}$$

in which Φ_j is the efficiency of step j and k_{other} is the rate constant for the competing steps. The calculated efficiencies are shown in Figure 6.9c. The average time constants for specific processes can be calculated as:

$$\tau_j = \frac{\sum_{i=1}^{2} a_i \times \frac{1}{k_j}}{\sum_{i=1}^{2} a_i} \qquad \text{Eq. 6.9}$$

The average charge separation time constant in the ^{1}BODIPY*-QD state is (6.33 ± 1.13) ns, which results in (53.0 ± 5.7) % of charge separation (to form BODIPY$^{+\cdot}$-QD$^{-\cdot}$) and (47.0 ± 5.0) % of decay back to the ground state. The average charge recombination rates from the BODIPY$^{+\cdot}$-QD$^{-\cdot}$ state to BODIPY triplet excited state and singlet ground state are (158 ± 28) ns and (123 ± 21) ns respectively, which results in (51.3 ± 4.1) % yield of ^{3}BODIPY* formation. From the energy alignment of CdSe QD and BODIPY shown in Figure 6.6, the driving force for charge recombination from BODIPY$^{+\cdot}$-QD$^{-\cdot}$ to form ground state is large enough ($\Delta G \approx -1.52$ eV) to fall into the Marcus inverted region, resulting in slow charge recombination rate.[70] Because the energy of ^{3}BODIPY* is unknown, we could not determine the exact driving force of charge recombination to form triplet excited state. However, the similar rates of the two charge recombination pathways and the difference in their driving force indicate the possible different coupling strengths of these two pathways. The efficiency of overall triplet excited state yield is determined to be Φ = (27.2 ± 3.0) %, limited by competing pathways in both the charge separation and recombination steps. The efficiency of charge separation can be improved by increasing the rate of ET from ^{1}BODIPY* to QD, which according to extensive previous study can be achieved by increasing the ET coupling strength and/or driving force.[31, 65, 71]

6.2.5 Mechanism of triplet state formation

Extensive previous studies in organic donor-acceptor complexes have shown that triplet excited states can be generated from charge separated state intermediates through radical pair intersystem crossing (RP-ISC) or spin-orbit charge transfer intersystem crossing (SOCT-ISC). The first mechanism involves conversion from spin-correlated singlet radical pair ^{1}(Acceptor$^{-\cdot}$-Donor$^{+\cdot}$) to triplet radical pair ^{3}(Acceptor$^{-\cdot}$-Donor$^{+\cdot}$) state when the hyperfine interactions within the radical centers are larger than the exchange interaction between them.[49, 54] In the second mechanism,

triplet excited state is formed if charge recombination is accompanied by a significant change of orbital angular momentum.[51-52] A previous study of TPD-CdS QD has shown that the TPD triplet state is generated from charge separated state by exciting either the CdS QD or TPD.[54] Detailed EPR characterization and magnetic field effect (MFE) of the ^{3}TPD* yield show that the RP-ISC mechanism with spin-correlated radical pair intermediates dominates in this system, although 20% of the triplets are formed through the SOCT-ISC. The dominance of RP-ISC can be understood by the large hyperfine interactions in nanocrystal systems, in which the spin of electron can be readily flipped compared to organic chromophores. Furthermore, because of the relatively large size of the particles (on the order of 3 nm in diameter) compared to organic chromophores, the center-to-center distance between the spins is relatively large, which may lead to small exchange interaction between the electron in the QD and on the surface adsorbed molecule.[72-73]

In our TA study, we cannot distinguish ^{1}(CdSe$^{-\cdot}$-BODIPY$^{+\cdot}$) from ^{3}(CdSe$^{-\cdot}$-BODIPY$^{+\cdot}$) radical pairs, and therefore cannot distinguish the RP-ISC or SOCT-ISC pathways for triplet formation. Because ^{3}BODIPY* are generated with similar time scales of charge separation (hundreds of picoseconds) and charge recombination (tens to hundreds of nanoseconds) to previously reported CdS-TPD complexes,[54] we propose that RP-ISC may also play a dominant role in CdSe-BODIPY complexes. One notable difference between our observation and the previous report is the nature of the electron in the QD in the radical pair state. In the study of CdS-TPD complexes, the optical signal of the QD was not directly observed and the g-factor measured by EPR indicates that the electron is localized on the QD surface.[54, 74] While our study does not directly measure g-factor, direct observation of the bleach of QD exciton band in the radical-pair state confirms that the electron is at the 1S level of the QD, delocalized throughout the whole particle. Future EPR characterization and MFE experiments are required to reveal whether the

spins in the $CdSe^{-\cdot}$-$BODIPY^{+\cdot}$ radical pair are correlated.

6.3 Conclusion

In summary, we have demonstrated the generation of long-lived triplet excited state of modified BODIPY attached on CdSe QDs. TA spectroscopy confirms that the photo-excitation of a BODIPY singlet state leads to electron transfer to the QD to form a charge separated state (with an oxidized BODIPY and CB electron in the QD) with a quantum efficiency of 53.0 %, competing with radiative and nonradiative decay within BODIPY. The charge separated state undergoes charge recombination to form BODIPY singlet ground state (48.7 %) and triplet exited state (51.3 %). The overall quantum efficiency for BODIPY triplet excited state generation from its singlet excited state is calculated to be (27.2 ± 3.0) %. Future experiments, such as EPR, are required to elucidate the mechanisms of triplet excited state generation from the radical pairs. This report suggests that triplet excited state formation through charge transfer intermediate may be a general approach for these QD-adsorbate hybrids. Furthermore, the observation of long-lived radical pairs suggest that these hybrid materials may be an interesting spintronics platform for further exploration.

6.4 Reference

1. Yang, P.; Zhao, J.; Wu, W.; Yu, X.; Liu, Y., Accessing the Long-Lived Triplet Excited States in Bodipy-Conjugated 2-(2-Hydroxyphenyl) Benzothiazole/Benzoxazoles and Applications as Organic Triplet Photosensitizers for Photooxidations. *The Journal of Organic Chemistry* **2012,** *77* (14), 6166-6178.
2. Sakuma, T.; Sakai, H.; Araki, Y.; Mori, T.; Wada, T.; Tkachenko, N. V.; Hasobe, T., Long-Lived Triplet Excited States of Bent-Shaped Pentacene Dimers by Intramolecular Singlet Fission. *The Journal of Physical Chemistry A* **2016,** *120* (11), 1867-1875.
3. Köhler, A.; Bässler, H., What controls triplet exciton transfer in organic semiconductors? *J. Mater. Chem.* **2011,** *21* (12), 4003-4011.

4. Zhao, J.; Wu, W.; Sun, J.; Guo, S., Triplet photosensitizers: from molecular design to applications. *Chemical Society Reviews* **2013,** *42* (12), 5323-5351.
5. Li, X. S.; Kolemen, S.; Yoon, J.; Akkaya, E. U., Activatable Photosensitizers: Agents for Selective Photodynamic Therapy. *Adv. Funct. Mater.* **2017,** *27* (5), 1604053.
6. Majumdar, P.; Nomula, R.; Zhao, J., Activatable triplet photosensitizers: magic bullets for targeted photodynamic therapy. *J. Mater. Chem. C* **2014,** *2* (30), 5982-5997.
7. Fernandez-Moreira, V.; Thorp-Greenwood, F. L.; Coogan, M. P., Application of d6 transition metal complexes in fluorescence cell imaging. *Chem Commun (Camb)* **2010,** *46* (2), 186-202.
8. Zhao, J.; Xu, K.; Yang, W.; Wang, Z.; Zhong, F., The triplet excited state of Bodipy: formation, modulation and application. *Chemical Society Reviews* **2015,** *44* (24), 8904-8939.
9. Welin, E. R.; Le, C.; Arias-Rotondo, D. M.; McCusker, J. K.; MacMillan, D. W. C., Photosensitized, energy transfer-mediated organometallic catalysis through electronically excited nickel(II). *Science* **2017,** *355* (6323), 380.
10. Kim, T.; McCarver, S. J.; Lee, C.; MacMillan, D. W. C., Sulfonamidation of Aryl and Heteroaryl Halides through Photosensitized Nickel Catalysis. *Angew Chem Int Ed Engl* **2018,** *57* (13), 3488-3492.
11. Strieth-Kalthoff, F.; James, M. J.; Teders, M.; Pitzer, L.; Glorius, F., Energy transfer catalysis mediated by visible light: principles, applications, directions. *Chem Soc Rev* **2018,** *47* (19), 7190-7202.
12. Singh-Rachford, T. N.; Castellano, F. N., Photon upconversion based on sensitized triplet–triplet annihilation. *Coord. Chem. Rev.* **2010,** *254* (21-22), 2560-2573.
13. Fan, C.; Wu, W.; Chruma, J. J.; Zhao, J.; Yang, C., Enhanced Triplet–Triplet Energy Transfer and Upconversion Fluorescence through Host–Guest Complexation. *Journal of the American Chemical Society* **2016,** *138* (47), 15405-15412.
14. Serevičius, T.; Komskis, R.; Adomėnas, P.; Adomėnienė, O.; Kreiza, G.; Jankauskas, V.; Kazlauskas, K.; Miasojedovas, A. n.; Jankus, V.; Monkman, A.; Juršėnas, S., Triplet–Triplet Annihilation in 9,10-Diphenylanthracene Derivatives: The Role of Intersystem Crossing and Exciton Diffusion. *The Journal of Physical Chemistry C* **2017,** *121* (15), 8515-8524.
15. Yogo, T.; Urano, Y.; Ishitsuka, Y.; Maniwa, F.; Nagano, T., Highly Efficient and Photostable Photosensitizer Based on BODIPY Chromophore. *Journal of the American Chemical Society* **2005,** *127* (35), 12162-12163.
16. McGlynn, S. P.; Daigre, J.; Smith, F. J., External Heavy‐Atom Spin—Orbital Coupling Effect. IV. Intersystem Crossing. *The Journal of Chemical Physics* **1963,** *39* (3), 675-679.
17. Kozlov, D. V.; Castellano, F. N., Anti-Stokes delayed fluorescence from metal–organic bichromophores. *Chemical Communications* **2004,** (24), 2860-2861.
18. Singh-Rachford, T. N.; Castellano, F. N., Triplet Sensitized Red-to-Blue Photon Upconversion. *The Journal of Physical Chemistry Letters* **2010,** *1* (1), 195-200.
19. Islangulov, R. R.; Kozlov, D. V.; Castellano, F. N., Low power upconversion using MLCT sensitizers. *Chem. Commun.* **2005,** (30), 3776-3778.
20. Nastasi, F.; Puntoriero, F.; Campagna, S.; Diring, S.; Ziessel, R., Photoinduced intercomponent processes in multichromophoric species made of Pt(II)-terpyridine-acetylide and dipyrromethene-BF2 subunits. *Phys. Chem. Chem. Phys.* **2008,** *10* (27), 3982-6.
21. Tabachnyk, M.; Ehrler, B.; Gelinas, S.; Bohm, M. L.; Walker, B. J.; Musselman, K. P.; Greenham, N. C.; Friend, R. H.; Rao, A., Resonant energy transfer of triplet excitons from pentacene to PbSe nanocrystals. *Nat Mater* **2014,** *13* (11), 1033-8.
22. Huang, Z.; Li, X.; Mahboub, M.; Hanson, K. M.; Nichols, V. M.; Le, H.; Tang, M. L.; Bardeen,

C. J., Hybrid Molecule-Nanocrystal Photon Upconversion Across the Visible and Near-Infrared. *Nano Lett* **2015,** *15* (8), 5552-7.
23. Mongin, C.; Garakyaraghi, S.; Razgoniaeva, N.; Zamkov, M.; Castellano, F. N., Direct observation of triplet energy transfer from semiconductor nanocrystals. *Science* **2016,** *351* (6271), 369-72.
24. Yanai, N.; Kimizuka, N., New Triplet Sensitization Routes for Photon Upconversion: Thermally Activated Delayed Fluorescence Molecules, Inorganic Nanocrystals, and Singlet-to-Triplet Absorption. *Acc. Chem. Res.* **2017,** *50* (10), 2487-2495.
25. Wu, M.; Congreve, D. N.; Wilson, M. W. B.; Jean, J.; Geva, N.; Welborn, M.; Van Voorhis, T.; Bulović, V.; Bawendi, M. G.; Baldo, M. A., Solid-state infrared-to-visible upconversion sensitized by colloidal nanocrystals. *Nat. Photon.* **2015,** *10*, 31-34.
26. Li, X.; Huang, Z.; Zavala, R.; Tang, M. L., Distance-Dependent Triplet Energy Transfer between CdSe Nanocrystals and Surface Bound Anthracene. *J. Phys. Chem. Lett.* **2016,** *7* (11), 1955-9.
27. Huang, Z.; Tang, M. L., Designing Transmitter Ligands That Mediate Energy Transfer between Semiconductor Nanocrystals and Molecules. *J. Am. Chem. Soc.* **2017,** *139* (28), 9412-9418.
28. Yu, W. W.; Qu, L. H.; Guo, W. Z.; Peng, X. G., Experimental determination of the extinction coefficient of CdTe, CdSe, and CdS nanocrystals. *Chem. Mater.* **2003,** *15* (14), 2854-2860.
29. Cademartiri, L.; Montanari, E.; Calestani, G.; Migliori, A.; Guagliardi, A.; Ozin, G. A., Size-Dependent Extinction Coefficients of PbS Quantum Dots. *J. Am. Chem. Soc.* **2006,** *128* (31), 10337-10346.
30. Moreels, I.; Lambert, K.; Smeets, D.; De Muynck, D.; Nollet, T.; Martins, J. C.; Vanhaecke, F.; Vantomme, A.; Delerue, C.; Allan, G.; Hens, Z., Size-dependent optical properties of colloidal PbS quantum dots. *ACS Nano* **2009,** *3* (10), 3023-30.
31. Zhu, H.; Song, N.; Lian, T., Controlling charge separation and recombination rates in CdSe/ZnS type I core-shell quantum dots by shell thicknesses. *J. Am. Chem. Soc.* **2010,** *132* (42), 15038-45.
32. Zhu, H.; Song, N.; Rodríguez-Córdoba, W.; Lian, T., Wave Function Engineering for Efficient Extraction of up to Nineteen Electrons from One CdSe/CdS Quasi-Type II Quantum Dot. *J. Am. Chem. Soc.* **2012,** *134* (9), 4250-4257.
33. Zhu, H.; Song, N.; Lian, T., Wave Function Engineering for Ultrafast Charge Separation and Slow Charge Recombination in Type II Core/Shell Quantum Dots. *Journal of the American Chemical Society* **2011,** *133* (22), 8762-8771.
34. Scholes, G. D.; Rumbles, G., Excitons in nanoscale systems. *Nat. Mater.* **2006,** *5* (9), 683-96.
35. de Mello Donegá, C.; Bode, M.; Meijerink, A., Size- and temperature-dependence of exciton lifetimes in CdSe quantum dots. *Phys. Rev. B* **2006,** *74* (8), 085320.
36. Efros, A. L.; Rosen, M.; Kuno, M.; Nirmal, M.; Norris, D. J.; Bawendi, M., Band-edge exciton in quantum dots of semiconductors with a degenerate valence band: Dark and bright exciton states. *Phys. Rev. B* **1996,** *54* (7), 4843-4856.
37. Piland, G. B.; Huang, Z. Y.; Tang, M. L.; Bardeen, C. J., Dynamics of Energy Transfer from CdSe Nanocrystals to Triplet States of Anthracene Ligand Molecules. *J. Phys. Chem. C* **2016,** *120* (11), 5883-5889.
38. L. J. Dexter, D., A Theory of Sensitized Luminescence in Solid. *J. Chem. Phys.* **1953,** *21*, 836-850.
39. Bender, J. A.; Raulerson, E. K.; Li, X.; Goldzak, T.; Xia, P.; Van Voorhis, T.; Tang, M. L.;

Roberts, S. T., Surface States Mediate Triplet Energy Transfer in Nanocrystal-Acene Composite Systems. *J. Am. Chem. Soc.* **2018,** *140* (24), 7543-7553.
40. Huang, Z.; Xu, Z.; Mahboub, M.; Li, X.; Taylor, J. W.; Harman, W. H.; Lian, T.; Tang, M. L., PbS/CdS Core-Shell Quantum Dots Suppress Charge Transfer and Enhance Triplet Transfer. *Angew. Chem. Int. Ed.* **2017,** *56* (52), 16583-16587.
41. Meir, N.; Pinkas, I.; Oron, D., NIR-to-visible upconversion in quantum dots via a ligand induced charge transfer state. *RSC Advances* **2019,** *9* (21), 12153-12161.
42. Nienhaus, L.; Correa-Baena, J.-P.; Wieghold, S.; Einzinger, M.; Lin, T.-A.; Shulenberger, K. E.; Klein, N. D.; Wu, M.; Bulović, V.; Buonassisi, T.; Baldo, M. A.; Bawendi, M. G., Triplet-Sensitization by Lead Halide Perovskite Thin Films for Near-Infrared-to-Visible Upconversion. *ACS Energy Letters* **2019,** *4* (4), 888-895.
43. Garakyaraghi, S.; Mongin, C.; Granger, D. B.; Anthony, J. E.; Castellano, F. N., Delayed Molecular Triplet Generation from Energized Lead Sulfide Quantum Dots. *J. Phys. Chem. Lett.* **2017,** *8* (7), 1458-1463.
44. Carbonera, D.; Di Valentin, M.; Corvaja, C.; Agostini, G.; Giacometti, G.; Liddell, P. A.; Kuciauskas, D.; Moore, A. L.; Moore, T. A.; Gust, D., EPR Investigation of Photoinduced Radical Pair Formation and Decay to a Triplet State in a Carotene−Porphyrin−Fullerene Triad. *Journal of the American Chemical Society* **1998,** *120* (18), 4398-4405.
45. Gust, D.; Moore, T. A.; Moore, A. L.; Lee, S.-J.; Bittersmann, E.; Luttrull, D. K.; Rehms, A. A.; DeGraziano, J. M.; Ma, X. C.; Gao, F.; Belford, R. E.; Trier, T. T., Efficient Multistep Photoinitiated Electron Transfer in a Molecular Pentad. *Science* **1990,** *248* (4952), 199.
46. Spenst, P.; Young, R. M.; Wasielewski, M. R.; Würthner, F., Guest and solvent modulated photo-driven charge separation and triplet generation in a perylene bisimide cyclophane. *Chemical Science* **2016,** *7* (8), 5428-5434.
47. Chen, K.; Yang, W.; Wang, Z.; Iagatti, A.; Bussotti, L.; Foggi, P.; Ji, W.; Zhao, J.; Di Donato, M., Triplet Excited State of BODIPY Accessed by Charge Recombination and Its Application in Triplet–Triplet Annihilation Upconversion. *The Journal of Physical Chemistry A* **2017,** *121* (40), 7550-7564.
48. Sartor, S. M.; McCarthy, B. G.; Pearson, R. M.; Miyake, G. M.; Damrauer, N. H., Exploiting Charge-Transfer States for Maximizing Intersystem Crossing Yields in Organic Photoredox Catalysts. *Journal of the American Chemical Society* **2018,** *140* (14), 4778-4781.
49. Steiner, U. E.; Ulrich, T., Magnetic field effects in chemical kinetics and related phenomena. *Chem. Rev.* **1989,** *89* (1), 51-147.
50. Dance, Z. E. X.; Mi, Q.; McCamant, D. W.; Ahrens, M. J.; Ratner, M. A.; Wasielewski, M. R., Time-Resolved EPR Studies of Photogenerated Radical Ion Pairs Separated by p-Phenylene Oligomers and of Triplet States Resulting from Charge Recombination. *J. Phys. Chem. B* **2006,** *110* (50), 25163-25173.
51. Filatov, M. A.; Karuthedath, S.; Polestshuk, P. M.; Callaghan, S.; Flanagan, K. J.; Telitchko, M.; Wiesner, T.; Laquai, F.; Senge, M. O., Control of triplet state generation in heavy atom-free BODIPY–anthracene dyads by media polarity and structural factors. *Phys. Chem. Chem. Phys.* **2018,** *20* (12), 8016-8031.
52. Zhao, Y.; Duan, R.; Zhao, J.; Li, C., Spin–orbit charge transfer intersystem crossing in perylenemonoimide–phenothiazine compact electron donor–acceptor dyads. *Chem. Commun.* **2018,** *54* (87), 12329-12332.
53. Lu, H.; Chen, X.; Anthony, J. E.; Johnson, J. C.; Beard, M. C., Sensitizing Singlet Fission with Perovskite Nanocrystals. *Journal of the American Chemical Society* **2019,** *141* (12), 4919-

4927.
54. Weinberg, D. J.; Dyar, S. M.; Khademi, Z.; Malicki, M.; Marder, S. R.; Wasielewski, M. R.; Weiss, E. A., Spin-Selective Charge Recombination in Complexes of CdS Quantum Dots and Organic Hole Acceptors. *J. Am. Chem. Soc.* **2014,** *136* (41), 14513-14518.
55. Burkard, G.; Engel, H.-A.; Loss, D., Spintronics and Quantum Dots for Quantum Computing and Quantum Communication. *Fortschritte der Physik* **2000,** *48* (9‐11), 965-986.
56. Stotz, J. A. H.; Hey, R.; Santos, P. V.; Ploog, K. H., Coherent spin transport through dynamic quantum dots. *Nature Materials* **2005,** *4* (8), 585-588.
57. Hong, X.; Wang, Z.; Yang, J.; Zheng, Q.; Zong, S.; Sheng, Y.; Zhu, D.; Tang, C.; Cui, Y., Silylated BODIPY dyes and their use in dye-encapsulated silica nanoparticles with switchable emitting wavelengths for cellular imaging. *Analyst* **2012,** *137* (18), 4140-4149.
58. Uppal, T.; Hu, X.; Fronczek, F. R.; Maschek, S.; Bobadova-Parvanova, P.; Vicente, M. G. H., Synthesis, Computational Modeling, and Properties of Benzo-Appended BODIPYs. *Chemistry – A European Journal* **2012,** *18* (13), 3893-3905.
59. Musser, A. J.; Rajendran, S. K.; Georgiou, K.; Gai, L.; Grant, R. T.; Shen, Z.; Cavazzini, M.; Ruseckas, A.; Turnbull, G. A.; Samuel, I. D. W.; Clark, J.; Lidzey, D. G., Intermolecular states in organic dye dispersions: excimers vs. aggregates. *Journal of Materials Chemistry C* **2017,** *5* (33), 8380-8389.
60. Ekimov, A. I.; Hache, F.; Schanne-Klein, M. C.; Ricard, D.; Flytzanis, C.; Kudryavtsev, I. A.; Yazeva, T. V.; Rodina, A. V.; Efros, A. L., Absorption and intensity-dependent photoluminescence measurements on CdSe quantum dots: assignment of the first electronic transitions. *J. Opt. Soc. Am. B* **1993,** *10* (1), 100-107.
61. Huang, Y.; Xu, Z.; Jin, S.; Li, C.; Warncke, K.; Evangelista, F. A.; Lian, T.; Egap, E., Conjugated Oligomers with Stable Radical Substituents: Synthesis, Single Crystal Structures, Electronic Structure, and Excited State Dynamics. *Chemistry of Materials* **2018,** *30* (21), 7840-7851.
62. Huang, J. E.; Huang, Z. Q.; Jin, S. Y.; Lian, T. Q., Exciton Dissociation in CdSe Quantum Dots by Hole Transfer to Phenothiazine. *Journal of Physical Chemistry C* **2008,** *112* (49), 19734-19738.
63. Huang, J.; Huang, Z.; Yang, Y.; Zhu, H.; Lian, T., Multiple Exciton Dissociation in CdSe Quantum Dots by Ultrafast Electron Transfer to Adsorbed Methylene Blue. *Journal of the American Chemical Society* **2010,** *132* (13), 4858-4864.
64. Valeur, B.; Berberan‐Santos, N., Mário, Excitation Energy Transfer. In *Molecular Fluorescence: Principles and Applications, Second Edition*, Wiley-VCH, Weinheim: 2012; pp 213‐261.
65. Zhu, H. M.; Lian, T. Q., Wavefunction engineering in quantum confined semiconductor nanoheterostructures for efficient charge separation and solar energy conversion. *Energy & Environmental Science* **2012,** *5* (11), 9406-9418.
66. Mochizuki, K.; Shi, L.; Mizukami, S.; Yamanaka, M.; Tanabe, M.; Gong, W.-T.; Palonpon, A. F.; Kawano, S.; Kawata, S.; Kikuchi, K.; Fujita, K., Nonlinear fluorescence imaging by photoinduced charge separation. *Japanese Journal of Applied Physics* **2015,** *54* (4), 042403.
67. de Juan, A.; Jaumot, J.; Tauler, R., Multivariate Curve Resolution (MCR). Solving the mixture analysis problem. *Analytical Methods* **2014,** *6* (14), 4964-4976.
68. Tauler, R., Multivariate curve resolution applied to second order data. *Chemometrics and Intelligent Laboratory Systems* **1995,** *30* (1), 133-146.
69. Delerue, C.; Allan, G.; Reynaud, C.; Guillois, O.; Ledoux, G.; Huisken, F., Multiexponential

photoluminescence decay in indirect-gap semiconductor nanocrystals. *Physical Review B* **2006,** *73* (23), 235318.
70. Marcus, R. A., Electron transfer reactions in chemistry. Theory and experiment. *Reviews of Modern Physics* **1993,** *65* (3), 599-610.
71. Zhu, H.; Yang, Y.; Hyeon-Deuk, K.; Califano, M.; Song, N.; Wang, Y.; Zhang, W.; Prezhdo, O. V.; Lian, T., Auger-assisted electron transfer from photoexcited semiconductor quantum dots. *Nano Lett* **2014,** *14* (3), 1263-9.
72. Roest, M. R.; Oliver, A. M.; Paddon-Row, M. N.; Verhoeven, J. W., Distance Dependence of Singlet and Triplet Charge Recombination Pathways in a Series of Rigid Bichromophoric Systems. *The Journal of Physical Chemistry A* **1997,** *101* (27), 4867-4871.
73. Weiss, E. A.; Ahrens, M. J.; Sinks, L. E.; Gusev, A. V.; Ratner, M. A.; Wasielewski, M. R., Making a Molecular Wire: Charge and Spin Transport through para-Phenylene Oligomers. *Journal of the American Chemical Society* **2004,** *126* (17), 5577-5584.
74. Khudyakov, I. V.; Serebrennikov, Y. A.; Turro, N. J., Spin-orbit coupling in free-radical reactions: on the way to heavy elements. *Chem. Rev.* **1993,** *93* (1), 537-570.

Chapter 7. Competition of Dexter, Förster and Charge Transfer Pathways for Quantum Dot Sensitized Triplet Generation

Reproduced in part with permission from: Jin, T.; Uhlikova, N.; Xu, Z.; Zhu, Y.; Huang, Y.; Egap, E.; Lian, T., *J. Chem. Phys.* **2020**, 152, 214702. Copyright AIP Publishing 2020

7.1 Introduction

Due to broad applications of long lived triplet excited states in triplet-triplet annihilation,[1-3] photodynamic therapy,[4-5] bioimaging[6-7] and light emitting devices,[8-9] extensive research efforts have been devoted to efficient generation of triplet excited states.[2, 10-12] Among various schemes for harvesting triplet excitons, sensitization by molecular antenna complexes has been proved to be promising especially for triplet emitters with limited light absorption range, small extinction coefficient or low intrinsic intersystem crossing efficiency.[10, 13-15] A typical sensitization scheme involves excitation of the antenna, efficient intersystem crossing for triplet exciton generation in the antenna and transfer of the triplet exciton to the acceptor through either direct Dexter energy transfer (DET)[16-18] or sequential charge transfer.[19-22] DET involves concerted electron and hole transfers from the donor to the acceptor. [17, 23-30]

In more recent years, quantum dot (QD)-sensitized triplet exciton generation has received intense interest,[2, 31-34] due to several advantages of QDs, including broad absorption range,[35-37] large extinction coefficient[38-39] and robust tunability in structures and photophysical properties.[40-43] Both solution and solid-state photon upconversion devices that are based on QD sensitized triplet generation have been reported,[44-46] and their efficiencies can often be optimized through the engineering of QD structures and surfaces.[47-50] Despite the impressive progress, the underlying

mechanism of QD sensitized triplet exciton generation remains ambiguous.[24, 51-54] It has been proposed that triplet excitons in acceptors are generated through direct DET from the excited QD.[31, 55] Triplet formation through charge separated intermediate state has also been reported.[52, 54, 56-57] In addition, Förster resonance energy transfer (FRET) from the QD to the acceptor (forming singlet excited state), if energetically allowed, may also compete with the DET pathway.[58] Therefore, it is important to evaluate how direct Dexter, Förster and charge transfer processes compete in QD-acceptor complexes.

In this chapter we investigate the competition of direct DET, FRET and charge transfer pathways for the formation of triplet excited state using CdSe QD with modified boron dipyrromethene (BODIPY) attached on surface as a model system. We show that upon the excitation of the CdSe QD, FRET and charge transfer pathways outcompete the direct DET process. Both pathways lead to the formation of a charge separated state ($QD^{-\cdot}$-$BODIPY^{+\cdot}$) consisting of an oxidized BODIPY and a conduction band (CB) edge electron in the QD, which eventually evolves into BODIPY triplet excited state (^{3}BODIPY*) through charge recombination as shown in Figure 7.1a.

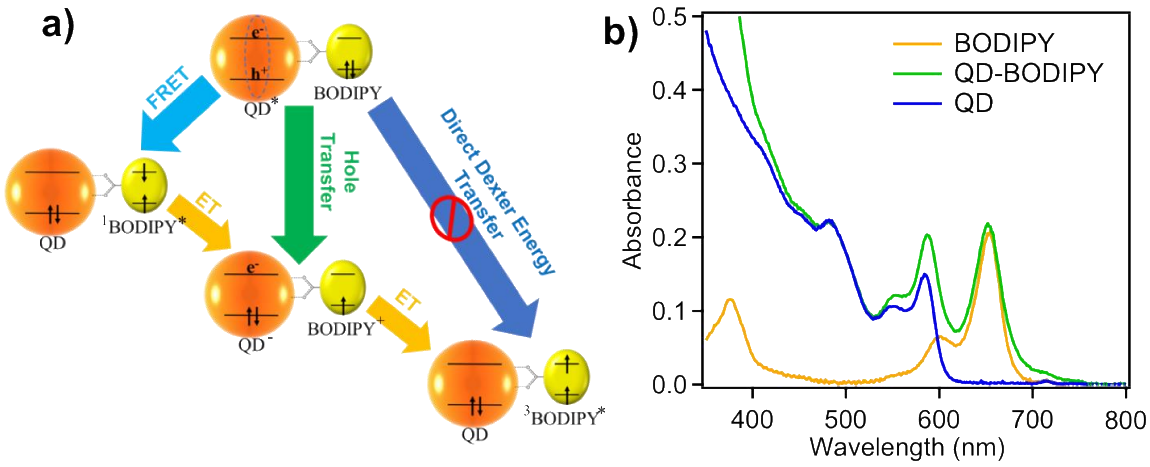

Figure 7.1: a) Scheme of possible QD-sensitized BODIPY triplet formation pathways in CdSe

QD-BODIPY complexes: i) direct DET from excited QDs (QD*-BODIPY) (navy blue arrow), ii) sequential hole transfer from QD*-BODIPY to form $QD^{-\cdot}$-$BODIPY^{+\cdot}$ (green arrow), followed by electron transfer (denoted as ET) back to BODIPY to form QD-^{3}BODIPY* (yellow arrow), and iii) FRET from QD to form QD-^{1}BODIPY* (light blue arrow) followed by electron transfer to QD to form $QD^{-\cdot}$-$BODIPY^{+\cdot}$ and back ET to form QD-^{3}BODIPY* (yellow arrows). b) UV-vis absorption spectra of CdSe QD (blue) (λ_{Amax} (ε) = 584 nm (2.15×10^5 $M^{-1}cm^{-1}$)), BODIPY (yellow) (λ_{Amax} (ε) = 656 nm (9.18×10^4 $M^{-1}cm^{-1}$)) and QD-BODIPY complex (green).

7.2 Results and discussion

7.2.1 Sample preparation and optical properties

CdSe QDs and modified BODIPY (Compound 3 in Scheme 2.1) were synthesized following procedures from previous literature[59] (see see Section 2.1.2, Section 2.1.4 and Figure 2.1-2.3). Figure 7.1b shows the UV-vis absorption spectra of CdSe QDs, free BODIPY and QD-BODIPY complexes. The absorption spectrum of free BODIPY shows a S_0-S_1 transition centered at 656 nm, as well as a higher energy transition (S_0-Sn) at 376 nm. The peak at 584 nm in the CdSe QD spectrum corresponds to the lowest energy $1S_{3/2}$-$1S_e$ exciton transition.[37] These transitions show negligible shift upon the adsorption of BODIPY onto QD. The absorption spectrum of QD-BODIPY shows additional spectral features in the range of 700-750 nm, which can be attributed to partial aggregation of BODIPY on the QD surface.[59]

7.2.2 Transient absorption spectra of QD and QD-BODIPY complex

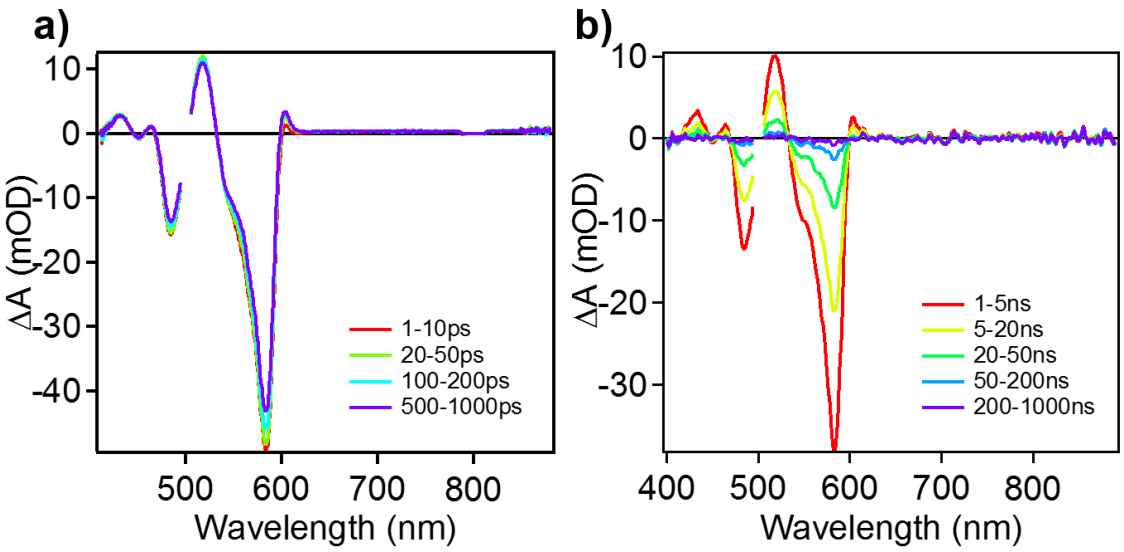

Figure 7.2: a) Femtosecond (1 ps to 1000 ps) and b) nanosecond (1 ns to 1000 ns) transient absorption (TA) spectra of free CdSe QD. The pump wavelength was set to be 500 nm.

Transient absorption spectra of free CdSe QD were collected with 500 nm excitation pulse. At delay time range of 1 ps-1 ns (Figure 7.2a), the main feature of the spectra is large exciton bleach (XB) peak centered at 584 nm resulting from state filling of 1S level by photoexcited electron.[60] The local dc electric field generated by photoexcited electron and hole pair induced the Stark effect, which contributes to the derivative-like features in the spectra.[41] The spectra shape evolution from 1 ps to 50 ps may be attributed to the change in dc electric field. At the nanosecond time scale (Figure 7.2b), there is no longer spectra shape evolution but the signal amplitude decay. The decay for QD signal can be well fit with four exponential function. (see Table 7.1).

The TA spectra of QD-BODIPY from 1 ps to 1 ns and from 1 ns to 1 μs after 500 nm excitation are shown in Figure 7.3a and Figure 7.3b**,** respectively. Because there is negligible absorption of BODIPY at 500 nm (Figure 7.1b), CdSe QDs are selectively excited at this wavelength. At delay time 1ps-1ns, QD XB, resulted from the state filling of conduction band 1S

electron level, is found to decay faster than that in free CdSe QD (see Figure 7.2), indicating that the adsorbed BODIPY induces electron or exciton transfer from the QD.[60-61] At the same delay time window, there is a growth of two negative peaks centered at 656 nm and 735 nm (see inset of Figure 7.3a). The negative peak at 656 nm can be assigned to the ground state bleach (GSB) of BODIPY and the negative peak at 735 nm is attributed to the stimulated emission (SE) of ^{1}BODIPY* with also contributions from the overlapping ground state bleach of BODIPY aggregates.[59] These two features indicate the formation of ^{1}BODIPY*, which is further supported by the photoinduced absorption (IA) peak at ~ 960 nm in the near infrared (NIR) TA spectra (see Figure 7.4) due to the S_1->Sn transition. Figure 7.4a and Figure 7.4b show the NIR TA spectra of CdSe QD and QD-BODIPY, respectively, within 1 ns after 500 nm excitation. For CdSe QD, a broad positive peak at 900 nm-1100 nm is observed in the delay time range, which is attributed to photoinduced absorption of CdSe QD.[62] Within 1 ns, there is only decay of the signal amplitude without any spectral shape change. For QD-BODIPY, the spectrum shape in initial time range is the same as that in CdSe QD. However, the broad QD photoinduced absorption signal decays to form a new spectral feature with a peak centered at ~960 nm. Previous study attributed this peak to be BODIPY singlet excited state absorption (S1->Sn),[59] suggesting BODIPY singlet excited state formation within 1 ns. ^{1}BODIPY* is formed by FRET from excited QD to BODIPY (shown as light blue arrow in Figure 7.1a), which agrees with the faster decay of QD XB. This process is allowed because of the large overlap of CdSe QD fluorescence spectrum and BODIPY absorption spectrum (see Figure 7.5).[63]

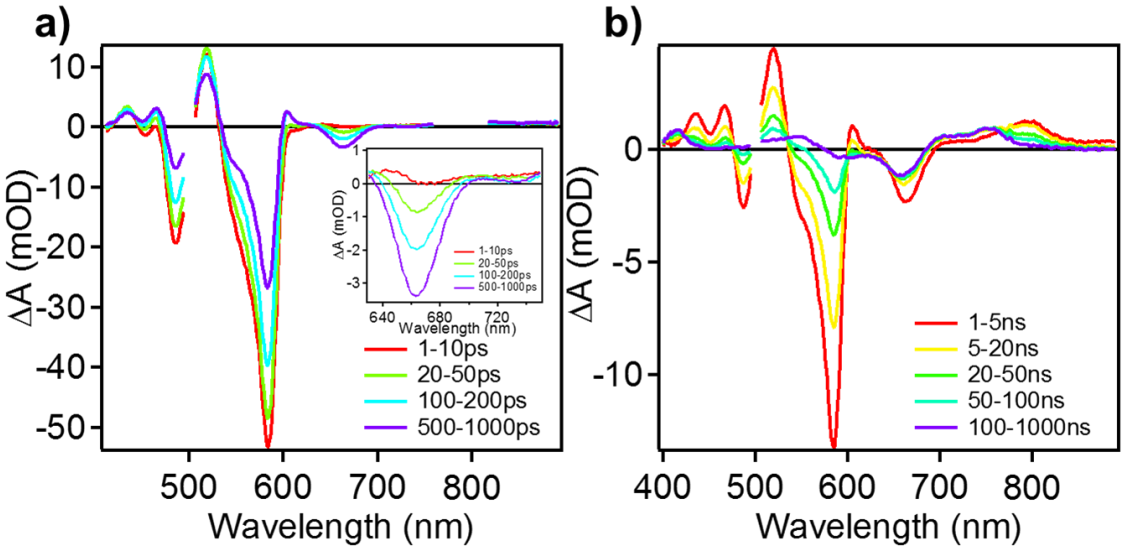

Figure 7.3: TA spectra of QD-BODIPY complexes measured with 500 nm pulse excitation at delay time windows of a) 1-1000 ps and b) 1-1000 ns. The inset in Figure 7.3a: the expanded view of the ^{1}BODIPY* spectral features from 630 to 750 nm.

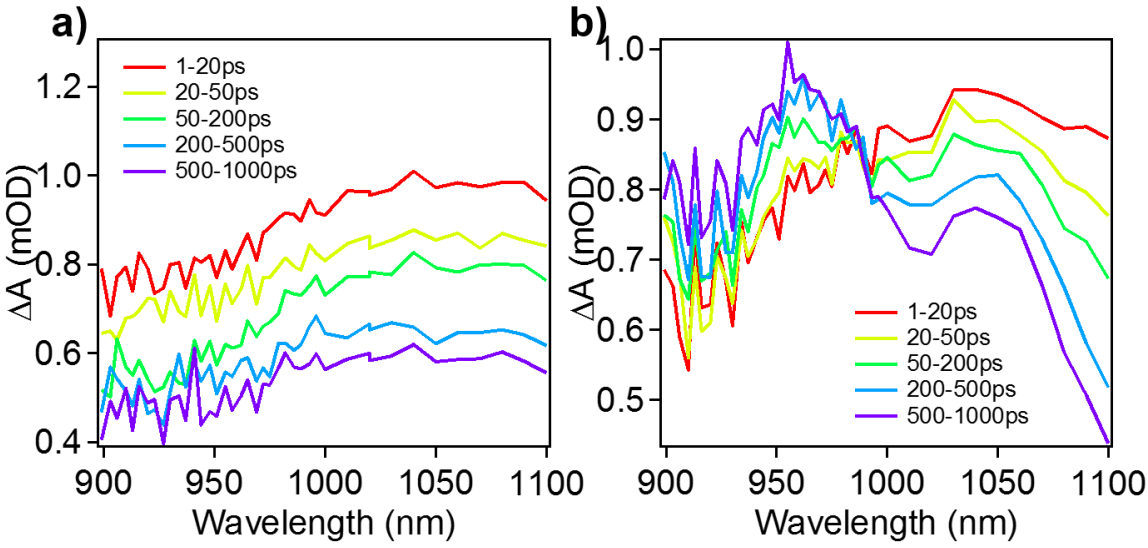

Figure 7.4: NIR TA spectra of a) CdSe QD and b) QD-BODIPY from 1 ps to 1 ns after 500 nm excitation.

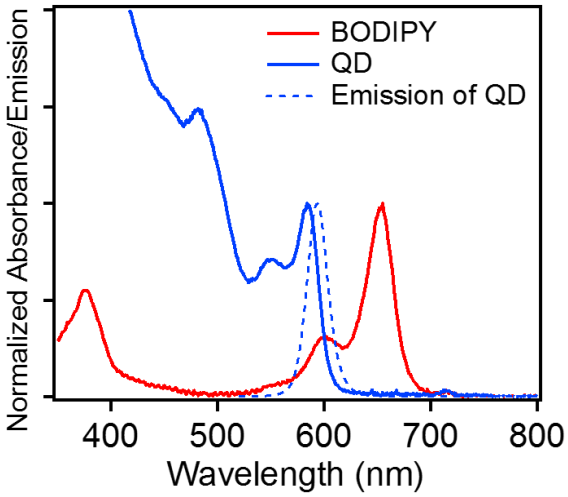

Figure 7.5: Absorption and emission spectra of free CdSe QD (blue solid line and blue dashed line, respectively) (λ_{Amax} (ε) = 584 nm (2.15×10^5 $M^{-1}cm^{-1}$), λ_{Emax} = 591 nm), and absorption spectrum of free BODIPY (red line) (λ_{Amax} (ε) = 656 nm (9.18×10^4 $M^{-1}cm^{-1}$)).

Interestingly, the transient spectra also show the formation of a positive peak centered at around 800 nm, which is not well resolved in the TA spectra at < 1ns (Figure 7.3a) because of the saturated probe intensity at this wavelength but can be observed in > 1ns TA spectra measured with a different probe source (Figure 7.3b). According to the results in Chapter 6, this peak can be assigned to BODIPY cation radical, which was produced by electron transfer from ^{1}BODIPY* to QD to form a charge separated (CS) state, $QD^{-\cdot}$-$BODIPY^{+\cdot}$, following the direct excitation of BODIPY.[59] With the excitation of QD, the same ^{1}BODIPY* can be populated by FRET, and thus the same CS state can also be generated by electron transfer from ^{1}BODIPY* to QD (shown as yellow arrow in Figure 7.1a).

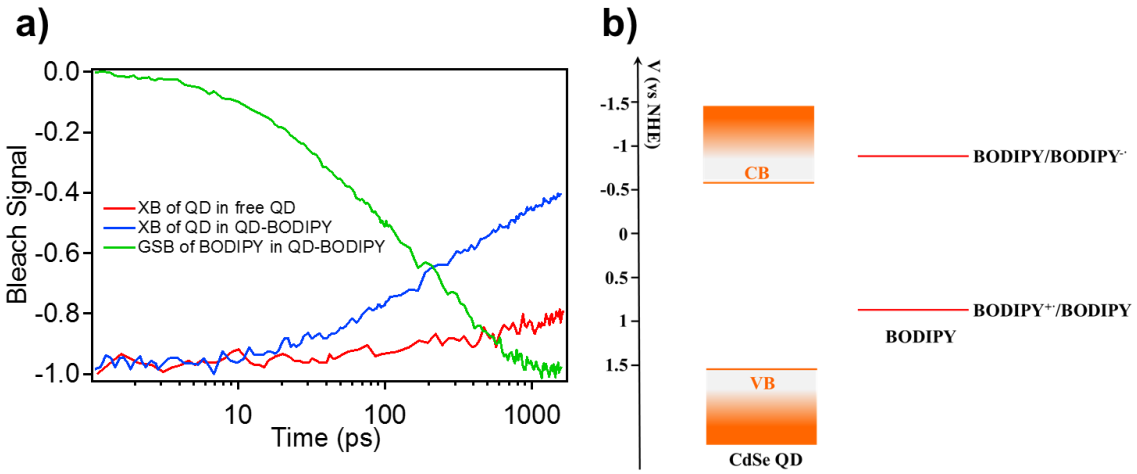

Figure 7.6: a) Comparison of TA kinetics of CdSe QD XB in free CdSe QDs (red) and QD-BODIPY complexes (blue), and BODIPY GSB kinetics in QD-BODIPY complexes (green line) measured with 500 nm excitation. The BODIPY GSB at this time range is mainly determined by formation of CS state through hole transfer from QD (growth of GSB), formation of QD-^{1}BODIPY* through FRET (growth of GSB) and formation of CS state through electron transfer from QD-^{1}BODIPY* (decrease of GSB). The kinetics of QD-XB in QD-BODIPY is mainly determined by FRET from QD to BODIPY (recovery of XB) and the following back electron transfer from ^{1}BODIPY* to QD (increase of XB amplitude). b) Reported energy alignment of CdSe QD and BODIPY.

Another possible pathway for forming the CS state is direct hole transfer from QD without going through ^{1}BODIPY* intermediate (shown as green arrow in Figure 7.1a), which is energetically allowed (Figure 7.6). Comparison of the kinetics of BODIPY GSB growth (at 656 nm) and QD XB decay (at 584 nm) of QD-BODIPY complexes (Figure 7.6a) shows that at delay time from 1 to 10 ps, there is substantial growth of BODIPY GSB signal, while there is negligible difference between the CdSe QD XB recovery in QD-BODIPY complex and that in free CdSe

QDs. Since XB is dominated by the state filling of the CdSe QD 1S conduction band level, this result suggests negligible FRET or electron transfer from the QD to BODIPY at this time range. Therefore, the BODIPY GSB signal growth at this time is caused by hole transfer from QD to BODIPY to form $QD^{-\cdot}$-$BODIPY^{+\cdot}$, which is consistent with the energy alignment of the conduction and valance band edges of QD and redox potential of BODIPY shown in Figure 7.6b.

On the > 1 ns time scale, the amplitude of the CS state signal decays while three positive peaks centered at 412, 570 and 750 nm are developing. These features can be attributed to ^{3}BODIPY* T_1->T_n absorption bands.[59] The amplitudes of these peaks reach maximum at 100 ns and decay on the > 1000 ns time scale.[59] The mechanisms for ^{3}BODIPY* formation will be further discussed below.

7.2.3 Spectra and kinetics analysis

Because of the large spectral and temporal overlaps of signals from different species in the TA spectra, we first extract the kinetics of each species by employing linear regression to fit the TA spectral evolution. The TA spectra contain time-dependent contribution of four species: QD*-BODIPY, $QD^{-\cdot}$-$BODIPY^{+\cdot}$, QD-^{1}BODIPY* and QD-^{3}BODIPY* whose representative spectra can be obtained independently as shown in Figure 7.7a. QD*-BODIPY spectrum is obtained from the averaged TA spectra of free CdSe QD (Figure 7.2). The TA spectra of $QD^{-\cdot}$-$BODIPY^{+\cdot}$, QD-^{1}BODIPY* and QD-^{3}BODIPY* were obtained in Chapter 6.[59] TA spectra at each delay time point are fit with linear regression to the sum of these four components to obtain the kinetics of each species. The result of the linear regression is shown in Figure 7.7b. In order to test the validity of the kinetics of involved species extracted from the linear regression fit described in the main text, we compare the original TA spectra of QD-BODIPY complex (in Figure 7.3) and the TA spectra reconstructed from linear regression analysis at four delay time points: 10 ps, 100 ps, 1000 ps and

10 ns. For the reconstructed spectra, amplitudes at each wavelength can be expressed as

$$K(\lambda,t) = x(t)A(\lambda) + y(t)B(\lambda) + z(t)C(\lambda) + u(t)D(\lambda) \qquad \text{Eq. 7.1}$$

in which $K(\lambda,t)$ is the amplitude of the reconstructed spectra at specific wavelength and time, x(t), y(t), z(t) and u(t) represent the kinetics for QD*-BODIPY, $QD^{-\cdot}$-$BODIPY^{+\cdot}$, QD-^{1}BODIPY* and QD-^{3}BODIPY* at the corresponding time (shown in Figure 7.7b), and $A(\lambda)$, $B(\lambda)$, $C(\lambda)$ and $D(\lambda)$ are the amplitudes of basis spectra of QD*-BODIPY, $QD^{-\cdot}$-$BODIPY^{+\cdot}$, QD-^{1}BODIPY* and QD-^{3}BODIPY* at the corresponding wavelength (shown in Figure 7.7a). The results are plotted in Figure 7.8, which shows that the original spectra and those reconstructed from linear regression result agree well with each other, indicating the validity of the result from linear regression. The kinetics traces in Figure 7.7b show a faster decay of CdSe QD exciton in QD-BODIPY complexes compared to free CdSe QDs (Figure 7.9) and the sequential formation of $QD^{-\cdot}$-$BODIPY^{+\cdot}$(CS), QD-^{1}BODIPY* and QD-^{3}BODIPY*.

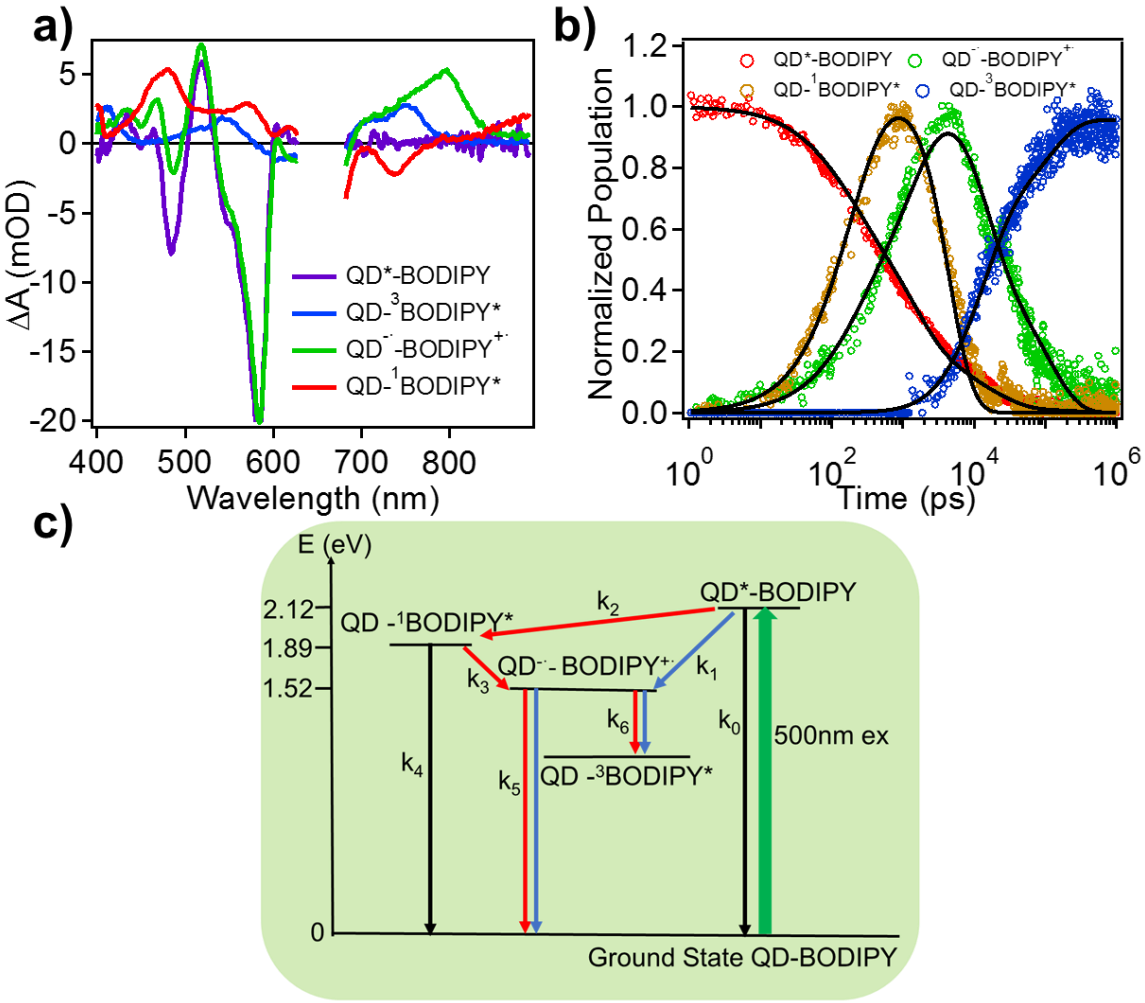

Figure 7.7: TA spectra and kinetics of involved species in QD-BODIPY complexes generated after the excitation of the QD. a) Spectra of QD*-BODIPY (purple line), QD-^{1}BODIPY* (red line), QD-^{3}BODIPY* (blue line) and QD$^{-\cdot}$-BODIPY$^{+\cdot}$ (green line) used as the basis to fit the time-dependent TA spectra. b) Kinetics traces (from 1 ps to 1 μs) of QD*-BODIPY (red dots), QD-^{1}BODIPY* (yellow dots), QD-^{3}BODIPY* (blue dots) and QD$^{-\cdot}$-BODIPY$^{+\cdot}$ (green dots) in QD-BODIPY complexes obtained from linear regression fitting of the TA spectra. The black lines correspond to the global fitting curves according to the kinetics model depicted in Figure 7.7c. c) Energetics of the relevant states generated by photoexcitation of QD-BODIPY complexes and the rate constant of their interconversion. Red and blue arrows represent the FRET and charge transfer

pathways, respectively, both leading to generation of QD-^{3}BODIPY*. Black arrows represent decay of various excited states to the ground state.

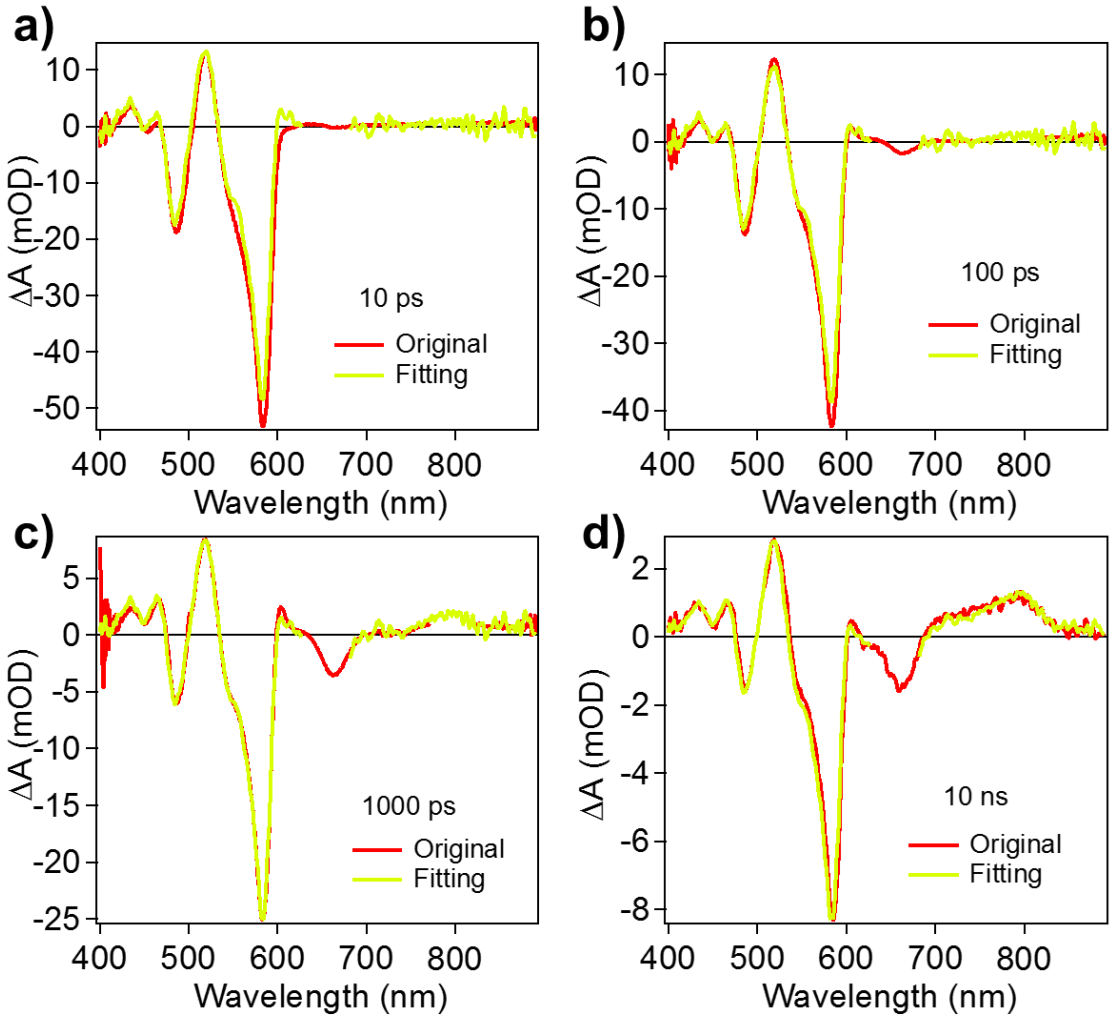

Figure 7.8: Comparison of original TA spectra of QD-BODIPY complex (red) and TA spectra reconstructed from linear regression analysis (yellow) at delay time of a). 10 ps, b). 100 ps, c).1000 ps and d) 10 ns.

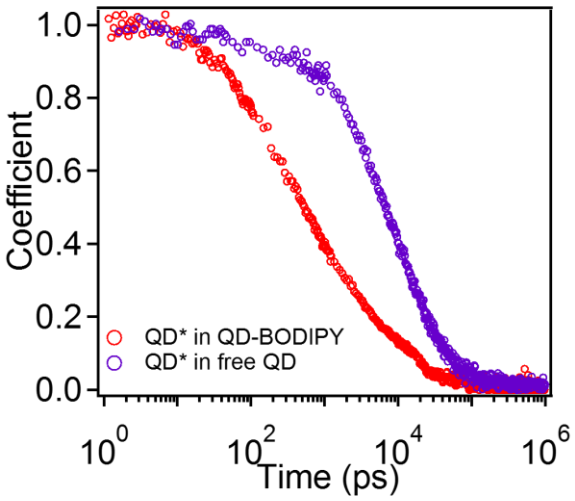

Figure 7.9: Comparison of CdSe QD exciton kinetics in QD-BODIPY complex (red dots) and in free QD (purple dots). QD exciton kinetics in QD-BODIPY was obtained from linear regression of TA spectra in Figure 7.3. QD exciton kinetics in free QD was obtained from extraction of QD XB kinetics in Figure 7.2.

Figure 7.7c shows the relevant states and processes involved in QD-BODIPY complexes after the excitation of the QD, including both the processes that lead to the triple generation and the competing processes that lead to the ground state formation. It has been shown in Chapter 6 that QD-^{1}BODIPY* (generated by direct excitation at 650 nm) can decay back to the ground state (rate constant k_4) or form CS state ($QD^{-\cdot}$-$BODIPY^{+\cdot}$) by electron transfer to the QD (with rate constant k_3); and this $QD^{-\cdot}$-$BODIPY^{+\cdot}$ radical pair intermediate can undergo charge recombination to form QD-^{3}BODIPY* (with rate constant k_6) or QD-BODIPY ground state (with rate constant k_5).[59] Because the same QD-^{1}BODIPY* can be generated by FRET from the excited QD (with rate constant k_2), all the subsequent photophysical processes emerging from QD-^{1}BODIPY* should take place with the same rate constants (k_3, k_4, k_5 and k_6),[59] which eventually result in the generation of QD-^{3}BODIPY* and ground state (shown in red arrows in Figure 7.7c). The rate

constants (k_3, k_4, k_5 and k_6) associated with these processes have already been determined from Chapter 6 except for k_2, which is used as a variable fitting parameter. The $QD^{-\cdot}$-$BODIPY^{+\cdot}$ CS state can also be generated by direct hole transfer from QD (with rate constant k_1), which is followed by charge recombination to generate QD-^{3}BODIPY* and ground state (shown in blue arrows in Figure 7.7c, with rate constant k_6 and k_5, respectively). This pathway for triplet excited state generation can be considered as sequential hole and electron transfer from the CdSe QD through a CS intermediate state. Another possible pathway for the formation of QD-^{3}BODIPY* is DET from excited QDs without any intermediate states. However, as shown in Figure 7.7b, QD-^{3}BODIPY* population begins to form after 1 ns, when only 20% of QD*-BODIPY remains. This indicates that > 80% of CdSe QD excitons undergo fast FRET and hole transfer within 1 ns, outcompeting the direct DET pathway. In order to illustrate the main contribution of ^{3}BODIPY* growth is from charge recombination of CS state, with negligible contribution from DET pathway, we compare the consumption of CS state with growth of ^{3}BODIPY*. The CS state population reaches maximum at ~5 ns (shown in Figure 7.7b), after which the consumption of CS state agrees well with ^{3}BODIPY* growth. Note that the small difference between the two kinetics at delay time range of 5 ns to 10 ns is present because there is still slight growth of CS state accompanied with CS state consumption at this range. In the later time range, the CS state kinetics is mostly composed of its consumption, which matches the growth of ^{3}BODIPY*. This comparison further supports the argument that the ^{3}BODIPY* growth is mainly from charge recombination pathway. This finding is consistent with previously reported DETs from QDs to acceptors, which are often relatively slow compared to FRET and charge transfer rates.[31-32]

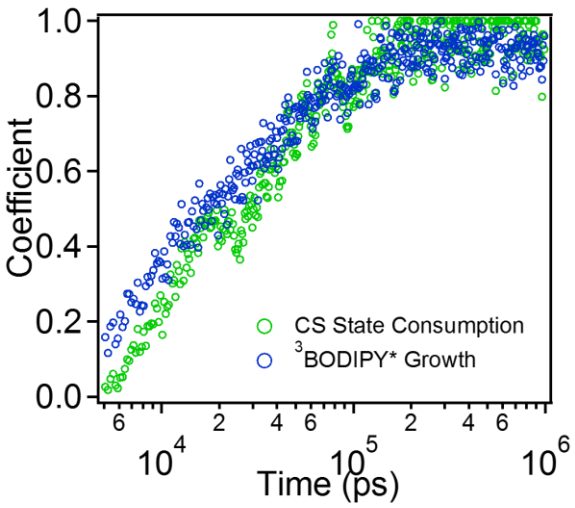

Figure 7.10: Comparison of normalized CS state consumption kinetics (green circles) and ^{3}BODIPY* growth kinetics (blue circles) obtained from Figure 7.7b at delay time range of 5 ns-1 μs.

The kinetics traces of QD*-BODIPY, $QD^{-\cdot}$-$BODIPY^{+\cdot}$, QD-^{1}BODIPY* and QD-^{3}BODIPY* were fit globally according to the kinetics model in Figure 7.7c. In the time range of 1 ps-1 μs, decay of QD-^{3}BODIPY* population can be neglected and thus was not included in the fitting. First, kinetics of CdSe QD exciton in free CdSe QDs (shown in Figure 7.9**)** was fit with four exponential function:

$$[QD]^*_{free} = [QD]_0 \sum_{i=1}^{4} a_i e^{-k_{0i}t} \qquad \text{Eq. 7.2}$$

in which a_i is the percentage of QD exciton with decay rate constant of k_{0i}. The number of exponentials (or extent of heterogeneity) depends on the quality of the sample.[64] XB kinetics in many core-only CdSe QD samples can be fit by 2-3 exponential functions.[64-65] However, this sample requires 4 exponentials, probably indicating relatively large heterogeneity. When the QD is attached with BODIPY, hole transfer and FRET to BODIPY are the additional decay channels of QD exciton, and the QD exciton population can be written as:

$$[QD]^* = p[QD]_0 \sum_{i=1}^{4} \sum_{f=1}^{2} \sum_{j=1}^{2} a_i c_{1j} c_{2f} e^{-(k_{0i}+k_{1j}+k_{2f})t} + (1-p)[QD]_0 \sum_{i=1}^{4} a_i e^{-k_{0i}t}$$

Eq. 7.3

In the equation above, p and (1-p) are the percentages of QD attached with one or more BODIPY and free QD with no BODIPY attached, respectively. Because of the different numbers of adsorbed BODIPY on QD surface, which could result in different apparent rates of hole transfer and FRET, two rate terms for hole transfer (k_{1j}) and FRET (k_{2f}) were included with percentage of c_{1j} and c_{2f} (j, f = 1 or 2), respectively.

^{1}BODIPY* (denoted as [S] in the kinetics equations) can be populated by FRET from QD (with rate constant k_2), and can decay to form CS state (with rate constant k_3) or ground state (with rate constant k_4):

$$\frac{d[S]}{dt} = k_2[QD]^* - (k_3 + k_4)[S] \qquad \text{Eq. 7.4}$$

CS state can be populated by electron transfer from ^{1}BODIPY* (with rate constant k_3) or by direct hole transfer from QD exciton (with rate constant k_2), and decay through charge recombination to form ground state (with rate constant k_5) or ^{3}BODIPY* (denoted as [T] in the kinetics equations) (with rate k_6):

$$\frac{d[CS]}{dt} = k_1[QD]^* + k_3[S] - (k_5 + k_6)[CS] \qquad \text{Eq. 7.5}$$

$$\frac{d[T]}{dt} = k_6[CS] \qquad \text{Eq. 7.6}$$

After substituting the first term of Equation 7.3 into Equation 7.4, Equation 7.5 and Equation 7.6 to solve these equations, we can obtain:

$$[S] = d \sum_{i=1}^{4} \sum_{f=1}^{2} \sum_{j=1}^{2} \sum_{u=1}^{2} \{b_u a_i c_{1j} c_{2f} \{\frac{k_{2f}}{k_{0i}+k_{1j}+k_{2f}-k_{3u}-k_{4u}} \Big[e^{-(k_{3u}+k_{4u})t} -$$

$$e^{-(k_{0i}+k_{1j}+k_{2f})t}\Big]\}\} \qquad \text{Eq. 7.7}$$

$$[CS] = e\sum_{f=1}^{2}\sum_{i=1}^{4}\sum_{j=1}^{2}\sum_{u=1}^{2}\{b_u\, a_i c_{1j} c_{2f}\{\frac{k_{1j}}{k_{5u}+k_{6u}-k_{0i}-k_{1j}-k_{2f}}[\, e^{-(k_{0i}+k_{1j}+k_{2f})t} -$$

$$e^{-(k_{5u}+k_{6u})t}] + \frac{k_{2f}k_{3u}}{(k_{0i}+k_{1j}+k_{2f}-k_{3u}-k_{4u})(k_{5u}+k_{6u}-k_{3u}-k_{4u})}[e^{-(k_{3u}+k_{4u})t} - e^{-(k_{5u}+k_{6u})t}] +$$

$$\frac{k_{2f}k_{3u}}{(k_{0i}+k_{1j}+k_{2f}-k_{3u}-k_{4u})((k_{0i}+k_{1j}+k_{2f}-k_{5u}-k_{6u})}[e^{-(k_{0i}+k_{1j}+k_{2f})t} - e^{-(k_{5u}+k_{6u})t}]\}\}$$ Eq. 7.8

$$[T] = g\sum_{i=1}^{4}\sum_{f=1}^{2}\sum_{j=1}^{2}\sum_{u=1}^{2}\{b_u a_i c_{1j} c_{2f}\{\frac{k_{1j}k_{6u}}{k_{5u}+k_{6u}-k_{0i}-k_{1j}-k_{2f}}[\frac{1-e^{-(k_{0i}+k_{1j}+k_{2f})t}}{k_{0i}+k_{1j}+k_{2f}} -$$

$$\frac{1-e^{-(k_{5u}+k_{6u})t}}{k_{5u}+k_{6u}}] + \frac{k_{2f}k_{3u}}{(k_{0i}+k_{1j}+k_{2f}-k_{3u}-k_{4u})(k_{5u}+k_{6u}-k_{3u}-k_{4u})}\left[\frac{1-e^{-(k_{3u}+k_{4u})t}}{k_{3u}+k_{4u}} - \frac{1-e^{-(k_{5u}+k_{6u})t}}{k_{5u}+k_{6u}}\right] +$$

$$\frac{k_{2f}k_{3u}}{(k_{0i}+k_{1j}+k_{2f}-k_{3u}-k_{4u})((k_{0i}+k_{1j}+k_{2f}-k_{5u}-k_{6u})}[\frac{1-e^{-(k_{0i}+k_{1j}+k_{2f})t}}{k_{0i}+k_{1j}+k_{2f}} - \frac{1-e^{-(k_{5u}+k_{6u})t}}{k_{5u}+k_{6u}}]\}\}$$ Eq. 7.9

in which two configurations of BODIPY binding to QD surface were assumed (with percentage of b_1 and b_2). The configurations of BODIPY binding could alter the rates of electron transfer from BODIPY to QD and the following charge recombination to form ground state and ^{3}BODIPY*. In Eq. 7.7, Eq. 7.8 and Eq. 7.9, d, e and g are the normalization factors. Eq. 7.3, Eq. 7.7, Eq. 7.8 and Eq. 7.9 were applied to global fit the kinetics traces in Figure 7.7b. b_u (u=1 or 2), k_{3u}, k_{4u}, k_{5u} and k_{6u} were predetermined from Chapter 6,[59] in which BODIPY in QD-BODIPY complex was excited with 650 nm pulse to form ^{1}BODIPY*. The result of the global fitting is shown in Figure 7.7b and Table 7.1, which agrees reasonably well with the measured kinetics.

Table 7.1: Global fitting parameters for kinetics traces of QD*-BODIPY, $QD^{-\cdot}$-$BODIPY^{+\cdot}$ (CS state), QD-^{1}BODIPY* and QD-^{3}BODIPY* in Figure 7.7b. a_i is the percentage of QD exciton with intrinsic decay rate constant k_{0i}. c_{1j} represents the percentage of QD-BODIPY complex with hole transfer rate constant k_{1j}. In the fitting result, k_{12} is extremely close to 0, indicating that the corresponding QD-BODIPY complex is inactive for hole transfer pathway. This component will not be shown in the table. c_{2f} corresponds to the percentage of QD-BODIPY complex with FRET

rate constant k_{2f}. b_u is the percentage of different configurations of BODIPY binding to QD surface. k_{3u} stands for the rate constant of electron transfer from BODIPY to QD after generation of ^{1}BODIPY*. k_{4u} is the rate constant of intrinsic decay of ^{1}BODIPY* to form ground state. k_{5u} and k_{6u} are the rate constants of charge recombination of CS state to form ground state and ^{3}BODIPY*, respectively. p is the percentage of QD with one or more BODIPY attached.

i	1	2	3	4
a_i	0.053±0.003	0.413±0.021	0.484±0.020	0.049±0.029
$1/k_{0i}$	(45.2±8.1) ps	(4.67±0.26) ns	(21.7±1.1) ns	(273±37) ns
j	1	2		
c_{1j}	0.243±0.014	0.757±0.014		
$1/k_{1j}$	(213±20) ps	/		
f	1	2		
c_{2f}	0.220±0.025	0.780±0.025		
$1/k_{2f}$	(193±20) ps	(1.47±0.09) ns		
u	1	2		
b_u	0.593	0.407		
$1/k_{3u}$	10.3 ns	569 ps		
$1/k_{4u}$	4.20 ns	4.20 ns		
$1/k_{5u}$	188 ns	28.6 ns		
$1/k_{6u}$	252 ns	23.0 ns		
p	0.720±0.008			

Efficiency of hole transfer, FRET and the final ^{3}BODIPY* generation can be determined from

branching ratio, which could be calculated from rate constants of the involved photophysical processes shown in Table 7.1. The efficiency of hole transfer is:

$$\eta_{hole\ transfer} = p\sum_{i=1}^{4}\sum_{f=1}^{2}\sum_{j=1}^{2}\left(a_i c_{1j} c_{2f}\frac{k_{1j}}{k_{0i}+k_{1j}+k_{2f}}\right) = 12.9(\pm 2.9)\% \quad \text{Eq. 7.10}$$

The efficiency of FRET is:

$$\eta_{FRET} = p\sum_{i=1}^{4}\sum_{f=1}^{2}\sum_{j=1}^{2}\left(a_i c_{1j} c_{2f}\frac{k_{2f}}{k_{0i}+k_{1j}+k_{2f}}\right) = 49.5(\pm 11.4)\% \quad \text{Eq. 7.11}$$

The efficiency of ^{3}BODIPY* generation from direct hole transfer pathway (blue arrows in Figure 7.7c) is:

$$\eta_{[T]\ from\ hole\ transfer} = p\sum_{i=1}^{4}\sum_{f=1}^{2}\sum_{j=1}^{2}\sum_{u=1}^{2}\left(a_i c_{1j} c_{2f}\frac{k_{1j}}{k_{0i}+k_{1j}+k_{2f}} * \frac{k_{6u}}{k_{5u}+k_{6u}}\right) =$$

$$6.18(\pm 1.39)\% \quad \text{Eq. 7.12}$$

The efficiency of ^{3}BODIPY* generation from FRET pathway (red arrows in Figure 7.7c) is:

$$\eta_{[T]\ from\ FRET} = p\sum_{i=1}^{4}\sum_{f=1}^{2}\sum_{j=1}^{2}\sum_{u=1}^{2}\left(a_i c_{1j} c_{2f}\frac{k_{2f}}{k_{0i}+k_{1j}+k_{2f}} * \frac{k_{3u}}{k_{3u}+k_{4u}} * \frac{k_{6u}}{k_{5u}+k_{6u}}\right) =$$

$$13.5(\pm 3.1)\% \quad \text{Eq. 7.13}$$

As shown in Figure 7.7c, the relatively low efficiency of ^{3}BODIPY* generation is mainly due to several loss channels, including the decay of QD*-BODIPY and QD-^{1}BODIPY* to the ground state and the recombination of CS state to form the ground state. Because of additional step of forming QD-^{1}BODIPY* for FRET pathway to generate CS state, this pathway experiences more loss channels than direct hole transfer pathway. In order to further increase the QD sensitized ^{3}BODIPY* generation efficiency, the efficiencies of both the hole transfer and FRET pathways should be improved.

7.2.4 Discussion

Our result demonstrates that in QD-BODIPY complexes, QD sensitized ^{3}BODIPY*

generation occurs through a CS intermediate state, generated through either direct hole transfer or sequential FRET/electron transfer **(Figure 1a**), while direct DET from the excited QD is not competitive. Similar indirect scheme of triplet generation through CS intermediates has been proposed in PbS QD-pentacene,[52] perovskite QD-tetracene [54] and CdS QD-alizarin complexes.[57] In these systems, hole transfer from the QD to acceptors are all energetically allowed and their rates are fast, outcompeting the direct DET process. While in systems such as CdSe QD-anthracene,[31-32] CdSe QD-oligothiophene[66] and perovskite QD-naphthalene,[54] charge transfer pathway is energetically uphill, and triplet excited state is generated exclusively through the slower direct DET pathway. While for triplet excited state generation through step-wise hole transfer/electron transfer pathways, the rate of each step depends on the coupling matrix elements for hole or electron transfer only,[67] direct DET is a concerted electron and hole transfer process, whose coupling matrix element is a product of both the electron and hole transfer integrals.[23, 27, 53] As a result, direct DET is often slower than sequential electron and hole transfer if both processes are energetically allowed. In addition, one should note that the energy of the CS state should be higher than that of the triplet excited state product to enable triplet excited state generation through the sequential charge transfer pathway.[10, 54, 56] Otherwise, the formation of CS state from hole transfer from QD could be detrimental to triplet sensitization, as it can only decay back to the ground state.[47]

Another significant finding of our study is that FRET from the QD to acceptor can also contribute to the generation of triplet excited state of the acceptor through CS intermediate state. The FRET pathway is often neglected in previous QD sensitized triplet exciton harvesting systems, either due to unfavorable spectral overlap,[52] or the resulting singlet excited state of the acceptor cannot lead to the formation of triplet excited state.[57] Our study suggests that the contribution of

FRET pathway to CS intermediate state and the triplet excited state product cannot be ignored if it is allowed and the resulting singlet excited state of the acceptor can form triplet state through charge transfer intermediates. Finally, because our study is based on TA kinetics, in which the CdSe QD exciton bleach signal mainly probes the conduction band edge electron population,[60] the nature of the hole states is not directly probed. Previous studies have demonstrated trapped hole transfer or trapped exciton energy transfer from nanocrystals to the acceptors.[68-69] Therefore, it is possible that the trapped holes and excitons also contribute to the ^{3}BODIPY* generation in CdSe QD/BODIPY complexes, and their relative contributions should be fully investigated in future studies.

7.3 Conclusion

In summary, we demonstrate QD-sensitized ^{3}BODIPY* generation in CdSe QD-BODIPY complexes by exciting the CdSe QD at 500 nm. A charge separated state ($QD^{-\cdot}$-$BODIPY^{+\cdot}$), which is populated by direct hole transfer from the QD* or the sequential FRET to BODIPY and electron transfer from ^{1}BODIPY* to QD, is shown to be the key intermediate state for ^{3}BODIPY* formation. From this intermediate state, further charge recombination (i.e. electron transfer from $QD^{-\cdot}$ to $BODIPY^{+\cdot}$) results in the generation of ^{3}BODIPY* or the ground state. In comparison to these indirect pathways, direct DET from the QD to BODIPY is not kinetically competitive because of its much slower rate. The overall ^{3}BODIPY* generation efficiency is determined to be (19.7±3.4) %, which may be further increased by improving the efficiency of hole transfer and FRET in future experiments. Our finding suggests that sequential charge transfer is an efficient way for QD sensitized triplet excited state formation, outcompeting the direct DET pathway.

7.4 Reference

1. Singh-Rachford, T. N.; Castellano, F. N., Photon upconversion based on sensitized triplet–triplet annihilation. *Coord. Chem. Rev.* **2010,** *254* (21-22), 2560-2573.
2. Yanai, N.; Kimizuka, N., New Triplet Sensitization Routes for Photon Upconversion: Thermally Activated Delayed Fluorescence Molecules, Inorganic Nanocrystals, and Singlet-to-Triplet Absorption. *Acc. Chem. Res.* **2017,** *50* (10), 2487-2495.
3. Serevičius, T.; Komskis, R.; Adomėnas, P.; Adomėnienė, O.; Kreiza, G.; Jankauskas, V.; Kazlauskas, K.; Miasojedovas, A. n.; Jankus, V.; Monkman, A.; Juršėnas, S., Triplet–Triplet Annihilation in 9,10-Diphenylanthracene Derivatives: The Role of Intersystem Crossing and Exciton Diffusion. *The Journal of Physical Chemistry C* **2017,** *121* (15), 8515-8524.
4. Li, X. S.; Kolemen, S.; Yoon, J.; Akkaya, E. U., Activatable Photosensitizers: Agents for Selective Photodynamic Therapy. *Adv. Funct. Mater.* **2017,** *27* (5), 1604053.
5. Majumdar, P.; Nomula, R.; Zhao, J., Activatable triplet photosensitizers: magic bullets for targeted photodynamic therapy. *J. Mater. Chem. C* **2014,** *2* (30), 5982-5997.
6. Wohnhaas, C.; Mailänder, V.; Dröge, M.; Filatov, M. A.; Busko, D.; Avlasevich, Y.; Baluschev, S.; Miteva, T.; Landfester, K.; Turshatov, A., Triplet–Triplet Annihilation Upconversion Based Nanocapsules for Bioimaging Under Excitation by Red and Deep-Red Light. *Macromolecular Bioscience* **2013,** *13* (10), 1422-1430.
7. You, Y., Phosphorescence bioimaging using cyclometalated Ir(III) complexes. *Curr Opin Chem Biol* **2013,** *17* (4), 699-707.
8. Minaev, B.; Baryshnikov, G.; Agren, H., Principles of phosphorescent organic light emitting devices. *Physical Chemistry Chemical Physics* **2014,** *16* (5), 1719-1758.
9. Liu, X.-K.; Chen, W.; Thachoth Chandran, H.; Qing, J.; Chen, Z.; Zhang, X.-H.; Lee, C.-S., High-Performance, Simplified Fluorescence and Phosphorescence Hybrid White Organic Light-Emitting Devices Allowing Complete Triplet Harvesting. *ACS Applied Materials & Interfaces* **2016,** *8* (39), 26135-26142.
10. Zhao, J.; Xu, K.; Yang, W.; Wang, Z.; Zhong, F., The triplet excited state of Bodipy: formation, modulation and application. *Chemical Society Reviews* **2015,** *44* (24), 8904-8939.
11. Jankus, V.; Data, P.; Graves, D.; McGuinness, C.; Santos, J.; Bryce, M. R.; Dias, F. B.; Monkman, A. P., Highly Efficient TADF OLEDs: How the Emitter–Host Interaction Controls Both the Excited State Species and Electrical Properties of the Devices to Achieve Near 100% Triplet Harvesting and High Efficiency. *Advanced Functional Materials* **2014,** *24* (39), 6178-6186.
12. Zhao, J.; Chen, K.; Hou, Y.; Che, Y.; Liu, L.; Jia, D., Recent progress in heavy atom-free organic compounds showing unexpected intersystem crossing (ISC) ability. *Organic & Biomolecular Chemistry* **2018,** *16* (20), 3692-3701.
13. Zhao, W.; Castellano, F. N., Upconverted Emission from Pyrene and Di-tert-butylpyrene Using Ir(ppy)3 as Triplet Sensitizer. *J. Phys. Chem. A* **2006,** *110* (40), 11440-11445.
14. Zhao, J.; Wu, W.; Sun, J.; Guo, S., Triplet photosensitizers: from molecular design to applications. *Chemical Society Reviews* **2013,** *42* (12), 5323-5351.
15. Kozlov, D. V.; Castellano, F. N., Anti-Stokes delayed fluorescence from metal–organic bichromophores. *Chemical Communications* **2004,** (24), 2860-2861.
16. Zhao, J.; Ji, S.; Guo, H., Triplet–triplet annihilation based upconversion: from triplet sensitizers and triplet acceptors to upconversion quantum yields. *RSC Advances* **2011,** *1* (6), 937-950.
17. L. J. Dexter, D., A Theory of Sensitized Luminescence in Solid. *J. Chem. Phys.* **1953,** *21*, 836-

850.
18. Tyson, D. S.; Bignozzi, C. A.; Castellano, F. N., Metal−Organic Approach to Binary Optical Memory. *Journal of the American Chemical Society* **2002,** *124* (17), 4562-4563.
19. Gust, D.; Moore, T. A.; Moore, A. L.; Lee, S.-J.; Bittersmann, E.; Luttrull, D. K.; Rehms, A. A.; DeGraziano, J. M.; Ma, X. C.; Gao, F.; Belford, R. E.; Trier, T. T., Efficient Multistep Photoinitiated Electron Transfer in a Molecular Pentad. *Science* **1990,** *248* (4952), 199.
20. Carbonera, D.; Di Valentin, M.; Corvaja, C.; Agostini, G.; Giacometti, G.; Liddell, P. A.; Kuciauskas, D.; Moore, A. L.; Moore, T. A.; Gust, D., EPR Investigation of Photoinduced Radical Pair Formation and Decay to a Triplet State in a Carotene−Porphyrin−Fullerene Triad. *Journal of the American Chemical Society* **1998,** *120* (18), 4398-4405.
21. Dance, Z. E. X.; Mi, Q.; McCamant, D. W.; Ahrens, M. J.; Ratner, M. A.; Wasielewski, M. R., Time-Resolved EPR Studies of Photogenerated Radical Ion Pairs Separated by p-Phenylene Oligomers and of Triplet States Resulting from Charge Recombination. *J. Phys. Chem. B* **2006,** *110* (50), 25163-25173.
22. Chen, K.; Yang, W.; Wang, Z.; Iagatti, A.; Bussotti, L.; Foggi, P.; Ji, W.; Zhao, J.; Di Donato, M., Triplet Excited State of BODIPY Accessed by Charge Recombination and Its Application in Triplet–Triplet Annihilation Upconversion. *The Journal of Physical Chemistry A* **2017,** *121* (40), 7550-7564.
23. Skourtis, S. S.; Liu, C.; Antoniou, P.; Virshup, A. M.; Beratan, D. N., Dexter energy transfer pathways. *Proc. Natl. Acad. Sci. U S A* **2016,** *113* (29), 8115-20.
24. You, Z.-Q.; Hsu, C.-P., Theory and calculation for the electronic coupling in excitation energy transfer. *Int. J. Quantum Chem.* **2014,** *114* (2), 102-115.
25. You, Z.-Q.; Hsu, C.-P.; Fleming, G. R., Triplet-triplet energy-transfer coupling: Theory and calculation. *The Journal of Chemical Physics* **2006,** *124* (4), 044506.
26. Lin, S. H., On the Theory of Non-Radiative Transfer of Electronic Excitation. *Proc. R. Soc. Lond. A.* **1973,** *335* (1600), 51.
27. Closs, G. L.; Johnson, M. D.; Miller, J. R.; Piotrowiak, P., A Connection between Intramolecular Long-Range Electron, Hole, and Triplet Energy Transfers. *J. Am. Chem. Soc.* **1989,** *111* (10), 3751-3753.
28. Subotnik, J. E.; Vura-Weis, J.; Sodt, A. J.; Ratner, M. A., Predicting accurate electronic excitation transfer rates via marcus theory with Boys or Edmiston-Ruedenberg localized diabatization. *J. Phys. Chem. A* **2010,** *114* (33), 8665-75.
29. Curutchet, C.; Voityuk, A. A., Distance Dependence of Triplet Energy Transfer in Water and Organic Solvents: A QM/MD Study. *The Journal of Physical Chemistry C* **2012,** *116* (42), 22179-22185.
30. Köhler, A.; Bässler, H., What controls triplet exciton transfer in organic semiconductors? *J. Mater. Chem.* **2011,** *21* (12), 4003-4011.
31. Mongin, C.; Garakyaraghi, S.; Razgoniaeva, N.; Zamkov, M.; Castellano, F. N., Direct observation of triplet energy transfer from semiconductor nanocrystals. *Science* **2016,** *351* (6271), 369-72.
32. Piland, G. B.; Huang, Z. Y.; Tang, M. L.; Bardeen, C. J., Dynamics of Energy Transfer from CdSe Nanocrystals to Triplet States of Anthracene Ligand Molecules. *J. Phys. Chem. C* **2016,** *120* (11), 5883-5889.
33. Li, X.; Huang, Z.; Zavala, R.; Tang, M. L., Distance-Dependent Triplet Energy Transfer between CdSe Nanocrystals and Surface Bound Anthracene. *J. Phys. Chem. Lett.* **2016,** *7* (11), 1955-9.

34. Luo, X.; Lai, R.; Li, Y.; Han, Y.; Liang, G.; Liu, X.; Ding, T.; Wang, J.; Wu, K., Triplet Energy Transfer from CsPbBr3 Nanocrystals Enabled by Quantum Confinement. *J. Am. Chem. Soc.* **2019,** *141* (10), 4186-4190.
35. Norris, D. J.; Bawendi, M. G., Structure in the lowest absorption feature of CdSe quantum dots. *The Journal of Chemical Physics* **1995,** *103* (13), 5260-5268.
36. Scholes, G. D.; Rumbles, G., Excitons in nanoscale systems. *Nat. Mater.* **2006,** *5* (9), 683-96.
37. Ekimov, A. I.; Hache, F.; Schanne-Klein, M. C.; Ricard, D.; Flytzanis, C.; Kudryavtsev, I. A.; Yazeva, T. V.; Rodina, A. V.; Efros, A. L., Absorption and intensity-dependent photoluminescence measurements on CdSe quantum dots: assignment of the first electronic transitions. *J. Opt. Soc. Am. B* **1993,** *10* (1), 100-107.
38. Yu, W. W.; Qu, L. H.; Guo, W. Z.; Peng, X. G., Experimental determination of the extinction coefficient of CdTe, CdSe, and CdS nanocrystals. *Chem. Mater.* **2003,** *15* (14), 2854-2860.
39. Cademartiri, L.; Montanari, E.; Calestani, G.; Migliori, A.; Guagliardi, A.; Ozin, G. A., Size-Dependent Extinction Coefficients of PbS Quantum Dots. *J. Am. Chem. Soc.* **2006,** *128* (31), 10337-10346.
40. Zhu, H. M.; Lian, T. Q., Wavefunction engineering in quantum confined semiconductor nanoheterostructures for efficient charge separation and solar energy conversion. *Energy & Environmental Science* **2012,** *5* (11), 9406-9418.
41. Zhu, H.; Song, N.; Lian, T., Controlling charge separation and recombination rates in CdSe/ZnS type I core-shell quantum dots by shell thicknesses. *J. Am. Chem. Soc.* **2010,** *132* (42), 15038-45.
42. Boles, M. A.; Ling, D.; Hyeon, T.; Talapin, D. V., The surface science of nanocrystals. *Nat Mater* **2016,** *15* (2), 141-53.
43. Kim, S.; Fisher, B.; Eisler, H. J.; Bawendi, M., Type-II quantum dots: CdTe/CdSe(core/shell) and CdSe/ZnTe(core/shell) heterostructures. *J Am Chem Soc* **2003,** *125* (38), 11466-7.
44. Wu, M.; Congreve, D. N.; Wilson, M. W. B.; Jean, J.; Geva, N.; Welborn, M.; Van Voorhis, T.; Bulović, V.; Bawendi, M. G.; Baldo, M. A., Solid-state infrared-to-visible upconversion sensitized by colloidal nanocrystals. *Nat. Photon.* **2015,** *10*, 31-34.
45. Huang, Z. Y.; Li, X.; Yip, B. D.; Rubalcava, J. M.; Bardeen, C. J.; Tang, M. L., Nanocrystal Size and Quantum Yield in the Upconversion of Green to Violet Light with CdSe and Anthracene Derivatives. *Chem. Mater.* **2015,** *27* (21), 7503-7507.
46. Huang, Z.; Tang, M. L., Designing Transmitter Ligands That Mediate Energy Transfer between Semiconductor Nanocrystals and Molecules. *J. Am. Chem. Soc.* **2017,** *139* (28), 9412-9418.
47. Huang, Z.; Xu, Z.; Mahboub, M.; Li, X.; Taylor, J. W.; Harman, W. H.; Lian, T.; Tang, M. L., PbS/CdS Core-Shell Quantum Dots Suppress Charge Transfer and Enhance Triplet Transfer. *Angew. Chem. Int. Ed.* **2017,** *56* (52), 16583-16587.
48. Mahboub, M.; Maghsoudiganjeh, H.; Pham, A. M.; Huang, Z. Y.; Tang, M. L., Triplet Energy Transfer from PbS(Se) Nanocrystals to Rubrene: the Relationship between the Upconversion Quantum Yield and Size. *Adv. Funct. Mater.* **2016,** *26* (33), 6091-6097.
49. Huang, Z. Y.; Xia, P.; Megerdich, N.; Fishman, D. A.; Vullev, V. I.; Tang, M. L., ZnS Shells Enhance Triplet Energy Transfer from CdSe Nanocrystals for Photon Upconversion. *ACS Photonics* **2018,** *5* (8), 3089-3096.
50. Huang, Z.; Li, X.; Mahboub, M.; Hanson, K. M.; Nichols, V. M.; Le, H.; Tang, M. L.; Bardeen, C. J., Hybrid Molecule-Nanocrystal Photon Upconversion Across the Visible and Near-Infrared. *Nano Lett* **2015,** *15* (8), 5552-7.

51. Bender, J. A.; Raulerson, E. K.; Li, X.; Goldzak, T.; Xia, P.; Van Voorhis, T.; Tang, M. L.; Roberts, S. T., Surface States Mediate Triplet Energy Transfer in Nanocrystal-Acene Composite Systems. *J. Am. Chem. Soc.* **2018,** *140* (24), 7543-7553.
52. Garakyaraghi, S.; Mongin, C.; Granger, D. B.; Anthony, J. E.; Castellano, F. N., Delayed Molecular Triplet Generation from Energized Lead Sulfide Quantum Dots. *J. Phys. Chem. Lett.* **2017,** *8* (7), 1458-1463.
53. Harcourt, R. D.; Scholes, G. D.; Ghiggino, K. P., Rate expressions for excitation transfer. II. Electronic considerations of direct and through–configuration exciton resonance interactions. *J. Chem. Phys.* **1994,** *101* (12), 10521-10525.
54. Luo, X.; Han, Y.; Chen, Z.; Li, Y.; Liang, G.; Liu, X.; Ding, T.; Nie, C.; Wang, M.; Castellano, F. N.; Wu, K., Mechanisms of triplet energy transfer across the inorganic nanocrystal/organic molecule interface. *Nat. Commun.* **2020,** *11* (1), 28.
55. de Mello Donegá, C.; Bode, M.; Meijerink, A., Size- and temperature-dependence of exciton lifetimes in CdSe quantum dots. *Phys. Rev. B* **2006,** *74* (8), 085320.
56. Weinberg, D. J.; Dyar, S. M.; Khademi, Z.; Malicki, M.; Marder, S. R.; Wasielewski, M. R.; Weiss, E. A., Spin-Selective Charge Recombination in Complexes of CdS Quantum Dots and Organic Hole Acceptors. *J. Am. Chem. Soc.* **2014,** *136* (41), 14513-14518.
57. Wang, J.; Ding, T.; Nie, C.; Wang, M.; Zhou, P.; Wu, K., Spin-Controlled Charge Recombination Pathways across the Inorganic/Organic Interface. *J. Am. Chem. Soc.* **2020,** *142* (10), 4723-4731.
58. Hoffman, J. B.; Choi, H.; Kamat, P. V., Size-Dependent Energy Transfer Pathways in CdSe Quantum Dot–Squaraine Light-Harvesting Assemblies: Förster versus Dexter. *The Journal of Physical Chemistry C* **2014,** *118* (32), 18453-18461.
59. Jin, T.; Uhlikova, N.; Xu, Z.; Zhu, Y.; Huang, Y.; Egap, E.; Lian, T., Enhanced triplet state generation through radical pair intermediates in BODIPY-quantum dot complexes. *J. Chem. Phys.* **2019,** *151* (24), 241101.
60. Huang, J. E.; Huang, Z. Q.; Jin, S. Y.; Lian, T. Q., Exciton Dissociation in CdSe Quantum Dots by Hole Transfer to Phenothiazine. *Journal of Physical Chemistry C* **2008,** *112* (49), 19734-19738.
61. Huang, J.; Huang, Z.; Yang, Y.; Zhu, H.; Lian, T., Multiple Exciton Dissociation in CdSe Quantum Dots by Ultrafast Electron Transfer to Adsorbed Methylene Blue. *Journal of the American Chemical Society* **2010,** *132* (13), 4858-4864.
62. McArthur, E. A.; Morris-Cohen, A. J.; Knowles, K. E.; Weiss, E. A., Charge Carrier Resolved Relaxation of the First Excitonic State in CdSe Quantum Dots Probed with Near-Infrared Transient Absorption Spectroscopy. *The Journal of Physical Chemistry B* **2010,** *114* (45), 14514-14520.
63. Valeur, B.; Berberan‐Santos, N., Mário, Excitation Energy Transfer. In *Molecular Fluorescence: Principles and Applications*, *Second Edition*, Wiley-VCH, Weinheim: 2012; pp 213–261.
64. Fisher, B. R.; Eisler, H.-J.; Stott, N. E.; Bawendi, M. G., Emission Intensity Dependence and Single-Exponential Behavior In Single Colloidal Quantum Dot Fluorescence Lifetimes. *The Journal of Physical Chemistry B* **2004,** *108* (1), 143-148.
65. Chen, J.; Wu, K.; Rudshteyn, B.; Jia, Y.; Ding, W.; Xie, Z. X.; Batista, V. S.; Lian, T., Ultrafast Photoinduced Interfacial Proton Coupled Electron Transfer from CdSe Quantum Dots to 4,4'-Bipyridine. *J. Am. Chem. Soc.* **2016,** *138* (3), 884-92.
66. Xu, Z.; Jin, T.; Huang, Y.; Mulla, K.; Evangelista, F. A.; Egap, E.; Lian, T., Direct triplet sensitization of oligothiophene by quantum dots. *Chem. Sci.* **2019,** *10* (24), 6120-6124.

67. Marcus, R. A., Electron transfer reactions in chemistry. Theory and experiment. *Reviews of Modern Physics* **1993,** *65* (3), 599-610.
68. Wu, K.; Du, Y.; Tang, H.; Chen, Z.; Lian, T., Efficient Extraction of Trapped Holes from Colloidal CdS Nanorods. *J Am Chem Soc* **2015,** *137* (32), 10224-30.
69. Han, Y.; He, S.; Luo, X.; Li, Y.; Chen, Z.; Kang, W.; Wang, X.; Wu, K., Triplet Sensitization by "Self-Trapped" Excitons of Nontoxic CuInS2 Nanocrystals for Efficient Photon Upconversion. *J. Am. Chem. Soc.* **2019,** *141* (33), 13033-13037.

Chapter 8. Conclusion and Outlook

Quantum dot (QD) sensitized or assisted molecular triplet excited state generation (TESG) is promising in applications involving triplet excited states, which include photon-upconversion, photodynamic therapy and photocatalytic reactions. Despite the emerging progress achieved in integrating QD-molecule complexes into these systems, the TESG mechanism in the complexes has remained ambiguous, which could impede further efficiency optimization and system design.

This dissertation aims to probe and unravel the TESG mechanism in QD-molecule complexes. In Chapter 3, we tested whether traditional triplet energy transfer (TET) theory in molecular donor-acceptor complexes is applicable in QD sensitized TET. Coupling strength of TET from CdSe/CdS core-shell QD to attached anthracene derivative (ACA) was measured and calculated based on results of transient absorption spectroscopy (TA) and time-resolved photoluminescence (TRPL). The results show the shallow dependence of TET coupling strength on CdS shell thickness compared to the dependence of electron transfer (ET) and hole transfer (HT) coupling strength on shell thickness and are contradictory to traditional TET theory. In order to rationalize the results, we propose that besides charge transfer virtual states, virtual exciton states with electron/hole in levels with higher energies than $1S_e$ and $1S_h$ could be involved in TET coupling strength due to smaller energy difference between $1S_h$ hole level and higher hole levels compared to molecules. The study reveals that simple application of TET theory in molecule systems to QD sensitized TET may not be appropriate.

In Chapter 4, we studied the correlation of bright and dark exciton states of QD, which are unique QD properties, with QD sensitized TET. Equilibrium between bright and dark states was systematically tuned by varying surrounding temperature, and TET dynamics was monitored with

TA. By analyzing kinetics of acceptor triplet excited state growth, we demonstrated the non-zero TET rate from both bright and dark states, with bright state TET rate larger than that of dark states. The results suggest significant contribution of bright states to TET and can be explained by the triplet-spin-like wavefunction components with the same electron and hole spins in both bright and dark state wavefunctions, although total angular momentum projection instead of electron/hole spin is the good quantum number in describing QD exciton states. The study indicates that simple analogy between QD bright/dark states and singlet/triplet excited states in molecules cannot be made, and mechanisms for QD sensitized TET are different from those for molecule sensitized TET in certain aspects.

In Chapter 5, we probed the role of QD trap states in QD sensitized TET by TA and TRPL. With CdSe QD-ACA as model systems, we show that both band edge excitons and trap states can undergo TET from QD to generate ACA triplet excited states. Rate of TET from band edge excitons is significantly larger than that from trap states, and rate of TET from trap states decreases with decreasing trap state energies. Because of the prevalence of trap state population in bare CdSe QD, the contribution of trap states to overall TET is larger than band edge excitons. The slower TET rate from trap states also suggest that passivating surface or optimizing synthesis to eliminate or decrease trap states can help to improve the overall TET rate from QD.

In Chapter 6 and Chapter 7, we studied the TESG in CdSe QD-modified boron dipyrromethene (BODIPY) complex with charge separated intermediate states with TA. In Chapter 6, it was demonstrated that excitation of BODIPY results in electron transfer from BODIPY to QD to form charge separated state, and charge recombination forms BODIPY triplet excited states. In Chapter 7, we demonstrated that excitation of CdSe QD in QD-BODIPY complex also leads to BODIPY triplet excited state formation with charge separated state intermediates.

The intermediate can be populated by hole transfer from QD to BODIPY or by Förster energy transfer from QD to BODIPY followed by electron transfer from BODIPY to QD. BODIPY triplet state generation through charge transfer state intermediate outcompetes the direct TET pathway, suggesting that such pathways are promising schemes for efficient TESG.

In future research of TESG mechanism in QD-molecule systems, more detailed theoretical calculation is necessary to quantitatively demonstrate the mechanisms. Theoretical evaluation in TET coupling strength involving higher QD exciton states will help to better rationalize the shallow shell thickness dependence of TET coupling strength in CdSe/CdS QD systems. Simulation to evaluate TET rate from wavefunction overlap between bright/dark states or trap states and acceptor triplet excited state will also help to clarify the role of these unique QD exciton properties in TESG mechanism. Although research shows the TESG in QD systems involving charge transfer intermediate states, the exact mechanism of charge recombination to form triplet states has been unclear and awaits future research. More interesting question is whether these proposed TESG mechanisms can be generalized to all QD-molecule systems, or additional consideration should be included for specific system. Solving all these unanswered problems will pave the way to future application of QD based TESG systems by providing mechanistic insights.